UNIVERSITY OF OXFORD

DEPARTMENT OF CHEMISTRY

Catalytic Conversion of Biomass-Derived Platform Molecules Over Zeolites

BY

IVO FREITAS TEIXEIRA

WOLFSON COLLEGE



A THESIS SUBMITTED FOR THE DEGREE

DOCTOR OF PHILOSOPHY

2017

Catalytic Conversion of Biomass-Derived Platform Molecules Over Zeolites

BY

Ivo Freitas Teixeira

705583

Wolfson College

Supervisor

Prof. S. C. Edman Tsang

Internal Assessor

Professor Kylie Vincent

A THESIS SUBMITTED FOR THE DEGREE

DOCTOR OF PHILOSOPHY

2017

Abstract

The conversion of lignocellulosic biomass to renewable fuels and chemicals has attracted significant attention as a key technology to enable the replacement of petroleum. Lignocellulosic biomass is the most promising renewable carbon energy source, as it is widely available around the world at a relatively low cost. Although it is the most abundant plant material resource, its conversion into chemicals faces a range of technological and economic challenges. In order to overcome these challenges, several different processes to obtain chemicals and biofuels from biomass are currently under development. The most promising is the multistep strategy using platform molecules as intermediates. The most important platform molecules that can be obtained from biomass in good yields are biomass-derived furans, such as furfural, 5-hydroxymethylfurfural (HMF), 2-methylfuran (MF), furan and 2,5-dimethylfuran (DMF). Recently, the Diels-Alder (DA) cycloaddition of biomass-derived furans, especially DMF, MF and furan, with dienes (mainly ethylene) has emerged as a prominent route to obtain aromatics, such as benzene, toluene and xylene (BTX). The BTX are essential for the petrochemical industry, since it is the raw material for the most consumed polymers and chemicals. As millions of tons of BTX are produced annually exclusively from fossil sources, it has now become extremely important develop technologies to obtain BTX from completely renewable sources.

In this context, the present thesis is focused on the investigation of a completely new/renewable facilitated process to convert DMF into aromatics over zeolites, which uses ethanol as a source of dienophile. The use of liquid ethanol instead of gaseous ethylene, as the source of dienophile in this one pot solvent free synthesis, renders the aromatics production in much simpler and renewable way, which avoids the use of

ethylene at high pressure. More importantly, both our studies, experimental and theoretical, demonstrate that the use of ethanol instead of ethylene, results in significantly higher rates and higher selectivity to aromatics, due to lower activation barriers over the solid acid sites. The reaction mechanism was investigated by combining high quality synchrotron X-Ray diffraction (SXRD) data and Rietveld refinement analysis with detailed kinetic measurements and high-level first principles calculations. The results confirm that the reaction takes place *via* a facilitated process, where the preferential protonation of the ethanol molecule by the Brønsted acid site (BAS) and the presence of a water molecule formed by the ethanol dehydration inside the restricted pore of the zeolite catalyst lead to lower activation barriers over the BAS, higher rates and higher selectivity to aromatics.

In this study, it was also demonstrated how the Ethanol/DMF reaction is influenced by the strength of the acid sites in the zeolites. Using SXRD in combination with the basic probe molecule pyridine and ^{27}Al NMR, it was possible to link the Brønsted sites in 3-D structure and global atomic arrangements with the acidity. After locating and determining the nature of the BAS, the selective site blockage strategy by K^+ exchange was employed to control the product distribution for the DMF transformation reaction into aromatics. Comparing the product distribution obtained for the pure catalyst and for the catalysts with the partially and totally blocked BAS, it was possible to confirm that the Diels-Alder cycloaddition is catalysed by strong acid sites while hydrolysis of furan takes place over weak acid sites. This was the first time that a study correlates the nature of the BAS with product distribution for the complex reaction of DMF conversion into aromatics *via* Diels-Alder cycloaddition. This understanding is extremely important to allow more superior catalytic performances for a wider range of Biomass-derived furans.

Finally, the novel catalytic reaction presented in this thesis was investigated as a new strategy to convert biomass-derived furan into aromatics with high selectivity to aromatics, while reducing the production of the side product benzofuran. The use of ethanol as a source of dienophile in the reaction with furan showed high selectivity to aromatics, especially for the highly desired aromatic product ethylbenzene, while the formation of the side product benzofuran formation was considerably reduced. Further investigations by detailed kinetic experiments, SXRD and FTIR experiments showed that the key step to prevent the benzofuran formation and favour the aromatic products is the alkylation of the furan molecule by an ethyl species formed from the ethanol dehydration. This step occurs before the Diels-Alder (DA) reaction and has a double effect to promote the aromatic products. The substituent alkyl groups on the furan ring create greater steric hindrance, thus avoiding the direct coupling reaction between two furan molecules to form benzofuran. Furthermore, the alkylated furans (dienophile) undergo DA cycloaddition more readily, due to its higher energy HOMO orbital.

The novel catalytic reaction presented in this thesis is a breakthrough in the conversion of biomass derivatives into aromatics, making the reaction simpler and entirely renewable. Moreover, this novel approach has proved to be versatile and very useful to allow better yields for challenging biomass-derived furans, such as furan itself. More generally, further investigations into Diels–Alder cycloaddition reactions with alcohols as a source of dienophiles may allow activity and stereochemistry to be tailored, extending its application far beyond biomass conversion.

Declaration

I confirm that this in my own work and the use of all material from other sources has been properly and full acknowledged.

Ivo F. Teixeira

Acknowledgements

First and foremost, I would like to thank Professor Edman Tsang for providing me the opportunity to join his research group and pursue my research interests with total independency under his guidance and support. I would also like to thank the CNPq and the program Science without Border (SwB) from Brazilian government for my scholarship and financial support. The Department of Chemistry and the University of Oxford are thanked for provision of research environment and facilities necessary for my research.

This thesis and all my publications in this four years are results of intense collaborations with many colleagues in our research group, which I would like to thank for the assistance and support: Dr. Benedict T.W. Lo and Dr. Lin Ye for the SXRD experiments and interpretations and thesis review; Dr. Abdullah Khan for the collaborations on Carbon Nitrides topic; Yung-Kang Peng for the collaborations on Trimethylphosphine-assisted Mapping of zeolites and metal oxides; In addition to all these peoples who have contributed to the understanding of my research, I am also thankful to Dr. Ian McPherson and Molly Li for being kind readers, their comments and correction were particular important to improve the quality of this manuscript. I would also like to thank the Tsang group members, past and present for their help and support and entertainment throughout my DPhil project. Dr Giannis Mpourmpakis and Pavio Kostetskyy (University of Pittsburgh, USA) are thanked for the theoretical calculations.

I would like to thank my parents and family for their unconditional love and support, especially my brother sorry for the years of absence. My friends Natália Vieira (in particular because she asked for it and deserve), Érica Neves, Priscila Lange,

Henrique Esteves, Alex Duarte, Wilian Cortopassi, Eric Mazzer, Sérgio Kogikoski, Diana Rostirolla for never let me have lunch alone. I would also like to thank all these friends again together with Vanessa Rodrigues, Livia Ribeiro, Ariane Gomes, Joana Guiro, Eduardo Rech, Rodolfo de Abreu and Luiza Lourenço for all the moments of “creative leisure” and inspiration, and above all for all the important knowledge shared. Thanks all the loyal friends which I left in Brazil Walace Doti, Tamyris Cunha and Marina Caneschi, especially Ingrid Silva for the resilient friendship.

Finally, I would like to thank Fernando owner of Fernando’s Café and its staff for the delicious Brazilian food, which made this four years much more bearable.

List of Publications

Biomass (Thesis Topic)

1. I. F. Teixeira, C. C. Tang, G. and S. C. E. Tsang, *Cycloaddition method for producing aromatic hydrocarbons*. Protocol Number at **Chinese Patent Office**: 201510656885.5, 2016.

2. I. F. Teixeira, B. T. W. Lo, P. Kostetskyy, M. Stamatakis, L. Ye, C. C. Tang, G. Mpourmpakis and S. C. E. Tsang, *From Biomass-Derived Furans to Aromatics with Ethanol over Zeolite.* **Angewandte Chemie International Edition**, 2016. 55: p. 13061-13066.
3. L. Ye, I. F. Teixeira, B. T. W. Lo, P. Zhao, and S.C. Edman Tsang, *Spatial Differentiation of Brønsted Acid Sites by Probe Molecule in Zeolite USY using Synchrotron X-ray Powder Diffraction.* **Chemical Communications,** 2017. Accepted.
4. I. F. Teixeira, B. T. W. Lo, P. Kostetskyy, L. Ye, G. Mpourmpakis and S. C. E. Tsang, *Direct Catalytic Conversion of Biomass-Derived Furan and Ethanol to Ethyl-benzene.* **ACS Catalysis**, 2017. Submitted.

Carbon Nitride (Collaboration with Dr. Abdullah Khan)

1. M. A. Khan, I. F. Teixeira, M. M. J. Li, Y. Koito and S. C. E. Tsang, *Graphitic carbon nitride catalysed photoacetalization of aldehydes/ketones under ambient conditions,* **Chemical Communications**, 2016. 52, p. 2772-2775.

2. M. A. Khan, I. F. Teixeira and S. C. E. Tsang, *Auto-tandem photo oxidation/acetalization of alcohols over carbon nitride*. **New Journal of Chemistry**, Submitted.

Trimethylphosphine-assisted Mapping (Collaboration with Mr. Yung-Kang Peng)

1. Y. K. Peng, L. Ye, J. Qu, L. Zhang, Y. Fu, I. F. Teixeira, I. J. McPherson, H. He and S. C. E. Tsang, *Trimethylphosphine-Assisted Surface Fingerprinting of Metal Oxide Nanoparticle by ^{31}P Solid-State NMR: A Zinc Oxide Case Study*. **Journal of the American Chemical Society**, 2016. 138, p. 2225-2234.

2. Y. K. Peng, Y. Fu, L. Zhang, I. F. Teixeira, L. Ye, H. He and S. C. E. Tsang, *Probe-Molecule-Assisted NMR Spectroscopy: A Comparison with Photoluminescence and Electron Paramagnetic Resonance Spectroscopy as a Characterization Tool in Facet-Specific Photocatalysis.* **ChemCatChem,** 2017. 9, p. 155-160

3. Y. K. Peng, Y. Hu, H. Chou, Y. Fu, I. F. Teixeira, H. He L. Zhang and S. C. E. Tsang. *Mapping of Titania Nanoparticles Promoted with Surface Groups Giving Implications to Facets Activities and Controls.* **Nature Communications,** 2017. Accepted.

Other Collaborations

1. G. Liu, H. Ma, I. F. Teixeira, Z. Sun, Q. Xia, X. Hong, and S. C. E. Tsang. *Hydrazine-Assisted Liquid Exfoliation of MoS_2 for Catalytic*

Hydrodeoxygenation of 4-Methylphenol. **Chemistry-A European Journal**, 2016. 22 (9), p. 2910-2914.

2. Y. Koito, G. J. Rees, J. V. Hanna, M. M. Li, Y. K. Peng, T. Puchtler, R. Taylor, T. Wang, H. Kobayashi, I. F. Teixeira, M. A. Khan, H. T. Kreissl and S. C. E. Tsang, *Structure–Activity Correlations for Brønsted Acid, Lewis Acid, and Photocatalyzed Reactions of Exfoliated Crystalline Niobium Oxides*. **ChemCatChem**, 2017. 9 (1), p. 144-154.

3. I. F. Silva, W. D. do Pim, I. F. Teixeira, W. P. Barros, A. P. C. Teixeira, G. M. do Nascimento, C. L. M. Pereira and H. O. Stumpf. *Selective Wrapping of Few-Walled Carbon Nanotubes by a Serpent-Like Heterobimetallic Coordination Polymer.* **The Journal of Physical Chemistry C,** 2016. 120 (2), p. 1245-1251.

4. I. T. Cunha, I. F. Teixeira, J. P. Mesquita, J. D. Ardisson, I. Binatti, F. V. Pereira and R. M. Lago. *Cellulose Nanocrystals Assembled on the Fe3O4Surface as Precursor to Prepare Interfaced C/Fe_3O_4 Composites for the Oxidation of Aqueous Sulfide.* **Journal of the Brazilian Chemical Society,** 2016. 27 (2), p. 363-371.

5. I. T. Cunha, I. F. Teixeira, A. S. Albuquerque, J. D. Ardisson, W. A. A. Macedo, H. S. Oliveira, J. C. Tristão, K. Sapag, and R. M. Lago. *Catalytic oxidation of aqueous sulfide in the presence of ferrites (MFe_2O_4, M= Fe, Cu, Co)*. **Catalysis Today,** 2016. 259, p. 222-227.

Thesis Contents

Abstract ... iii

Declaration ... vi

Acknowledgments ... vii

List of Publications ... ix

Thesis Contents ... xii

List of Figures ... xvii

List of Tables ... xxviii

List of Abbreviations ... xxxi

Chapter 1: Introduction ... 2

Overview ... 3

1.1 Energy ... 4

1.1.1 The Global Energy Perspective ... 4

1.1.2 The Global Energy Challenge: Consumption of Fossil Fuels ... 5

1.2 Global Warming ... 6

1.3 Biomass: An Alternative Energy Source ... 8

1.3.1 Lignocellulosic Biomass Sources ... 9

1.3.1.1 Lignocellulosic Waste Material ... 9

1.3.1.2 Virgin Biomass ... 11

1.3.2 Biomass Demand ... 12

1.3.3 Lignocellulosic Biomass Composition ... 14

1.3.4 Platform Molecules ... 15

1.3.4.1 Biomass-Derived Furans ... 17

1.3.4.2 Other Platform Molecules ... 21

1.3.4.3 Ethanol 23

1.3.5 From Biomass-Derived Furans to Aromatics 25

1.3.5.1 Diels-Alder Cycloaddition 27

1.3.5.2 Challenges on the Biomass-Derived Furans Conversion into Aromatics 29

1.4 Zeolites 31

1.4.1 ZSM-5 and USY 35

1.4.2 Zeolites as an Acid Catalyst 36

1.4.3 Zeolites on Biomass Valorisation 39

1.5 Aim and Objectives 39

1.6 Thesis Overview 40

1.7 References 41

Chapter 2: Analytical Techniques 52

2.1 Introduction 53

2.2 X-Ray Diffraction (XRD) 54

2.3 Synchrotron X-Ray Diffraction (SXRD) 56

2.4 Transmission Electron Microscopy (TEM) 58

2.5 Scanning Electron Microscopy (SEM) 61

2.6 Thermogravimetric Analysis (TGA) 63

2.7 Temperature-Programmed Desorption (TPD) 64

2.8 ^{27}Al ssNMR – Aluminium Environment 66

2.9 ^{31}P ssNMR – Acid Sites Determination 67

2.10 BET surface area analysis 67

2.11 Inductive Coupled Plasma-Atomic Emission Spectroscopy (ICP- AES) 70

2.12 Fourier Transform Infrared (FTIR) spectroscopy 70

2.13 References 73

Chapter 3: Experimental Methods 77

3.1 Zeolites 78

3.2 Zeolites Modifications 78

3.3 Characterisation Procedures 79

3.3.1 X-Ray Diffraction (XRD) 79
3.3.2 Transmission Electron Microscopy (TEM) 79
3.3.3 Scanning Electron Microscopy (SEM) 79
3.3.4 Thermogravimetric Analysis (TGA) 80
3.3.5 Temperature-Programmed Desorption (TPD) 80
3.3.6 ^{27}Al ssNMR – Aluminium Environment 80
3.3.7 ^{31}P ssNMR – Acid Sites Determination 81
3.3.8 BET surface area analysis 81
3.3.9 Inductive Coupled Plasma-Atomic Emission Spectroscopy (ICP- AES) 81

3.4 Catalytic Tests 82

3.4.1 Catalytic Conversion of 2,5-Dimethylfuran into Aromatics 82
3.4.2 Catalytic Conversion of Furan into Aromatics 83

3.5 Mechanistic Investigation 83

3.5.1 SXRD and Rietveld refinement 83
3.5.1.1 HZSM-5 84
3.5.1.2 USY 85
3.5.2 Experiments with Deuterated Ethanol 87
3.5.3 Theoretical Calculations 87
3.5.4 Fourier Transform Infrared (FTIR) 89

3.6 References 90

Chapter 4: Facilitated Process to Convert DMF and Ethanol into Xylene 93

Overview **94**

4.1 Introduction **96**

4.2 Catalytic Performance **98**

4.2.1 Zeolite Samples 99

4.2.2 Reaction Optimization 103

4.3 Kinetic Studies **106**

4.3.1 Activation Energy Estimation 108

4.4 Mechanistic Investigation **109**

4.4.1 Theoretical Calculations 109

4.4.2 SXRD Experiments 117

4.4.3 Experiments with Deuterated Ethanol 121

4.5 Conclusions **123**

4.6 References **124**

Chapter 5: Influence of the Site Blockages in the Conversion of DMF into Aromatics **128**

Overview **129**

5.1 Introduction **130**

5.2 ^{27}Al and ^{31}P MAS NMR **133**

5.3 SXRD Experiments **135**

5.4 Catalytic Performance **142**

5.5 Conclusions **148**

5.6 References **150**

Chapter 6: A New Strategy to Convert Biomass-Derived Furan into Aromatics **155**

Overview **156**

6.1 Introduction **157**

6.2 Catalytic Performance 159

6.3 Kinetic Studies 166

6.4 SXRD Experiments 169

6.5 FTIR Experiments 172

6.6 Mechanism 174

6.7 Conclusions 175

6.8 References 176

Chapter 7: Conclusions and Future Perspective 180

7.1 Conclusions 181

7.2 Future Perspective 183

7.2.1 Alcohol Chain Length and Group Position 183

7.2.2 Stereoselectivity 185

7.3 References 187

Appendix 188

8.1 X-Ray Diffraction (XRD) 189

8.2 Thermogravimetric Analysis (TGA) 192

8.3 Scanning Electron Microscopy (SEM) 195

8.4 Transmission Electron Microscopy (TEM) 199

8.5 BET surface area analysis 200

8.6 Diffusional controlled (mass limitations) reaction 201

8.7 Crystallographic and atomic parameters 204

8.8 References 224

List of Figures

Figure 1.1 Examples of lignocellulosic biomass sources. a) Pine tree waste; b) Rice straws; c) Corn stover; d) Sugarcane bagasse; e) Mountain of sugarcane bagasse waste in an ethanol/sugar industry.[22] 10

Figure 1.2 Sources of energy used in the United States during 2009.[31] 13

Figure 1.3 Schematic representation of lignocellulosic biomass; a) Cellulose structure; b) The building blocks of lignin, p-coumaryl, coniferyl, and sinapyl alcohol; c) Hemicellulose structure.[31] 14

Figure 1.4 Fractionation of lignocellulosic biomass and reaction pathways to produce the platform molecules from hemicellulose and cellulose.[41](Adapted) . 17

Figure 1.5 Biomass-derived furans obtained from HMF and furfural. 18

Figure 1.6 Conversion of carbon chain extend HMF into liquid fuels.[68] 20

Figure 1.7 Levulinic acid conversion into GVL and subsequently into liquid alkanes.[42] 22

Figure 1.8 Ethanol dehydration catalysed by sulphuric acid (homogeneous) and a solid acid catalyst (heterogeneous). 24

Figure 1.9 Scheme of the chain of the main polymers derived from BTX aromatics. 25

Figure 1.10 Conversion of biomass-derived furans into aromatics through a Diels-Alder cycloaddition with ethylene followed by dehydration. 27

Figure 1.11 Scheme of the [4+2]-cycloaddition between a conjugated diene and an alkene (dienophile); Schematic representation of the molecular orbitals involved in the reactions and its orbital diagram..... 28

Figure 1.12 Scheme of the 2,5-dimethylfuran (DMF) hydrolysis into 2,5-hexanedione (in equilibrium) and the formation of other side products from the 2,5-hexanedione decomposition/polymerization. 30

Figure 1.13 Benzofuran (side product) formation from the reaction between two furan molecules, followed by a dehydration. 30

Figure 1.14 Images of different zeolites on different length scales. a) Scanning electron microscopy (SEM) image for ZSM-5; b) Transmission electron microscopy (TEM) image for ZSM-5; c) HRTEM image for ITQ-39;[114] d) HRTEM image of an approximately 2.5 nm thick ITQ-2 layer, viewed along the 10-ring channels;[115] e) HRTEM image of the MWW-type zeolite sample.[115] 32

Figure 1.15 a) Structure for the zeolites ZSM-5 projection along [010]; b) Schematic representation of the straight and sinusoidal channel structure for ZSM-5 zeolite; c) Structure for the zeolites USY viewed along [111] showing the supercage and sodalite cages. 35

Figure 1.16 Schematic representation of the Brønsted acid sites (BAS) formation by Al^{3+} exchange. 36

Figure 1.17 Schematic representation of the Lewis acid sites (LAS) a) formed by dehydration at high temperature; b) Extra-framework-Al species ($Al(OH)_3$ and $Al(OH)_2^+$) generated by mild steaming. 36

Figure 1.18 Examples of chemical reactions catalysed by zeolites where the 'shape selectivity' phenomenon improves the product selectivity; a) Catalytic cracking of alkanes with long chains into shorter ones; b) Toluene transalkylation into benzene and xylene; c) Toluene alkylation producing p-xylene and water 38

Figure 2.1 Illustration of Bragg's Law derived by treating layers of atom as reflecting planes. X-rays interfere constructively when the additional path length 2 d sin θ is equal to integral multiple of the wavelength λ.[4] 55

Figure 2.2. Schematic of a synchrotron X-ray facility.[9] 57

Figure 2.5: A schematic of various possible emitted signals resulting from the electron-surface interaction.[15] 63

Figure 2.6: a) TPD-TGA result for n-propylamine desorption from HZSM-5; b) The MS signal as a function of temperature during the amine TPD.[20] 65

Figure 2.7 The IUPAC six main types of gas physisorption isotherms classification.[30] 68

Figure 2.8 Typical set up for an FTIR spectrophotometer. 72

Figure 3.1 Schematic representation of the Brønsted acid sites formation from the ammonium decomposition. 78

Figure 4.1 A one-pot synthesis for p-xylene production from 2,5-dimethylfuran (DMF) and ethanol over zeolite. 97

Figure 4.2 Conversion and selectivity for DMF transformation into aromatics catalysed by zeolite H-USY (Si/Al=6) with ethylene generated in situ from ethanol compared with only pressure of ethylene (40 bar). Reaction conditions: temperature 300 °C, molar ratio ethanol/DMF 1:1 and reaction time 12 h in 100 mL reactor. 99

Figure 4.3 Conversion and selectivity for DMF transformation into xylene (mainly p-xylene) and alkylaromatics catalysed by different zeolites. Reaction conditions: temperature 300°C, molar ratio ethanol/DMF 1:1 for 12 h in 100mL reactor. 101

Figure 4.4 Carbon yield for DMF transformation into xylene (mainly p-xylene) and alkylaromatics catalysed by different zeolites. Reaction conditions: temperature 300 °C, molar ratio ethanol/DMF 1:1 for 12 h in 100 mL reactor..... 102

Figure 4.5 Conversion and selectivity for DMF transformation into aromatics catalysed by zeolite HZSM-5 (Si/Al=19) at different temperatures. Reaction conditions: molar ratio ethanol/DMF 1:1 and reaction time 12 h in 100 mL reactor. 103

Figure 4.6 Conversion and carbon yield for DMF transformation into aromatics catalysed by zeolite H-USY (Si/Al=7.3) with different molar ratios Ethanol/DMF. Reaction conditions: temperature 300 °C, molar ratio ethanol/DMF 1:1 and reaction time 12 h in 100 mL reactor. 105

Figure 4.7. Kinetic data derived for 0.14 mole DMF transformation over 0.4 g zeolite H-USY (Si/Al=6) with ethylene generated in situ from ethanol (0.14 mole) versus pressurized ethylene (40 bar, 0.45 mole) in 100 mL at 300 ºC..... 107

Figure 4.8. First order fitting and constant rate values for DMF transformation into aromatics catalysed by zeolite H-USY (Si/Al=6) with ethylene generated in situ from ethanol and only pressure of ethylene (40 bar). Reaction conditions: temperature 300 °C in 100 mL reactor..... 108

Figure 4.9 Arrhenius plot for the estimation of apparent activation energy of ethanol/DMF, obtained from the reaction catalysed by 0.4 g zeolite H-USY (Si/Al=6) with ethylene generated in situ from ethanol (0.14 mole) in 100 mL at 230, 280, 250 and 300 °C..... 109

Figure 4.10 M06-2X calculated potential (free) energy landscape of two different pathways for p-xylene formation: (i) ethanol (black) and (ii) ethylene (red) route, with relevant transition states shown as insets. The distinction of consequence between the two pathways lies on the preferred protonation of ethanol over DMF as a first step, compared to the protonation of DMF in the case of the ethylene route. All the energies are reported with respect to the energy of the reacting species and a proton at infinite separation. 111

Figure 4.11 HOMO-LUMO orbital analysis at the initial state of the DA reaction of the ethanol/DMF and ethylene/DMF pathways..... 112

Figure 4.12 a) ONIOM3 partitioning scheme applied on the H-ZSM-5 zeolite framework. The different layers are illustrated as follows: High Level with ball-and-stick, Intermediate Level with stick and Low Level with line representations. b-e) Ground state adsorbate conformations of ethanol, DMF, ethylene and ethanol-DMF dimer, respectively. For visual clarity, the zeolite framework for all adsorbate configurations is shown in line representation, except for the BA site which is shown in ball and stick (as are the adsorbates). 115

Figure 4.13 Rietveld refinement profiles of HZSM-5 pre-adsorbed with a) ethanol, c) DMF, and e) ethanol/DMF at 25 °C, and the corresponding crystal structures viewing from the [010] direction are displayed; b) ethanol, d) DMF, f) ethanol/DMF. Their crystallographic/atomic parameters from Rietveld refinement are summarised in Table 4.6 and Tables A1-A3 in Appendix. Atoms are represented in ball/sticks: white = Si/Al, red = O, black = C. For clarity hydrogen atoms are not plotted. 118

Figure 4.14. Kinetic data obtained for the ethanol and its isotopes (ethanol-d and ethanol-d6) reacted with (0.14 mole) of DMF to obtain aromatics, the reaction was catalysed by 0.4 g zeolite H-USY (Si/Al=6) in 100 mL at 300°C. 121

Figure 5.1 Schematic representation of the conversion of 2,5-dimethylfuran (DMF) into aromatics by Diels-Alder cycloaddition with ethylene, *in situ* generated by dehydration of ethanol, and the DMF hydrolysis equilibria forming 2,5-hexanedione. 132

Figure 5.2 ^{27}Al MAS NMR spectra of a) H-USY (Si/Al=325) and b) H-USY (Si/Al=7.3), ^{31}P MAS NMR spectra and the deconvolution curves of (trimethylphosphine oxide) TMPO adsorbed on c) H-USY (Si/Al=325) and d) H-USY (Si/Al=7.3)..... 134

Figure 5.3 SXRD patterns and Rietveld refinement data of a) H-USY (Si/Al=325) and b) H-USY (Si/Al=7.3). The insets highlight the 20 – 55^{o} 2θ range to illustrate the quality of the refinement. The structure of c) H-USY (Si/Al=325) and d) H-USY (Si/Al=7.3) with stick models without symmetrically appearing 4-CN extra-framework Al^{3+}. Grey represents the USY; Blue represents Al (4-CN extra-framework Al^{3+} species). 137

Figure 5.4 SXRD diffraction patterns and Rietveld refinement data of a) H-USY (Si/Al=325) and b) H-USY (Si/Al=7.3) after pyridine adsorption. The zooms highlight the 20 – 55^{o} 2θ region to illustrate the quality of the refinement. The structures of c) H-USY (Si/Al=325) and d) H-USY (Si/Al=7.3) with stick models without symmetrically appearing 4-CN extra-framework Al^{3+} species and pyridine. Grey represents the USY; Blue ball represents Al (4-CN extra-framework Al^{3+} species); Green represents N of pyridine, black represents C of pyridine. 138

Figure 5.5 Kinetic data derived for 0.14 mole DMF transformation over 0.4 g catalyst with ethylene generated in situ from ethanol (0.14 mole) in 100 mL at 250 °C. ... 143

Figure 5.6 SXRD diffraction patterns and Rietveld refinement data of a) partially blocked H-USY-7.3 (P-K-USY7.3) and b) totally blocked H-USY-7.3 (T-K-USY7.3) after K^+ exchange. The zooms highlight the 20 – 60º 2θ region to illustrate the quality of the refinement. The structures of c) P-K-USY7.3 and d) T-K-USY7.3 with stick models without symmetrically appearing 4-CN extra-framework Al^{3+} and K^+ species. Grey represents the USY; Blue ball represents Al (4-CN extra-framework Al^{3+} species); Dark blue and purple represents K^+..... 145

Figure 5.7 Kinetic data derived for 0.14 mole DMF transformation over 0.4 g catalyst with ethylene generated in situ from ethanol (0.14 mole) in 100 mL at 250 °C. ... 147

Figure 5.8 Conversion and selectivity for DMF transformation into aromatics catalysed by H-USY-7.3, H-USY-325, partially blocked H-USY-7.3 (P-K-USY7.3) and totally blocked H-USY-7.3 (T-K-USY7.3). Reaction conditions: 250 °C, molar ratio ethanol/DMF 1:1 and reaction time 24 h. 148

Figure 6.1 Furan conversion into aromatics and the side product benzofuran... 158

Figure 6.2 Conversion and selectivity for furan conversion into aromatics catalysed by zeolite H-USY (Si/Al=325) with ethylene or ethanol, under optimized reaction conditions. Temperature 300 °C, reaction time 8 h, and (black) molar ratio of ethanol to furan of 10:1, (gray) 40 bar of ethylene. 160

Figure 6.3 Conversion and selectivity for furan transformation into aromatics catalysed by 0.4g of zeolite H-USY (Si/Al=325). Reaction conditions: temperature 300 °C, 10:1 Ethanol/Furan molar ratio and reaction time 8 h in 100 mL reactor. 161

Figure 6.4 Conversion and selectivity for furan transformation into aromatics catalysed by different zeolites. Reaction conditions: temperature 300 °C, 0.4 g of catalyst, molar ratio Ethanol/Furan of 10:1 and reaction time 8 h. 162

Figure 6.5 Conversion and selectivity for furan transformation into aromatics catalysed by 0.4 g of H-USY zeolite (Si/Al=325) with different molar ratios of ethanol to furan. Reaction conditions: temperature 300 °C and reaction time 8 h in a 100 mL reactor. 164

Figure 6.6 Conversion and selectivity for furan transformation into aromatics catalysed by 0.4 g of zeolite H-USY (Si/Al=325) with different molar ratios Ethanol/Furan. Reaction conditions: temperature 300 °C and reaction time 8 h in 100 mL reactor. 165

Figure 6.7 a) Initial production rate of ethylfuran and aromatics catalysed by 0.4 g of zeolite H-USY (Si/Al=325) with different molar ratios Ethanol/Furan at 300 °C in a 100 mL reactor; b) Reaction initial rate for the products ethylfuran and aromatics catalysed by 0.4 g of zeolite H-USY (Si/Al=6) with different molar ratios Ethanol/Furan at 300 °C in 100 mL reactor. 166

Figure 6.8 Arrhenius plot for the conversion of furan into aromatics over 0.4 g of H-USY (Si/Al=6) and the estimated activation energy. 168

Figure 6.9 First order fitting and constant rate values for furan transformation into aromatics catalysed by zeolite H-USY (Si/Al=325) with ethylene generated in situ from ethanol. Reaction conditions: temperature 300 °C, 10:1 Ethanol/Furan molar ratio in 100 mL reactor. 169

Figure 6.10 SXRD and Rietveld refinement profiles of a) furan and 5 bar of ethylene, b) equimolar of ethanol to furan, c) and d) their corresponding crystal structures showing a fraction of a unit cell for illustration. All the symmetry related molecules are disregarded for clarity. The crystallographic and atomic parameters from Rietveld refinement are summarized in Tables A8-A11 in Appendix. Atoms are represented in ball/sticks: white = Si/Al, red = O, black = C. No hydrogen atoms are plotted for clarity. 171

Figure 6.11 IR spectra for H-USY (Si/Al=6) with different molar ratios of Ethanol/Furan measured at room temperature..... 173

Figure 6.12 Furan alkylation, followed by DA cycloaddition and dehydration, catalyzed by the Brønsted acid sites in zeolite catalysts. 174

Figure 7.1 Schematic representation of the DA reactions using different alcohols as a source of dienophile; a) Ethanol; b) Propanol; c) Isopropanol; d) Butanol; e) 3-Buten-1-ol. 184

Figure 7.2 Schematic representation of the DA reaction using stereoisomers as a source of dienophile. 185

Figure A1. XRD patterns for the zeolites H-ZSM-5 with different Si/Al ratios compared with its reference obtained from IZA database..... 189

Figure A2. XRD patterns for the zeolites H-USY with different Si/Al ratios compared with its reference obtained from IZA database..... 190

Figure A3. XRD patterns for the zeolite H-Beta with different Si/Al=25 compared with its reference obtained from IZA database..... 191

Figure A4. XRD patterns for the zeolites H-USY (Si/Al=7.3) before and after exchanging with K^+ compared with its reference obtained from IZA database. No potassium oxide peaks are observed confirming that all the potassium present in the zeolite is K^+ attached to the zeolite framework replacing protons, as also confirmed by the SXRD experiments. 192

Figure A5. TGA curves for zeolites with different shapes and Si/Al ratios under flow of air (60 $mL.min^{-1}$). All the samples present a weight loss between 50 and 200 °C, which is related to water molecules adsorbed on the zeolites surface..... 193

Figure A6. TGA curves for zeolite H-ZSM-5 (Si/Al=25) under flow of air (60 $mL.min^{-1}$) before and after catalyses the DMF/Ethanol reaction. The weight loss between 400 and 650 °C is related to oligomers and carbon produced from side reactions, mainly from ketones polymerization. 194

Figure A7. TGA curves for zeolite H-USY (Si/Al=325) under flow of air (60 $mL.min^{-1}$) before and after catalyses the DMF/Ethanol reaction. The weight loss between 400 and 650 °C is related to oligomers and carbon produced from side reactions, mainly from ketones polymerization. 195

Figure A8. SEM micrographs for zeolites H-ZSM-5 with different Si/Al ratios. 196

Figure A9. SEM micrographs for the zeolite H-ZSM-5 (Si/Al=19) in two different magnifications. In general, the sample is composed by particles with less than 1µm. 196

Figure A10. SEM images for zeolites H-USY with different Si/Al ratios..... 197

Figure A11. SEM micrographs for the zeolite H-USY (Si/Al=6) in four different magnifications. In general, the sample is composed by particles with size around 1µm. 198

Figure A12. SEM images for the zeolite H-USY (Si/Al=7.3) before and after the partial or total proton exchange with K^+. No significant morphological modifications can be noted. 198

Figure A13. TEM images for the zeolites H-ZSM-5 (Si/Al=19) and H-USY (Si/Al=6). 199

Figure A14. Nitrogen adsorption-desorption isotherms of various zeolite samples. 200

Figure A14. Pore distribution for zeolite samples with different shapes. 201

Figure A15. Rietveld refinement derived crystal structures of a unit cell of H-USY (Si/Al=6) pre-adsorbed with (a) ethylene and furan, and (b) ethanol and furan. Their corresponding atomic parameters are summarized in Tables A8-A9. Symmetry for the adsorbed molecules is disregarded for clarity. Atoms are displayed in the ball-and-stick model, with red = oxygen, white = silicon/aluminium, and black = carbon. 218

Figure A16. (a,b) Rietveld refinement profiles, and the derived crystal structures of a unit cell (c,d), a zoom-in (e,f), of H-USY (Si/Al=6) pre-adsorbed with ethanol and furan at ratios of 3:1 and 10:1. Their corresponding atomic parameters are summarized in Tables A10-A11. Symmetry for the adsorbed molecules is disregarded for clarity. Atoms are displayed in the ball-and-stick model, with red = oxygen, white = silicon/aluminium, and black = carbon. 219

List of Tables

Table 1.1 Types of lignocellulosic biomass and their chemical composition[30] ... 12

Table 1.2 Classification of some common commercial zeolites[113, 117] 34

Table 4.1 Acid site concentrations and surface area of the zeolite samples 100

Table 4.2. Reaction rate and reaction rate per mol of reactant (ethanol or ethylene) for DMF transformation into aromatics per gram of zeolite H-USY (Si/Al=6) with ethylene generated in situ from ethanol and only pressure of ethylene (40 bar). Reaction conditions: temperature 300 °C 106

Table 4.3 CBS-QB3 calculated gas phase proton affinities (PA) of reaction species. Note that negative values indicate exothermicity 110

Table 4.4. DFT calculated barriers for the elementary steps in the ethylene/DMF and ethanol/DMF routes. Reported values include electronic energies, total free energies, enthalpies and entropies at T= 300 °C (experimental temperature) 113

Table 4.5 Calculated ONIOM BEs of relevant adsorbates in the ethanol and ethylene routes within the H-ZSM-5 pore. Negative values indicate exothermic, while positive values indicate endothermic adsorption..... 116

Table 4.6 Crystallographic parameters of the H-ZSM-5 samples measured at 25 °C, dehydrated, pre-adsorbed with ethanol, DMF, and an equimolar mixture of DMF and ethanol 120

Table 4.7 Measured kinetic isotope effect (KIE) for the DMF transformation into aromatics replacing ethanol by deuterated ethanol (ethanol-d and ethanol-d6). Reaction conditions: 0.4 g of H-USY (Si/Al=6), temperature 300 °C, 0.14 mole of DMF and 0.14 mole of deuterated ethanol 122

Table 5.1 Crystallographic data and details of the USY samples before and after pyridine-adsorbed 140

Table 5.2 Strong and weak Brønsted acid sites per unit cell, obtained by SXRD diffraction patterns and Rietveld refinement data after pyridine adsorption 144

Table 5.3 Crystallographic data and details of the USY samples potassium loading 146

Table 6.1 Acid site concentrations and surface area of the zeolite samples 163

Table A1(a). Atomic parameters from the Rietveld refinement of H-ZSM-5 pre-adsorbed with ethanol measured at 25 °C (R_{wp} = 7.649%, R_{exp} = 3.365%, X^2= 2.274) 205

Table A1(b). Translational and rotational axes for the matrices describing the adsorbate ethanol molecules, together with their corresponding systematic errors 207

Table A2(a). Atomic parameters from the Rietveld refinement of H-ZSM-5 pre-adsorbed with DMF measured at 25 °C (R_{wp} = 8.457%, R_{exp} = 3.339%, X^2 = 2.533) 208

Table A2(b). Translational and rotational axes for the matrices describing the adsorbate DMF molecules, together with their corresponding systematic errors 211

Table A3(a). Atomic parameters from the Rietveld refinement of H-ZSM-5 pre-adsorbed with limited DMF and ethanol at 25 °C (R_{wp} = 9.005%, R_{exp} = 5.259%, X^2 = 1.712) 211

Table A3(b). Translational and rotational axes for the matrices describing the adsorbate molecules, together with their corresponding systematic errors..... 213

Table A4. Crystallographic information files from the Rietveld refinement of H-USY (Si/Al=325)..... 215

Table A5. Crystallographic information files from the Rietveld refinement of H-USY (Si/Al=7.3)..... 215

Table A6. Crystallographic information files from the Rietveld refinement of Py-H-USY (Si/Al=325) 215

Table A7. Crystallographic information files from the Rietveld refinement of Py-H-USY (Si/Al=7.3) 216

Table A8. Atomic parameters derived from the SXRD measurements of H-USY (Si/Al=6) pre-adsorbed with ethylene and furan, measured at 25 °C. R_{wp} = 9.165%, space group = Fd-3m, a = 24.40977(7) Å 220

Table A9. Atomic parameters derived from the SXRD measurements of H-USY (Si/Al=6) pre-adsorbed with ethanol and furan at a ratio of 1:1, measured at 25 °C. Rwp = 7.936%, space group = Fd-3m, a = 24.42246(7) Å 220

Table A10. Atomic parameters derived from the SXRD measurements of H-USY (Si/Al=6) pre-adsorbed with ethanol and furan at a ratio of 3:1, measured at 25 °C. R_{wp} = 7.631%, space group = Fd-3m, a = 24.40260(8) Å 222

Table A11. Atomic parameters derived from the SXRD measurements of H-USY (Si/Al=6) pre-adsorbed with ethanol and furan at a ratio of 10:1, measured at 25 °C. R_{wp} = 7.281%, space group = Fd-3m, a = 24.42587(10) Å 223

List of Abbreviations

AES - Atomic Emission Spectroscopy

BAS - Brønsted Acid Site

BTX - Benzene, Toluene and Xylene

BET - Brunauer- Emmett-Teller

DA - Diels-Alder

DFT - Density Function Theory

DMF - 2,5-Dimethylfuran

FTIR - Fourier Transform Infrared

FF - Furfural

GDP - Gross Domestic Product

GVL - Gamma-valerolactone

HMF- 5-(hydroxymethyl)furfural

HOMO - Highest Occupied Molecular Orbital

ICP - Inductive Coupled Plasma

IPCC - Intergovernmental Panel on Climate Change

LA - Levulinic Acid

LUMO - Lowest Unoccupied Molecular Orbital

MF - 2-Methylfuran

NMR- Nuclear Magnetic Resonance

PET - Polyethylene Terephthalate

SEM - Scanning Electron Spectroscopy

SXRD - Synchrotron X-Ray Diffraction

TEM - Transmission Electron Spectroscopy

TGA - Thermogravimetric Analysis

TPD - Temperature-Programmed Desorption

XRD - X-ray Diffraction

Chapter 1

Introduction

Chapter 1: Introduction

Overview **3**

1.1 Energy **4**

1.1.1 The Global Energy Perspective 4

1.1.2 The Global Energy Challenge: Consumption of Fossil Fuels 5

1.2 Global Warming **6**

1.3 Biomass: An Alternative Energy Source **8**

1.3.1 Lignocellulosic Biomass Sources 9

1.3.2 Biomass Demand 12

1.3.3 Lignocellulosic Biomass Composition 14

1.3.4 Platform Molecules 15

1.3.5 From Biomass-Derived Furans to Aromatics 25

1.4 Zeolites **31**

1.4.1 ZSM-5 and USY 35

1.4.2 Zeolites as an Acid Catalyst 36

1.4.3 Zeolites on Biomass Valorisation 39

1.5 Aim and Objectives **39**

1.6 Thesis Overview **40**

1.7 References **41**

Overview

This chapter aims to introduce the global energy picture and justify the need for sustainable energy sources. In this context, the climate change topic will be addressed and the potential of the biomass, as source of liquid fuels and chemical feedstocks, will be thoroughly explored. About the biomass topic first it will be present the most important sources of lignocellulosic biomass, its composition and review the most promising and recent technologies involved in the catalytic conversion of lignocellulosic biomass into fuels and valuable chemicals. Further, this catalytic conversion consisting of two main steps; the first one focuses on how the platform molecules are obtained from lignocellulosic biomass (especially furan biomass-derived furans), whereas the second on how these platform molecules are converted into liquid fuels with different chain length and a range of essential petrochemical feedstocks (e.g. aromatics). Besides, the most common strategy to transform biomass-derived furans into aromatics (Diel-Alder cycloaddition followed by dehydration) and its biggest challenges will be addressed with a detailed review of this topic literature. Finally, the main properties of the zeolites as solid acid catalysts will be presented, highlighting its potential in the biomass valorisation process.

1.1 Energy

The supply of sustainable energy is certainly the most important scientific and technical challenge facing humanity in the 21st century. Meeting global energy demand in a sustainable fashion will require not only increased energy efficiency and new methods of using existing carbon-based fuels but also a daunting amount of new carbon-neutral energy.[1]

1.1.1 The Global Energy Perspective

Nocera *et al.* estimated the global energy consumption in terms of average consumption rate in terawatts (TW) instead of absolute consumption in Joules.[1] The average consumption rate reflects well the power generation and the increment needed in the next years, in terms of more comprehendible numbers. In 2014, the average consumption rate was 17.7 TW,[2] 86% of this energy was obtained from fossil fuels, with roughly equal parts from oil, coal, and natural gas. Nuclear power accounted for ca. 0.8 TW of primary (thermal) energy, and the remainder of the energy supply came mostly from unsustainable biomass (e.g. forest biomass), with a relatively small contribution from renewable sources.[3] By estimating the growth of the globally averaged gross domestic product (GDP) per capita, energy intensity (i.e., the energy consumed per unit of GDP) and world population, it is possible to project the global average consumption rate for the future years. This method was developed by the Intergovernmental Panel on Climate Change (IPCC), an organization jointly established by the World Meteorological Organization and the United Nations Environment Program. Their projections based on “moderated” assumptions estimated the world energy consumption rate would grow by

2.3% per year, from 17.7 in 2014 to ca. 40.8 TW in 2050, due to population and economic growth.[1, 4]

1.1.2 The Global Energy Challenge: Consumption of Fossil Fuels

Many sources indicate that there are ample fossil energy reserves to supply the energy consumption growth at some reasonable cost. The World Energy Assessment Report estimates of the total reserves and of the global resource base,[5] including both conventional and unconventional sources, provide a benchmark for evaluating the total available global fossil energy base. Based on 1998 consumption rates, 40-80 years of proven conventional and unconventional oil reserves exist globally, and 50-150 years of oil are available if the estimated resource base is included. Sixty to 160 years of reserves of natural gas are present, and between 207 and 590 years of gas resources, not including the natural gas potentially available as methane clathrates in the continental shelves, are in the estimated resource base. Similarly, a 1000 to 2000 year supply of coal, shales, and tar sands is in the estimated resource base. Hence the estimated fossil energy resources could support a 25 to 30 TW energy consumption rate globally for at least several centuries.[1]

On the other hand, the consumption of fossil energy at this high rate will produce a potentially significant global issue, since the carbon emission rate is projected to nearly double from 6.6 gigatons of carbon per year (GtC yr^{-1}) in 2001 to 11.0 GtC yr^{-1} by 2050.[6] On the timescale of many centuries, CO_2 emissions are essentially cumulative in the atmosphere. Data from the Vostok ice core indicate that the atmospheric CO_2 concentration has been between 210 and 300 ppm for the past 420,000 yr,[7] and more recent studies of Dome Concordia ice cores have extended this time period to 650,000

yr.[8] Over the same time period, the atmospheric CO_2 concentration has been highly correlated with temperature swings that have repeatedly caused ice ages on the planet. The CO_2 concentrations in the past 50 yr have been rising because of anthropogenic CO_2 emissions from fossil fuel consumption, and they are now in excess of 380 ppm.[1] Climate models predict a variety of different global responses to levels of CO_2 at or in excess of 550 ppm in the atmosphere. In some models moderate changes are predicted, whereas in others, relatively serious sea level rises, changes in the hydrological cycle, and other effects are predicted.[9] Tipping points involving vicious cycle, such as the accelerated loss of permafrost, which could release further CO_2 which then could accelerate still further permafrost loss, are of substantive concern. What can be said with certainty is that the atmospheric CO_2 concentrations are being increased and without severe intervention will continue to increase, because of anthropogenic sources, to levels that have not been present on the planet in at least the past 650,000 yr and probably in the past 20 million yr.[1] Due to the greenhouse effect promoted by CO_2, the recent increase in atmospheric CO_2 levels has been pointed out by experts as the main reason for the global warming.

1.2 Global Warming

Global warming, also referred to as climate change, is the observed century-scale rise in the average temperature of the Earth's climate system and its related effects.[9] Recently, climate changes denier social groups have emerged, propagating the idea that there has been a “pause” or a “slowdown” in rising global temperatures, but several recent studies, have confirmed that global warming has continued at a pace similar to that of the last half of the 20th century, and the slowdown was just an illusion.[10]

In 2013, the IPCC Fifth Assessment Report concluded that "It is extremely likely that human influence has been the dominant cause of the observed warming since the mid-20th century."[11] The emission of greenhouse gases such as CO_2, methane and nitrous oxide, were the largest human influence on global warming. Climate model projections reported by Stocker *et al.* indicated that during the 21st century the global surface temperature is likely to rise a further 0.3 to 1.7 °C for their lowest emissions scenario and 2.6 to 4.8 °C for the highest emissions scenario.[11]

Future climate change and associated impacts will differ from region to region around the globe.[12] Anticipated effects include warming global temperature, rising sea levels, changing precipitation, and expansion of deserts in the subtropics.[13] Warming is expected to be greatest in the Arctic, with the continuing retreat of glaciers, permafrost and sea ice. Moreover, a series of other events are likely, such as heat waves, droughts, heavy rainfall with floods and heavy snowfall, ocean acidification and species extinctions due to shifting temperature regimes.[4] Humankind will be significantly threatened, due to food insecurity from decreasing crop yields and the abandonment of populated areas due to rising sea levels.[14] Because the climate system has a large "inertia" and greenhouse gases will stay in the atmosphere for a long period of time, many of these effects will not only exist for decades or centuries, but will persist for tens of thousands of years.[15] In order to avoid this catastrophic scenario the CO_2 excess concentrations must be kept lower than 550 ppm, in other words the projected carbon intensity (kg of C emitted to the atmosphere as CO_2 per year per W of power produced from the fuel) in 2050 to achieve the energy global demand (40.8 TW) has to be approximately 0.45 kg of C yr^{-1} W^{-1}, which is lower than any of the fossil fuels.[1] The only way one can reach this value of the mean

carbon intensity is through a significant contribution of carbon-free power to the total energy mix, such as biomass, solar and nuclear fission. As it will be quite challenging to meet the energy demand in the next decades, all the three options will play a vital role. Herein this introduction will focus on the biomass, exposing its potential and the state-of-the-art to convert it into fuels and chemicals.

1.3 Biomass: An Alternative Energy Source

Biomass is biological material derived from living, or recently living organisms. In the context of biomass for energy this is often used to mean plant based material, but biomass can equally apply to both animal and vegetable derived material (e.g. agriculture residues, algae, municipal solid waste).[16] It is carbon based and is composed of a mixture of organic molecules containing hydrogen, usually including atoms of oxygen, often nitrogen and also small quantities of other atoms, including alkali, alkaline earth and heavy metals.[16] Biomass was the first energy source used by humankind with the combustion of wood. The vital difference between biomass and fossil fuels is biomass takes carbon out of the atmosphere while it is growing, and returns it as it is burned. If it is managed on a sustainable basis, biomass is harvested as part of a constantly replenished crop. This is either during woodland or arboricultural management a continuous programme of replanting with the new growth taking up CO_2 from the atmosphere, at the same time as it is released by combustion of the previous harvest. This maintains a closed carbon cycle with no net increase in atmospheric CO_2 levels.[16, 17]

When biomass is derived from plant-based materials, it is called lignocellulosic biomass. Lignocellulosic biomass is the most abundantly available raw material on the

Earth to produce bio-fuels and can be obtained from a range of sources; most of them agriculture residues.[18]

1.3.1 Lignocellulosic Biomass Sources

There are many sources of lignocellulosic biomass. Some, with high market values such as good quality, large timber, are very unlikely to become available for energy applications. However, there are huge resources of residues, by-products and waste that exist in the world which could potentially become available, in quantity, at relatively low cost, or even negative cost where there is currently a requirement to pay for disposal. The lignocellulosic waste, by-products and low value feedstock with the highest potential to be converted into chemicals and biofuels are broadly classified into waste biomass (forestry and agriculture residues), virgin biomass (grasses and fast growing forest) and municipal solid waste.

1.3.1.1 Lignocellulosic Waste Material

The residues generated from the forest products industry could be divided into two categories: (1) logging residues, generated from logging operations, for example from sawdust and (2) industrial by-products, generated by the forest industries during processing of timber, plywood, particleboard, pulpwood, etc.[19, 20] In general, less than 66% of the volume is removed from the forest for further processing, the remaining quantity is left on-site, burnt on-site or utilised as woodfuel, e.g. split firewood or fuel chips. After processing, only 28% of the tree becomes sawn wood, etc. the remainder being residues.[19]

Another important sources of lignocellulosic biomass is agricultural crop residues. Agricultural wastes are renewable and abundant resources, which can be classified into

two large groups: field residues and processing residues. Field residues represent materials left in an agricultural field after harvesting the crop, and they include straw and stalks, leaves, and seed pods. Processing residues, such as husks, seeds, bagasse and roots, are those materials left after the processing of the crop into a usable resource. Harvesting of cereals, vegetables, and fruits generates huge amounts of crop residues.[21]

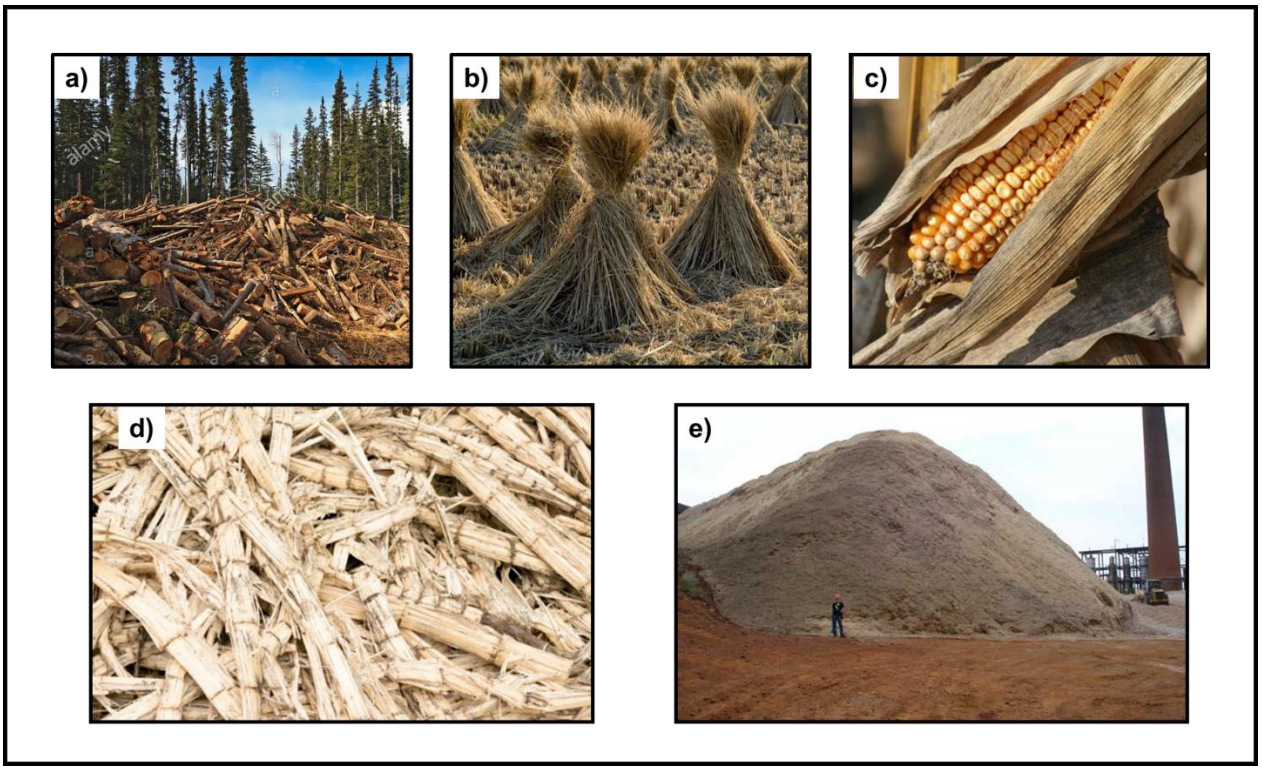


Figure 1.1 Examples of lignocellulosic biomass sources. **a)** Pine tree waste; **b)** Rice straws; **c)** Corn stover; **d)** Sugarcane bagasse; **e)** Mountain of sugarcane bagasse waste in an ethanol/sugar industry.[22]

Wheat straw, rice straw, corn stover, and sugarcane bagasse are the major agricultural wastes in terms of quantity of biomass availability (**Figure 1.1**). Kim *et al.* estimated that in 2002 there was 73.9 billion tons of dry wasted crops in the world.[23] Sugarcane is among the principal agricultural crops cultivated in tropical countries. Bagasse is the residue obtained from the sugarcane after it is crushed to obtain the juice

used for sugar and ethanol production. Thus it has an advantage over other crop residues as it is a by-product, already collected at the ethanol refinery and does not require special and costly collection and transportation.[21]

1.3.1.2 Virgin Biomass

Forages and particularly cultivated grasses are seen as a prominent candidate for cellulosic biomass production and among the various forms of biomass available for conversion into chemicals and fuels, they seem to be very promising as future biomass feedstock.[21] Besides avoiding ‘‘food versus fuel’’ conflict, they are considered to have environmental, energetic and economic advantages over food crops for biomass transformation into chemical feedstocks and fuels.[24, 25] These plants can grow quickly even in marginal and erosive soils and respond to nitrogen fertilization with remarkable increase in biomass yield.[26]

Fast growing short rotation forest trees can play an important role as feedstock for bioenergy production.[27] There are two types of woody materials from forest trees: softwoods and hardwoods. Softwoods originate from conifers and gymnosperm trees.[28] Unlike hardwoods, softwoods possess lower densities and grow faster. These trees comprise of evergreen species such as cedar, pine, spruce, cypress, redwood and hemlock. Hardwoods are mainly found in the Northern hemisphere and include trees such as oak, poplar, willow, aspen, and cottonwood.[21, 29]

Sources and types of lignocellulosic biomass are shown in **Table 1.1**.

Table 1.1 Types of lignocellulosic biomass and their chemical composition[30]

Lignocellulosic Biomass		Cellulose (%)	Hemicellulose (%)	Lignin (%)
Hardwood	Poplar	50.8-53.3	26.2-28.7	15.5-16.3
	Oak	40.4	35.9	24.1
	Eucalyptus	54.1	18.4	21.5
Softwood	Pine	42.0-50.0	24.0-27.0	20.0
	Douglas fir	44.0	11.0	27.0
	Spruce	45.5	22.9	27.9
Agricultural Waste	Wheat Straw	35.0-39.0	23.0-30.0	12.0-16.0
	Barley Hull	34.0	36.0	13.8-19.0
	Barley Straw	36.0-43.0	24.0-33.0	6.3-9.8
	Rice Straw	29.2-34.7	23.0-25.9	17.0-19.0
	Rice Husks	28.7-35.6	12.0-29.3	15.4-20.0
	Oat Straw	31.0-35.0	20.0-26.0	10.0-15.0
	Ray Straw	36.2-47.0	19.0-24.5	9.9-24.0
	Corn Cobs	33.7-41.2	31.9-36.0	6.1-15.9
	Corn Stalks	35.0-39.6	16.8-35.0	7.0-18.4
	Sugarcane Bagasse	25.0-45.0	28.0-32.0	15.0-25.0
	Sorghum Straw	32.0-35.0	24.0-27.0	15.0-21.0
Grasses	Grasses	25.0-40.0	25.0-50.0	10.0-30.0
	Switchgrass	35.0-40.0	25.0-30.0	15.0-20.0

1.3.2 Biomass Demand

The lignocellulosic biomass conversion into sustainable chemicals and fuels is of major interest to reduce dependence on fossil fuel sources. In the United States, the second largest energy consumer on earth, surpassed by China in 2013, renewable sources accounted only 8% in its energy consumption in 2009, with fossil fuels comprising the majority (83%), see **Figure 1.2**.[31]

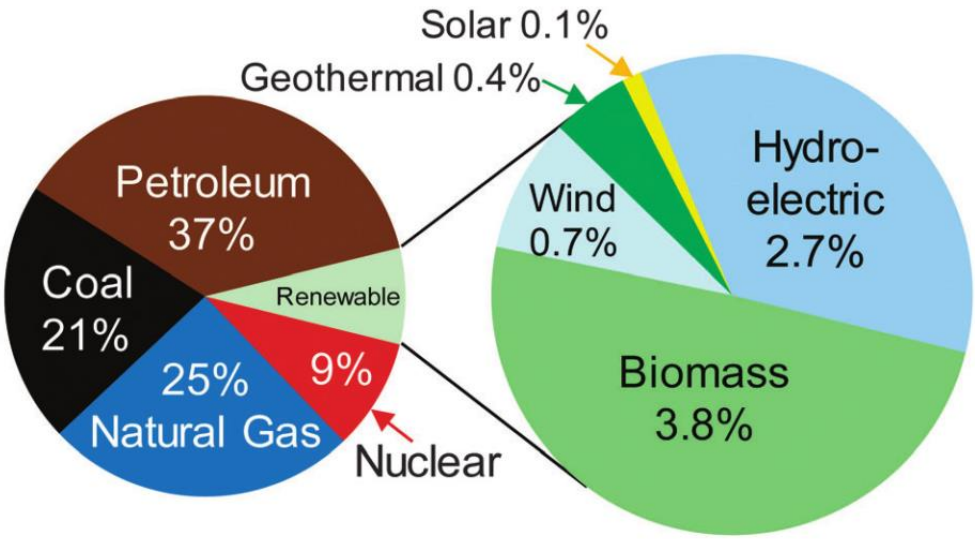


Figure 1.2 Sources of energy used in the United States during 2009.[31]

The Department of Energy forecasted that by 2035, the amount of liquid fuels consumed in the U.S. from biofuels should increase 200% due to the Federal Renewable Fuels Standard, which requires 36 billion gallons of renewable fuel to be blended into transportation fuels by 2022.[32] The demand for renewable fuels have been covered by the production of starch-derived ethanol and biodiesel; however, there remains a lack of inexpensive feedstock for these processes, due to its competition with food resources.[3] Ideally, liquid fuels would be made from second generation feedstocks (e.g., crop and forest harvest residues),[3] be compatible with current combustion engines, and be chemically identical to those obtained from petroleum. In this scenario the lignocellulosic biomass has emerged as a promising feedstock, due to its abundancy in the form of wood, agricultural residues (e.g., sugarcane bagasse and wheat straw), energy crops (e.g., switch grass) and waste streams (e.g., pulp and paper mill and food waste).[29, 31]

In addition to the production of fuels, it is of interest to replace petroleum derived chemicals with similar products derived from biomass, in particular the classical

petrochemical feedstocks benzene, toluene, xylene, ethylene, propylene, 1,3-butadiene and methanol.[33] Chemicals from renewable sources can reduce the environmental impact of their manufacture and/or disposal, for example, biodegradable plastics.[34] Combination of the production of chemicals and fuels into an integrated biomass refinery, also known as the concept of biorefining,[35-37] would reduce the price of the final products, which is one of the main impediments to wide-spread biomass use.[38, 39]

1.3.3 Lignocellulosic Biomass Composition

Lignocellulosic biomass is the most promising renewable carbon energy source, as it is widely available around the world at a relatively low cost. It is composed of three main fractions: cellulose, hemicellulose, and lignin (**Figure 1.3**).[31]

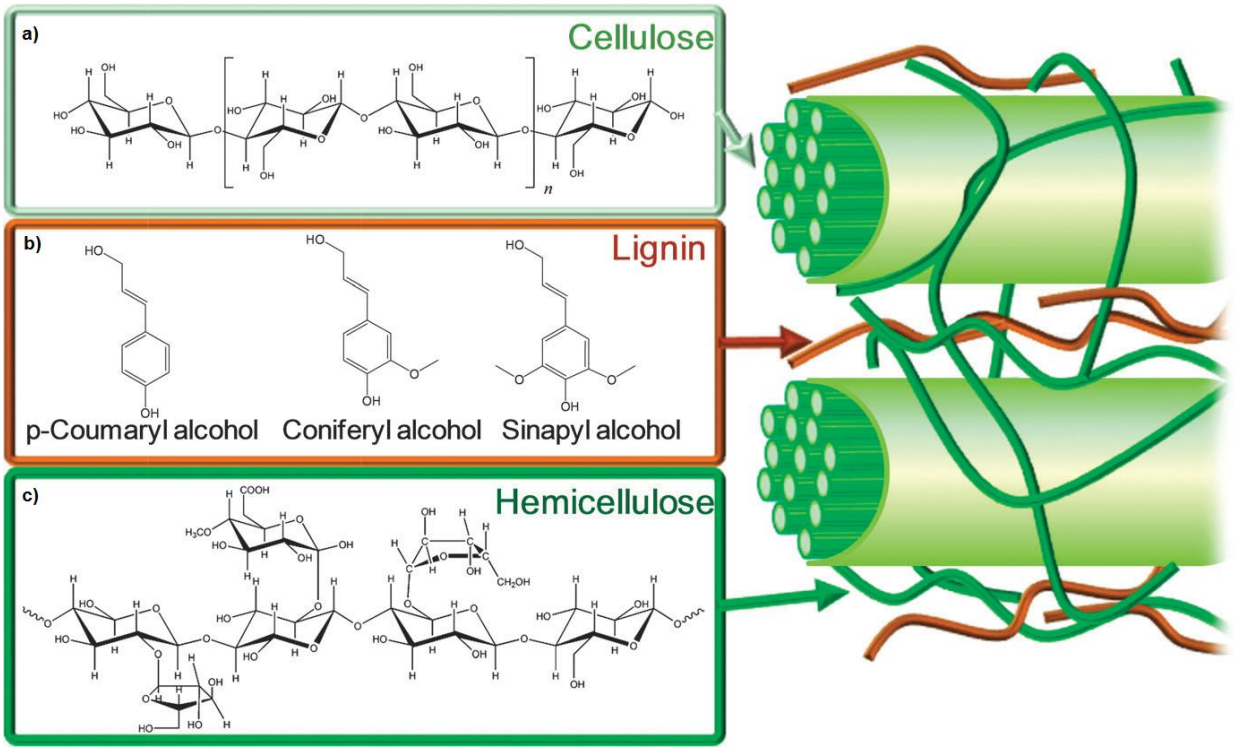


Figure 1.3 Schematic representation of lignocellulosic biomass; **a)** Cellulose structure; **b)** The building blocks of lignin, p-coumaryl, coniferyl, and sinapyl alcohol; **c)** Hemicellulose structure.[31]

Cellulose makes up 40–50% of lignocellulosic biomass and is a homopolymer consisting of β-D-glucopyranose units linked *via* β-glycosidic bonds (**Figure 1.3a**) which can be deconstructed into glucose monomers. Hemicellulose accounts for between 15–30% of lignocellulosic biomass, and unlike cellulose, is amorphous with a low degree of polymerization being a branched polymer (**Figure 1.3c**). The structure of the hemicellulose varies depending on the source of the lignocellulose and may consist of pentoses, hexoses and uronic acids. Lignin, which makes up the final 15–30% of the lignocellulosic biomass, is rich in aromatic functionality, and consists of three primary monomers (**Figure 1.3b**).[31] These units are linked by a range of strong C-C and C-O-C bonds, which are difficult to break. Due to these strong bonds and its highly cross-linked structure, upgrading lignin to feedstock chemical is an arduous task, which usually involves drastic conditions, for example high temperatures around 600°C.[40, 41]

1.3.4 Platform Molecules

Although lignocellulosic biomass is the most abundant plant material resource, its exploitation has been limited by its composite nature and rigid structure.[42] In view of these facts, the conversion of these feedstocks into valuable products has been investigated usually in multiple steps using platform molecules as intermediates.[42-50]

The success of the oil industry during the last century can be explained in terms of efficient and complete utilization of petroleum resources by optimised technologies in highly integrated facilities. The enormous and complex petrochemical industry, however, can be essentially constructed from a few platform chemicals for the production of a multitude of chemicals and specialty products. These platform chemicals include benzene, toluene, xylene, ethylene, propylene, 1,3-butadiene and methanol. Following a

similar approach, a future biomass-based industry could achieve the desired conversion of a variety of bio-feedstocks into fuels and valuable chemicals through the processing of carefully-selected biomass derived platform molecules in an integrated facility denoted as biorefinery.[51]

As shown in **Figure 1.4**, cellulose can be converted into glucose by chemical or enzymatic hydrolysis.[52] The conversion of glucose to 5-(hydroxymethyl)furfural (HMF) involves the isomerization of glucose to fructose, which has recently been demonstrated to afford higher yields when catalysed by a Lewis acid,[53] followed by a series of dehydrations catalysed by a Brønsted acid.[52] HMF can be further converted into other platform chemicals, for example, levulinic acid (LA), *via* a series of dehydration and hydrolysis (**Figure 1.4**).[54, 55] Other notable platform molecules are furfural and furfuryl alcohol. Furfural is produced by the hydrolysis and dehydration of xylose obtained from hemicellulose and the furfuryl alcohol can be easily obtained by the furfural hydrogenation (**Figure 1.4**).[56] Although these platform molecules can already be obtained from biomass in relatively good yields (>90%),[33, 44, 45, 57-60] many studies are still being conducted on this topic aiming to make this process simpler and more economically feasible.[58]

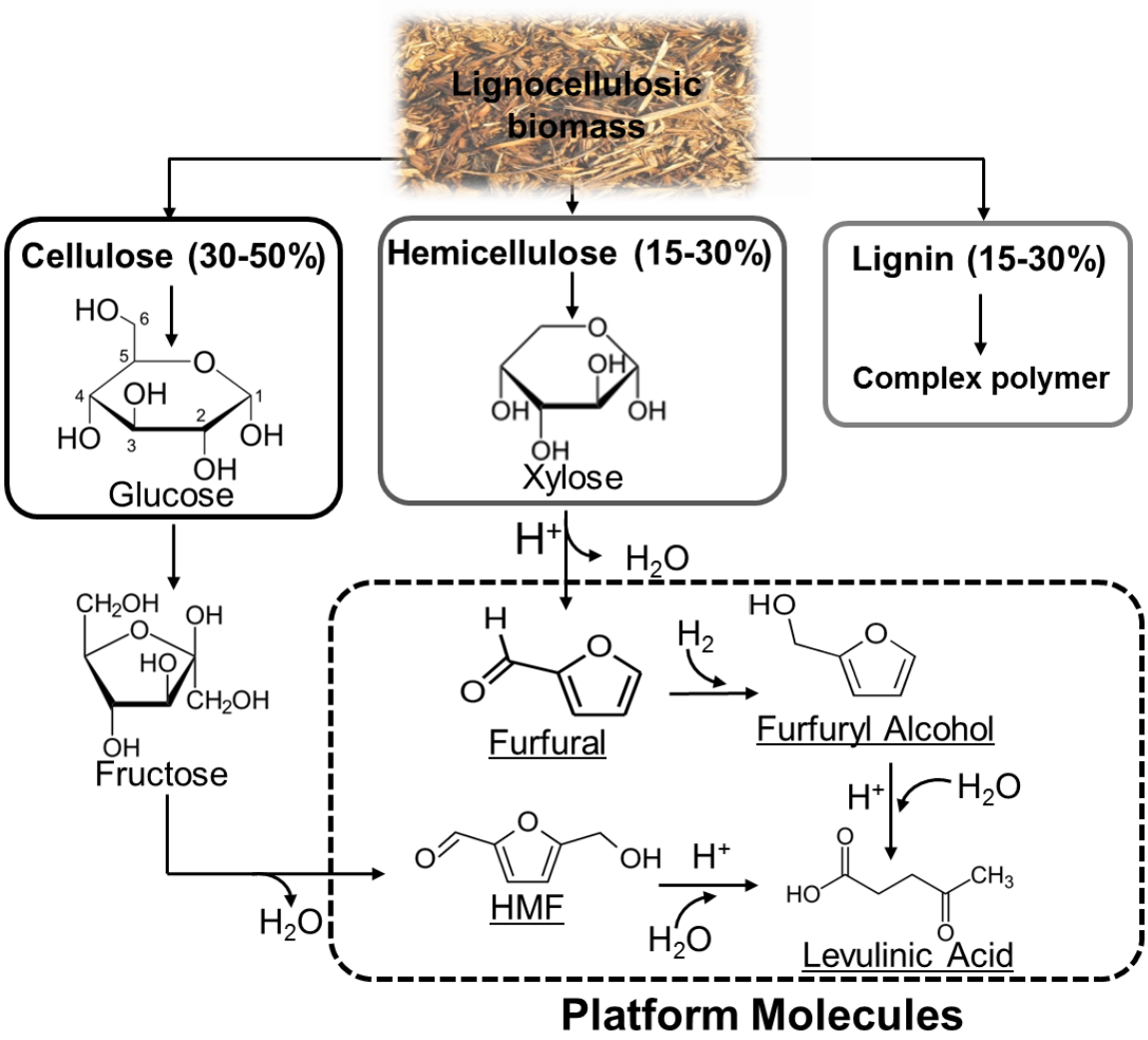


Figure 1.4 Fractionation of lignocellulosic biomass and reaction pathways to produce the platform molecules from hemicellulose and cellulose.[41](Adapted)

1.3.4.1 Biomass-Derived Furans

Among all the platform molecules defined by the US Department of Energy and recently revisited by Bozell *et al.*,[35] it is important to highlight the biomass-derived furans. They are the most important products derived from the lignocellulosic biomass catalytic conversion, molecules such as HMF, furfural and furfuryl alcohol represents the products with highest selectivity reported for the process of lignocellulosic biomass valorisation.

From these molecules, it is possible to obtain a series of other important platform molecules (**Figure 1.5**).

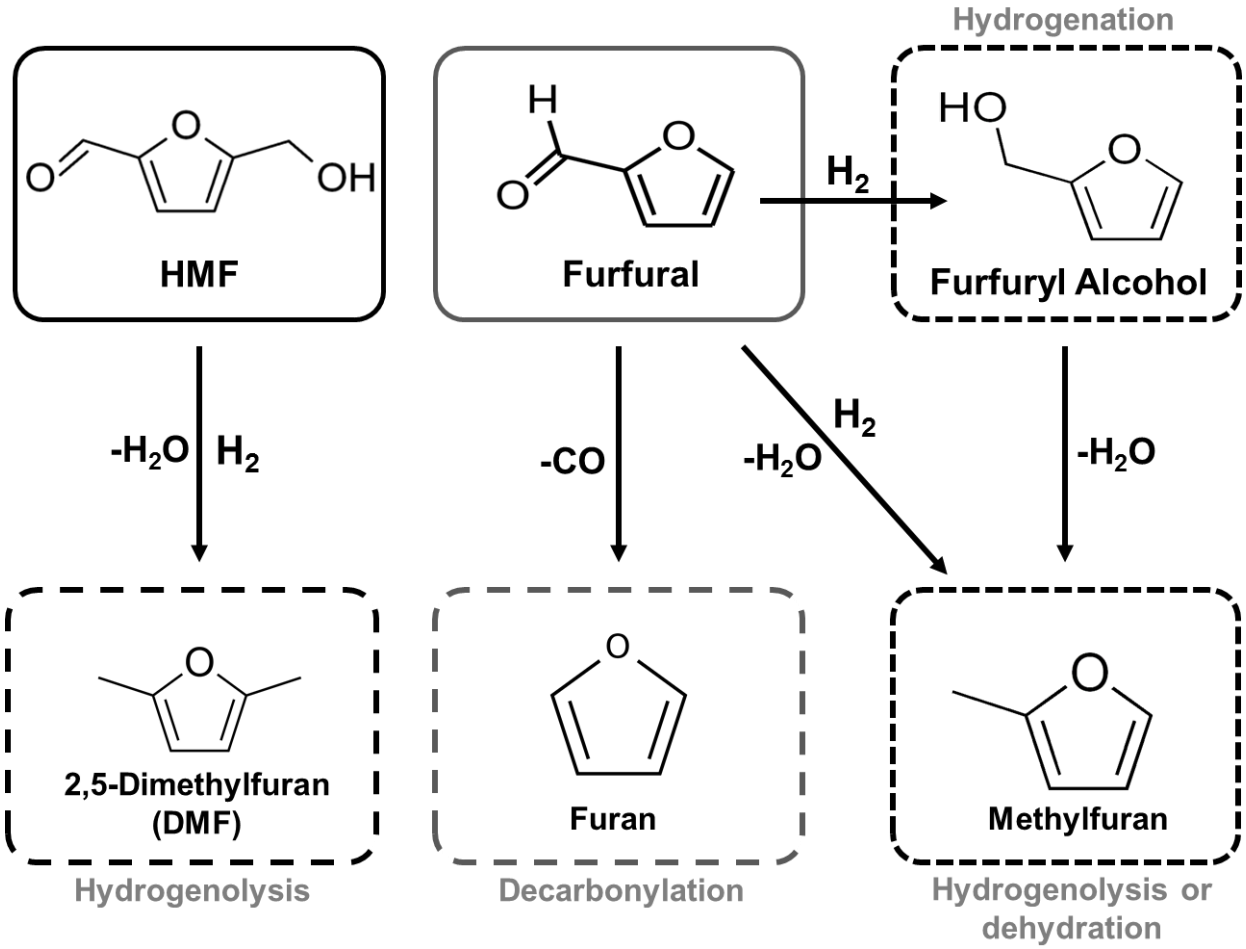


Figure 1.5 Biomass-derived furans obtained from HMF and furfural.

Dumesic *et al.* were the first to report the hydrogenolysis of HMF, directly obtained from glucose or fructose, into 2,5-dimethylfuran (DMF) over copper-ruthenium (CuRu) catalyst.[46] Controlling the reaction conditions, such as solvent, temperature and salt concentration, the DMF can be obtained in good yields (>75%). Furthermore, the DMF has a high energy density (37 $MJ.kg^{-1}$) and a relatively high boiling point (92°C), which makes it very suitable to be used as a liquid transportation fuel.[46]

Other important platform molecules with a furan ring can be obtained from furfural (**Figure 1.5**). As mentioned above furfural can be hydrogenated into furfuryl alcohol by Cu-based catalysts (e.g. Cu/chromite,[61, 62] Cu/C,[63] Cu/MgO[64]) with excellent yields (>98%).[31] Furan and 2-methylfuran also are derived from the further conversion of furfural (**Figure 1.5**), the first one by its decarbonylation catalysed by Pd/SiO_2 (97% yield)[65, 66] and the second one by the direct hydrogenolysis of the furfural by Pd/C at room temperature and 0.2 MPa H_2 (50% yield)[66] or by its hydrogenation into furfuryl alcohol, followed by its dehydration catalysed by acid catalyst (99% overall yield).[31]

As the cellulose is a homopolymer constituted only by glucose monomers, its hydrolysis is, in general, simpler than the hemicellulose.[67] Consequently HMF is the most widespread biomass-derived platform molecule. HMF has been investigated as an important precursor to liquid fuels, however, its six-carbon chain is in general too short for transportation fuel purposes (that is, they have low boiling points and lack sufficient specific energy density for this purpose). Reacting HMF with small chain ketones, which are common products from biomass valorisation process, it is possible elongate their carbon chain by aldol reactions, tuning it before a hydrogenation step. Thus it is possible choose the liquid fuel chain length obtained at the end of the reaction.[68]

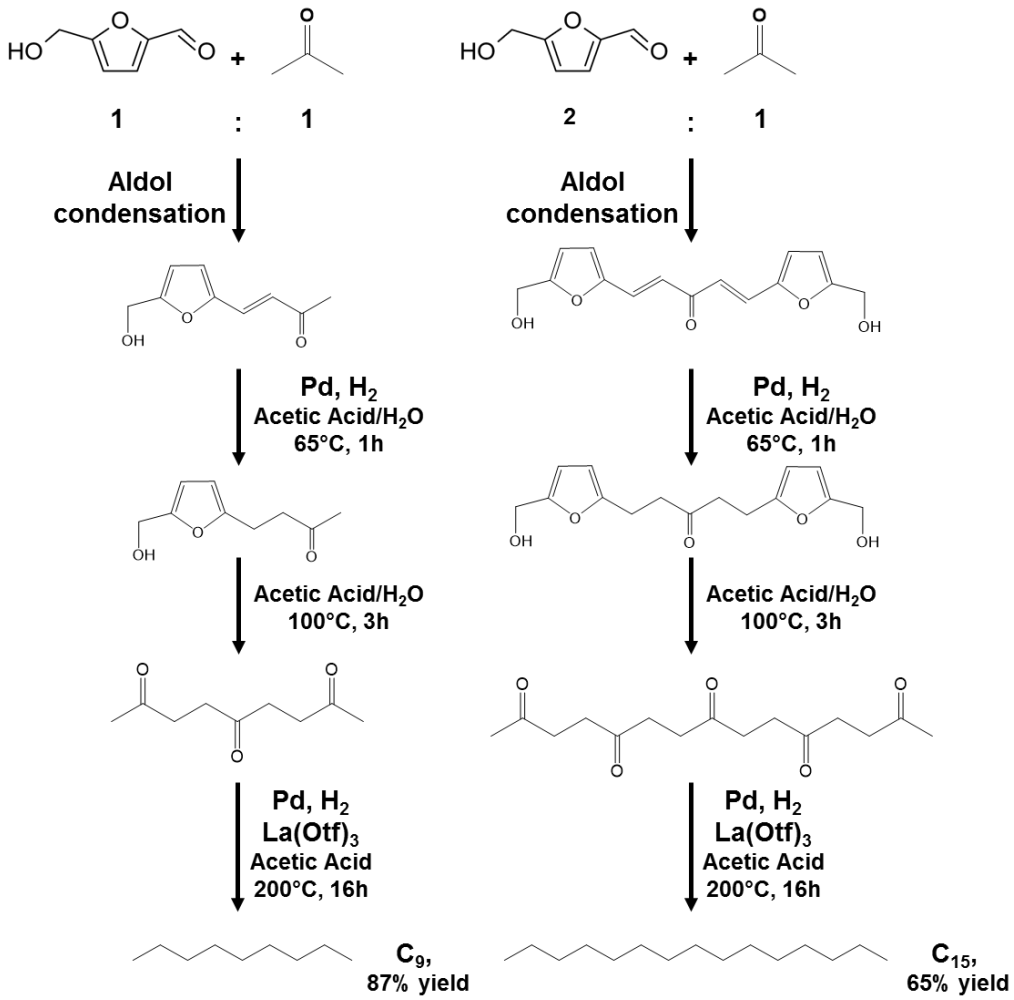


Figure 1.6 Conversion of carbon chain extended HMF into liquid fuels.[68]

Gordon *et al.* reported this strategy reacting HMF and acetone in an aldol reaction, by the control of the reactants proportions they could tune the resulting carbon chain length to achieve a liquid fuel suitable range (C_8-C_{16}).[68] After the aldol reaction step, the product is hydrogenated under mild conditions catalysed by Pd/C under atmospheric pressure of H_2 in order to remove selectively the exocyclic unsaturation. This is a key step to allow the success of the next step, the full hydrogenation of the furan ring promoting the ring opening into polyketones. Finally the polyketones can be easily hydrogenated into linear alkanes with relatively high yields.[68] Similar approaches were

reported using furfural instead of HMF, making it possible to obtain different length liquid fuels.[42]

1.3.4.2 Other Platform Molecules

As shown in **Figure 1.4,** levulinic acid (4-oxopentanoic acid) can be obtained from two different routes, one from cellulose through HMF and another from hemicellulose through furfural, therefore can be considered one of the most important compounds in the selected list of platform molecules derived from biomass.[35, 42] Levulinic acid is synthesized from HMF by its hydration in acidic media producing equimolar amounts of formic acid and levulinic acid (**Figure 1.4**). Additionally, levulinic acid also can be obtained from the hydrolysis of furfuryl alcohol catalysed by acid.[69] Moreover, levulinic acid is the precursor to another important platform molecule: the gamma-valerolactone (GVL), as shown in **Figure 1.7**.

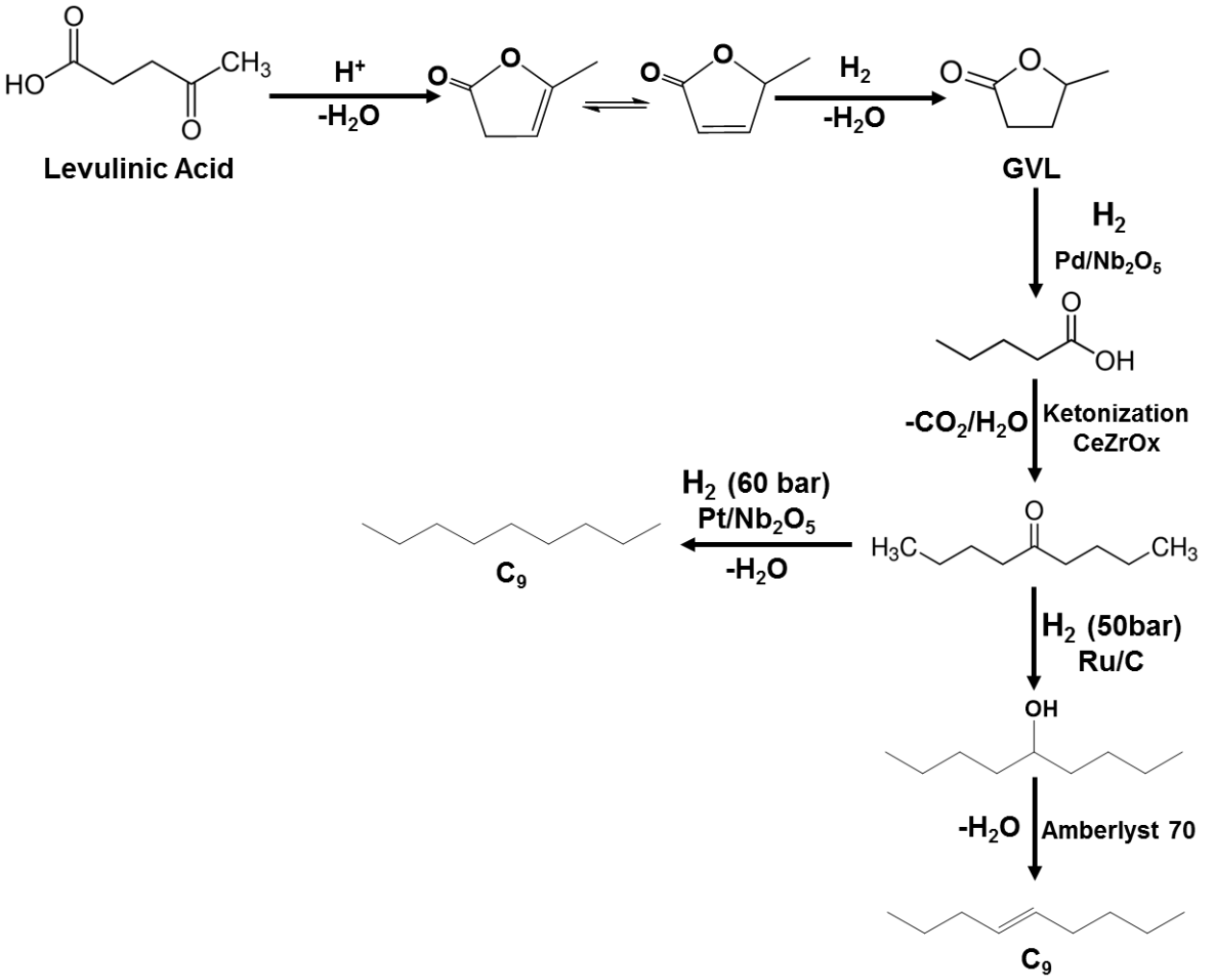


Figure 1.7 Levulinic acid conversion into GVL and subsequently into liquid alkanes.[42]

GVL is a five-carbon lactone which has applications in the production of perfumes, food additives[70] and as a solvent as well as a precursor for other green solvents.[41, 71] It can be obtained from levulinic acid, with excellent yields (99%), by its acid catalysed dehydration into angelica lactone followed by a hydrogenation.[42, 72]

It is possible to transform levulinic acid into liquid fuels with suitable chain length to be transportation fuels (e.g. C_9), *via* a GVL intermediate. First, the GVL is hydrogenated using Pd/Nb_2O_5 into pentanoic acid at yields higher than 92% *via* a ring opening reaction.[73, 74] Serrano-Ruiz *et al.* were able to perform the ketonization of two pentanoic

acid molecules over $CeZrO_x$ to achieve nearly quantitative yields of 5-nonanone while removing one equivalent each of H_2O and CO_2.[73] 5-Nonanone can be upgraded to liquid alkanes, through its hydrogenation/dehydration to nonane using Pt/Nb_2O_5 at 60 bar of H_2 and temperatures around 260°C, which possess adequate cetane number to be blended with diesel fuel.[42] Alternatively, 5-nonanone can be hydrogenated to 5-nonanol over Ru/C, at 50 bar and 150°C. The 5-nonanol can be dehydrated over an acid catalyst (e.g. Amberlyst 70) at 150°C to produce nonene.

1.3.4.3 Ethanol

Ethanol is a widely used biofuel with excellent properties, such as high energy density (26 $MJ.kg^{-1}$) and boiling point (78.4 °C). Most ethanol produced to date as biofuel is generated from biomass, more specifically by the fermentation of sugars from sugarcane (*Saccharum officinarum*) or conversion of starch from corn (*Zea mays*).[75] World ethanol production for transport fuel tripled between 2000 and 2007 from 17 to more than 52 billion litres, reaching a production record of 63 billion litres in 2011 with the United States of America and Brazil being the top producers, accounting for 62.2% and 25% of global production, respectively.[76] Most of the ethanol produced is used to blend with transportation fuel, e.g. E10 in USA and E25 in Brazil.[77] However, a dilemma has been created due the ‘‘food versus fuel’’ conflict,[78] as a possible solution for this dilemma the ‘‘next generation biofuels’’ mostly based on cellulose have rapidly gained importance.[79, 80] Thus, the production of ethanol from the lignocellulosic biomass of non-crop plants or non-edible parts of plants is considered a sustainable solution for biofuel production. This is despite the current difficulties related to the costs, high energy inputs,

and harsh conditions required to process the complex cell wall polymers into fermentable sugars.[80]

Apart from being an excellent liquid fuel, ethanol also has some other possible applications, for example it can be dehydrated to give ethylene, which is an essential feedstock for the petrochemical industry, since it is the monomer for the widely-used polymer polyethylene.[81] The dehydration of ethanol into ethylene can be catalysed by mineral acid (e.g. sulphuric acid and phosphoric acids) or heterogeneous acid catalysts (e.g. γ-alumina and zeolites) at temperatures higher than 150 °C (**Figure 1.8**).[82-85]

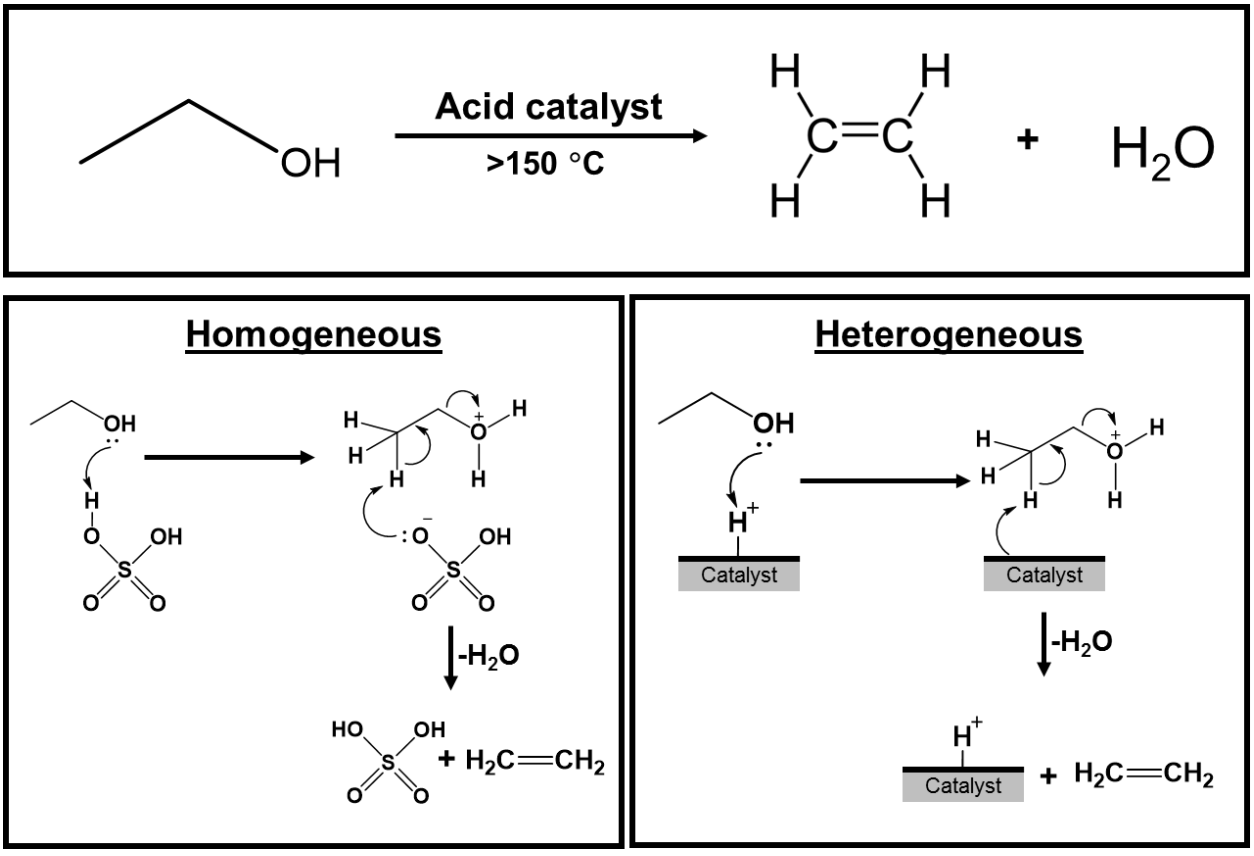


Figure 1.8 Ethanol dehydration catalysed by sulphuric acid (homogeneous) and a solid acid catalyst (heterogeneous).

1.3.5 From Biomass-Derived Furans to Aromatics

About 75% of crude oil goes towards transportation fuels and only 2.5% goes towards petrochemical feedstocks.[2] However, chemical products (e.g. polymers precursors) are much more valuable than fuels. As the economic viability is one of the main factors that prevent the substitution of petroleum by biomass derivatives sources, it is much more likely that chemical feedstocks (e.g. benzene, toluene and xylene) will be first replaced by biomass-derived sources than transportation fuels.

Chemical production is dominated in terms of volume by five major products: benzene/toluene/xylene (BTX), methanol, ethylene, ammonia and propylene.[2] Among them it is important to highlight the aromatics (BTX), as they are the major feedstock for the production of the most consumed polymers (**Figure 1.9**), such as polystyrene, polycarbonate, polyurethane and polyester.[3]

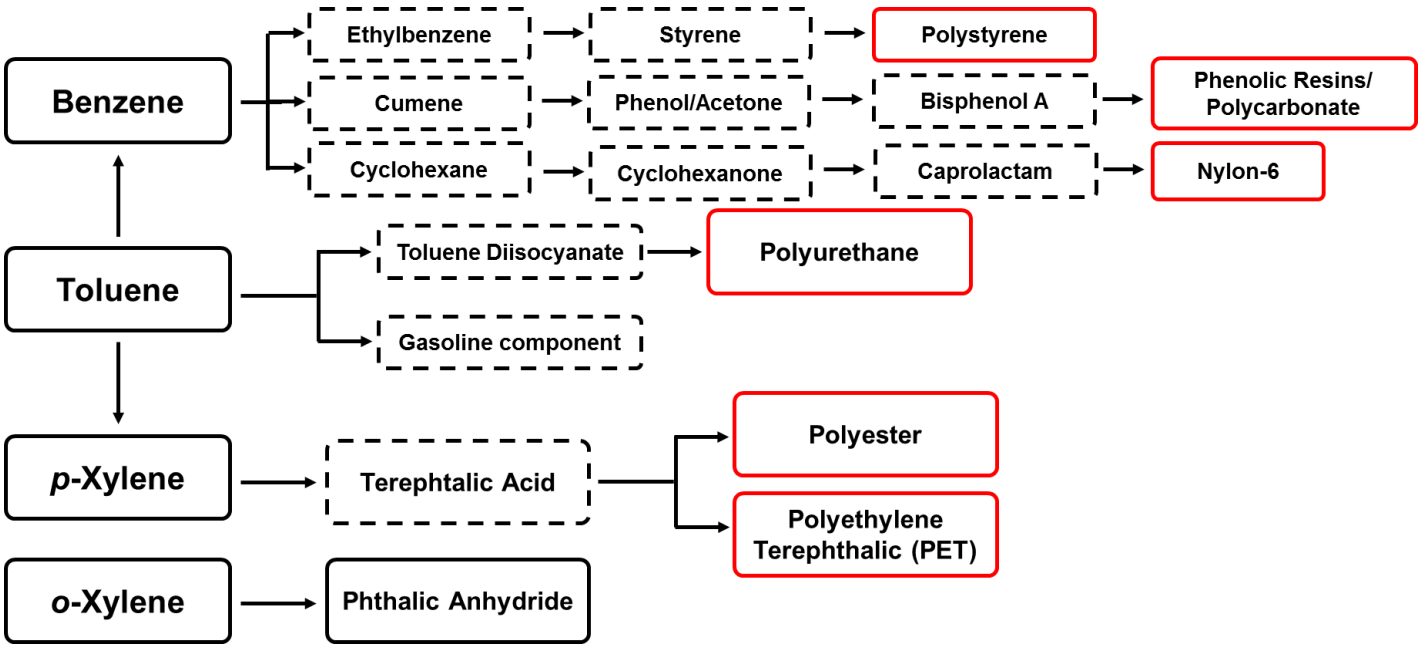


Figure 1.9 Scheme of the chain of the main polymers derived from BTX aromatics.

Among the BTX feedstocks benzene and xylene are the most consumed, estimated at more than 40 million tons and 2.8 million tons in 2010, respectively.[2] Much less toluene is consumed therefore most of it is transalkylated over zeolites into benzene and xylene.[86] As shown in the scheme above benzene and xylene are the most consumed aromatics feedstocks, because the first is the precursor for polystyrene, polycarbonate and nylon, while xylene is the precursor for polyester and polyethylene terephthalate (PET). Due to the size (100 billion dollar a year) and importance of the BTX market, it is a perfect target to be replaced by renewable sources.

A common strategy to obtain aromatics from biomass-derived furans is through a two-step reaction, first a Diels-Alder cycloaddition with ethylene followed by dehydration (**Figure 1.10**).[87-97]

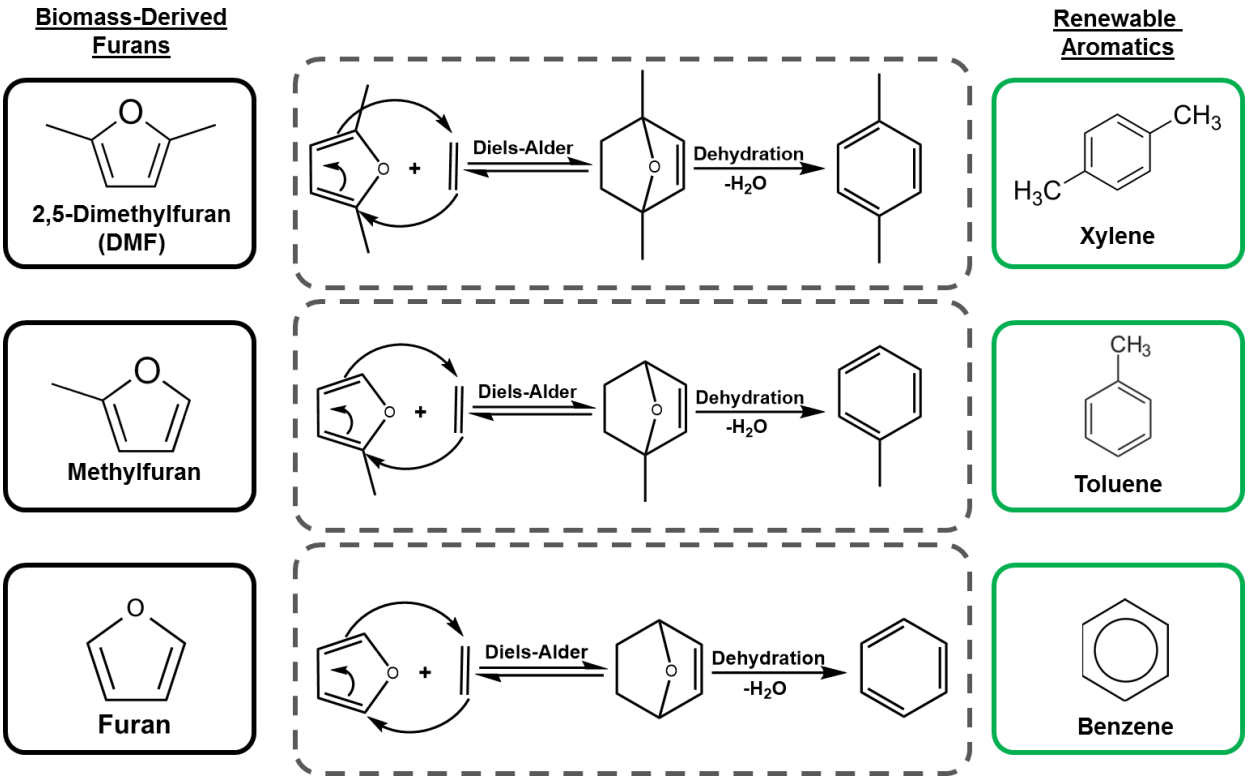


Figure 1.10 Conversion of biomass-derived furans into aromatics through a Diels-Alder cycloaddition with ethylene followed by dehydration.

The initial step in the conversion of renewable furans into aromatics is a Diels-Alder reaction with ethylene, where the furans derivatives are the diene and ethylene the dienophile in the [4+2]-cycloaddition,[98, 99] forming a oxabicyclic cycloadduct intermediate, which can be dehydrated by acid catalysts into aromatics.[87-97]

1.3.5.1 Diels-Alder Cycloaddition

The most common Diels-Alder (DA) reaction is the [4+2]-cycloaddition between a conjugated diene and an alkene or alkyne, commonly termed the dienophile, to form a 6-membered ring (**Figure 1.11**). The Diels–Alder reaction is particularly useful in synthetic organic chemistry as a reliable method for forming 6-membered systems with good control over regio- and stereochemical properties.[100, 101]

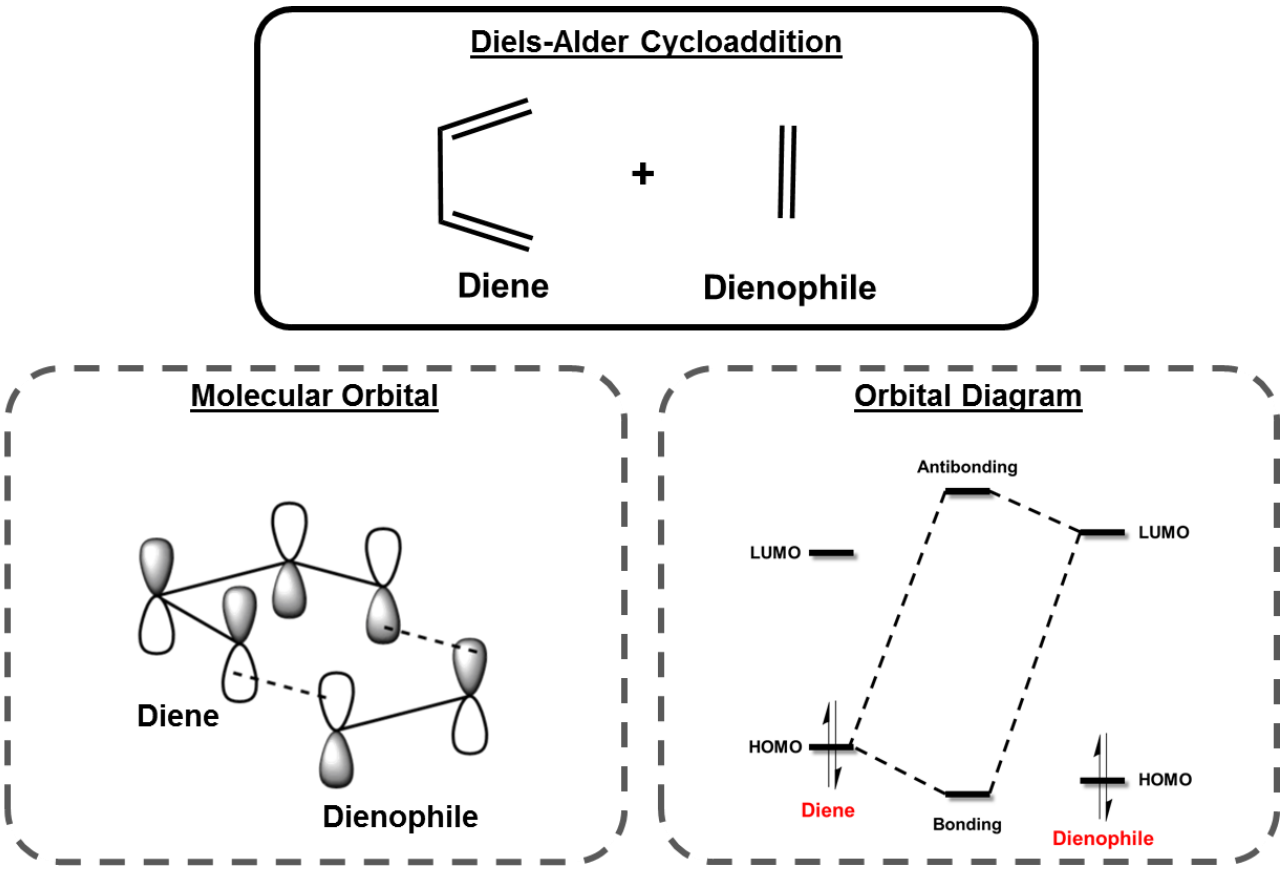


Figure 1.11 Scheme of the [4+2]-cycloaddition between a conjugated diene and an alkene (dienophile); Schematic representation of the molecular orbitals involved in the reactions and its orbital diagram.

The Diels–Alder reaction goes in a single step and it is governed by the orbital symmetry considerations. The reaction proceeds through the overlap interaction of a 4π electron system (diene) with a 2π electron system (dienophile), an interaction that is thermally allowed as a 4n+2 cycloaddition.[102] It is known that furans undergo [4+2]-cycloaddition with a number of dienophiles, however, the reaction environment and functionality of the diene and dienophile leads to significant variation in activity and stereochemistry.[99]

Employing ethylene as the dienophile in the Diels-Alder reaction is inherently difficult; ethylene lacks an electron withdrawing group, which can promote the reaction by

closing the HOMO-LUMO gap of the interacting molecules.[89] Nevertheless this reaction can be facilitated by a catalyst, such as zeolites. Zeolites are catalysts commonly used in the process of biomass valorisation and they can facilitate the Diels-Alder cycloaddition *via* an adsorption of the dienophile on its active sites, narrowing the HOMO-LUMO gap and thus facilitating the reaction.[103]

1.3.5.2 Challenges on the Biomass-Derived Furans Conversion into Aromatics

Although the Diels-Alder (DA) cycloaddition followed by the oxabicyclic dehydration strategy has been extensively studied to convert biomass-derived furans into aromatics, there are still many challenges to overcome.[104] Firstly, the process is not completely renewable since the dienophile commonly used (ethylene) comes from fossil sources. Second, this batch synthesis needs high ethylene gas pressure from a gas store,[87-97] which makes the process more cumbersome and less safe to handle. The majority of the studies using this strategy perform the reaction with solvent (n-heptane).[87, 89, 90, 94, 96, 97, 105] Other more specific difficulties are associated with the starting biomass-derived furan molecules.

The selectivity in the transformation of DMF into xylene is limited by the side product 2,5-hexanedione (**Figure 1.12**). The 2,5-hexanedione is generated by the hydrolysis of DMF by water leading to a ring-opened product, which despite being a reversible reaction, easily polymerizes or decomposes into other side products and coke. Avoiding the formation of 2,5-hexanedione is essential for the reaction success, since in some cases the diketone can be the major product for the reaction.[87, 106]

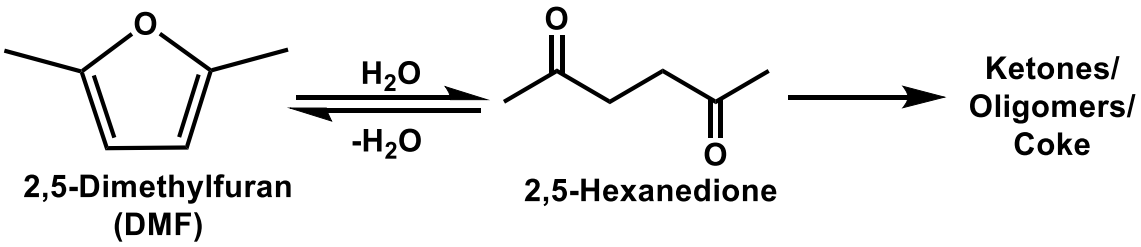


Figure 1.12 Scheme of the 2,5-dimethylfuran (DMF) hydrolysis into 2,5-hexanedione (in equilibrium) and the formation of other side products from the 2,5-hexanedione decomposition/polymerization.

The conversion of furan into benzene is quite challenging due to the coupling reactions between two molecules of furan forming benzofurans (**Figure 1.13**). Chang *et al.* reported only 5% of selectivity to benzene at 250 °C using Zr-BEA zeolite as catalyst [92] and 35% using BEA zeolite under extremely high pressure of ethylene (62 bar).[94] Cheng *et al.* showed that under temperatures lower than 600°C the major products of the furan conversion are benzofuran and coke (60% carbon selectivity), at higher temperatures the benzofuran intermediates can be further converted into aromatics,[107] however, it is clear that the benzofuran is an inevitable product in the reaction of furan conversion into aromatics.

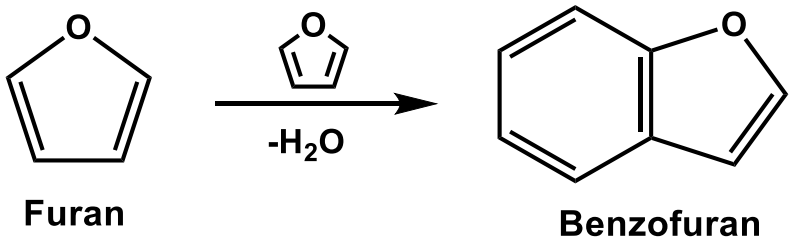


Figure 1.13 Benzofuran (side product) formation from the reaction between two furan molecules, followed by a dehydration.

1.4 Zeolites

Upgrading biomass and its derivatives into valuable chemicals is quite challenging due to their high oxygen–content, complex structure and low solubility, among other features. In general, the only feasible options to remove oxygen from biomass-derived molecules involves hydrogenation/hydrogenolysis by H_2 or dehydration by Brønsted acid sites. A widely used acid catalyst to upgrade biomass and its derivatives are zeolites, due to their stability, high surface area, unique and versatile porous structure and Lewis/ Brønsted acid sites.

Zeolites are a unique class of aluminosilicates. They are formed by tetrahedral sites of SiO_4 and AlO_4 connected in a crystalline structure with a network of well-defined micropores. The micropores are in molecular dimensions, its diameter is in a size range (0.3 to 1 nm) comparable to the size of molecules and chemical reactions (**Figure 1.14**). Therefore, based on size exclusion, zeolites can be used as molecular sieves to separate relatively large molecules from smaller ones.[108, 109] Moreover, substitution of tetravalent silicon by trivalent aluminium in the framework gives rise to a net negative charge, which is compensated by cations, e.g. H^+, Na^+, NH_4^+. Furthermore, if these cations are exchanged by protons (H^+), Brønsted acid sites (BAS) are formed, enabling the application of zeolites as a solid acid catalyst.[109-113]

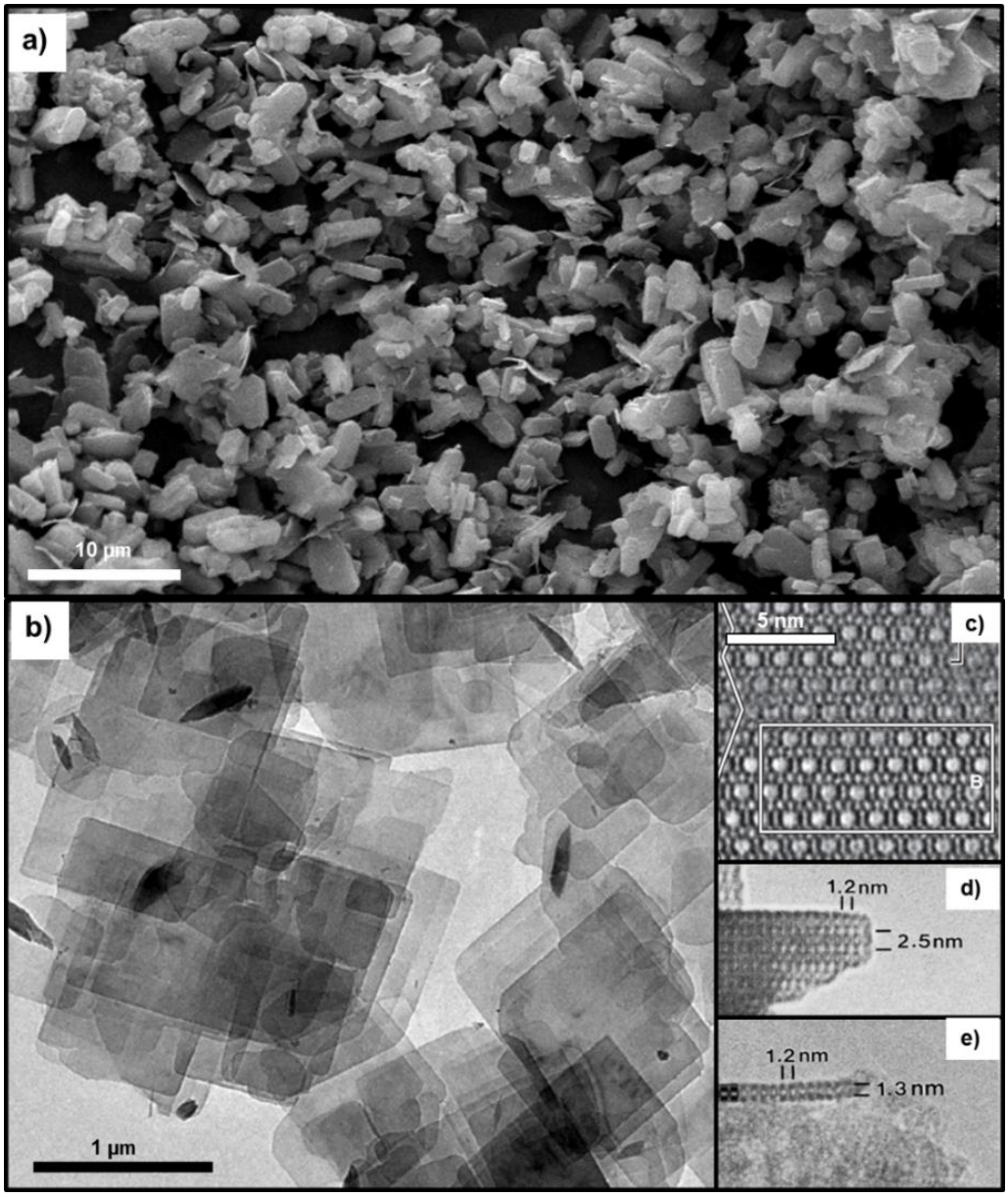


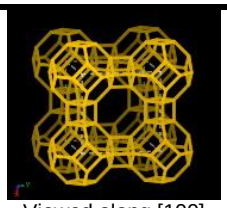
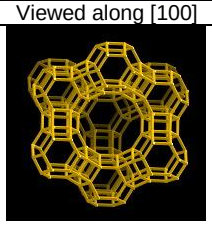
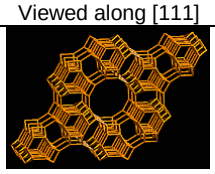
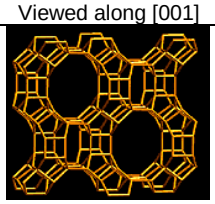
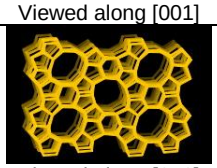
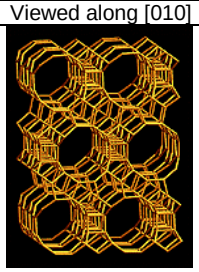
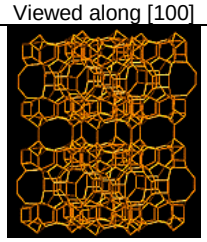
Figure 1.14 Images of different zeolites on different length scales. **a)** Scanning electron microscopy (SEM) image for ZSM-5; **b)** Transmission electron microscopy (TEM) image for ZSM-5; **c)** HRTEM image for ITQ-39;[114] **d)** HRTEM image of an approximately 2.5 nm thick ITQ-2 layer, viewed along the 10-ring channels;[115] **e)** HRTEM image of the MWW-type zeolite sample.[115]

Theoretically several million frameworks are possible only changing the SiO_4 or AlO_4 tetrahedra connectivity and proportions in zeolites,[116] of which more than 200 have been synthesized experimentally.[117] A particular framework topology can be ascribed to

various zeolites based on differences in composition (mostly Si/Al ratio) or crystal morphology. These differences usually originate from zeolite synthesis by varying the template used, composition, crystallization time and temperature.

Zeolites are typically classified by their pore size and composition. **Table 1.2** summarizes the most common commercial zeolites and shows their frameworks. The size of the pores is typically expressed as the number of Si or Al atoms on the smallest possible cross-section (e.g. 8-, 10-, or 12-membered rings (MRs)). Moreover, they can be further categorized by their Si/Al ratio.[113, 117]

Table 1.2 Classification of some common commercial zeolites[113, 117]

Zeolite	Framework Type	Pore size MR	Pore size Å	Framework Image
A	LTA	8	4.1×4.1	 Viewed along [100]
X	FAU	12	7.4×7.4	 Viewed along [111]
Y	FAU	12	7.4×7.4	
L	LTL	12	7.1×7.1	 Viewed along [001]
Mordenite	MOR	12	7.0×6.5	 Viewed along [001]
		8	5.7×2.6	
ZSM-5	MFI	10	5.5×5.1	 Viewed along [010]
		10	5.6×5.3	
Beta	BEA	12	6.7×6.6	 Viewed along [100]
		12	5.6×5.6	
MCM-22	MWW	10	5.5×4.0	 Viewed along [001]
		10	5.1×4.1	

1.4.1 ZSM-5 and USY

The zeolites ZSM-5 and USY (ultra-stable Y) were the framework types most used in this thesis. ZSM-5 is composed of several pentasil units linked together by oxygen bridges to form pentasil chains. These chains are interconnected by oxygen forming corrugated sheets with 10-ring holes, which is connected by oxygen bridges to form a structure with straight 10-ring channels running parallel to the corrugations and sinusoidal 10-ring channels perpendicular to the sheets (**Figure 1.15**).

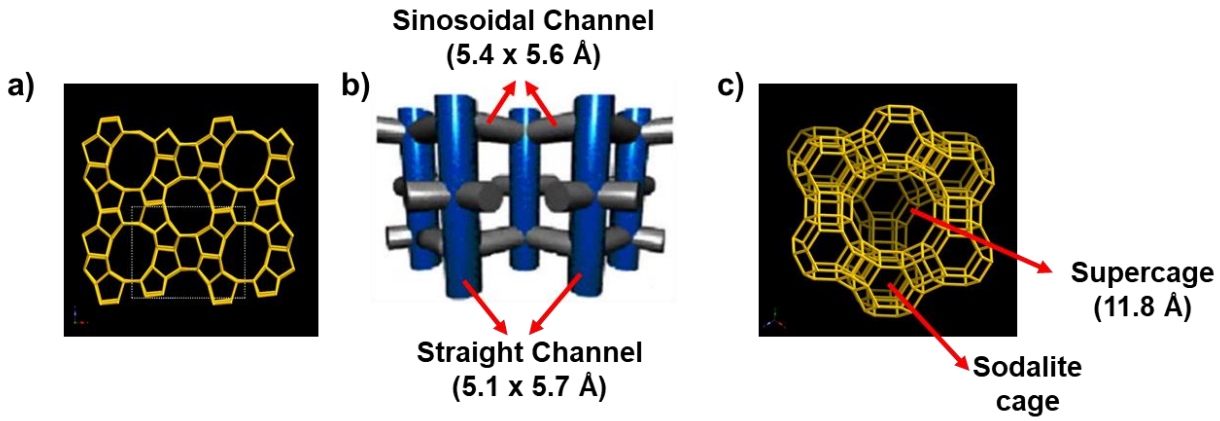


Figure 1.15 a) Structure for the zeolites ZSM-5 projection along [010]; b) Schematic representation of the straight and sinusoidal channel structure for ZSM-5 zeolite; c) Structure for the zeolites USY viewed along [111] showing the supercage and sodalite cages.

The USY (ultra-stable Y) is a dealuminated zeolite Y. When the zeolite Y is submitted to steaming or acid leaching its FAU framework is stabilized originating the ultra-stable Y zeolite (USY). This treatment stabilizes the zeolites structure, which becomes more resistant to water in the reaction medium. Furthermore, it can create mesopores and consequently increases the zeolites surface area. Despite all these modifications its framework remains the same (**Figure 1.15c**).

1.4.2 Zeolites as an Acid Catalyst

The exceptional performance of zeolites catalysing reactions stems from their strong acidity and unique microporours structures.[109-113] Their acidic properties are caused by Brønsted and/or Lewis acid sites (LAS). When tetravalent Si^{4+} is substituted for trivalent Al^{3+}, the substitution creates charge imbalance that is compensated by cations (e.g., H^+ and Na^+). In the H^+-form, a H^+ moves close to the substituted Al atom to form a BAS. In principle, this H^+ can be populated on either one of the four O atoms bonded to each framework-Al site (**Figure 1.16**).

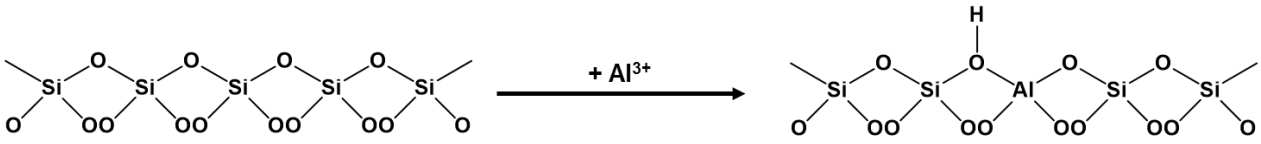


Figure 1.16 Schematic representation of the Brønsted acid sites (BAS) formation by Al^{3+} exchange.

The Lewis acid sites (LAS) are generated by (i) the dehydration of the BAS at high temperature (**Figure 1.17a**) and (ii) mild steaming of zeolites leading to the dislodging of the framework-Al generating extra-framework-Al species which are LAS (**Figure 1.17b)**.

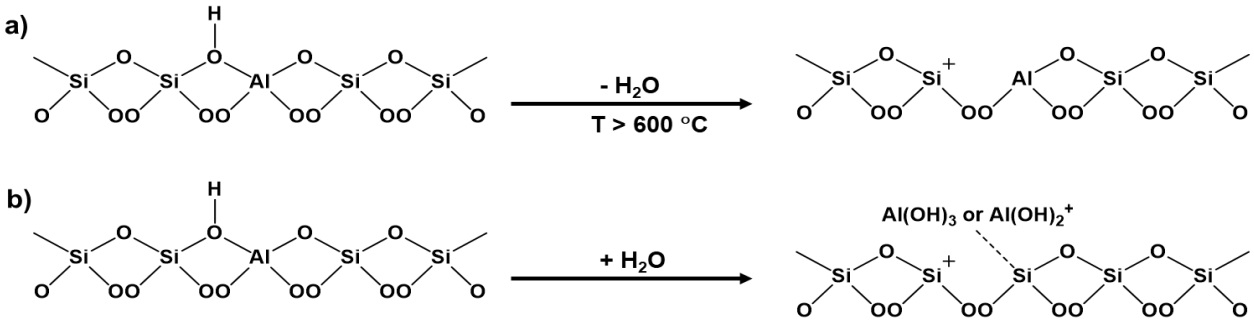


Figure 1.17 Schematic representation of the Lewis acid sites (LAS) **a)** formed by dehydration at high temperature; **b)** Extra-framework-Al species ($Al(OH)_3$ and $Al(OH)_2^+$) generated by mild steaming.

The narrow product distribution for reactions catalysed by the zeolites is related with the 'shape selectivity' phenomenon, i.e. the confinement imposed by the zeolite micropores pushes the conversion of a reagent into a specific product.[86, 109-113]

The 'shape selectivity' phenomenon occurs in many distinguished ways, depending on whether the pore size limits the entrance of the reacting molecule, the departure of the product molecule, or the formation of certain transition states (**Figure 1.18**). For example, in the catalytic cracking of long alkanes, only linear chains are small enough to enter the micropores and be cracked into shorter molecules (**Figure 1.18a**). Toluene transalkylation and its alkylation by methanol tends to produce *p*-xylene as the major product (**Figure 1.18b** and **Figure 1.18c**), as the *m*- and *o*-xylene are too bulky to diffuse out of the zeolite's pores.[86]

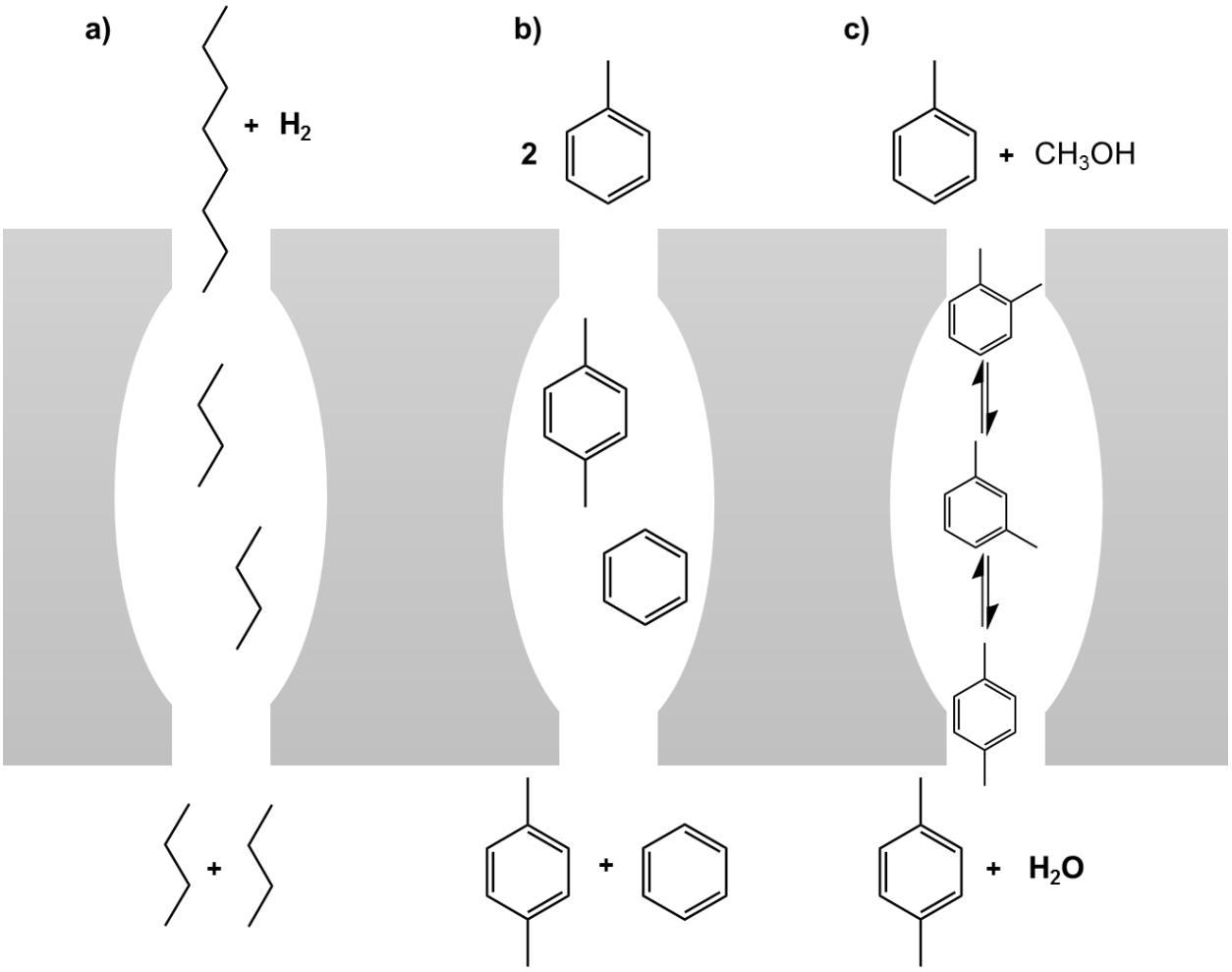


Figure 1.18 Examples of chemical reactions catalysed by zeolites where the 'shape selectivity' phenomenon improves the product selectivity; **a)** Catalytic cracking of alkanes with long chains into shorter ones; **b)** Toluene transalkylation into benzene and xylene; **c)** Toluene alkylation producing *p*-xylene and water.

Zeolite catalysts play a key role in many of biomass conversion routes, due to their controllable pore structure and the presence of Lewis/Brønsted acid sites on its internal surface. In conclusion, zeolites are very suitable to catalyse the conversion of biomass-derived furans into aromatics, because of their porous structures that can promote the Diels-Alder cycloaddition[103] and catalyse the oxabicyclic dehydration.[87-97]

1.4.3 Zeolites on Biomass Valorisation

Zeolites are today an integral part of any oil refinery and although they initially emerged as catalysts for the conversion of petroleum, they are likely to play an important role in future bio-refineries as well.[118] In addition to zeolites' ability to catalyses Diels-Alder cycloaddition and the oxabicyclic dehydration, they are also able to catalyse a range of important reactions on biomass valorisation. Zeolites can be used in the selective transformation of sugars into platform molecules,[119, 120] catalytic conversion of sugars to lactates,[121, 122] catalytic fast pyrolysis of lignocellulose,[123, 124] upgrading of pyrolysis oil[125, 126] and dehydration of alcohols.[127-130] This last reaction, along with the DA cycloaddition, are especially important for this thesis.

1.5 Aim and Objectives

The aim of this thesis is to investigate the conversion of biomass-derived furans into aromatics *via* Diels-Alder cycloaddition through a completely innovative approach, where common dienophiles (alkenes) are replaced by an alcohol.

The objective of this thesis is to systematically study this new reaction, trying to understand its mechanism and exploit its advantages to the conversion of biomass-derived furans. Furthermore, this thesis aims to use techniques developed in the research group to locate the zeolites BAS on its framework by synchrotron X-ray diffraction and Rietveld refinement and to use this to tune the zeolites catalytic activity for this new reaction.

1.6 Thesis Overview

This thesis will present its most important contributions for the field of the conversion of biomass-derived furans into aromatics in three results and discussion chapters, where the first one (**Chapter 4**) will present a completely new/renewable facilitated process to convert DMF and ethanol into xylene. The process is catalysed by zeolites and a detailed study of the reaction mechanism is also presented. The second chapter (**Chapter 5**) will be focused on the control of the zeolites acidity properties by selective blocking with K^+ exchange and how it can influence the product distribution for the conversion of DMF into aromatics. The last chapter (**Chapter 6**) will show how this new reaction can be adapted to reduce the benzofuran formation, a recurrent problem on the conversion of furan into aromatics, increasing the aromatic yields and promoting relatively high selectivity to valuable aromatic products (e.g. ethylbenzene).

1.7 References

1. Lewis, N.S. and D.G. Nocera, *Powering the planet: Chemical challenges in solar energy utilization.* **Proceedings of the National Academy of Sciences**, 2006. 103: p. 15729-15735.

2. Finley, M., *BP statistical review of world energy*. 2013.

3. Administration, E.I., *Annual Energy Outlook.* **Department of Energy**, 2010. 92010: p. 1-15.

4. Hoffert, M.I., K. Caldeira, A.K. Jain, E.F. Haites, et al., *Energy implications of future stabilization of atmospheric CO_2 content.* **Nature**, 1998. 395: p. 881-884.

5. Anderson, D., J. Goldemberg, and T.B. Johansson, *World Energy Assessment: Overview: 2004 Update*. 2004: United Nations Publications.

6. Moss, R.H., J.A. Edmonds, K.A. Hibbard, M.R. Manning, et al., *The next generation of scenarios for climate change research and assessment.* **Nature**, 2010. 463: p. 747-756.

7. Petit, J.R., J. Jouzel, D. Raynaud, N.I. Barkov, et al., *Climate and atmospheric history of the past 420,000 years from the Vostok ice core, Antarctica.* **Nature**, 1999. 399: p. 429-436.

8. Siegenthaler, U., T.F. Stocker, E. Monnin, D. Lüthi, et al., *Stable Carbon Cycle-Climate Relationship During the Late Pleistocene.* **Science**, 2005. 310: p. 1313-1317.

9. Bernstein, L., P. Bosch, O. Canziani, Z. Chen, et al., *Climate change 2007: synthesis report. Summary for policymakers*, in *Climate change 2007: synthesis report. Summary for policymakers*. 2007, IPCC.

10. Karl, T.R., A. Arguez, B. Huang, J.H. Lawrimore, et al., *Possible artifacts of data biases in the recent global surface warming hiatus.* **Science**, 2015. 348: p. 1469-1472.

11. Stocker, T., *Climate change 2013: the physical science basis: Working Group I contribution to the Fifth assessment report of the Intergovernmental Panel on Climate Change*. 2014: Cambridge University Press.

12. Solomon, S., D. Qin, M. Manning, Z. Chen, et al., *IPCC fourth assessment report (AR4).* **Climate change**, 2007.

13. Lu, J., G.A. Vecchi, and T. Reichler, *Expansion of the Hadley cell under global warming.* **Geophysical Research Letters**, 2007. 34: p. n/a-n/a.

14. Battisti, D.S. and R.L. Naylor, *Historical Warnings of Future Food Insecurity with Unprecedented Seasonal Heat.* **Science**, 2009. 323: p. 240-244.

15. Clark, P.U., J.D. Shakun, S.A. Marcott, A.C. Mix, et al., *Consequences of twenty-first-century policy for multi-millennial climate and sea-level change.* **Nature Climate Change**, 2016.

16. Research, F. *What is biomass*. 2017 [Accessed on 23 May 2017].

17. Tilman, D., J. Hill, and C. Lehman, *Carbon-negative biofuels from low-input high-diversity grassland biomass.* **Science**, 2006. 314: p. 1598-1600.

18. Carroll, A. and C. Somerville, *Cellulosic biofuels.* **Annual review of plant biology**, 2009. 60: p. 165-182.

19. Parikka, M., *Global biomass fuel resources.* **Biomass and Bioenergy**, 2004. 27: p. 613-620.

20. Parikka, M., *Biosims—a model for calculation of woody biomass in Sweden, vol. 27.* **Uppsala, Sweden: Swedish University of Agricultural Sciences, Silvestria**, 1997.

21. Hadar, Y., *Sources for lignocellulosic raw materials for the production of ethanol*, in *Lignocellulose Conversion*. 2013, Springer. p. 21-38.

22. UNICA. http://english.unica.com.br/. 2017 [Accessed on 23 May 2017].

23. Kim, S. and B.E. Dale, *Global potential bioethanol production from wasted crops and crop residues.* **Biomass and Bioenergy**, 2004. 26: p. 361-375.

24. Hill, J., E. Nelson, D. Tilman, S. Polasky, et al., *Environmental, economic, and energetic costs and benefits of biodiesel and ethanol biofuels.* **Proceedings of the National Academy of sciences**, 2006. 103: p. 11206-11210.

25. Chandel, A.K. and O.V. Singh, *Weedy lignocellulosic feedstock and microbial metabolic engineering: advancing the generation of 'Biofuel'.* **Applied microbiology and biotechnology**, 2011. 89: p. 1289-1303.

26. Muir, J.P., M.A. Sanderson, W.R. Ocumpaugh, R.M. Jones, et al., *Biomass production of 'Alamo'switchgrass in response to nitrogen, phosphorus, and row spacing.* **Agronomy Journal**, 2001. 93: p. 896-901.

27. Séguin, A., *How could forest trees play an important role as feedstock for bioenergy production?* **Current Opinion in Environmental Sustainability**, 2011. 3: p. 90-94.

28. Sanchez, O.J. and C.A. Cardona, *Trends in biotechnological production of fuel ethanol from different feedstocks.* **Bioresource technology**, 2008. 99: p. 5270-5295.

29. Perlack, R.D., L.L. Wright, A.F. Turhollow, R.L. Graham, et al., *Biomass as feedstock for a bioenergy and bioproducts industry: the technical feasibility of a billion-ton annual supply*. 2005, DTIC Document.

30. Isikgor, F.H. and C.R. Becer, *Lignocellulosic biomass: a sustainable platform for the production of bio-based chemicals and polymers.* **Polymer Chemistry**, 2015. 6: p. 4497-4559.

31. Alonso, D.M., S.G. Wettstein, and J.A. Dumesic, *Bimetallic catalysts for upgrading of biomass to fuels and chemicals.* **Chem. Soc. Rev.**, 2012. 41: p. 8075-8098.

32. Agency, E.P. *Renewable Fuel Standard (RFS)*. 2011 [cited 2017 May 23 2017].

33. Zhu, S., J. Wang, and W. Fan, *Graphene-based catalysis for biomass conversion.* **Catalysis Science & Technology**, 2015. 5: p. 3845-3858.

34. Gross, R.A. and B. Kalra, *Biodegradable polymers for the environment.* **Science**, 2002. 297: p. 803-807.

35. Bozell, J.J. and G.R. Petersen, *Technology development for the production of biobased products from biorefinery carbohydrates—the US Department of Energy's "Top 10" revisited.* **Green Chemistry**, 2010. 12: p. 539-554.

36. Stöcker, M., *Biofuels and biomass-to-liquid fuels in the biorefinery: Catalytic conversion of lignocellulosic biomass using porous materials.* **Angewandte Chemie International Edition**, 2008. 47: p. 9200-9211.

37. Bungay, H.R., *Biomass refining.* **Science**, 1982. 218: p. 643-646.

38. Cherubini, F., *The biorefinery concept: using biomass instead of oil for producing energy and chemicals.* **Energy Conversion and Management**, 2010. 51: p. 1412-1421.

39. Kopetz, H., *Renewable resources: Build a biomass energy market.* **Nature**, 2013. 494: p. 29-31.

40. Kobayashi, H., H. Ohta, and A. Fukuoka, *Conversion of lignocellulose into renewable chemicals by heterogeneous catalysis.* **Catalysis Science & Technology**, 2012. 2: p. 869-883.

41. Alonso, D.M., S.G. Wettstein, and J.A. Dumesic, *Gamma-valerolactone, a sustainable platform molecule derived from lignocellulosic biomass.* **Green Chemistry**, 2013. 15: p. 584-595.

42. Climent, M.J., A. Corma, and S. Iborra, *Conversion of biomass platform molecules into fuel additives and liquid hydrocarbon fuels.* **Green Chemistry**, 2014. 16: p. 516-547.

43. Luterbacher, J.S., D. Martin Alonso, and J.A. Dumesic, *Targeted chemical upgrading of lignocellulosic biomass to platform molecules.* **Green Chemistry**, 2014. 16: p. 4816-4838.

44. Kunkes, E.L., D.A. Simonetti, R.M. West, J.C. Serrano-Ruiz, et al., *Catalytic conversion of biomass to monofunctional hydrocarbons and targeted liquid-fuel classes.* **Science**, 2008. 322: p. 417-421.

45. Roman-Leshkov, Y., J.N. Chheda, and J.A. Dumesic, *Phase modifiers promote efficient production of hydroxymethylfurfural from fructose.* **Science**, 2006. 312: p. 1933-7.

46. Roman-Leshkov, Y., C.J. Barrett, Z.Y. Liu, and J.A. Dumesic, *Production of dimethylfuran for liquid fuels from biomass-derived carbohydrates.* **Nature**, 2007. 447: p. 982-985.

47. Huber, G.W., S. Iborra, and A. Corma, *Synthesis of transportation fuels from biomass: chemistry, catalysts, and engineering.* **Chemical reviews**, 2006. 106.

48. Huber, G.W., J.N. Chheda, C.J. Barrett, and J.A. Dumesic, *Production of liquid alkanes by aqueous-phase processing of biomass-derived carbohydrates.* **Science**, 2005. 308: p. 1446-1450.

49. Tuck, C.O., E. Pérez, I.T. Horváth, R.A. Sheldon, et al., *Valorization of Biomass: Deriving More Value from Waste.* **Science**, 2012. 337: p. 695-699.

50. Bozell, J.J., *Connecting Biomass and Petroleum Processing with a Chemical Bridge.* **Science**, 2010. 329: p. 522-523.

51. Serrano-Ruiz, J.C., R. Luque, and A. Sepulveda-Escribano, *Transformations of biomass-derived platform molecules: from high added-value chemicals to fuels via aqueous-phase processing.* **Chemical Society Reviews**, 2011. 40: p. 5266-5281.

52. Rinaldi, R. and F. Schueth, *Acid Hydrolysis of Cellulose as the Entry Point into Biorefinery Schemes.* **ChemSusChem**, 2009. 2: p. 1096-1107.

53. Kreissl, H.T., K. Nakagawa, Y.-K. Peng, Y. Koito, et al., *Niobium oxides: correlation of acidity with structure and catalytic performance in sucrose conversion to 5-hydroxymethylfurfural.* **Journal of Catalysis**, 2016. 338: p. 329-339.

54. Serrano-Ruiz, J.C., R. Luque, and A. Sepulveda-Escribano, *Transformations of biomass-derived platform molecules: from high added-value chemicals to fuels via aqueous-phase processing.* **Chem. Soc. Rev.**, 2011. 40: p. 5266-5281.

55. Gallo, J.M.R., D.M. Alonso, M.A. Mellmer, and J.A. Dumesic, *Production and upgrading of 5-hydroxymethylfurfural using heterogeneous catalysts and biomass-derived solvents.* **Green Chem.**, 2013. 15: p. 85-90.

56. Lange, J.-P., E. van der Heide, J. van Buijtenen, and R. Price, *Furfural-a Promising Platform for Lignocellulosic Biofuels.* **ChemSusChem**, 2012. 5: p. 150-166.

57. Rosatella, A.A., S.P. Simeonov, R.F. Frade, and C.A. Afonso, *5-Hydroxymethylfurfural (HMF) as a building block platform: Biological properties, synthesis and synthetic applications.* **Green Chemistry**, 2011. 13: p. 754-793.

58. Mukherjee, A., M.-J. Dumont, and V. Raghavan, *Review: sustainable production of hydroxymethylfurfural and levulinic acid: challenges and opportunities.* **Biomass and Bioenergy**, 2015. 72: p. 143-183.

59. Agirrezabal-Telleria, I., I. Gandarias, and P. Arias, *Heterogeneous acid-catalysts for the production of furan-derived compounds (furfural and hydroxymethylfurfural) from renewable carbohydrates: a review.* **Catalysis Today**, 2014. 234: p. 42-58.

60. Antunes, M.M., P.A. Russo, P.V. Wiper, J.M. Veiga, et al., *Sulfonated graphene oxide as effective catalyst for conversion of 5-(hydroxymethyl)-2-furfural into biofuels.* **ChemSusChem**, 2014. 7: p. 804-812.

61. Rao, R., A. Dandekar, R. Baker, and M. Vannice, *Properties of copper chromite catalysts in hydrogenation reactions.* **Journal of Catalysis**, 1997. 171: p. 406-419.

62. Seo, G. and H. Chon, *Hydrogenation of furfural over copper-containing catalysts.* **Journal of Catalysis**, 1981. 67: p. 424-429.

63. Rao, R.S., R.T.K. Baker, and M.A. Vannice, *Furfural hydrogenation over carbon-supported copper.* **Catalysis Letters**, 1999. 60: p. 51-57.

64. Nagaraja, B., V.S. Kumar, V. Shasikala, A. Padmasri, et al., *A highly efficient Cu/MgO catalyst for vapour phase hydrogenation of furfural to furfuryl alcohol.* **Catalysis communications**, 2003. 4: p. 287-293.

65. Pushkarev, V.V., N. Musselwhite, K. An, S. Alayoglu, et al., *High Structure Sensitivity of Vapor-Phase Furfural Decarbonylation/Hydrogenation Reaction Network as a Function of Size and Shape of Pt Nanoparticles.* **Nano Letters**, 2012. 12: p. 5196-5201.

66. Lange, J.P., E. van der Heide, J. van Buijtenen, and R. Price, *Furfural—a promising platform for lignocellulosic biofuels.* **ChemSusChem**, 2012. 5: p. 150-166.

67. Chiaramonti, D., M. Prussi, S. Ferrero, L. Oriani, et al., *Review of pretreatment processes for lignocellulosic ethanol production, and development of an innovative method.* **Biomass & Bioenergy**, 2012. 46: p. 25-35.

68. Sutton, A.D., F.D. Waldie, R. Wu, M. Schlaf, et al., *The hydrodeoxygenation of bioderived furans into alkanes.* **Nat Chem**, 2013. 5: p. 428-432.

69. Maldonado, G.M.G., R.S. Assary, J. Dumesic, and L.A. Curtiss, *Experimental and theoretical studies of the acid-catalyzed conversion of furfuryl alcohol to levulinic acid in aqueous solution.* **Energy & Environmental Science**, 2012. 5: p. 6981-6989.

70. Horváth, I.T., H. Mehdi, V. Fábos, L. Boda, et al., *γ-Valerolactone—a sustainable liquid for energy and carbon-based chemicals.* **Green Chemistry**, 2008. 10: p. 238-242.

71. Fegyverneki, D., L. Orha, G. Láng, and I.T. Horváth, *Gamma-valerolactone-based solvents.* **Tetrahedron**, 2010. 66: p. 1078-1081.

72. Di Mondo, D., D. Ashok, F. Waldie, N. Schrier, et al., *Stainless steel as a catalyst for the total deoxygenation of glycerol and levulinic acid in aqueous acidic medium.* **Acs Catalysis**, 2011. 1: p. 355-364.

73. Serrano-Ruiz, J.C., D. Wang, and J.A. Dumesic, *Catalytic upgrading of levulinic acid to 5-nonanone.* **Green Chemistry**, 2010. 12: p. 574-577.

74. Serrano-Ruiz, J.C., D.J. Braden, R.M. West, and J.A. Dumesic, *Conversion of cellulose to hydrocarbon fuels by progressive removal of oxygen.* **Applied Catalysis B: Environmental**, 2010. 100: p. 184-189.

75. Goldemberg, J., *Ethanol for a sustainable energy future.* **Science**, 2007. 315: p. 808-810.

76. Energy, E.E.R. *Alternative Fuels Data Center*. 2017 [Accessed May 26 2017].

77. Innovation, A.I., *Ethanol industry outlook.* **Report Renewable Fuels Association**, 2012.

78. Kullander, S., *Food security: crops for people not for cars.* **AMBIO: A Journal of the Human Environment**, 2010. 39: p. 249-256.

79. Valentine, J., J. Clifton-Brown, A. Hastings, P. Robson, et al., *Food vs. fuel: the use of land for lignocellulosic 'next generation'energy crops that minimize competition with primary food production.* **Gcb Bioenergy**, 2012. 4: p. 1-19.

80. Faraco, V., *Lignocellulose conversion*. 2013: Springer.

81. Bos, H.L., K.P.H. Meesters, S.G. Conijn, W.J. Corré, et al., *Accounting for the constrained availability of land: a comparison of bio-based ethanol, polyethylene, and PLA with regard to non-renewable energy use and land use.* **Biofuels, Bioproducts and Biorefining**, 2012. 6: p. 146-158.

82. Zhang, M. and Y. Yu, *Dehydration of Ethanol to Ethylene.* **Industrial & Engineering Chemistry Research**, 2013. 52: p. 9505-9514.

83. Kagyrmanova, A.P., V.A. Chumachenko, V.N. Korotkikh, V.N. Kashkin, et al., *Catalytic dehydration of bioethanol to ethylene: Pilot-scale studies and process simulation.* **Chemical Engineering Journal**, 2011. 176–177: p. 188-194.

84. Phung, T.K., L. Proietti Hernández, A. Lagazzo, and G. Busca, *Dehydration of ethanol over zeolites, silica alumina and alumina: Lewis acidity, Brønsted acidity and confinement effects.* **Applied Catalysis A: General**, 2015. 493: p. 77-89.

85. DeWilde, J.F., H. Chiang, D.A. Hickman, C.R. Ho, et al., *Kinetics and Mechanism of Ethanol Dehydration on γ-Al2O3: The Critical Role of Dimer Inhibition.* **ACS Catalysis**, 2013. 3: p. 798-807.

86. Gallego, E.M., M.T. Portilla, C. Paris, A. León-Escamilla, et al., *"Ab initio" synthesis of zeolites for preestablished catalytic reactions.* **Science**, 2017. 355: p. 1051-1054.

87. Williams, C.L., C.-C. Chang, P. Do, N. Nikbin, et al., *Cycloaddition of Biomass-Derived Furans for Catalytic Production of Renewable p-Xylene.* **ACS Catalysis**, 2012. 2: p. 935-939.

88. Jae, J., G.A. Tompsett, A.J. Foster, K.D. Hammond, et al., *Investigation into the shape selectivity of zeolite catalysts for biomass conversion.* **J. Catal.**, 2011. 279: p. 257-268.

89. Williams, C.L., *Production of Sustainable Aromatics from Biorenewable Furans*, in *Department of Chemical Engineering*. 2014, University of Massachusetts: Amherst.

90. Williams, C.L., K.P. Vinter, C.-C. Chang, R. Xiong, et al., *Kinetic regimes in the tandem reactions of H-BEA catalyzed formation of p-xylene from dimethylfuran.* **Catalysis Science & Technology**, 2016. 6: p. 178-187.

91. Cheng, Y.-T. and G.W. Huber, *Production of targeted aromatics by using Diels–Alder classes of reactions with furans and olefins over ZSM-5.* **Green Chemistry**, 2012. 14: p. 3114-3114.

92. Chang, C.-C., H. Je Cho, J. Yu, R.J. Gorte, et al., *Lewis acid zeolites for tandem Diels-Alder cycloaddition and dehydration of biomass-derived dimethylfuran and ethylene to renewable p-xylene.* **Green Chemistry**, 2016. 18: p. 1368-1376.

93. Wang, D., C.M. Osmundsen, E. Taarning, and J.A. Dumesic, *Selective production of aromatics from alkylfurans over solid acid catalysts.* **ChemCatChem**, 2013. 5: p. 2044-2050.

94. Chang, C.-C., S.K. Green, C.L. Williams, P.J. Dauenhauer, et al., *Ultra-selective cycloaddition of dimethylfuran for renewable p-xylene with H-BEA.* **Green Chemistry**, 2014. 16: p. 585-588.

95. Nikbin, N., S. Feng, S. Caratzoulas, and D.G. Vlachos, *p-Xylene formation by dehydrative aromatization of a Diels–Alder product in Lewis and Brønsted acidic zeolites.* **The Journal of Physical Chemistry C**, 2014. 118: p. 24415-24424.

96. Patet, R.E., N. Nikbin, C.L. Williams, S.K. Green, et al., *Kinetic regime change in the tandem dehydrative aromatization of furan Diels–Alder products.* **ACS Catalysis**, 2015. 5: p. 2367-2375.

97. Green, S.K., R.E. Patet, N. Nikbin, C.L. Williams, et al., *Diels–Alder cycloaddition of 2-methylfuran and ethylene for renewable toluene.* **Applied Catalysis B: Environmental**, 2016. 180: p. 487-496.

98. Sauer, J. and R. Sustmann, *Mechanistic Aspects of Diels-Alder Reactions: A Critical Survey.* **Angewandte Chemie International Edition in English**, 1980. 19: p. 779-807.

99. Kappe, C.O., S.S. Murphree, and A. Padwa, *Synthetic applications of furan Diels-Alder chemistry.* **Tetrahedron**, 1997. 53: p. 14179-14233.

100. Holmes, H., *The Diels-Alder Reaction Ethylenic and Acetylenic Dienophiles*. 1948: Wiley Online Library.

101. Diels, O. and K. Alder, *Synthesen in der hydro-aromatischen Reihe, II. Mitteilung: Über Cantharidin.* **European Journal of Inorganic Chemistry**, 1929. 62: p. 554-562.

102. Clayden, J. and N.W. Greeves, *Organic chemistry*. 2012.

103. Bornholdt, K. and H. Lechert, *Catalysis of a liquid-phase Diels-Alder reaction by zeolites Y, EMT, ZSM-5 and beta.* **Studies in Surface Science and Catalysis**, 1995. 94: p. 619-626.

104. Settle, A.E., L. Berstis, N.A. Rorrer, Y. Roman-Leshkov, et al., *Heterogeneous Diels-Alder catalysis for biomass-derived aromatic compounds.* **Green Chemistry**, 2017.

105. Ragauskas, A.J., C.K. Williams, B.H. Davison, G. Britovsek, et al., *The path forward for biofuels and biomaterials.* **Science**, 2006. 311: p. 484-489.

106. Do, P.T., J.R. McAtee, D.A. Watson, and R.F. Lobo, *Elucidation of Diels–Alder reaction network of 2, 5-dimethylfuran and ethylene on HY zeolite catalyst.* **ACS catalysis**, 2012. 3: p. 41-46.

107. Cheng, Y.-T. and G.W. Huber, *Chemistry of Furan Conversion into Aromatics and Olefins over HZSM-5: A Model Biomass Conversion Reaction.* **ACS Catalysis**, 2011. 1: p. 611-628.

108. Pearce, H., *Zeolite molecular sieves—Structure, chemistry and use: by DA Breck*. 1975, Elsevier: New York.

109. Corma, A., *From microporous to mesoporous molecular sieve materials and their use in catalysis.* **Chemical reviews**, 1997. 97: p. 2373-2420.

110. Pérez-Ramírez, J., D. Verboekend, A. Bonilla, and S. Abelló, *Zeolite Catalysts with Tunable Hierarchy Factor by Pore-Growth Moderators.* **Advanced Functional Materials**, 2009. 19: p. 3972-3979.

111. Corma, A., *Inorganic solid acids and their use in acid-catalyzed hydrocarbon reactions.* **Chemical Reviews**, 1995. 95: p. 559-614.

112. Corma, A., H. García, and F. Llabrés i Xamena, *Engineering metal organic frameworks for heterogeneous catalysis.* **Chemical Reviews**, 2010. 110: p. 4606-4655.

113. Verboekend, D., *New hierarchical zeolite catalysts by post-synthetic design.* 2012.

114. Willhammar, T., J. Sun, W. Wan, P. Oleynikov, et al., *Structure and catalytic properties of the most complex intergrown zeolite ITQ-39 determined by electron crystallography.* **Nat Chem**, 2012. 4: p. 188-194.

115. Corma, A., V. Fornes, S.B. Pergher, T.L.M. Maesen, et al., *Delaminated zeolite precursors as selective acidic catalysts.* **Nature**, 1998. 396: p. 353-356.

116. Sartbaeva, A., S.A. Wells, M. Treacy, and M. Thorpe, *The flexibility window in zeolites.* **Nature materials**, 2006. 5: p. 962-965.

117. Association, I.Z. *Database of Zeolite Structures*. 2017 [Accessed May 31 2017].

118. Taarning, E., C.M. Osmundsen, X. Yang, B. Voss, et al., *Zeolite-catalyzed biomass conversion to fuels and chemicals.* **Energy & Environmental Science**, 2011. 4: p. 793-804.

119. Corma, A., S. Iborra, and A. Velty, *Chemical Routes for the Transformation of Biomass into Chemicals.* **Chemical Reviews**, 2007. 107: p. 2411-2502.

120. Kamm, B., *Production of Platform Chemicals and Synthesis Gas from Biomass.* **Angewandte Chemie International Edition**, 2007. 46: p. 5056-5058.

121. Taarning, E., S. Saravanamurugan, M. Spangsberg Holm, J. Xiong, et al., *Zeolite-Catalyzed Isomerization of Triose Sugars.* **ChemSusChem**, 2009. 2: p. 625-627.

122. Holm, M.S., S. Saravanamurugan, and E. Taarning, *Conversion of Sugars to Lactic Acid Derivatives Using Heterogeneous Zeotype Catalysts.* **Science**, 2010. 328: p. 602-605.

123. Lappas, A.A., S. Bezergianni, and I.A. Vasalos, *Production of biofuels via co-processing in conventional refining processes.* **Catalysis Today**, 2009. 145: p. 55-62.

124. Carlson, T.R., T.P. Vispute, and G.W. Huber, *Green Gasoline by Catalytic Fast Pyrolysis of Solid Biomass Derived Compounds.* **ChemSusChem**, 2008. 1: p. 397-400.

125. Samolada, M.C., A. Papafotica, and I.A. Vasalos, *Catalyst Evaluation for Catalytic Biomass Pyrolysis.* **Energy & Fuels**, 2000. 14: p. 1161-1167.

126. Samolada, M.C., W. Baldauf, and I.A. Vasalos, *Production of a bio-gasoline by upgrading biomass flash pyrolysis liquids via hydrogen processing and catalytic cracking.* **Fuel**, 1998. 77: p. 1667-1675.

127. Takahara, I., M. Saito, M. Inaba, and K. Murata, *Dehydration of Ethanol into Ethylene over Solid Acid Catalysts.* **Catalysis Letters**, 2005. 105: p. 249-252.

128. Bjørgen, M., F. Joensen, K.-P. Lillerud, U. Olsbye, et al., *The mechanisms of ethene and propene formation from methanol over high silica H-ZSM-5 and H-beta.* **Catalysis Today**, 2009. 142: p. 90-97.

129. Calsavara, V., M.L. Baesso, and N.R.C. Fernandes-Machado, *Transformation of ethanol into hydrocarbons on ZSM-5 zeolites modified with iron in different ways.* **Fuel**, 2008. 87: p. 1628-1636.

130. Mentzel, U.V., S. Shunmugavel, S.L. Hruby, C.H. Christensen, et al., *High Yield of Liquid Range Olefins Obtained by Converting i-Propanol over Zeolite H-ZSM-5.* **Journal of the American Chemical Society**, 2009. 131: p. 17009-17013.

Chapter 2

Analytical Techniques

Chapter 2: Analytical Techniques

2.1 Introduction 53

2.2 X-Ray Diffraction (XRD) 54

2.3 Synchrotron X-Ray Diffraction (SXRD) 56

2.4 Transmission Electron Microscopy (TEM) 58

2.5 Scanning Electron Microscopy (SEM) 61

2.6 Thermogravimetric Analysis (TGA) 63

2.7 Temperature-Programmed Desorption (TPD) 64

2.8 ^{27}Al ssNMR – Aluminium Environment 66

2.9 ^{31}P ssNMR – Acid Sites Determination 67

2.10 BET surface area analysis 67

2.11 Inductive Coupled Plasma-Atomic Emission Spectroscopy (ICP- AES) 70

2.12 Fourier Transform Infrared (FTIR) spectroscopy 70

2.13 References 73

2.1 Introduction

Zeolites are crystalline aluminosilicates displaying ordered networks of micropores and active acid sites. As their catalytic properties are completely related to their porous structure, crystallinity, and acid sites concentration/composition, it is essential to characterize these properties to understand and control catalytic activity. Thus, the most commonly used analytical techniques to characterize zeolites are X-ray powder diffraction (XRD), Brunauer-Emmett-Teller (BET) surface area analysis, transmission electron microscopy (TEM), scanning electron microscopy (SEM) and ammonia temperature-programmed desorption (TPD). The XRD technique is widely used to confirm the zeolite's phase and define its crystallinity degree, the electron microscopy techniques TEM and SEM help to analyse its porous structure and surface texture, while the BET can estimate its surface area and its pore size and volume. Another important technique is the TPD of ammonia or propylamine which can give valuable information about the acid sites, differentiating the Lewis acid sites from the Brønsted acid sites and quantifying both. All these techniques were used in this work to characterize zeolites applied in the conversion of biomass-derived furans into aromatics, however, more sophisticated techniques were needed to explain some of the results obtained here. Synchrotron X-ray powder diffraction (SXRD) combined with Rietveld refinement were used to elucidate adsorbate structures in zeolite, which allowed to link the strength of the acid sites with their location in the zeolites framework and to understand the interactions between reactants and the acid sites inside the zeolite's pores. Furthermore, ^{27}Al Solid-state NMR (ssNMR) and ^{31}P ssNMR of adsorbed probe molecules were used to better understand the nature and strength of the active acid sites.

The aim of this chapter is to present and briefly explain the analytical techniques most used in this work for zeolites characterization, the results of which will be presented and discussed in subsequent chapters. In particular, details concerning specific instrument types, operational parameters, theoretical principles and examples of information obtained from such techniques are briefly covered.

2.2 X-Ray Diffraction (XRD)

X-ray diffraction (XRD) is one of the most widely used diffractions technique for structure determination in solid state chemistry and material science. This technique is used to determine the atom positions which make up a solid compound, providing a description of structures in terms of features, such as bond lengths, bond angles and relative positions of ions and molecules in unit cell.[1, 2] It also provides information on the composition, phase composition and size of crystallite materials.[3] In this work this technique is used mainly to confirm the zeolite's phase and synchrotron X-ray powder diffraction (SXRD) combined with Rietveld refinement to elucidate adsorbate structures in zeolite.

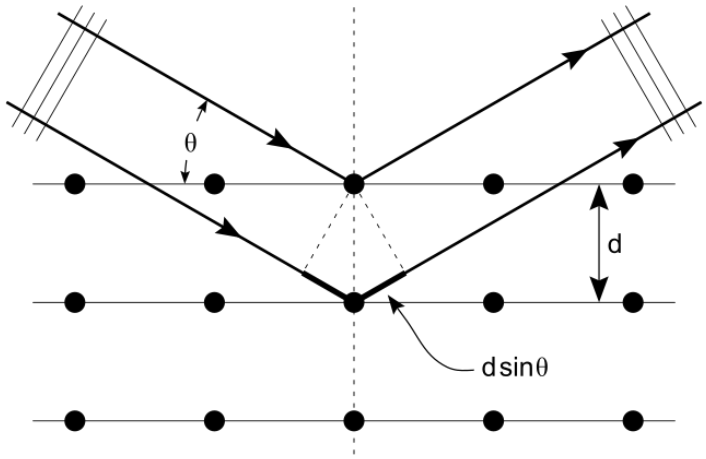


Figure 2.1 Illustration of Bragg's Law derived by treating layers of atom as reflecting planes. X-rays interfere constructively when the additional path length 2 *d* sin *θ* is equal to integral multiple of the wavelength λ.[4]

When an X-ray beam impinges upon a crystal, it generates a unique pattern of diffracted X-rays, distributed according to Bragg's law (**Figure 2.1**).[4] In short, Bragg's law has to be satisfied for diffraction to occur, where intense peaks of diffracted X-rays are detected at certain X-ray wavelengths and incident radiation angles (*θ*). Bragg peaks are observed when the scattered X-ray beams constructively interfere (where n is an integer). The Bragg's law can be described by the equation below:

$$n\lambda = 2d\ sin\ \theta \tag{2.1}$$

where *d* is the inter-planar distance,

θ is the scattering angle,

n is an integer, and

λ is the wavelength of the incident X-ray.

Powdered crystalline solids contain enormous number of crystallites oriented at random relative to incident beam. Then intensity of diffracted X-ray is measured as a

function of angle with detector to obtain the diffraction pattern. Using peak positions and full width half maximum (FWHM) of each peak, the lattice spacing and crystallite size can be calculated.[5]

Single-crystal XRD and powder XRD (PXRD) can be used to study the structure of zeolites. As zeolites can be rarely found in single crystal form, powder XRD is mostly applied to obtain diffraction pattern for these materials.[6] For a known synthesized zeolite, it is possible to check the quality of the structure by comparing the diffractogram with the computer-generated standard patterns from "The International Zeolite Association (IZA)".[7] Therefore, the XRD pattern can be used as a fingerprint for different materials as well as zeolite structures.[6, 8] When studying zeolite chemistry, PXRD is more commonly used than single-crystal XRD, since zeolites samples are commonly found in polycrystalline form. The PXRD shows a true representation of bulk behaviour, even when the specimen is subjected to non-ambient or *operando* conditions. But a major disadvantage of PXRD is the overlap of Bragg peaks, which prevents the most accurate determination of the structure. Here the use of high resolution synchrotron X-ray powder diffraction (SXPD) can mitigate the issue to some extent.

2.3 Synchrotron X-Ray Diffraction (SXRD)

Synchrotron X-ray beams are generated by a large particle accelerator where very fast electrons (approaching the speed of light) are accelerated in magnetic lattices such as bending magnets and insertion devices (undulators and wigglers).[9] It can generate a very powerful X-ray beam, in particular at today's 3rd generation synchrotron facilities such as Diamond Light Source (UK), SPring-8 (Japan), Advanced Photon Source (USA) and European Synchrotron Radiation Facility (France). **Figure 2.2**

exemplifies a typical synchrotron facility. By harnessing the power of the synchrotron X-ray beams, purposely built beamlines (tangential to the main storage ring) are used to probe the minute details of material.

The unique properties of synchrotron light have several advantages: 1) a high brightness (intense and tight collimation); 2) horizontal polarisation, which reduces the fall in intensity as a function of 2θ and tuneable X-ray wavelength, avoiding the X-ray absorption problems of certain atoms, consequently reducing sample fluorescence which leads to high backgrounds. For these reasons, SXRD has many benefits over laboratory analogues.[9-11]

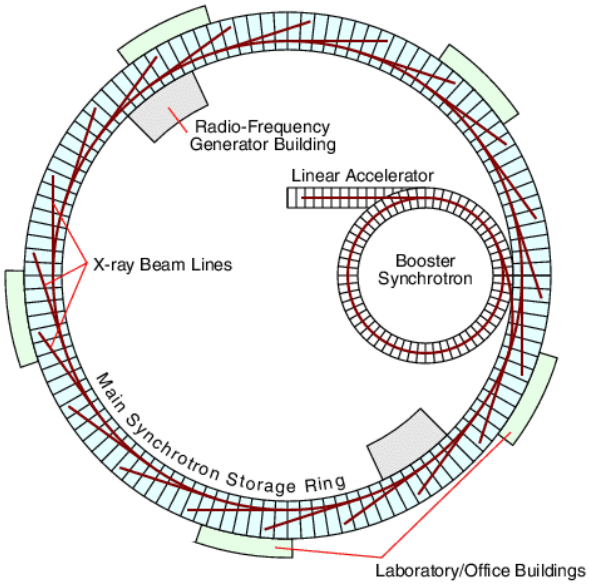


Figure 2.2. Schematic of a synchrotron X-ray facility.[9]

These features allow higher resolution data to be obtained with relative short collection times. This high-quality data allows the application of Rietveld refinement with more accuracy, making it possible to, for example, determine the position of probe molecules and their interactions with the zeolite framework. When SXRD is employed in

zeolite studies, it is mainly applied for the following purposes: Investigation of new zeolite materials where high brightness instrument can accurately determine the structures; Extreme temperature and/or pressure study, which cannot be done using a laboratory diffractometer; *In situ*/*operando* study, technologically permissible to develop dedicated sample environments.[9]

Herein, *in situ/operando* SXRD experiments (described in **Chapter 3**) were performed with ZSM-5 and USY samples under reaction conditions, in order to obtain insights about the reactions mechanisms and the reactants interactions with the zeolite's active acid sites.

2.4 Transmission Electron Microscopy (TEM)

TEM is a valuable analytical technique for the characterization of materials at the nanoscale. It extends the resolution available for morphological studies beyond that available under visible light illumination, which is limited by its wavelength (390 to 700 nm). To obtain images of lattice planes and structures with nanoscale dimensions a wavelength is needed with much smaller dimension, such as high voltage electron beams.[12]

In order to achieve the sufficiently high resolution the electron gun replaces the light source and is maintained at a high voltage (typically 100-400 kV), the beam in general is generated by a lanthanum hexaboride (LaB_6) crystals source capable of generating the electron beam with current density of the order of 1×10^6 A m^{-2}. As it is a transmission technique, the sample must be a thin layer or it will completely block the electron beam. The sample is exposed to this high energy electron beam that interacts

with sample specimen to form high resolution image on the fluorescent screen or a diffraction pattern.

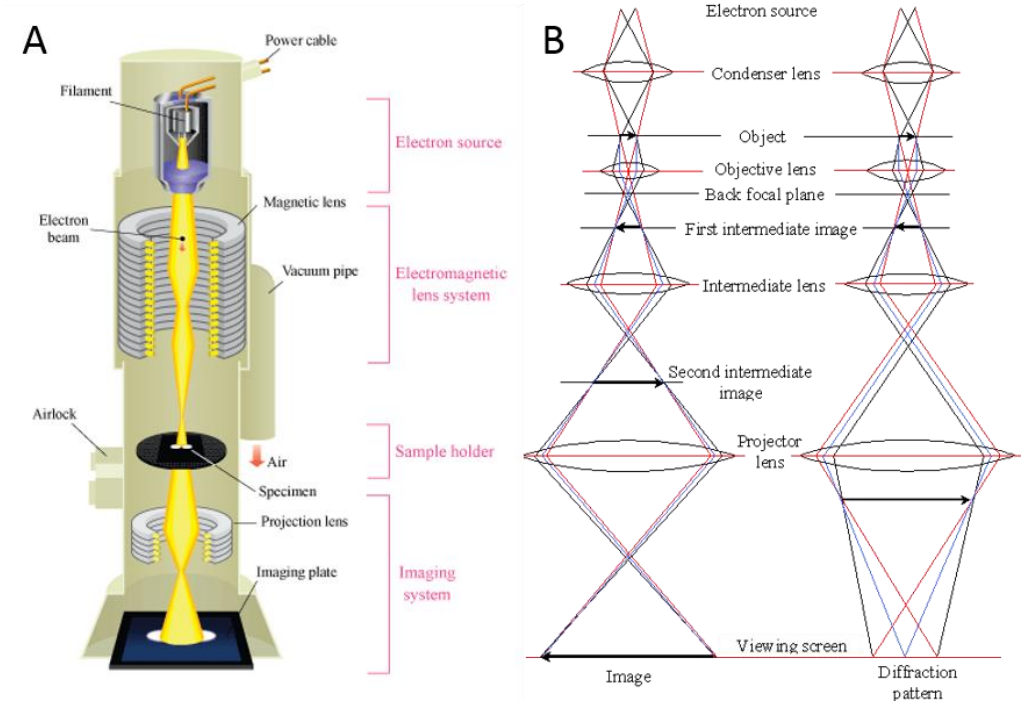


Figure 2.3 a) Cross section diagram of typical TEM instrument and its most essential parts; **b)** When imaging system is focused on the specimen (front focal plane of the objective) an image of the specimen is formed on the fluorescent screen, while diffraction pattern results when imaging system is focused on back plane of the objective.

The TEM uses the electron beam upside down, unlike the optical microscopy, and the recording system lies usually at the bottom (**Figure 2.3**). To obtain TEM images, it is essential for electron to pass through the specimen. This is generally achieved to by mechanical thinning, electrochemical thinning, ion milling or by drop-dry methods using dispersion of the nanomaterials, to ensure the thickness of specimen is less than 100 nm. The high energy electrons from gun are focused by an electromagnetic condenser lens system, whose focus in turn is controlled by varying the lens current. In order to focus the

first image when the beam strikes the sample, elastically scattered electrons transmitted through the specimen are refocused by the projection lens by controlling their current and similarly the final image is also generated by electromagnetic lenses to focus the image onto a phosphor screen. Furthermore, as the high energy electron beam has a very limited path length in air, the microscope column is kept under a vacuum of 10^{-7} Torr during operation.

Given that the maximum beam divergence in electron microscope is less than 1°, the Rayleigh criterion for the image of a point source can be reduced to following equation:

$$\delta_d = \frac{0.61\,\lambda o}{n \sin \alpha} \tag{2.2}$$

Where α is the semi-angle subtended at the object by the lens, λ_0 is the wavelength of radiation in the object space and n is the refractive index. From the equation, a wavelength of $\lambda_0 < 0.1$ nm is needed to resolve the crystal lattices on atomic scale and thus electrons are the ideal choice to achieve such resolution (at 200 kV has $\lambda_0 = 2.5$ pm).

In practice is possible to improve the microscope resolution by increasing the accelerating voltage, however, most samples are liable to radiation damage after a prolonged exposure. In practice, the resolution of TEM is much worse than the theoretical Rayleigh limit, due to the non-spherical nature of the lenses. This can be improved by reducing aberration coefficients for the electromagnetic lenses.

In TEM diffraction mode, similar to XRD, selected area electron diffraction (SAED) can be used to reveal a specific ordered structure of the sample, depending upon the long-range order (diffraction pattern comprises of an array of spots) or superimposed

crystallographic orientations (concentric rings pattern). Crystal lattices can be determined by measuring the spacing ratios as well as lattice parameter.

2.5 Scanning Electron Microscopy (SEM)

Scanning electron microscopy (SEM) is one of the easiest and most used techniques to determine the morphology of a material.[13] The main parts of an SEM instrument are illustrated in **Figure 2.4**. It works in a very similar way to TEM fashion, the electron beam is also generated by single crystal/filament of tungsten or lanthanum hexaboride (LaB_6). Electromagnetic lenses are used to focus the electron beam and make a tiny spot of the electron beam. After the beam passed through scanning coil/objective lens, the beam is scanned along the surface sample in a raster fashion.[13] The instrument operates under vacuum condition to avoid further collisions between electrons beam and gas molecules to preserve their energy.[14]

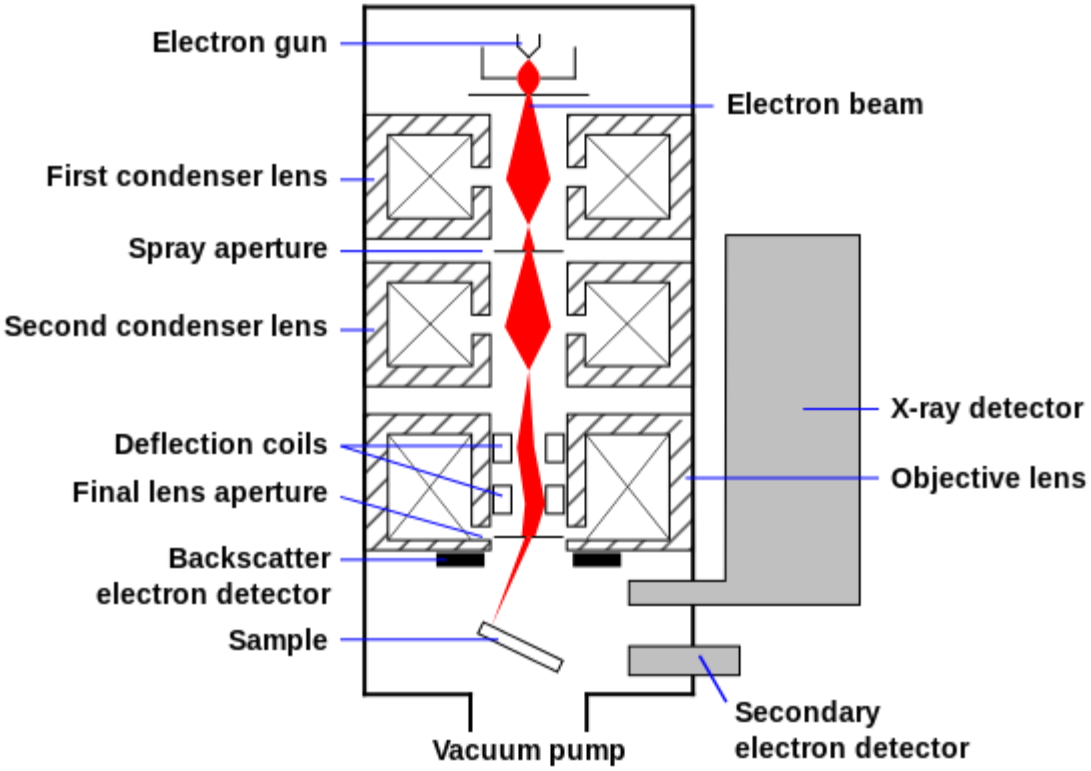


Figure 2.4 Schematic representation of a scanning electron microscopy (SEM).[14]

When the primary electrons collide with the sample's surface atoms, a number of signals, such as secondary (SE), backscattered (BSE), transmitted, auger and diffracted electrons, as well as characteristic X-rays (EDX) are emitted (**Figure 2.5**). The energy transferred by the beam for the surface atoms excites the its electrons and results in emission of secondary electrons, which have low energy (5-50 eV) and can be collected by a detector to create an image.

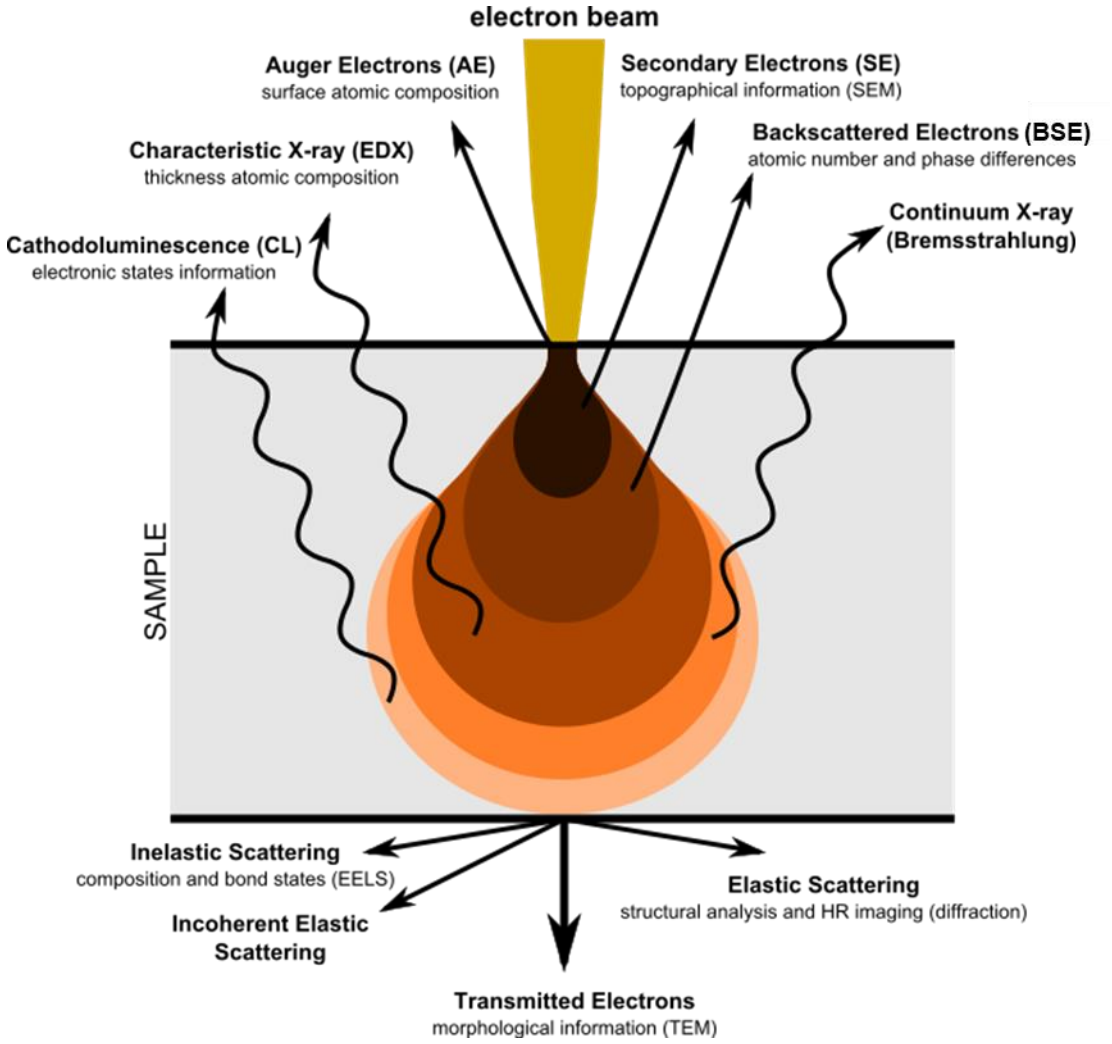


Figure 2.5: A schematic of various possible emitted signals resulting from the electron-surface interaction.[15]

2.6 Thermogravimetric Analysis (TGA)

Thermogravimetric Analysis (TGA) is one of the analytical methods to study the stability or transformation/reaction of a material by monitoring the weight loss along a temperature range. The TGA equipment is composed by a precise microbalance, crucible which is then loaded with sample and a programmable furnace. Any weight change from phenomena such as oxidation, reduction, desorption, and decomposition can be observed in the TGA. This can predict the thermal stability of a material at elevated

temperatures. Upon heating, any adsorbed molecules on zeolites, such as water and ammonia, desorb accordingly.[16] Another important application of this technique is to quantify the carbon deposition on zeolites surface after catalytic reactions. As the TGA analysis can be performed under flow of different gases, when the analysis is performed under air or oxygen is possible to identify and quantify the weight loss due to the carbon oxidation into CO_2.[17]

2.7 Temperature-Programmed Desorption (TPD)

Temperature-Programmed Desorption (TPD) is one of the most widely used and flexible techniques for characterizing the acid sites on zeolites. The activity of zeolites depends on many factors, but the Brønsted-acid site density is usually one of the most crucial parameters.

TPD of adsorbed ammonia in zeolites pores is a widely used method for characterization of Brønsted acid site densities due to the simplicity of the technique. As the ammonia molecule is very basic it is capable of bonding strongly to the Brønsted acid sites.[18] It also can bond less strongly to Lewis acid sites, however, in some cases it might be difficult to distinguish between Brønsted and Lewis acid sites.[19] This difficulty can be solved performing a TPD of amines instead of ammonia, with ammonia commonly replaced by propylamine.

The TPD of amines is based on the fact that alkylammonium ions, formed when alkyl amines are protonated by Brønsted sites, decompose to ammonia and olefins in a well-defined temperature range *via* a reaction similar to the Hofmann-elimination

reaction.[19-23] The reactions involved in amine TPD techniques can be described as follows:

$$HRNH_2 + Z\text{-}OH\ (Brønsted\ site) \longrightarrow HRNH_3^+\cdots ZO^- \quad (2.3)$$

$$HRNH_3^+\cdots ZO^- \longrightarrow R + NH_3 + ZOH \quad (2.4)$$

As the decomposition temperature for the alkyl ammonium ions are the same for all Brønsted acid sites, if the sites are strong enough to protonate the amine the elimination reaction will occur. Furthermore, as the reaction happens in the same way for different amines, as long as the amine is small enough to access the acid site it can be used as a probe in this technique.[20]

The acid concentration is obtained from the detection/quantification of the ammonia or olefin signal, which can be easily differentiated from the amine, by gas chromatography (GC) or mass spectroscopy (MS), as exampled in **Figure 2.6**.

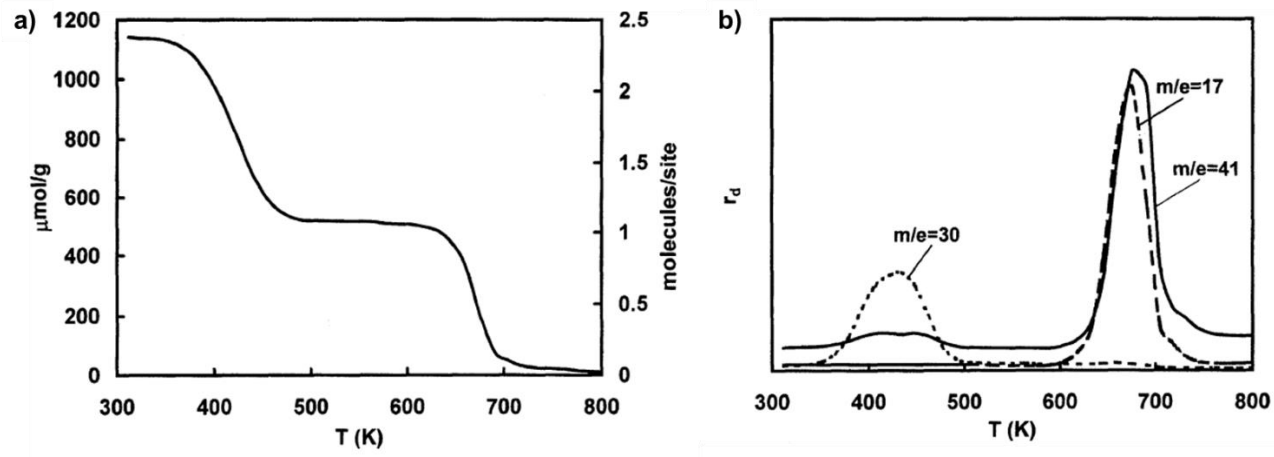


Figure 2.6: a) TPD-TGA result for n-propylamine desorption from HZSM-5; **b)** The MS signal as a function of temperature during the amine TPD.[20]

The TPD-TGA data shows that the desorption happens in two well-defined events, the first from 400 to 500K due the desorption of unreacted amine molecules (m/e=30) and the second from 650 to 725K related with the amine decomposition into propene (m/e=41) and ammonia (m/e=17).[20]

2.8 ^{27}Al ssNMR – Aluminium Environment

Solid-state NMR is one of the primary tools used in the structural characterization of zeolites catalysts. It can easily differentiate BAS and LAS, the coordination of Al (framework-Al or extra-framework-Al), the distribution of Al between the tetrahedral sites, among other information about the aluminium species environment.[24]

The principle of ssNMR spectroscopy is like that of the solution state analogues. NMR is a physical phenomenon in which nuclei exposed to a magnetic field absorb and re-emit electromagnetic radiation. This energy is at a specific resonance frequency (radio waves) which depends on the strength of the magnetic field and the magnetic properties of the isotope of the atoms. In contrast to traditional solution state NMR spectroscopy where the interactions between the nuclei are isotropic, the interactions in ssNMR are anisotropic due to the absence of sample mobility. The anisotropy leads to peak broadening in the ssNMR spectra, which means that there will be significant peak overlap if the peaks are near. There are various techniques for reducing the problems of line broadening, hence increasing the resolution of the ssNMR spectra. In the modern high-resolution ssNMR instruments, the following techniques are mostly pre-installed: magic angle spinning (MAS), macroscopic sample orientation, and radio frequency irradiation.[25]

The ^{27}Al ssNMR can give valuable information about the aluminium environment, differentiating framework and non-framework aluminium species and their coordination (6-coordinated and 4-coordinated). From this information, it is possible to infer about the Brønsted and Lewis acid sites.

2.9 ^{31}P ssNMR – Acid Sites Determination

In ^{31}P-TMP (Trimethylphosphine) probe ssNMR experiment, the peak position reflects the adsorption environment of the TMP molecule, and the peak area suggests the quantity ratio between the interaction of TMP and acid sites. The technique principle is basically the same from ^{27}Al ssNMR explained above, however, herein the NMR signal comes from a probe molecule the TMP, which shifts its signal position according to the interaction degree with the acid sites in the zeolite. When Brønsted acidity is present, a protonated adduct, $[(CH_3)_3PH]^+$, is formed, and this is characterized by a chemical shift of approximately -4 ppm and a JP-H coupling of approximately 500 Hz.[26, 27] Coordination with Lewis acids results in more negative chemical shifts (typically -40 to -50 ppm).[28, 29]

ssNMR is an excellent technique to accurately determine the acid properties of zeolites. Its major limitation is its inability to reveal the sorption chemistry from a structural perspective, i.e., the location of the acid sites and adsorbed molecules cannot be easily elucidated without other supporting techniques.

2.10 BET surface area analysis

The determination of surface area of powders and porous materials depends on measurement of adsorption. After Langmuir's comprehensive review on the nature of adsorption (1916-1918) the most significant contributions were made by Brunauer and

Emmett (1935, 1937) and later developed into Brunauer-Emmett-Teller (BET) theory in 1938. From BET analysis, it is possible determine the zeolites porosity (i.e. the fraction of voids over total volume), surface texture, the pore sizes, the shape of pores and their pore distribution.

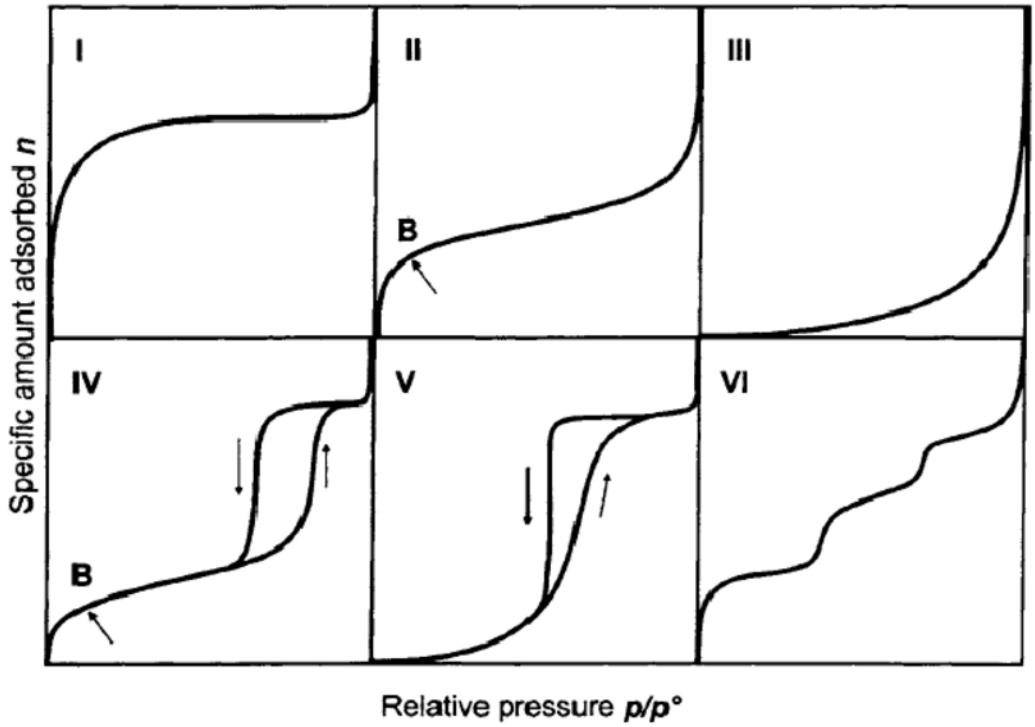


Figure 2.7 The IUPAC six main types of gas physisorption isotherms classification.[30]

An absorption isotherm is a plot of the volume of gas adsorbed *vs*. the relative pressure (p/p^0) at a fixed temperature. Different theories can be used to interpret isotherms which lead to valuable information on surface properties. Most of the physisorption isotherms can be categorized into six types according to IUPAC, as shown in **Figure 2.7**. Isotherm of type I or Langmuir isotherm is characteristic for only monolayer adsorption, requiring a narrow relative pressure range to attain the plateau which is indicative of a limited range of pore sizes, which is typical of many microporous

adsorbents (pore widths below 2 nm). The type II isotherm is typical unrestricted monolayer-multilayer adsorption on heterogeneous substrate. The type III behaviour is relatively rare, and corresponds to the situation where adsorbate-adsorbent interaction are weak, while Type IV isotherms, with a hysteresis loop, indicate the presence of mesopores. A type V isotherm exhibits a hysteresis loop and is associated with mechanism of pore filling, also indicating the weak adsorbate-adsorbent interaction similar to the type III. Type VI stepped isotherm, is associated with layer-by-layer adsorption on highly uniform surfaces, usually when the temperature is near the melting point for the adsorbed gas. Type II and IV are typical isotherms of zeolite materials.[5, 8]

Conventionally surface area analysis is performed by N_2 adsorption/desorption. From these data it is not only possible to caluclate the BET surface area, but also the materials' pore size ditribution and shapes. In addition, the shapes of the adsorption/desorption isotherms can provide information on the nature of the material studied, as exemplified above. In the BET method two stages are involved in the evaluation of the surface area from physisorption isotherm data. In the first stage a BET plot is constructed to derive the value of monolayer capacity ($\boldsymbol{n}_m$) followed by the next stage which is the calculation of the specific surface area (a_{BET}), from $\boldsymbol{n}_m$ by careful consideration of average area, σ, occupied by each molecule in monolayer (i.e. the molecular cross-sectional area).[31]

2.11 Inductive Coupled Plasma-Atomic Emission Spectroscopy (ICP-AES)

Inductive Coupled Plasma-Atomic Emission Spectroscopy (ICP-AES) is an emission spectroscopic technique, where first the sample's atoms are excited by an Inductive Coupled Plasma (ICP), followed by the measurement of the electromagnetic radiation emitted from decaying by Atomic Emission Spectroscopy (AES). Consequently, the characteristic emission energy by different excited atoms/ions allows the elemental identification.[32, 33] ICP-AES provides quantitative elemental information of a sample, where the intensity of the emission shows the concentration of the corresponding element. The main advantage of this technique is that it can simultaneously determine a series of cations, among then Si and Al, which represent most of the zeolites composition.[34]

Once an aqueous sample or solid sample is dissolved in a known volume of acid/alkali solution, it is injected into the ICP-AES instrument, where it is turned into a fine aerosol by a nebulizer, and then thermally excited by an argon ICP that has a temperature close to 7,000 °C. The thermally excited electrons relax to the ground state emitting electromagnetic radiation, for which the energy is element specific.[35]

2.12 Fourier Transform Infrared (FTIR) spectroscopy

Fourier transform infrared spectroscopy (FTIR) is a technique commonly used to obtain an infrared spectrum of absorption or emission of a solid, liquid or gas.[2] It is possible to simultaneously collects high spectral resolution data over a wide spectral range, unlike the dispersive spectrometer which measures intensity over a narrow range

of wavelengths at a time. Since different molecules have different bond energies, infrared absorption is an useful tool for both quantitative and qualitative analysis of samples. Besides, it is used to investigate the interaction between molecules and solid surfaces − for example IR absorption spectra of pre-adsorbed molecules, such as gases (CO and NO)[36] and liquids (ethanol and furan),[37-39] can reveal information about the adsorption sites on heterogeneous catalysts.[3, 36]

The absorption of infrared radiation is associated with a change in vibrational energy level, such that $\Delta E = hv$. The absorbed energy is eventually released as heat and the molecules revert from the excited state to the original state.

A bond in a molecule behaves like two balls connected to a spring, acting as simple harmonic oscillator, for which solution of the Schrödinger equation gives the energies:[2]

$$Ev = \left(v + \frac{1}{2}\right) h\omega \qquad (2.5)$$

where $\omega = (k / \mu)^{1/2}$, v = 0, 1, 2,.., and μ is effective mass of oscillator. For diatomic molecules composed of atom m_A and m_B, $\mu = (m_A m_B / m_A + m_B)$. This effective mass is different for isotopologues which in turn lead to changes in E_v. A nonlinear molecule consisting of N atoms can vibrate in $3N-6$ different independent modes and $3N-5$ ways if it is linear. Only those modes that cause dipole moment to fluctuate in congruence with the changing electric field of the electromagnetic radiation are IR active. The lowest level of these mode has zero-point energy, lowest vibrational energy that a bond can possess.

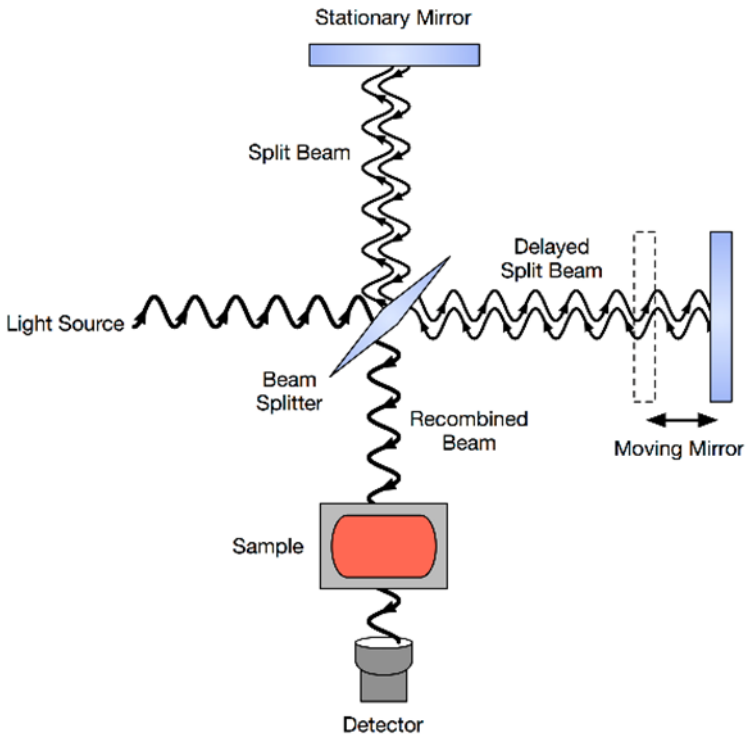


Figure 2.8 Typical set up for an FTIR spectrophotometer.

An FTIR produces a source of incoherent infrared light using a heated filament. The radiation is funnelled through an interferometer where the beam first splits and is recombined by set a of mirrors. It is then directed to the sample and subsequently focused on the detector. The IR spectrum of a compound is obtained by exposing the sample to light in the infrared region and recording an interferogram: a plot of intensity against the difference in the two optical paths. The spectrum is extracted from the interferogram by Fourier transformation, which converts information in time domain to the frequency domain. This means that all frequencies are measured simultaneously.

2.13 References

1. Duckett, S., B. Gilbert, and M. Cockett, *Foundations of Molecular Structure Determination*. 2015: Oxford University Press, USA.

2. Weller, M., T. Overton, J. Rourke, and F. Armstrong, *Inorganic chemistry*. 2014: Oxford University Press, USA.

3. Eley, C.W., *The rational design of photocatalytic semiconductor nanocrystals*. 2014, University of Oxford.

4. Bragg, W.L. *The structure of some crystals as indicated by their diffraction of X-rays*. in *Proceedings of the Royal Society of London A: Mathematical, Physical and Engineering Sciences*. 1913: The Royal Society.

5. Khan, M.A., *Carbon nitride based materials for heterogeneous photocatalysis*, in *Department of Chemistry*. 2016, University of Oxford: Oxford.

6. Kokotailo, G. and C. Fyfe, *Zeolite structure analysis with powder x-ray diffraction and solid-state nmr techniques.* **Rigaku J**, 1995. 12.

7. Association, I.Z. *Database of Zeolite Structures*. 2017 [Accessed May 31 2017].

8. Etemadi, S., *Catalytic investigations of zeolite based methanol to hydrocarbons catalysts*. 2015.

9. Willmott, P., *An introduction to synchrotron radiation: techniques and applications*. 2011: John Wiley & Sons.

10. Cullity, B. and S. Stock, *Principles of X-ray diffraction.* **Rading, MA: Addison-Wesley**, 1978.

11. Cockcroft, J.K. and A.N. Fitch, *Experimental setups*, in *Powder Diffraction*. 2008. p. 20-57.

12. Brandon, D. and W.D. Kaplan, *Microstructural characterization of materials*. 2013: John Wiley & Sons.

13. Chorkendorff, I. and J.W. Niemantsverdriet, *Concepts of modern catalysis and kinetics*. 2006: John Wiley & Sons.

14. Kalantar-zadeh, K. and B. Fry, *Nanotechnology-enabled sensors*. 2007: Springer Science & Business Media.

15. Goldstein, J., D.E. Newbury, P. Echlin, D.C. Joy, et al., *Scanning electron microscopy and X-ray microanalysis: a text for biologists, materials scientists, and geologists*. 2012: Springer Science & Business Media.

16. Coats, A.W. and J.P. Redfern, *Thermogravimetric analysis. A review.* **Analyst**, 1963. 88: p. 906-924.

17. Teixeira, I.F., T.P.V. Medeiros, P.E. Freitas, M.G. Rosmaninho, et al., *Carbon deposition and oxidation using the waste red mud: A route to store, transport and use offshore gas lost in petroleum exploration.* **Fuel**, 2014. 124: p. 7-13.

18. Niwa, M. and N. Katada, *Measurements of acidic property of zeolites by temperature programmed desorption of ammonia.* **Catalysis Surveys from Asia**, 1997. 1: p. 215-226.

19. Juskelis, M.V., J.P. Slanga, T.G. Roberie, and A.W. Peters, *A comparison of CaO, Beta, and a dealuminated Y by ammonia TPD and by temperature programmed 2-propylamine cracking.* **Journal of Catalysis**, 1992. 138: p. 391-394.

20. Kresnawahjuesa, O., R.J. Gorte, D. De Oliveira, and L. Lau, *A simple, inexpensive, and reliable method for measuring Brønsted-acid site densities in solid acids.* **Catalysis letters**, 2002. 82: p. 155-160.

21. Biaglow, A., C. Gittleman, R. Gorte, and R. Madon, *2-Propanamine adsorption on a fluid catalytic cracking catalyst.* **Journal of Catalysis**, 1991. 129: p. 88-93.

22. Tittensor, J., R. Gorte, and D. Chapman, *Isopropylamine adsorption for the characterization of acid sites in silica-alumina catalysts.* **Journal of Catalysis**, 1992. 138: p. 714-720.

23. Kofke, T.G., R. Gorte, G. Kokotailo, and W. Farneth, *Stoichiometric adsorption complexes in H-ZSM-5, H-ZSM-12, and H-mordenite zeolites.* **Journal of Catalysis**, 1989. 115: p. 265-272.

24. Li, S. and F. Deng, *Solid-State NMR Studies of Zeolites*, in *Zeolites in Sustainable Chemistry: Synthesis, Characterization and Catalytic Applications*, F.-S. Xiao and X. Meng, Editors. 2016, Springer Berlin Heidelberg: Berlin, Heidelberg. p. 231-268.

25. Frydman, L. and J.S. Harwood, *Isotropic Spectra of Half-Integer Quadrupolar Spins from Bidimensional Magic-Angle Spinning NMR.* **Journal of the American Chemical Society**, 1995. 117: p. 5367-5368.

26. Zhao, B., H. Pan, and J.H. Lunsford, *Characterization of [(CH3) 3P− H]+ Complexes in Normal HY, Dealuminated HY, and H-ZSM-5 Zeolites Using 31P Solid-State NMR Spectroscopy.* **Langmuir**, 1999. 15: p. 2761-2765.

27. Rothwell, W.P., W.X. Shen, and J.H. Lunsford, *Solid-state phosphorus-31 NMR of a chemisorbed phosphonium ion in HY zeolite: observation of proton-phosphorus-31 coupling in the solid-state.* **Journal of the American Chemical Society**, 1984. 106: p. 2452-2453.

28. Chu, P.-J., R.R. Carvajal, and J.H. Lunsford, *Direct NMR spinning sideband analysis for a dipolar coupled system: structure elucidation of a proton—trimethylphosphine complex in LaH-Y zeolites.* **Chemical physics letters**, 1990. 175: p. 407-412.

29. Chu, P.-J., J.H. Lunsford, and D.J. Zalewski, *Structural information from the J-coupled multiplet of a $(CH_3)_3$ P- $AlCl_3$ coordination complex on zeolite Y.* **Journal of Magnetic Resonance (1969)**, 1990. 87: p. 68-79.

30. Sing, K.S., *The use of gas adsorption for the characterization of porous solids.* **Colloids and Surfaces**, 1989. 38: p. 113-124.

31. Rouquerol, J., F. Rouquerol, P. Llewellyn, G. Maurin, et al., *Adsorption by powders and porous solids: principles, methodology and applications*. 2013: Academic press.

32. Todolí, J.L. and J.M. Mermet, *Elemental analysis of liquid microsamples through inductively coupled plasma spectrochemistry.* **TrAC Trends in Analytical Chemistry**, 2005. 24: p. 107-116.

33. Stefánsson, A., I. Gunnarsson, and N. Giroud, *New methods for the direct determination of dissolved inorganic, organic and total carbon in natural waters by Reagent-Free™ Ion Chromatography and inductively coupled plasma atomic emission spectrometry.* **Analytica chimica acta**, 2007. 582: p. 69-74.

34. Debras, G., E.G. Derouane, J.-P. Gilson, Z. Gabelica, et al., *Prompt nuclear and atomic reactions for elemental analysis of zeolites I. A discussion of the experimental methods.* **Zeolites**, 1983. 3: p. 37-42.

35. Skujins, S., *Handbook for ICP-AES (Varian-Vista). A short Guide To Vista Series ICP-AES Operation. Varian Int. AG, Zug, Version 1.0.* **Switzerland Soc. Food Sci. Technol**, 1998. 29: p. 221-227.

36. Ryczkowski, J., *IR spectroscopy in catalysis.* **Catalysis Today**, 2001. 68: p. 263-381.

37. Duan, H.Q., R. Yan, L.C.C. Koe, and X.L. Wang, *Combined effect of adsorption and biodegradation of biological activated carbon on H2S biotrickling filtration.* **Chemosphere**, 2007. 66: p. 1684-1691.

38. Kondo, J.N., K. Ito, E. Yoda, F. Wakabayashi, et al., *An ethoxy intermediate in ethanol dehydration on Brønsted acid sites in zeolite.* **The Journal of Physical Chemistry B**, 2005. 109: p. 10969-10972.

39. Spoto, G., F. Geobaldo, S. Bordiga, C. Lamberti, et al., *Heterocycles oligomerization in acidic zeolites: a UV-visible and IR study.* **Topics in Catalysis**, 1999. 8: p. 279-292.

Chapter 3

Experimental Methods

Chapter 3: Experimental Methods

3.1 Zeolites 78

3.2 Zeolites Modifications 78

3.3 Characterisation Procedures 79

3.3.1 X-Ray Diffraction (XRD) 79
3.3.2 Transmission Electron Microscopy (TEM) 79
3.3.3 Scanning Electron Microscopy (SEM) 79
3.3.4 Thermogravimetric Analysis (TGA) 80
3.3.5 Temperature-Programmed Desorption (TPD) 80
3.3.6 ^{27}Al ssNMR – Aluminium Environment 80
3.3.7 ^{31}P ssNMR – Acid Sites Determination 81
3.3.8 BET surface area analysis 81
3.3.9 Inductive Coupled Plasma-Atomic Emission Spectroscopy (ICP- AES) 81

3.4 Catalytic Tests 82

3.4.1 Catalytic Conversion of 2,5-Dimethylfuran into Aromatics 82
3.4.2 Catalytic Conversion of Furan into Aromatics 83

3.5 Mechanistic Investigation 83

3.5.1 SXRD and Rietveld refinement 83
3.5.2 Experiments with Deuterated Ethanol 87
3.5.3 Theoretical Calculations 87
3.5.4 Fourier Transform Infrared (FTIR) 89

3.6 References 90

3.1 Zeolites

All the zeolites used in this thesis are commercial samples provided by SINOPEC-China and SCG-Thailand (manufactured by TOSOH). The samples were calcined at 450 °C in a tubular furnace under a flow of air for 4 h, in order to remove the ammonium and activate the Brønsted acid sites (**Figure 3.1**). Then, the sample was cooled and stored in dry air for further use.

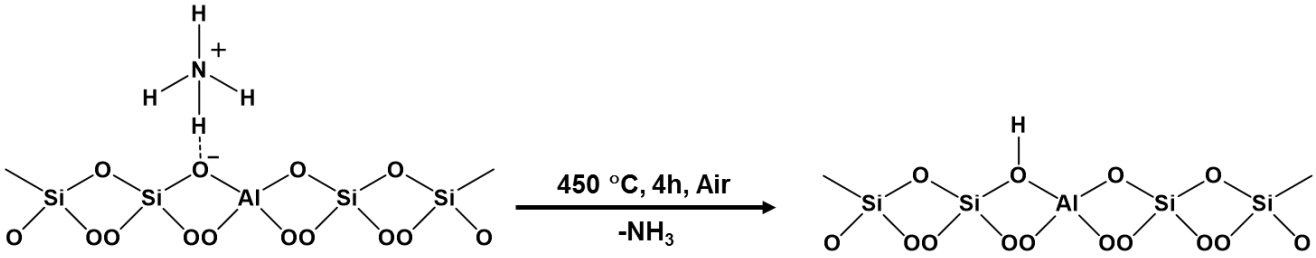


Figure 3.1 Schematic representation of the Brønsted acid sites formation from the ammonium decomposition.

3.2 Zeolites Modifications

In order to control the zeolites acidity, the sample USY (Si/Al=7.3) had some of its Brønsted acid sites selectively exchanged by potassium ions. The amount of potassium was calculated to obtain two different samples: one partially (0.3 Blocked/Total BAS) and another totally exchanged (1.0 Blocked/Total BAS) H-USY (Si/Al=7.3) named as P-K-USY7.3 (partially exchanged USY7.3) and T-K-USY7.3 (totally exchanged USY7.3), respectively. The samples were prepared by impregnating commercial 1 g of H-USY7.3 zeolite with 1 mL solution of KNO_2 (P-K-USY7.3: 0.18 $mol.L^{-1}$; T-K-USY7.3: 0.62 $mol.L^{-1}$). The samples were dried overnight at 100 °C and then calcined at 450 °C for 3 h.

3.3 Characterisation Procedures

All the samples used in this thesis were fully characterized by powder XRD, TEM, SEM, ammonia TPD, ICP-AES and BET surface area.

3.3.1 X-Ray Diffraction (XRD)

X-ray diffractions (XRD) patterns were measured on PANanlytical X'Pert Pro PW 1710 diffractometer operating in Bragg–Brentano focusing geometry and using Cu*K*α radiation (k = 1.5418 Å) from a generator operating at 40 kV and 40 mA. The samples were prepared by placing a layer of dry powdered sample onto fixed depth glass slide and the surface was pressed to be level. The patterns were collected from 5° to 80° in 2Θ. The phase identification of zeolites were carried out by comparing the collected diffraction patterns with the public files from International Zeolite Association (IZA).[1]

3.3.2 Transmission Electron Microscopy (TEM)

Transmission electron microscopy (TEM) images were recorded on JEOL 2010 equipped with a high-resolution pole piece running at 200 kV accelerating voltage. Samples were prepared by dispersing the powder samples in ethanol solution which was then sonicated for 10 min before being deposited and dried on Agar Scientific 400 mesh Cu holey carbon support.

3.3.3 Scanning Electron Microscopy (SEM)

Scanning electron microscopy (SEM) images were taken on JEOL 6500F FEG SEM with voltage of 5 kV and working distance of 10 mm.

3.3.4 Thermogravimetric Analysis (TGA)

Thermogravimetric analysis (TGA) was performed for all the samples to quantify surface moisture and evaluate its thermal stability. TGA was used also to quantify the carbon deposition after catalytic reactions through the weight loss related with the carbon oxidation into CO_2. TGA measurements were performed using a TGA Q50 (TA Instruments) under flow of air (60 $mL.min^{-1}$) until 900 °C with temperature rate of 10 $°C.min^{-1}$.

3.3.5 Temperature-Programmed Desorption (TPD)

The acidities of the catalysts were measured by NH_3 temperature programmed desorption (NH_3-TPD). The sample was heated up to 500 °C at 20 $°C.min^{-1}$, and held for 30 min, then cooled down to 100 °C. The surface of the catalyst was saturated with NH_3 for an hour at this temperature, and then the excess NH_3 was purged with N_2 flow at 100 °C. TPD of NH_3 was measured with a TCD detector by increasing the temperature from 100 to 800 °C at 15 $°C.min^{-1}$.

3.3.6 ^{27}Al ssNMR – Aluminium Environment

All the ssNMR measurements were performed on 400WB AVANCE III Spectrometer (Fudan University, China) at room temperature in collaboration with Dr Lin Ye (University of Oxford). The pre-treatment was carried out under vacuum (10^{-1} Pa) at 300 °C for 2 h. According to the electron density difference between four- and six-coordinate Al, ^{27}Al ssNMR was used to study the coordination of Al in zeolite samples.[2, 3] The ^{27}Al ssNMR spectrum was obtained at the Larmor frequency of 104.34 MHz. The one pulse sequence was adopted, with a 10° pulse, a delay time of 0.4 s and a scanning number of 8000. The chemical shift was referenced to 1 M $AlCl_3$ aqueous solution.

3.3.7 ^{31}P ssNMR – Acid Sites Determination

The ^{31}P MAS ssNMR measurement were performed in collaboration with Will Yung-Kang Peng (DPhil student-University of Oxford). In a typical experiment, the sample was introduced into a glass tube connected to a vacuum system. The pre-treatment was carried out for 2 h under vacuum (10^{-1} Pa) at 300 °C. After exposing the sample to TMP vapour at room temperature, the glass tube was then isolated and immersed in liquid nitrogen. After that, the content of the glass tube was kept in a glove box. ^{31}P NMR spectra were acquired at a resonance frequency of 161.9 MHz, using 30° pulses with a recycle delay of 15 s at a speed of 12 kHz. $NH_4H_2PO_4$ was used as a standard sample for chemical shift reference and the external intensity standard to quantify the signal in the ^{31}P ssNMR spectra.

3.3.8 BET surface area analysis

N_2 sorption was carried out using a micromeritics TriStar II using the BET method. All the samples were outgassed at 150 °C for 6 h prior to measurements. N_2 gas adsorbate was used with 2 min equilibration time at each point. The diameter volumetric distribution and mean pore diameter was determined by the Barrett–Joyner–Halenda (BJH) method, from the adsorption branch of isotherm, and the total pore volumes were estimated from the adsorbed amount at the constant C, where a relative pressure of P/P_0 = 0.90 was set.

3.3.9 Inductive Coupled Plasma-Atomic Emission Spectroscopy (ICP- AES)

The composition of the catalysts was determined by the ICP- AES technique at SRIFT-Sinopec, China. First 0.2 g of the sample was fused in 1 g of lithium metaborate at 900 °C, followed by dissolution of the fuseate with a 2% (v/v) solution of nitric acid.[4]

The instrument used for determining the major elements was a Hitachi P-4010/ICP-AES, using Helium (He) as a collision gas.

3.4 Catalytic Tests

3.4.1 Catalytic Conversion of 2,5-Dimethylfuran into Aromatics

Reactions were carried out in a 100 mL, high-pressure, high temperature Parr benchtop reactor using zeolite catalysts provided by Sinopec and SCG. In a typical experiment 15 mL of the model compound 2,5-Dimethylfuran (99% Sigma-Aldrich), 8.2 mL of ethanol (99.5% Sigma-Aldrich) and 0.4 g of zeolite catalysts were sealed in a batch reactor stirred by a magnetic bar at 750 rpm over a temperature range of 200 to 300 °C and 1.0 mL of tridecane as an internal standard. The reaction vessel was flushed with inert gas (N_2) at 1 bar. The reactions performed with ethylene instead of ethanol were performed in similar conditions, however, the 8.2 mL of ethanol were replaced by 40 bar of ethylene (at 25°C), which is equivalent to 5 times the ethanol used previously. The reactions were heated under the maximum rate allowed by the benchtop reactor, which in a typical experiment (300 °C) takes 30 min to reach the programmed temperature. The reaction starting time was defined as the moment when the reaction reached the set temperature.

Liquid products were identified and quantified using a gas chromatograph/mass spectrometer (Agilent 6890 and Agilent MSD 5973 (N)) calibrated with pure standards. After reaction, the autoclave was cooled down to −60 °C in a dry ice/acetone bath. Here, the gas phase was analysed by a Perkin Elmer Autosystem XL Arnel Gas phase GC-FID-Methanator, in order to determinate the concentrations of CO, CH_4, CO_2, C_2H_4 and C_2H_6 after the reaction. The catalyst was separated by filtration, washed with acetone and dried

overnight (80 °C). Then it was analysed by thermogravimetric analyses (TA instruments Q50), the samples were heated at 10 °C.min^{-1} from room temperature to 900 °C under air to quantify the coke on the catalyst surface and close the reaction carbon balance.

Conversion and selectivity were defined as:

$$\text{Conversion } (\%) = \frac{DMF\ consumed\ (mol)}{DMF\ Total\ (mol)} x\ 100 \quad (3.1)$$

$$\text{Selectivity } (\%) = \frac{Product\ (mol)}{DMF\ consumed\ (mol)} x\ 100 \quad (3.2)$$

3.4.2 Catalytic Conversion of Furan into Aromatics

Reactions were carried out in a 100 mL, high-pressure, high temperature Parr benchtop reactor using zeolite catalysts provided by Sinopec and SCG. In a typical experiment 5 mL of furan (99% Sigma-Aldrich), 12 mL of ethanol (99.5% Sigma-Aldrich) and 0.4 g of zeolite catalysts were used over a temperature range of 200 to 300 °C and 0.5 mL of tridecane as an internal standard. The reaction vessel was flushed with inert gas (N_2). Liquid products were identified and quantified using a gas chromatograph/mass spectrometer (Agilent 6890 and Agilent MSD 5973 (N)) calibrated with pure standards. Following the reaction carbon balance was determined as above.

3.5 Mechanistic Investigation

3.5.1 SXRD and Rietveld refinement

All the SXRD data were collected at Beamline I11 (Diamond Light Source-UK)[5] in collaboration with Dr. Benedict T.W. Lo (University of Oxford) and Dr. Lin Ye (University of Oxford). The energy of the incident X-ray flux was set at 15 keV. The wavelength and

the 2θ-zero point were refined using a diffraction pattern obtained from a high-quality Si powder (SRM640c). The high-resolution SXRD data were obtained from the zeolite samples using the multiple-analyser crystals (MAC) detectors. The patterns were collected in the 2θ range of 0-150° with 0.001° data binning. Each MAC pattern was collected for an hour for good statistics. In total, there are 4190 *hkl* reflections measured within the 2θ refinement region of 3-55°, of which at least 300 independent *hkl* reflections are observed. From a mathematical perspective, the number of variables should not exceed the number of observables. In the Rietveld refinements performed in this work, the number of structural parameters has not exceeded 170.

3.5.1.1 HZSM-5

The zeolite sample was first treated under vacuum at 200 °C for 2 h before adsorption with ethanol and/or DMF vapour. For pure ethanol or DMF uptake experiment, a saturated vapour pressure of adsorbate was used. For the equimolar ethanol/DMF uptake experiment, an equimolar mixture of ethanol/DMF was used. The total number of mole of ethanol/DMF introduced to the reactor chamber containing the zeolite was set at 75% of the total number of BAS.

Using the TOPAS software, the lattice parameters were refined using the Le Bail method, and also Rietveld refinement analyses of the diffraction patterns were performed. The starting coordinates used were based on the H-ZSM-5 zeolite model by Heo *et al.* for sample refinement.[6] The background curve was fitted by a Chebyshev polynomial with an average of 20 coefficients. The Thompson-Cox-Hastings pseudo-Voigt peak function proposed by Thompson *et al.* was applied.[7] The scale factor and lattice parameters were allowed to vary for all the histograms. The refined structural parameters

for each data histogram were the fractional coordinates (*x,y,z*) and isotropic displacement factors (B_{eq}) for all atoms, and the site occupancy factors (SOF), translation and rotation axes for the two rigid body Z-matrices describing the adsorbate molecules within the zeolitic framework (with fixed bond distance and angles). The B_{eq} were constrained in the following way: all the T-sites (T=Al, Si) share the same value, and the values for the O-sites are twice the B_{eq} for the T-sites. A restraint was applied to the distance on the hydrogen atoms between the adsorbate molecules (an anti-bump command in TOPAS) [H*-H_a* > 2.2], and the weighting was slowing reduced to 10 at the final stage of the refinement. The position errors of the atoms of the adsorbate molecules are estimated from the percentage errors of the translation axis. The final refined atomic parameters for each data histogram were carried out using the Rietveld method with the fractional atomic coordinates (*x, y, z*), SOF and isotropic displacement factors (B_{eq}) for all the atoms.

3.5.1.2 USY

Since all samples were treated at 200 °C under vacuum 2h before use, the adsorbed water should be removed completely. Afterwards, a saturated vapour pressure of pyridine was used. The total number of mole of pyridine introduced to the reactor chamber containing the zeolite was set at 75% of the total number of BAS.

Using the TOPAS software, the diffraction patterns were analyzed by Rietveld refinement methods to obtain structural details. The starting coordinates were based on the Y zeolite model by Hriljac *et al.* for structural refinement.[8] The Thompson-Cox-Hastings pseudo-Voigt peak function[9] was applied to describe the diffraction peaks. The scale factor and lattice parameters were allowed to refine for all the diffraction patterns. The refined structural parameters for pattern were the fractional coordinates (x, y, z) and

isotropic displacement factors (B_{eq}) for all USY atoms, and the site occupancy factors (SOF), translation and rotation axes for the rigid body Z-matrices describing the adsorbed pyridine molecules within the USY framework. The quality of the Rietveld refinements of synchrotron XRD data has been assured with a low goodness-of-fit (Gof) factor, a low weighted profile factor (R_{wp}) and a well-fitted pattern with acceptable temperature factor (B_{eq}) within experimental errors. All the errors of the atom-atom distances were calculated from the square root of the $(X_{error})^2+(Y_{error})^2+(Z_{error})^2$ multiplied by the measure distances. Accounting to the size of extra-framework Al^{3+} species, Al^{3+} and $Al(OH)^{2+}$ were used to fitting the data in H-USY (Si/Al=7.3), and the R_{wp} was found to be 9.561 and 14.540 which indicated only one Al^{3+} ion in the sodalite cage of H-USY (Si/Al=7.3).

The rigid body of pyridine molecule was added into USY one by one (Py1, Py2, Py3,…). R factors were used to gauge the quality of refinement. With the progressive increase in the number of pyridine molecules, the R-factors were found decreasing, which indicates the use of a higher number of pyridine is approaching to the real structure in H-USY (Si/Al=7.3). It was until the third pyridine, the R-factor was almost unchanged. However, the pseudo ‘third’ pyridine appeared at a position very close to Py2 (within 0.9 Å) which shared the site occupancy of Py2. Thus, the Py3 was excluded considering it to not be a genuine position, possibly arising from the distortion/displacement of Py2 by thermal motion, etc. As a result, 2 pyridine molecules were used to fitting all the synchrotron PXRD data accordingly. In H-USY (Si/Al=325), with the progressive increase in the number of pyridine molecules to 2, the occupancy of the Py2 was decreased to zero. As a result, 1 pyridine molecule was used to fitting all the synchrotron PXRD data accordingly.

3.5.2 Experiments with Deuterated Ethanol

The reactions with deuterated ethanol were carried out under the same conditions, only replacing the regular ethanol by ethanol-d or ethanol-d6 (D, 99%; <6% D_2O; Cambridge Isotope Laboratories). As the DMF conversion is strongly affected by the water concentration and the deuterated ethanol has a significantly higher concentration of water, these reactants were dried with anhydrous Na_2SO_4 (99% Sigma-Aldrich) just before the reaction. All the conditions were kept the same used for the DMF catalytic tests, however, the amounts of ethanol were adjusted according to their molar masses, 8.1 mL of ethanol-d6 and 8.3 mL of ethanol-d were used in respective reactions.

3.5.3 Theoretical Calculations

In collaboration with Dr Giannis Mpourmpakis (University of Pittsburgh, USA) *Ab-initio* electronic structure calculations were performed to study the Brønsted acid-catalysed p-xylene formation from ethanol and 2,5-dimethylfuran (DMF). Detailed reaction energetics were calculated at the M06-2X/6-311+G(d,p)[10, 11] level of theory, as implemented in the Gaussian 09[12] package. The BA site has been modelled as a proton in our calculations. An identical computational approach has been shown to be effective in calculating the reaction energetics in the production of p-xylene via cycloaddition between ethylene and DMF.[13, 14] Reaction pathways were first mapped by scanning the potential energy surface (PES) along the reaction coordinate. The energy maximum found along each reaction coordinate was relaxed to a saddle point to locate the actual transition state. All transition states and local minima were obtained by full optimizations and verified by vibrational frequency and Intrinsic Reaction Coordinate (IRC) calculations.[15] In addition, proton affinities (PA) of all relevant reaction species were

calculated at the CBS-QB3[16] level of theory, chosen for its accuracy in calculating gas-phase thermochemistry as reported in our previous work.[17] Proton affinity was used to quantify the thermodynamic preference of the different species to bind the acidic proton and it is calculated according to Equation (3.1):

$$PA = E_{molecule+H^+} - E_{molecule} \quad (3.1)$$

where $E_{molecule+H^+}$ and $E_{molecule}$ are the total electronic energies of the protonated and neutral species, respectively, as the electronic energy of a proton is zero.

In order to investigate the adsorption behavior of EtOH, DMF and Ethylene in the pores of the zeolite, again in collaboration with Dr Giannis Mpourmpakis (University of Pittsburgh, USA) used the ONIOM method (Our Own N-layered Integrated Molecular Orbital and Molecular Mechanics), first developed by Morokuma *et al*.[18] It is a hybrid method that can be applied to large systems using multiple levels of theory. The ONIOM3 (three-layer) method was used for these calculations, applying Molecular Mechanics (UFF) for the Low-Level calculations, a Semi-Empirical (PM6) method for the Intermediate-Model, and quantum mechanical calculations using the hybrid density functional of Truhlar and Zhao (M06-2X/6-311+G(d,p)) for the High-Level system.[19, 20]

The atoms in the Low- and Intermediate-layers were kept frozen in their crystallographic positions, while the High-Level atoms were allowed to relax during geometry optimisations. The gas phase electronic binding energies of the adsorbates were calculated using the following equation:

$$BE = E_{ONIOM3,ads} - E_{ONIOM3,zeolite} - E_{adsorbate} \quad (3.2)$$

where $E_{ONIOM3,ads}$ and $E_{ONIOM3, zeolite}$ are the energies of the adsorbate species in the zeolite and the empty zeolite pore system, respectively, and $E_{adsorbate}$ is the (high-level) electronic energy of the adsorbates.

3.5.4 Fourier Transform Infrared (FTIR)

The Fourier transform infrared (FTIR) was performed for the zeolite H-USY (Si/Al=6) loaded with ethanol/furan mixes with different molar ratios (3:1 and 10:1). The zeolite sample was first treated under vacuum at 200 °C for 2 h before adsorption with ethanol and/or furan vapour. For the mix Ethanol/Furan uptake experiment, a mixture of ethanol/DMF with 3:1 or 10:1 molar ratio was used. The total number of mole of Ethanol/Furan introduced to the reactor chamber containing the zeolite was set at 100% of the total number of BAS. The experiment was performed on a Nicolet 6700 FT-IR spectrometer with a MCT detector cooled. Liquid nitrogen was added to cool the detector compartment after 30 min the IR beam was aligned for the best signal. All the powdered samples were pressed onto the flat crystal (ZnSe) of the ATR accessory to form a film. The obtained spectra are represent averages of 128 scans with 2 cm^{-1} resolution over the wavenumber range 650 to 4000 cm^{-1}.

3.6 References

1. Association, I.Z. *Database of Zeolite Structures*. 2017 [Accessed May 31 2017].

2. Ye, L., B.T.W. Lo, J. Qu, I. Wilkinson, et al., *Probing atomic positions of adsorbed ammonia molecules in zeolite.* **Chemical Communications**, 2016. 52: p. 3422-3425.

3. Li, S. and F. Deng, *Solid-State NMR Studies of Zeolites*, in *Zeolites in Sustainable Chemistry: Synthesis, Characterization and Catalytic Applications*, F.-S. Xiao and X. Meng, Editors. 2016, Springer Berlin Heidelberg: Berlin, Heidelberg. p. 231-268.

4. Hensen, E.J.M., Q. Zhu, R.A.J. Janssen, P.C.M.M. Magusin, et al., *Selective oxidation of benzene to phenol with nitrous oxide over MFI zeolites: 1. On the role of iron and aluminum.* **Journal of Catalysis**, 2005. 233: p. 123-135.

5. Thompson, S.P., J.E. Parker, J. Marchal, J. Potter, et al., *Fast X-ray powder diffraction on I11 at Diamond.* **J. Synchrotron Radiat.**, 2011. 18: p. 637-648.

6. Heo, N.H., C.W. Kim, H.J. Kwon, G.H. Kim, et al., *Detailed Determination of the Tl+ Positions in Zeolite Tl-ZSM-5. Single-Crystal Structures of Fully Dehydrated Tl-ZSM-5 and H-ZSM-5 (MFI, Si/Al = 29). Additional Evidence for a Nonrandom Distribution of Framework Aluminum.* **J. Phys. Chem. C**, 2009. 113: p. 19937-19956.

7. Thompson, P., D.E. Cox, and J.B. Hastings, *Rietveld refinement of Debye-Scherrer synchrotron x-ray data from alumina.* **J. Appl. Crystallogr.**, 1987. 20: p. 79-83.

8. Colligan, M., P.M. Forster, A.K. Cheetham, Y. Lee, et al., *Synchrotron X-ray powder diffraction and computational investigation of purely siliceous zeolite Y under pressure.* **J. Am. Chem. Soc.**, 2004. 126: p. 12015-12022.

9. Thompson, P., D.E. Cox, and J.B. Hastings, *Rietveld refinement of debye-scherrer synchrotron x-ray data from Al_2O_3.* **J. Appl. Crystallogr.**, 1987. 20: p. 79-83.

10. Zhao, Y. and D.G. Truhlar, *The M06 suite of density functionals for main group thermochemistry, thermochemical kinetics, noncovalent interactions, excited states, and transition elements: two new functionals and systematic testing of four M06-class functionals and 12 other functionals.* **Theoretical Chemistry Accounts**, 2008. 120: p. 215-241.

11. Zhao, Y. and D.G. Truhlar, *A new local density functional for main-group thermochemistry, transition metal bonding, thermochemical kinetics, and noncovalent interactions.* **Journal of Chemical Physics**, 2006. 125.

12. Frisch, M.J., G.W. Trucks, H.B. Schlegel, G.E. Scuseria, et al., *Gaussian, Inc., Wallingford CT.* 2010.

13. Williams, C.L., C.-C. Chang, D. Phuong, N. Nikbin, et al., *Cycloaddition of Biomass-Derived Furans for Catalytic Production of Renewable p-Xylene.* **ACS Catalysis**, 2012. 2: p. 935-939.

14. Nikbin, N., P.T. Do, S. Caratzoulas, R.F. Lobo, et al., *A DFT study of the acid-catalyzed conversion of 2,5-dimethylfuran and ethylene to p-xylene.* **Journal of Catalysis**, 2013. 297: p. 35-43.

15. Hratchian, H.P. and H.B. Schlegel, *Accurate reaction paths using a Hessian based predictor-corrector integrator.* **Journal of Chemical Physics**, 2004. 120: p. 9918-9924.

16. Montgomery, J.A.F., M. J.; Ochterski, J. W.; Petersson, G. Alfonso, D., *A Complete Basis set Model Chemistry. VI. Use of Density Functional Geometries and Frequencies.* **J. Chem. Phys**. 1999, 110 (6),2822−2827.

17. Kostestkyy, P., J.P. Maheswari, and G. Mpourmpakis, *Understanding the Importance of Carbenium Ions in the Conversion of Biomass-Derived Alcohols with First-Principles Calculations.* **Journal of Physical Chemistry C**, 2015. 119: p. 16139-16147.

18. Morokuma, K., R. Froese, S. Dapprich, I. Komaromi, et al. *The ONIOM (our own integrated N-layered molecular orbital and molecular mechanics) method, and its applications to calculations of large molecular systems*. in *Abstracts of Papers of the American Chemical Society*. 1998: Amer Chemical Soc 1155 16th St, NW, Washington, Dc 20036 USA.

19. Stewart, J.J., *Optimization of parameters for semiempirical methods V: modification of NDDO approximations and application to 70 elements.* **Journal of Molecular modeling**, 2007. 13: p. 1173-1213.

20. Rappé, A.K., C.J. Casewit, K. Colwell, W. Goddard Iii, et al., *UFF, a full periodic table force field for molecular mechanics and molecular dynamics simulations.* **Journal of the American chemical society**, 1992. 114: p. 10024-10035.

Chapter 4

Facilitated Process to Convert DMF and Ethanol into Xylene

Chapter 4: Facilitated Process to Convert DMF and Ethanol into Xylene

Overview **94**

4.1 Introduction **96**

4.2 Catalytic Performance **98**

4.2.1 Zeolite Samples 99

4.2.2 Reaction Optimization 103

4.3 Kinetic Studies **106**

4.3.1 Activation Energy Estimation 108

4.4 Mechanistic Investigation **109**

4.4.1 Theoretical Calculations 109

4.4.2 SXRD Experiments 117

4.4.3 Experiments with Deuterated Ethanol 121

4.5 Conclusions **123**

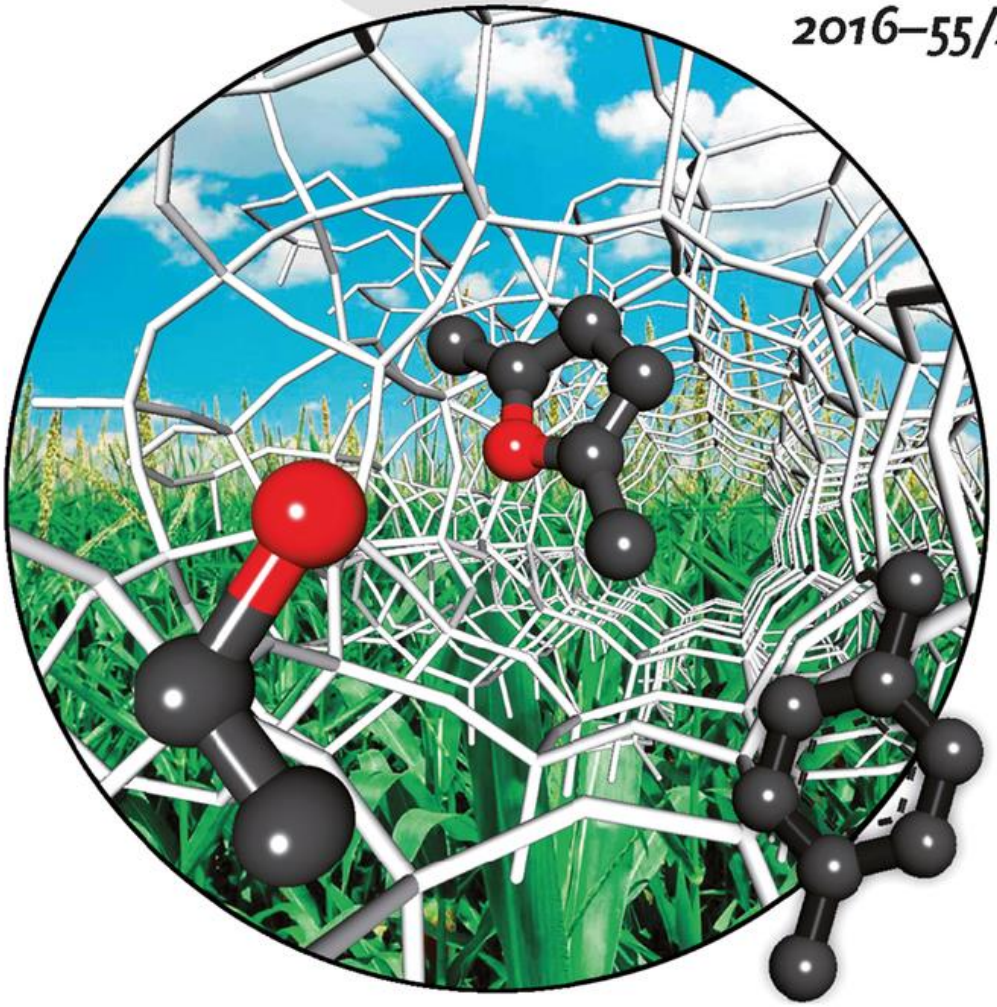
4.6 References **124**

Overview

This chapter reports a novel catalytic conversion of the biomass-derived furan 2,5-dimethylfuran (DMF) and ethanol to aromatics over zeolite catalysts. Aromatics are formed *via* Diels-Alder (DA) cycloaddition with ethylene, which is produced *in situ* from ethanol dehydration (ED). The use of liquid ethanol instead of gaseous ethylene, as the source of dienophile in this one pot synthesis, renders the aromatics production a much simpler and renewable process and circumvents the use of ethylene at high pressure. More importantly, both our experiments and theoretical studies demonstrate that the use of ethanol instead of ethylene results in significantly higher rates and higher selectivity to aromatics, due to lower activation barriers over the solid acid sites. Synchrotron diffraction experiments and proton affinity calculations clearly suggest that a preferred protonation of ethanol over the furan is a key step facilitating the DA and dehydration reactions in the acid sites of the zeolite. The synchrotron diffraction experiments and its interpretation was performed in collaboration with Dr. Benedict T. W. Lo from our group. I was responsible for all the catalytic tests presented in this chapter, including kinetic evaluations and experiments with deuterated ethanol. I also helped to plan and prepare the samples used in SXRD experiments and assisted in interpretation of the data. The data refinement was done exclusively by Dr. Benedict T. W. Lo. The DFT calculations were performed by Dr Giannis Mpourmpakis (University of Pittsburgh, USA) and I helped to set the experiment conditions and interpret the results.

The work in this chapter was published in Angewandte Chemie International Edition as an inside back cover, 'From Biomass-Derived Furans to Aromatics with Ethanol over Zeolite'.[1]

A Journal of the Gesellschaft Deutscher Chemiker
Angewandte
GDCh
International Edition
Chemie
www.angewandte.org
2016–55/42



Liquid lunch anyone?

Ethylene produced in situ from ethanol dehydration over zeolite is used for the catalytic conversion of biomass-derived furans into aromatic compounds by Diels–Alder cycloaddition. In their Communication on page 13061 ff., G. Mpourmpakis, S. C. E. Tsang et al. describe a rapid and renewable one-pot synthesis of aromatic compounds using liquid ethanol as a source of dienophile instead of pressurized ethylene gas.

WILEY-VCH

4.1 Introduction

Over the past century our society has become heavily dependent on fossil fuel sources such as coal, gas and oil to produce our daily needs of energy and chemicals.[2] The carbon dioxide produced by these non-renewable carbon sources has been significantly altering the climate on Earth[3] and our heavy reliance make them more expensive and less abundant.[2] Conversion of lignocellulosic biomass to renewable fuels and chemicals has attracted significant attention as a key technology to enable the replacement of petroleum.[4, 5] Lignocellulosic biomass is the most promising renewable carbon based energy source, as it is widely available around the world at a relatively low cost. It is composed of three main fractions: cellulose, hemicellulose, and lignin.[6] Although it is the most abundant plant material resource, its exploitation has been limited by its composite nature and rigid structure.[7] In view of these facts, the conversion of biomass feedstocks into valuable products has been investigated, usually in multistep processes using platform molecules as intermediates.[8] Bio-derived furans, such as furfural (FF), furfuryl alcohol (FA), 2-methylfuran (MF), and 2,5-dimethylfuran (DMF), are important platform molecules that can be produced by hydrolysis and subsequent dehydration of hemicellulose and cellulose from biomass in good yields.[9] It has recently been demonstrated that these platform molecules with a furan ring can be converted into aromatics (particularly p-xylene) by a Diels-Alder cycloaddition with an alkene (usually ethylene or propylene), followed by dehydration over a moderately acidic zeolite.[10-12] However, this process is not completely renewable, since the alkene gas added usually comes from fossil sources.[10-12] Another disadvantage of this batch synthesis is the need to apply high ethylene gas pressure from gas store,[10-12] which makes the process more

cumbersome and less safe to handle. The present work involved investigation of the catalytic conversion of 2,5-dimethylfuran (DMF) into aromatics by Diels-Alder cycloaddition with ethylene, *in situ* generated by dehydration of bio-derived ethanol over zeolite (**Figure 4.1**).

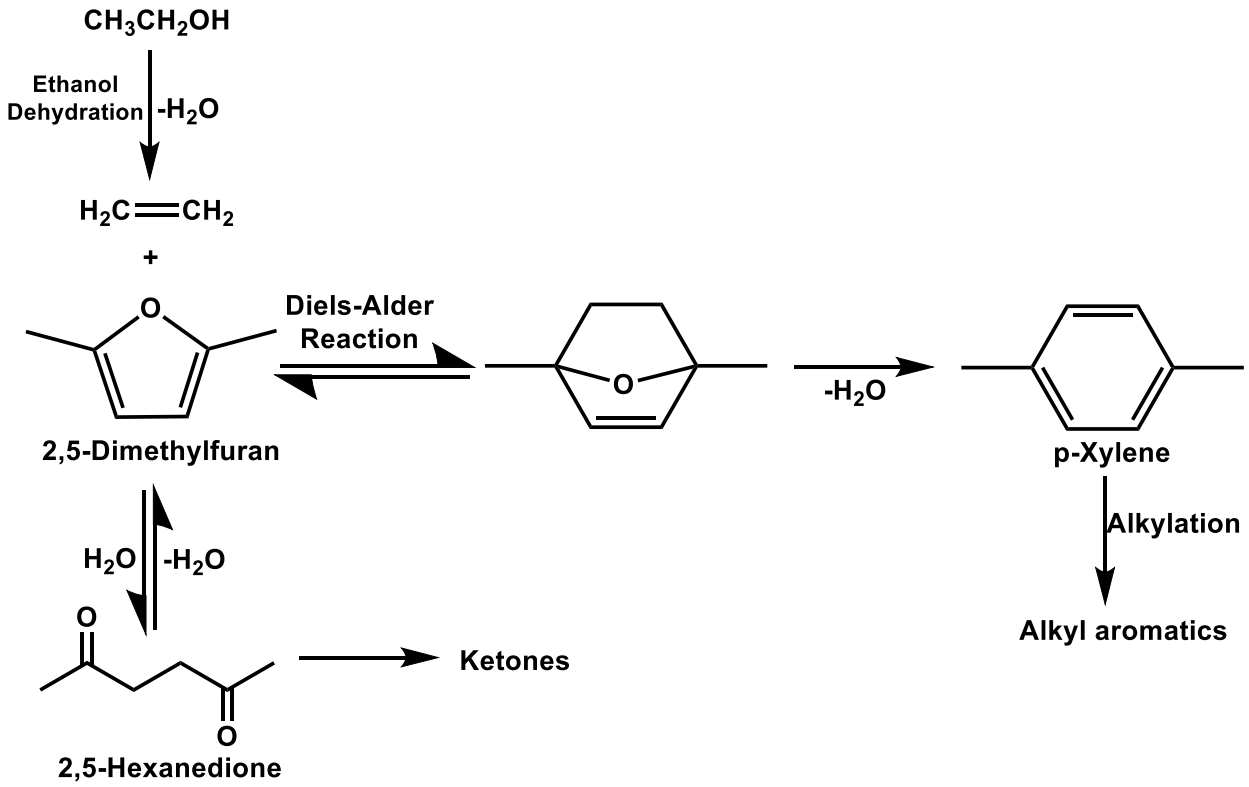


Figure 4.1 A one-pot synthesis for p-xylene production from 2,5-dimethylfuran (DMF) and ethanol over zeolite.

Reactions were carried out in a single pot synthesis, using liquid ethanol and furan in a batch reactor, without the need for high-pressure ethylene. It is generally accepted that ethylene can be produced by the dehydration of ethanol over acid or basic sites of the zeolites.[13, 14] Although one would expect slower kinetics in the conversion of DMF using ethanol instead of ethylene due to the competition for the active sites (e.g. ethanol dehydration also takes place on acid sites), it actually achieves much higher rates

and lower activation barriers due to hitherto unreported facilitated fundamental steps for the coupling of ethanol and furan to form aromatics. It is believed from this work, the new process using ethanol as a renewable dienophile is demonstrated to be technical and economically more attractive in the conversion of biomass-derived furans to aromatics over zeolites.

4.2 Catalytic Performance

The catalytic conversion of ethanol and DMF (ethanol/DMF) was first compared against ethylene/DMF under comparable reaction conditions as reported by Williams *et al*.[10] When compared with ethanol as the source of dienophile, over the same H-USY-6 (**Figure 4.2**), the ethanol pathway exhibits higher conversion (97% against 71% to ethylene). Despite the fact that a slightly lower selectivity to p-xylene (67%) is obtained than that of using ethylene, the use of ethanol produces more alkylated aromatics (23% against 5% in ethylene reaction) over the H-USY-6 (Si/Al = 6), resulting in higher overall selectivity in the production of aromatics (90%). Apart from the alkylated xylene products (for example, 1-ethyl-2,5-dimethylbenzene as ethyl substituted p-xylene) as in the case of ethylene, the use of ethanol also produces a very small quantity of aromatics with oxygen-containing substituent groups. As the reactions were performed in sealed batch reactors, the pressure increases with temperature increment. Reactions performed with ethanol started with 1 bar of internal pressure and typically reaches 60 bar during the first hour of reaction (300 °C) due the ethanol dehydration into ethylene. Reactions with ethylene were started at 40 bar and typically reaches 150 bar at 300 °C.

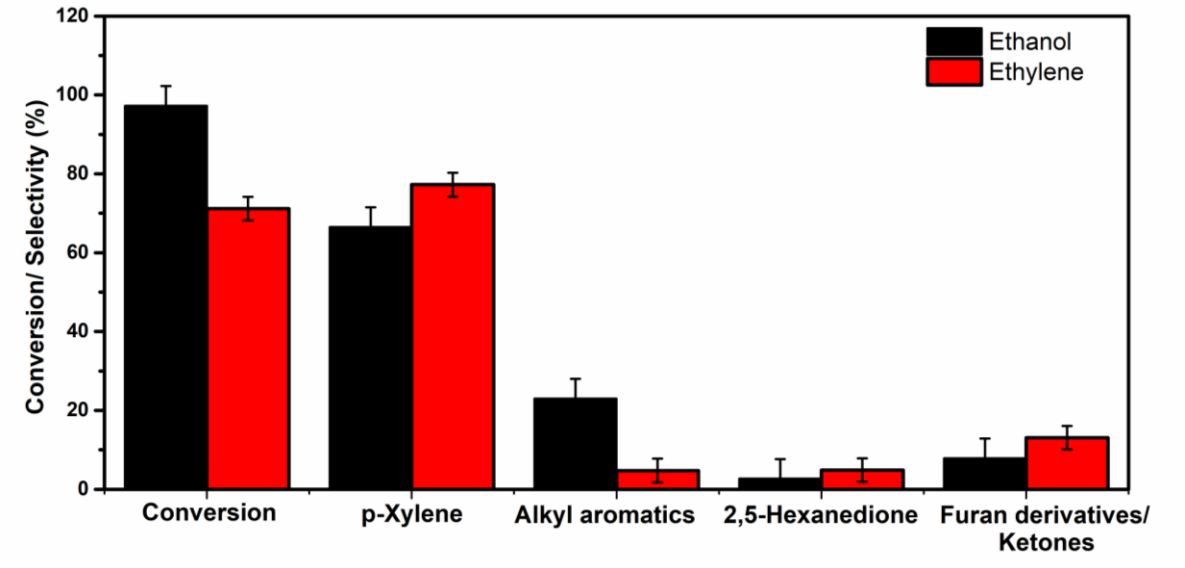


Figure 4.2 Conversion and selectivity for DMF transformation into aromatics catalysed by zeolite H-USY (Si/Al=6) with ethylene generated *in situ* from ethanol compared with only a pressure of ethylene (40 bar). Reaction conditions: temperature 300 °C, molar ratio ethanol/DMF 1:1 and reaction time 12 h in 100 mL reactor.

The reaction conditions for the ethanol/DMF reaction over zeolite were carefully considered as similar to those reported for ethylene/DMF reactions in the literature ensuring no mass transfer limitations, see Appendix.[10-12]

4.2.1 Zeolite Samples

A range of zeolites with different shapes (pore structure and size) and different acidities (Si/Al ratios) were tested for the ethanol/DMF reaction. All the samples tested are commercial samples and they were fully characterized by powder XRD, TEM, SEM, propylamine TPD and BET surface area (see Appendix), the main properties are summarized in **Table 4.1**.

Table 4.1 Acid site concentrations and surface area of the zeolite samples

Zeolite Samples	Si/Al[i]	BAS conc.[ii] (mmol g^{-1})	Surface Area[iii] (m^2 g^{-1})	Turnover frequency[iv] (10^2 h^{-1})
H-ZSM-5	19	0.76	349	0.63
	25	0.31	311	1.50
	60	0.03	309	14.95
	252	-	329	-
H-USY	5	1.1	650	0.23
	6	0.55	735	2.57
	7.3	0.63	550	4.75
	325	0.052	620	5.02

[i] from ICP-AES;
[ii] Obtained using ammonia-TPD;
[iii] from BET over $0.05 < P/P_0 < 0.3$;
[iv] rate per mole of DMF to mole of products per BAS per hour.

Figure 4.3 shows a nearly complete conversion of DMF after it is mixed with liquid ethanol at 1:1 mole ratio over all zeolites (~80-95%). The condensable products include the desirable product, p-xylene from the DA and dehydration reactions (**Figure 4.1**), alkylated aromatics (i.e. acid-catalysed substitution of p-xylene), 2,5-hexanedione (hydrolysis of DMF, see **Figure 4.1**), furan-derived products and coke (condensation of 2,5 hexanedione, etc). This type of product distribution is similar to the one originating from the DMF reacting with ethylene,[10, 11] strongly suggesting that the *in situ* production of ethylene from ethanol is coupled with the DA cycloaddition to DMF. Interestingly, the catalytic performance appears to be greatly influenced by the nature of zeolite and the acidic content used (**Figure 4.3**). The zeolite H-USY-6 with intermediate acidic content (Si/Al=6) gives the best selectivity for aromatics compared with other Si/Al ratios. This H-USY also shows much higher yield than HZSM-5 of Si/Al= 19 or 25 with comparable Brønsted acid concentrations, suggesting H-USY has a preferred pore structure (**Figure 4.3** and **Figure 4.4**).

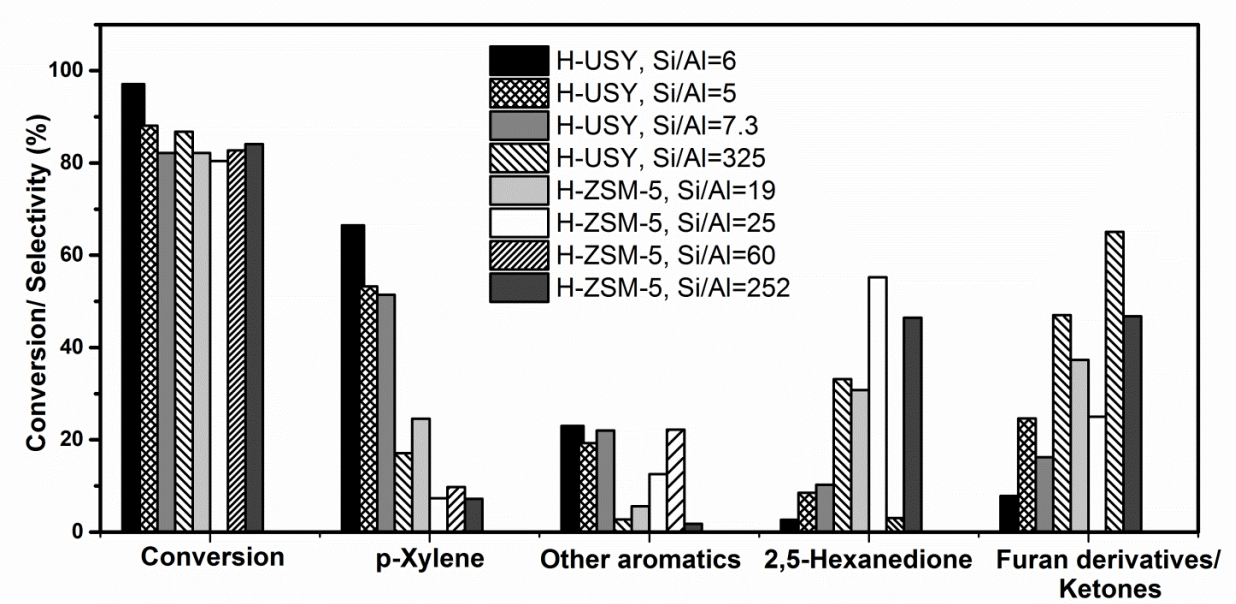


Figure 4.3 Conversion and selectivity for DMF transformation into xylene (mainly p-xylene) and alkylaromatics catalysed by different zeolites. Reaction conditions: temperature 300°C, molar ratio ethanol/DMF 1:1 for 12 h in 100 mL reactor.

On the other hand, for ethylene used as a co-reactant, Williams *et al.* have demonstrated that their HY samples also give higher catalytic performance than HZSM-5 samples, yielding about 50% selectivity towards p-xylene (total aromatics of 60%) in DMF/ethylene at 300 ˚C, without additional solvent inclusion.[10, 11] The selectivity data presented in **Figure 4.3** were compared after 12 hours of reaction, in order to compare the product selectivity when the reaction reaches equilibrium, which makes the comparison simpler, since the product distribution changes significantly with reaction time.

After every reaction, the reactor was cooled down to −60 °C by dry ice/acetone bath and the gas phase was analysed by GC-FID-Methanator, to determinate the concentrations of CO, CH_4 and CO_2 after the reaction. In order to close the carbon balance for the reaction all catalysts were separated by filtration washed with acetone,

dried overnight (80 °C) and then analysed by thermogravimetric analysis (TGA) to quantify the deposited carbon (coke), see data in the Appendix. Using these quantification methods together with the quantification of the liquid products by GC-MS it was possible close the carbon balance for all the reactions within less than 5% error.

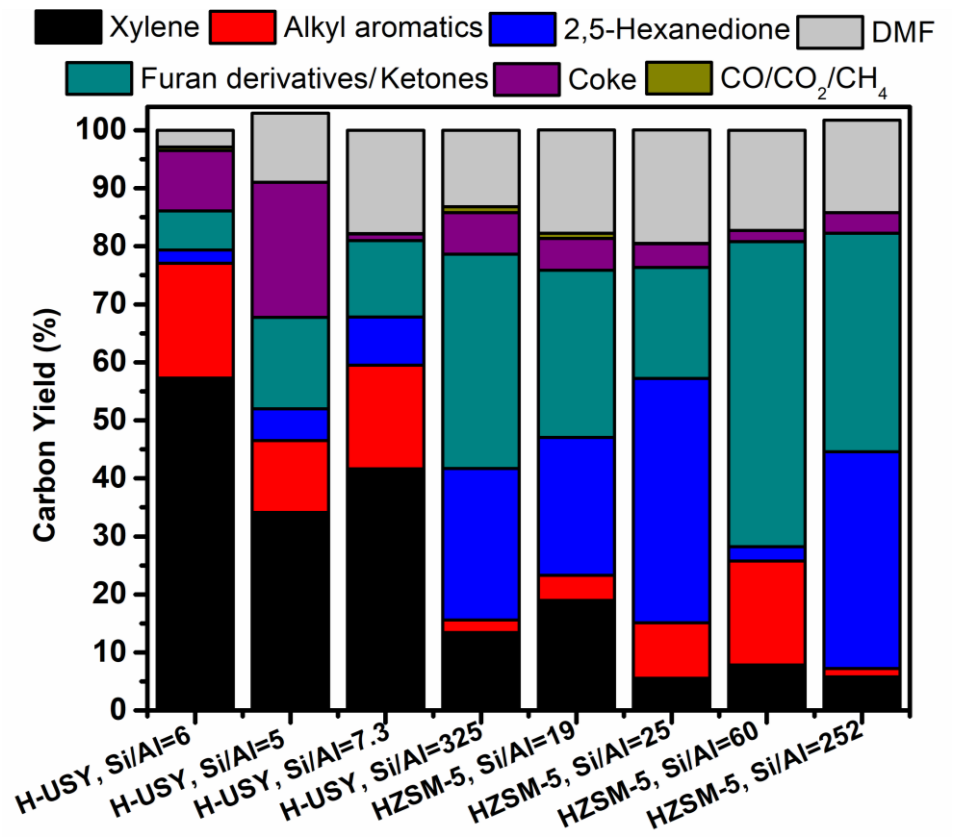


Figure 4.4 Carbon yield for DMF transformation into xylene (mainly p-xylene) and alkylaromatics catalysed by different zeolites. Reaction conditions: temperature 300 °C, molar ratio ethanol/DMF 1:1 for 12 h in 100 mL reactor.

Figure 4.4 shows high yields for aromatics, especially for the zeolites with USY shapes. The gas products (CO, CO_2 and CH_4) are almost insignificant, representing less than 1% of products. The deposited carbon (coke) in general is greater for USY shaped zeolites and in a same shape more acidic zeolites tend to promote more carbon deposition, for example 23% for H-USY (Si/Al=5) against 7% for the least acidic H-USY

(Si/Al=325) and 5.5% for HZSM-5 (Si/Al=19) against 1.9% for the less acidic HZSM-5 (Si/Al=60).

4.2.2 Reaction Optimization

The conversion of DMF into aromatics over zeolites was also optimized for a range of parameters, such as time, temperature and ethanol/DMF ratio (**Figure 4.5** and **Figure 4.6**). The ethanol/DMF reaction catalysed by HZSM-5 (Si/Al=19) was performed at three different temperatures: 230, 280 and 300 °C. Despite the significant differences to the reaction rate at the three temperatures after 12h the conversion is essentially the same, since the reaction reaches equilibrium. However, the product selectivity is significantly affected. Higher temperatures favour the xylene product, while lower temperatures promote furan derivatives/ketones and alkylated products.

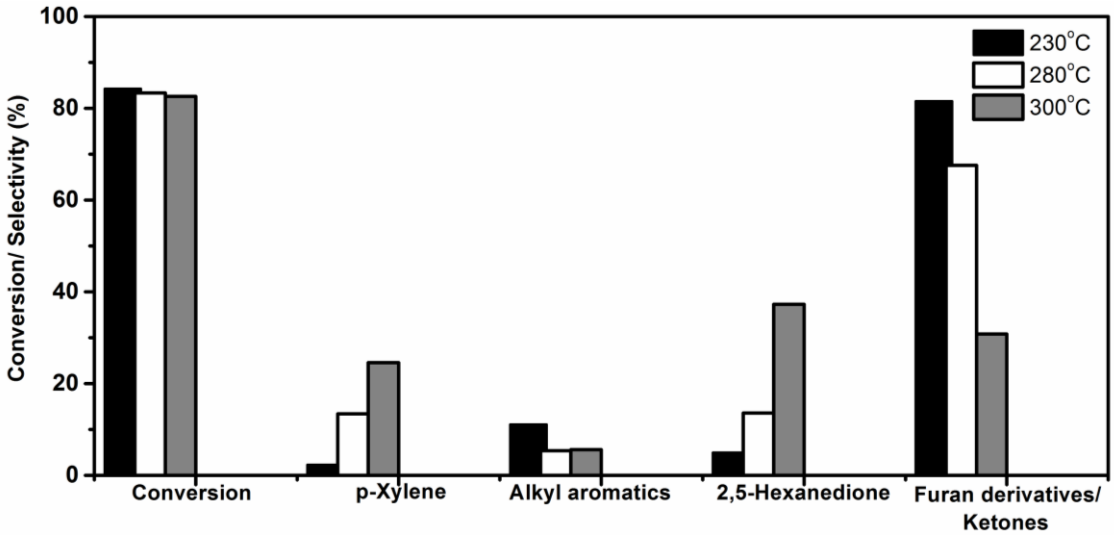


Figure 4.5 Conversion and selectivity for DMF transformation into aromatics catalysed by zeolite HZSM-5 (Si/Al=19) at different temperatures. Reaction conditions: molar ratio ethanol/DMF 1:1 and reaction time 12 h in 100 mL reactor.

The conversion of DMF into aromatics over zeolites was also optimized for different ethanol/DMF molar ratios (**Figure 4.6**). The best ethanol/DMF ratio was in equimolar conditions (1:1), where almost complete conversions of DMF and ethanol were achieved to the p-xylene and derivative products based on their carbon balances. Using larger amounts of ethanol significantly promoted the formation of side products from DMF including the diketone and furan derivatives. The larger amount of 2,5-hexadione under excess ethanol might be explained by the increase in water concentration from the dehydration of ethanol, consequently promoting the DMF hydrolysis to 2,5-hexanedione and their condensed products. The study reflects the importance of a proper balance of ethanol dehydration (ED) versus Diels-Alder (DA) reactions over limited acid sites in the zeolite (**Figure 4.1**), which reduces unnecessary consumption of ethanol for the tandem reactions.

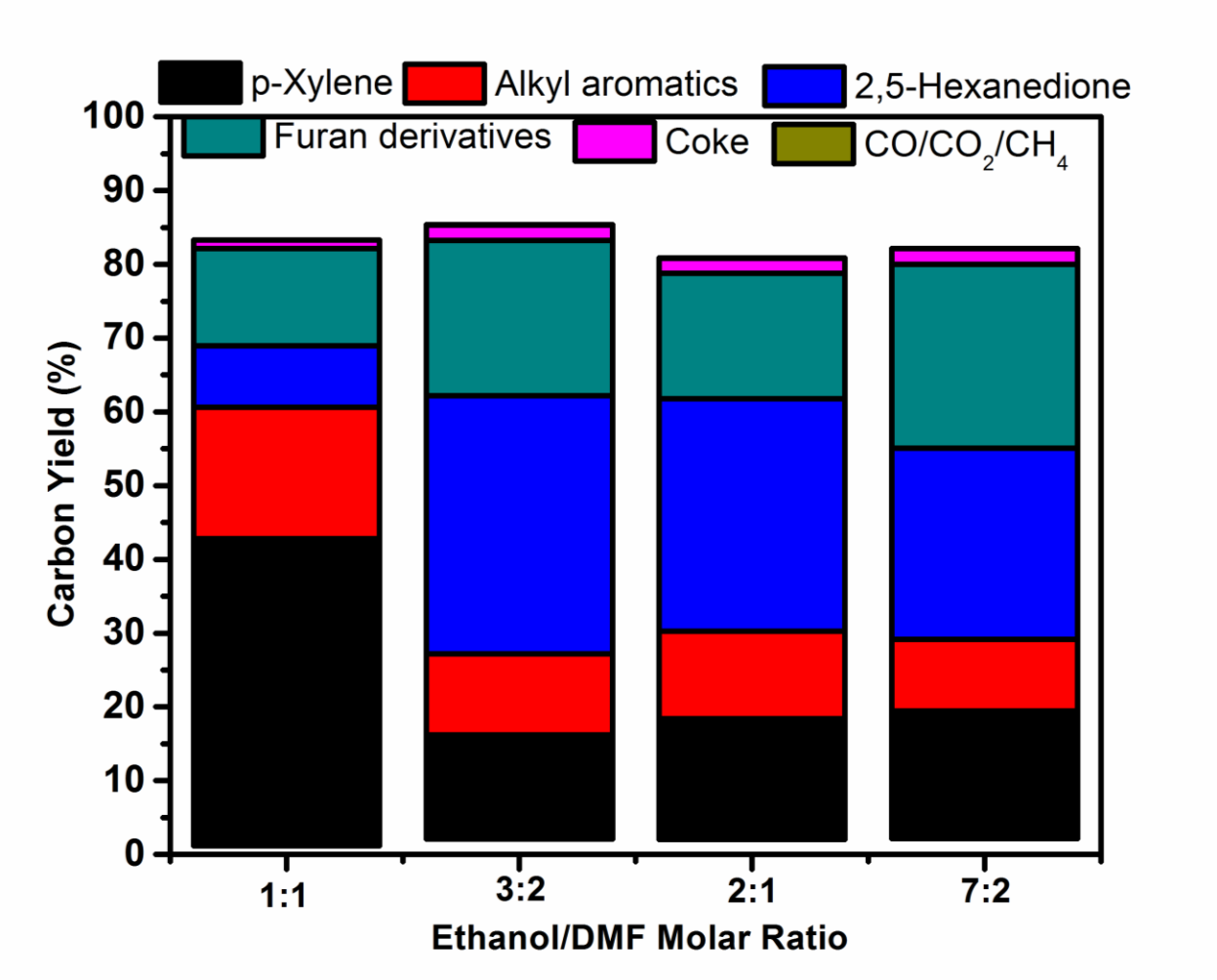


Figure 4.6 Conversion and carbon yield for DMF transformation into aromatics catalysed by zeolite H-USY (Si/Al=7.3) with different molar ratios Ethanol/DMF. Reaction conditions: temperature 300 °C, molar ratio ethanol/DMF 1:1 and reaction time 12 h in 100 mL reactor.

We were intrigued by the generally high rates of DMF conversion per BAS over the zeolites studied, using ethanol as the dienophile (0.2-15 × 10^2 h^{-1}). Typically, the initial DMF conversion rate of 0.14 mol $g_{cat}^{-1}h^{-1}$ is achieved over H-USY-6 (estimated acid site concentration 0.55 mmol g^{-1}) at 300 ˚C using ethanol, compared to 0.03 mol $g_{cat}^{-1}h^{-1}$ using ethylene (nearly 5 times more active) at the same conditions based on first two-hour evaluation (**Table 4.2**).

Table 4.2. Reaction rate and reaction rate per mol of reactant (ethanol or ethylene) for DMF transformation into aromatics per gram of zeolite H-USY (Si/Al=6) with ethylene generated *in situ* from ethanol and only pressure of ethylene (40 bar). Reaction conditions: temperature 300 °C

Reactant	Rate (mol/g.h)	Rate (molDMF/molEtOH or C_2H_4.g.h)
Ethanol	0.141	1.017
Ethylene	0.034	0.075

4.3 Kinetic Studies

More detailed kinetics studies were performed using liquid ethanol (0.14 mol) versus pressurized ethylene (40 bar, 0.45 mol) to react with 0.14 mole DMF over our H-USY-6 in a batch reactor under identical conditions. Despite the lower quantity of ethanol used, the reaction again showed a higher reaction rate (**Figure 4.7** and **Figure 4.8**). This is rather unexpected, since competition for limited acid sites in zeolite catalyst for dehydration of ethanol (to produce *in situ* ethylene), DA cycloaddition and dehydration of oxa-norbornene to p-xylene (and substituted aromatics) should result in a lower rate relative to ethylene as a dienophile source. This observation may reveal important mechanistic details, which could lead to new ways of obtaining higher productivity of aromatics at greater selectivity from cycloaddition of furans that is urgently needed in the practical catalytic biomass conversions.

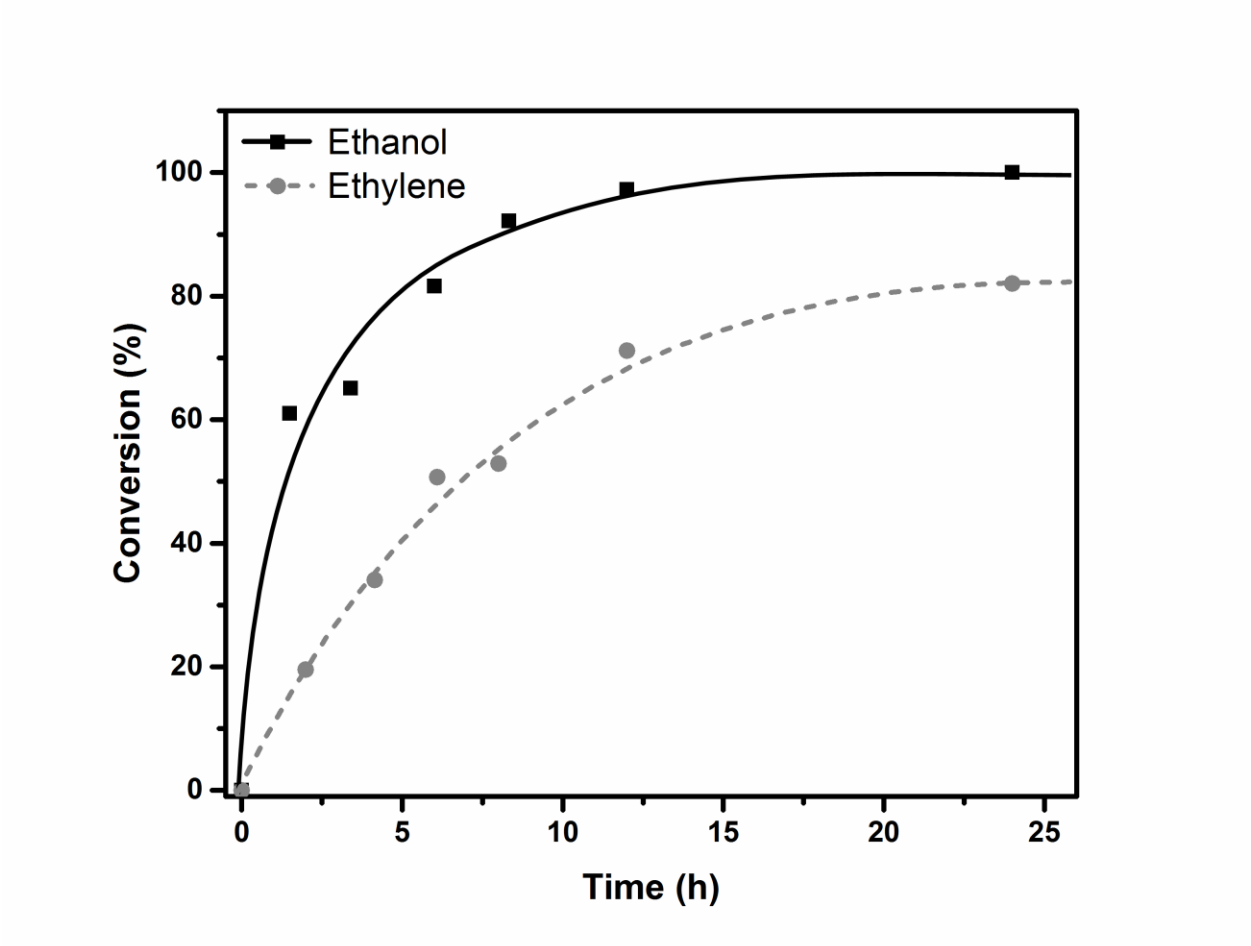


Figure 4.7. Kinetic data derived for 0.14 mole DMF transformation over 0.4 g zeolite H-USY (Si/Al=6) with ethylene generated *in situ* from ethanol (0.14 mole) versus pressurized ethylene (40 bar, 0.45 mole) in 100 mL at 300 ^{o}C.

The kinetic experiment for both reactions fitted as first order reaction (**Figure 4.8**), where the reaction with ethanol showed a larger reaction constant rate (0.281 h^{-1}) than the reaction performed under pressure of ethylene (0.102 h^{-1}).

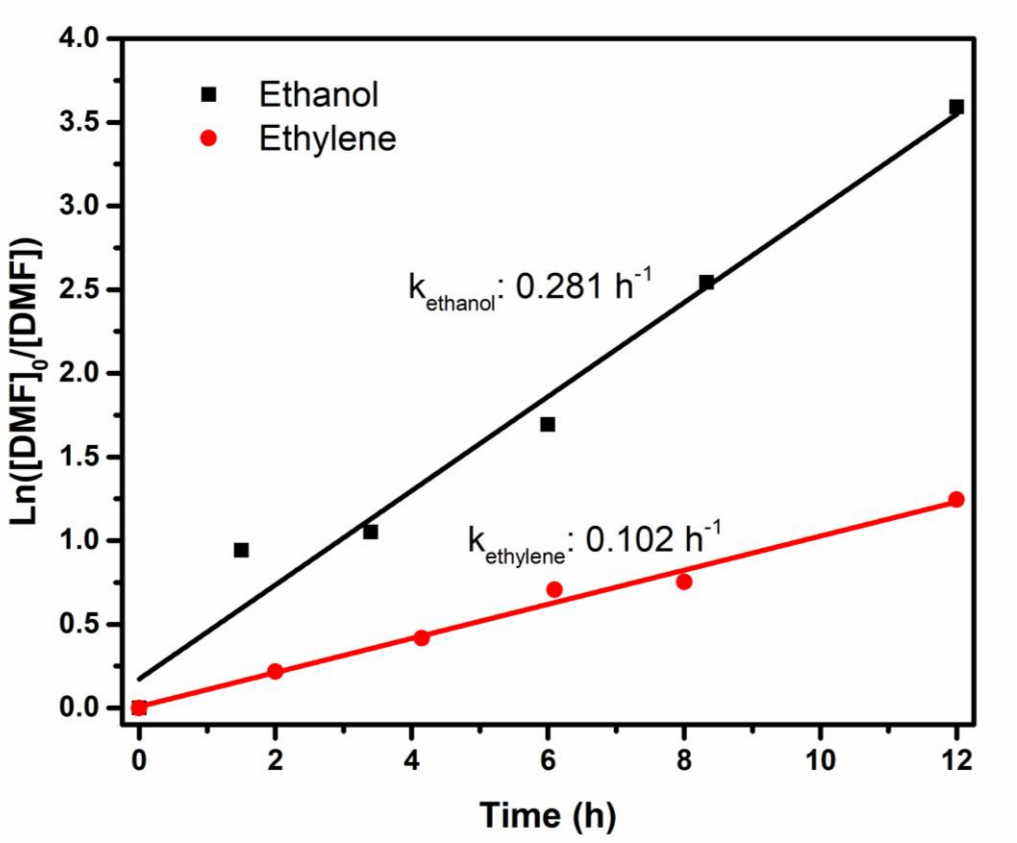


Figure 4.8. First order fitting and constant rate values for DMF transformation into aromatics catalysed by zeolite H-USY (Si/Al=6) with ethylene generated *in situ* from ethanol and only pressure of ethylene (40 bar). Reaction conditions: temperature 300 °C in 100 mL reactor.

4.3.1 Activation Energy Estimation

Arrhenius plots were generated by the evaluation of the reaction kinetics at different temperatures (230, 280, 250 and 300 °C). From the Arrhenius plots it was possible to estimate the apparent activation energy for the ethanol route (**Figure 4.9**). The value of 55±4 kJ mol^{-1} was significantly lower than the value using ethylene (~100.0 kJ mol^{-1}),[15] giving ΔE_a = ~44 kJ mol^{-1} between the ethanol and ethylene routes. This implies that the reaction profiles involving the two dienophiles of different origins could be significantly different from each other.

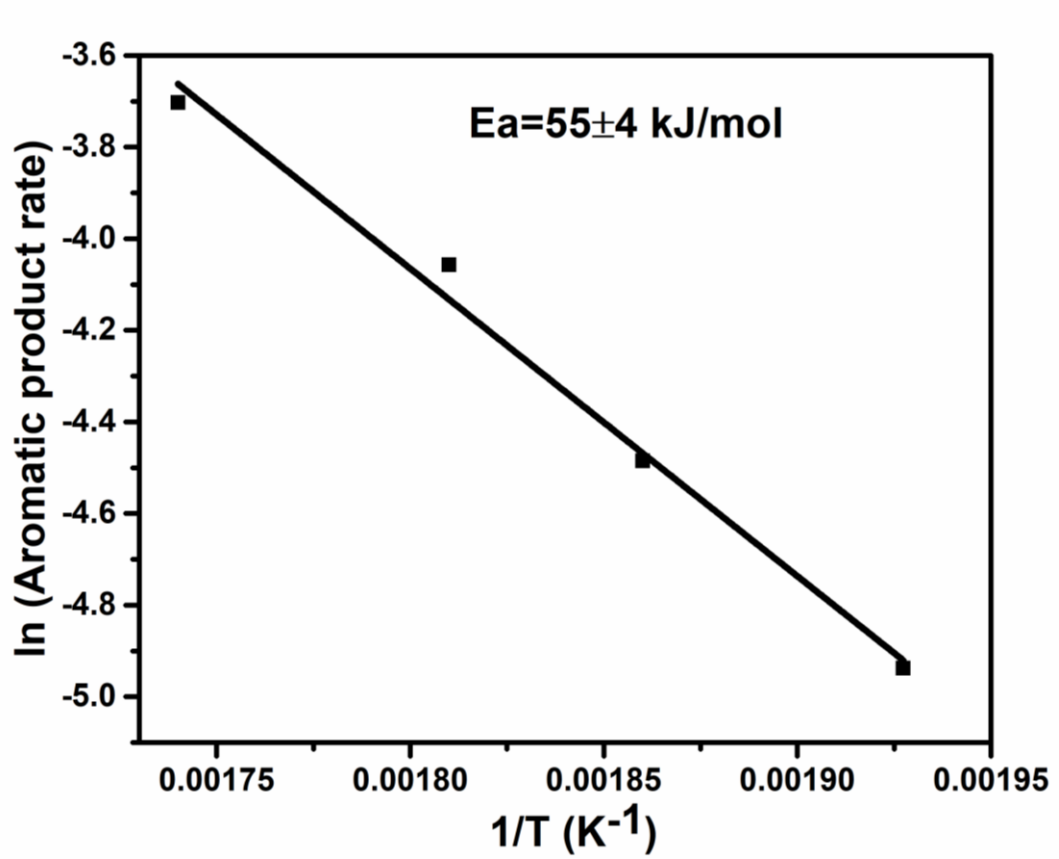


Figure 4.9 Arrhenius plot for the estimation of apparent activation energy of ethanol/DMF, obtained from the reaction catalysed by 0.4 g zeolite H-USY (Si/Al=6) with ethylene generated *in situ* from ethanol (0.14 mole) in 100 mL at 230, 280, 250 and 300 °C.

4.4 Mechanistic Investigation

In order to further investigate the influence of ethanol on the reaction mechanism, theoretical and experimental studies (SXRD and deuterated ethanol experiments) were performed.

4.4.1 Theoretical Calculations

Density Functional Theory (DFT), electronic structure methods were performed, in collaboration with Dr Giannis Mpourmpakis (University of Pittsburgh, USA), in order to calculate the energy profile of the elementary steps of the two different reactions (p-xylene

formation involving DMF + ethanol, or DMF + ethylene, demonstrated as black and red paths in **Figure 4.10**, respectively). In the ethylene route (red), the first step is the direct protonation of the DMF oxygen (from the zeolite proton) (**Table 4.3**, *vide-infra* analysis on proton affinities). The subsequent steps that appear to determine the overall rate (showing higher barriers) are: i) the Diels-Alder (DA‡, step II) cycloaddition and ii) the dehydration of the cycloadduct (oxa-norbornene *via* the C-O‡ and C-H‡ steps, IV and VI, respectively). This ethylene route has been originally analysed by Caratzoulas *et al.* [10, 16] with the same theoretical approach as our calculations. Due to their comparable energy barriers of the two steps, Dauenhauer and coworkers[10, 11] have recently reported the DA‡ step being the rate-limiting if the Brønsted acid site concentration is above 2 mM, which can change to the dehydration step of cycloadduct at lower acid site concentration.

Table 4.3 CBS-QB3 calculated gas phase proton affinities (PA) of reaction species. Note that negative values indicate exothermicity

Reaction species	**Gas phase proton affinity (kJ mol^{-1})**
Ethylene	-677.3
Water	-682.2
DMF (C)	-732.3
p-xylene	-770.8
Ethanol	-779.1

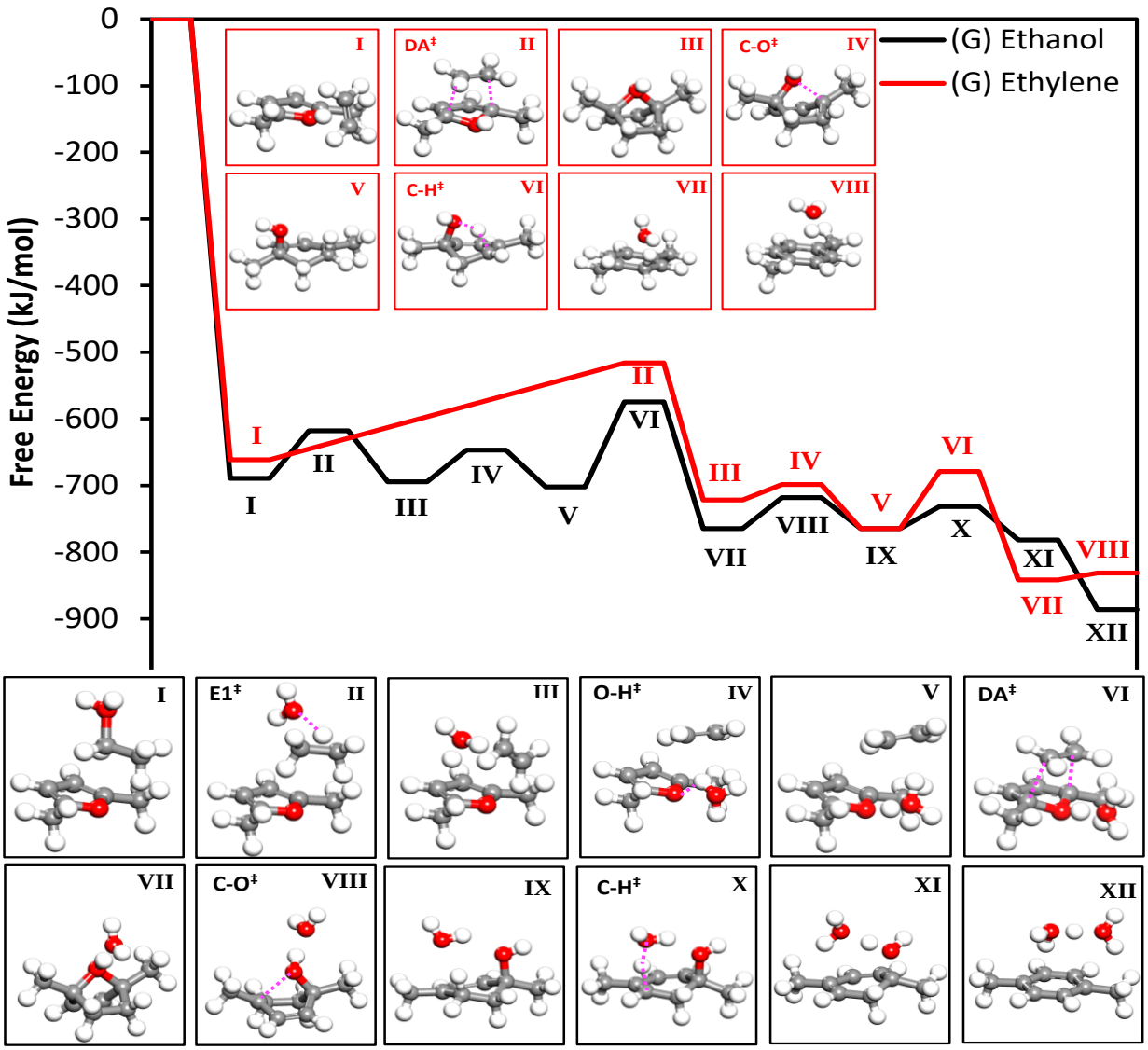


Figure 4.10 M06-2X calculated potential (free) energy landscape of two different pathways for p-xylene formation: (i) ethanol (black) and (ii) ethylene (red) route, with relevant transition states shown as insets. The distinction of consequence between the two pathways lies on the preferred protonation of ethanol over DMF as a first step, compared to the protonation of DMF in the case of the ethylene route. All the energies are reported with respect to the energy of the reacting species and a proton at infinite separation.

In the case of ethanol and DMF (black pathway of **Figure 4.10**), there is a cascade of reactions: ethanol will be first preferentially protonated instead of DMF on the acid site, followed by dehydration of the protonated ethanol (*via* E1 mechanism, step II)

to ethylene and a protonated water molecule (hydronium ion, H_3O^+). The formation of this protonated water molecule plays a key role in the subsequent steps of the reaction mechanism. First, this hydronium forms a weaker hydrogen bond with the ring oxygen of DMF (O-H‡, step IV). At state V, the protonated water is stabilized through hydrogen bonds between the ethylene and the DMF with a configuration which is close to the DA‡ transition state (step VI). This configuration is significantly different from that of state I in the ethylene (red) path since the LUMO of ethylene as dienophile comes closer to the HOMO of DMF as diene but with lower energy gap than that of ethylene route (**Figure 4.11**). Thus, these geometrical and electronic effects clearly result in decreasing the DA barrier of the ethanol path by almost 11 kJ/mol as compared to the ethylene case (96.7 vs. 107.9 kJ/mol, see **Table 4.4**).

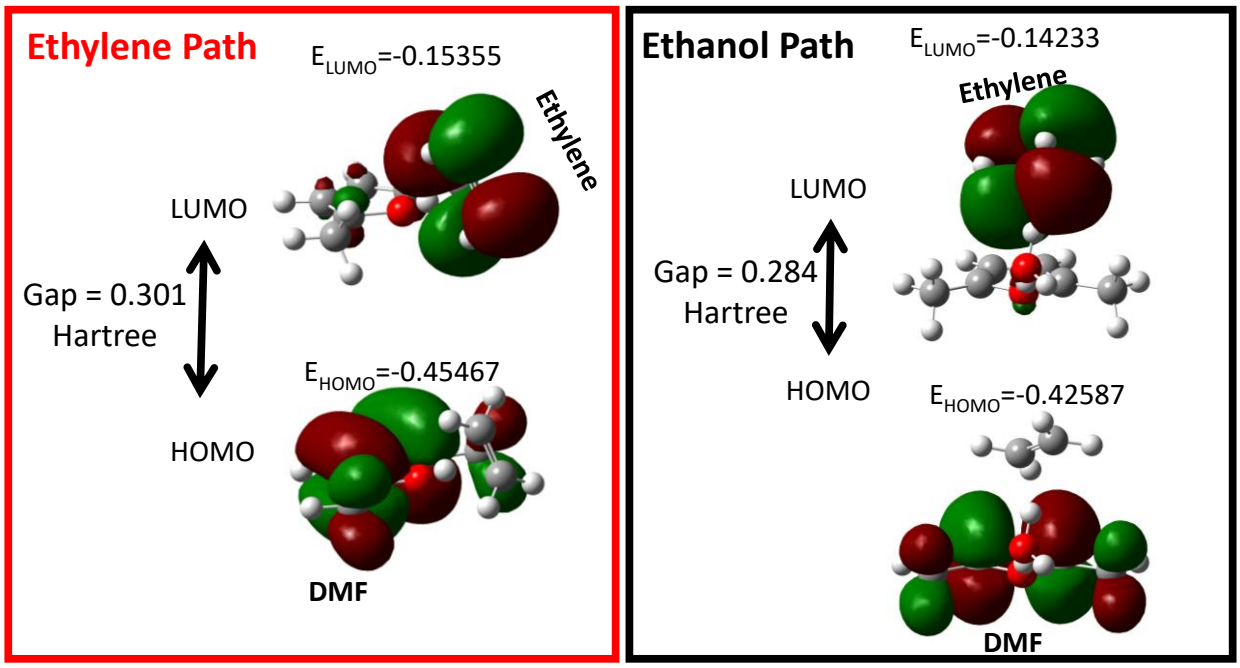


Figure 4.11 HOMO-LUMO orbital analysis at the initial state of the DA reaction of the ethanol/DMF and ethylene/DMF pathways.

In addition, the involvement of this water molecule further changes the entropic contributions at the Diels-Alder (DA) transition state in a way that favors the ethanol route (see **Table 4.4** entropy (S) and free energy (G) values). Thus, lower free energy barriers are clearly obtained for ethanol (127.6 kJ mol^{-1}) compared to that of the ethylene route (145.2 kJ mol^{-1}) with the observed difference being well beyond the realms of DFT error at this level of theory (~4 kJ mol^{-1}). [17, 18] Also, this additional water produced from the dehydration of ethanol can facilitate the C-O cleavage (C-O‡) and in particular, the C-H dissociation (C-H‡) by mediating the hydrogen transfer with lower barriers (black line), forming the second water molecule, compared to the ethylene route (red line).

Table 4.4. DFT calculated barriers for the elementary steps in the ethylene/DMF and ethanol/DMF routes. Reported values include electronic energies, total free energies, enthalpies and entropies at T= 300 °C (experimental temperature)

Pathway	Elementary step	Enthalpy (kJ mol^{-1})	Entropy (J mol^{-1} K^{-1})	Total Gibbs free energy (kJ mol^{-1})	Electronic stabilisation energy (kJ mol^{-1})
Ethylene/DMF	DA‡	109.0	-63.2	145.2	107.9
	C-O‡	25.4	3.5	23.4	33.7
	C-H‡	69.9	-27.4	85.6	84.0
Ethanol/DMF	E1‡	77.6	10.5	71.6	93.3
	O-H‡	38.5	-15.4	47.3	36.4
	DA‡	96.3	-54.7	127.6	96.7
	C-O‡	53.6	11.6	46.9	59.9
	C-H‡	17.1	-28.5	33.5	59.9

The catalytic cycle is completed by a final proton transfer, to form p-xylene and a proton, stabilized by two water molecules. The corresponding free energies, enthalpies

and entropies of all the barriers involved in the two mechanisms are presented in **Table 4.4**. Furthermore, to assess the overall kinetic behaviour of the two different mechanisms (ethanol vs. ethylene), the energetic span model of Kozuch *et al*.[19] was applied by using as input the free energy data presented in **Table 4.4** and **Figure 4.10**. The calculated E-span barrier is 115.1 kJ mol^{-1} for the ethanol route and 155.4 kJ mol^{-1} for the ethylene. Although one would expect a deviation between the calculated E-span barriers and the experimentally obtained apparent activation energies (**Figure 4.9**), the calculated E-span activation energy difference between the two paths was found to be ΔE_a = 40.3 kJ mol^{-1}, which is in perfect agreement with the experimental observations (ΔE_a = ~44 kJ mol^{-1}).

In order to investigate the adsorption behaviour of ethanol, DMF and Ethylene in the pores of the zeolite, the ONIOM method (Our Own N-layered Integrated Molecular Orbital and Molecular Mechanics) was used, first developed by Morokuma et al.[20] It is a hybrid method that can be applied to large systems using multiple levels of theory. The ONIOM3 (three-layer) method was used for these calculations, applying Molecular Mechanics (UFF) for the Low-Level calculations, a Semi-Empirical (PM6) method for the Intermediate-Model, and quantum mechanical calculations using the hybrid density functional of Truhlar and Zhao (M06-2X/6-311+G(d,p)) for the High-Level system.[21-23] **Figure 4.12a** shows the three-layer partitioning scheme chosen for the system, which consists of an 18-atom High Level, 316-atom Intermediate Level and a 152-atom Low Level model. A single Brønsted acid site (BAS) was included at the intersection of straight and sinusoidal channels, adjacent to a framework Al site. All the adsorbates were included in the High-Level of theory.

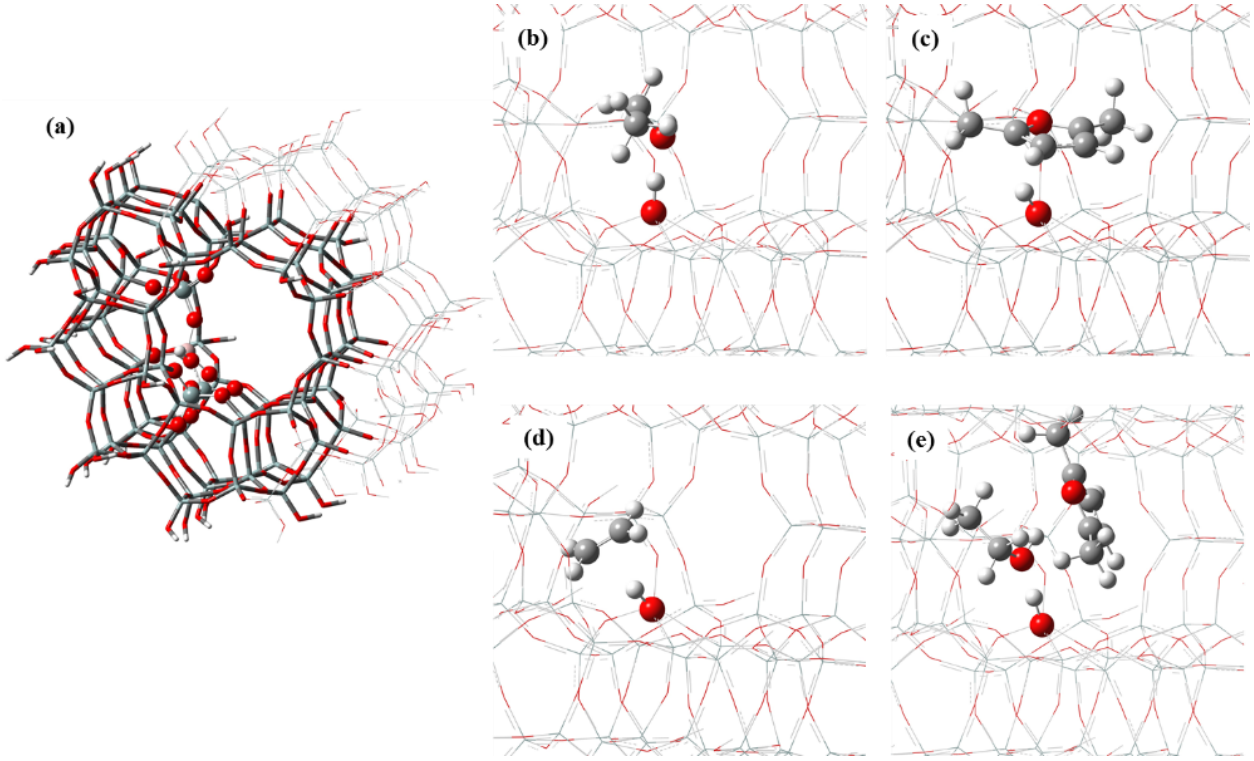


Figure 4.12 a) ONIOM3 partitioning scheme applied on the H-ZSM-5 zeolite framework. The different layers are illustrated as follows: High Level with ball-and-stick, Intermediate Level with stick and Low Level with line representations. **b-e)** Ground state adsorbate conformations of ethanol, DMF, ethylene and ethanol-DMF dimer, respectively. For visual clarity, the zeolite framework for all adsorbate configurations is shown in line representation, except for the BA site which is shown in ball and stick (as are the adsorbates).

The atoms in the Low and Intermediate layers were kept frozen in their crystallographic positions, while the High-Level atoms were allowed to relax during geometry optimizations. The gas-phase electronic binding energies (BEs) of adsorbates were calculated using the following equation:

$$\mathrm{BE} = \mathrm{E}_{\mathrm{ONIOM3,ads}} - \mathrm{E}_{\mathrm{ONIOM3,zeolite}} - \mathrm{E}_{\mathrm{adsorbate}} \quad (4.1)$$

Where $\mathrm{E}_{\mathrm{ONIOM3,ads}}$ and $\mathrm{E}_{\mathrm{ONIOM3,zeolite}}$ are the energies of the adsorbed reactants in the zeolite and the empty zeolite pore system, respectively, and $\mathrm{E}_{\mathrm{adsorbate}}$ is the (high-level) electronic energy of the adsorbates.

The calculated BEs of individual reactants and the ethanol-DMF dimer within the zeolite pore are shown in **Table 4.5** along with ground state geometries in **Figure 4.12**. Our results clearly demonstrate the ethanol adsorption preference by the BA over ethylene and DMF.

Table 4.5 Calculated ONIOM BEs of relevant adsorbates in the ethanol and ethylene routes within the H-ZSM-5 pore. Negative values indicate exothermic, while positive values indicate endothermic adsorption

Species	BE (kJ/mol)
Ethanol	-70.1
DMF	+16.5
Ethylene	-24.1
Ethanol-DMF	-35.8

The calculations demonstrate that ethanol binds the BA site more strongly than ethylene or DMF, with binding energies of -70.1, -24.1 and +16.5 kJ.mol^{-1}, respectively. (see **Table 4.5** and adsorption geometries in **Figure 4.12**). The slightly endothermic value of DMF adsorption compared to the highly exothermic value of ethanol, indicates the steric hindrance of DMF adsorption into the pore of the H-ZSM-5 zeolite. This adsorption preference of ethanol for the BA over the DMF is in perfect agreement with the experimental observations (SXRD) of **Figure 4.13** in the next section.

In view of the higher adsorption energy of ethanol over ethylene, there may be a higher local concentration of adsorbed ethanol and dehydrated ‘ethylene’ inside the zeolite cavity from feeding ethanol instead of ethylene gas in their rate comparison (**Figure 4.7**). This may account for the large difference in their rates, despite the fact that the concentration of ethylene (0.45 mole) was actually set higher than ethanol (0.14 mole).

4.4.2 SXRD Experiments

One reason we observed the subtle rate-enhanced aromatics production from ethanol/DMF is because of the favoured protonation of ethanol as the key step in decreasing the barriers of both the DA and cycloadduct dehydration steps (**Figure 4.10**). It is crucially important to experimentally verify this preferred protonation in the pore of the zeolite. Combining SXRD with Rietveld refinement to elucidate the adsorbate structures at an atomistic level, it was possible to experimentally verify the reactants' preferential protonation. **Figure 4.13** shows the Rietveld refinement profiles and the corresponding crystal structures of H-ZSM-5 pre-adsorbed (**Figure 4.13a** and **4.13b**) only with ethanol, (**Figure 4.13c** and **4.13d**) only with DMF, and (**Figure 4.13e** and **4.13f**) with an equimolar mixture of ethanol and DMF, within acceptable errors (**Table 4.6**).

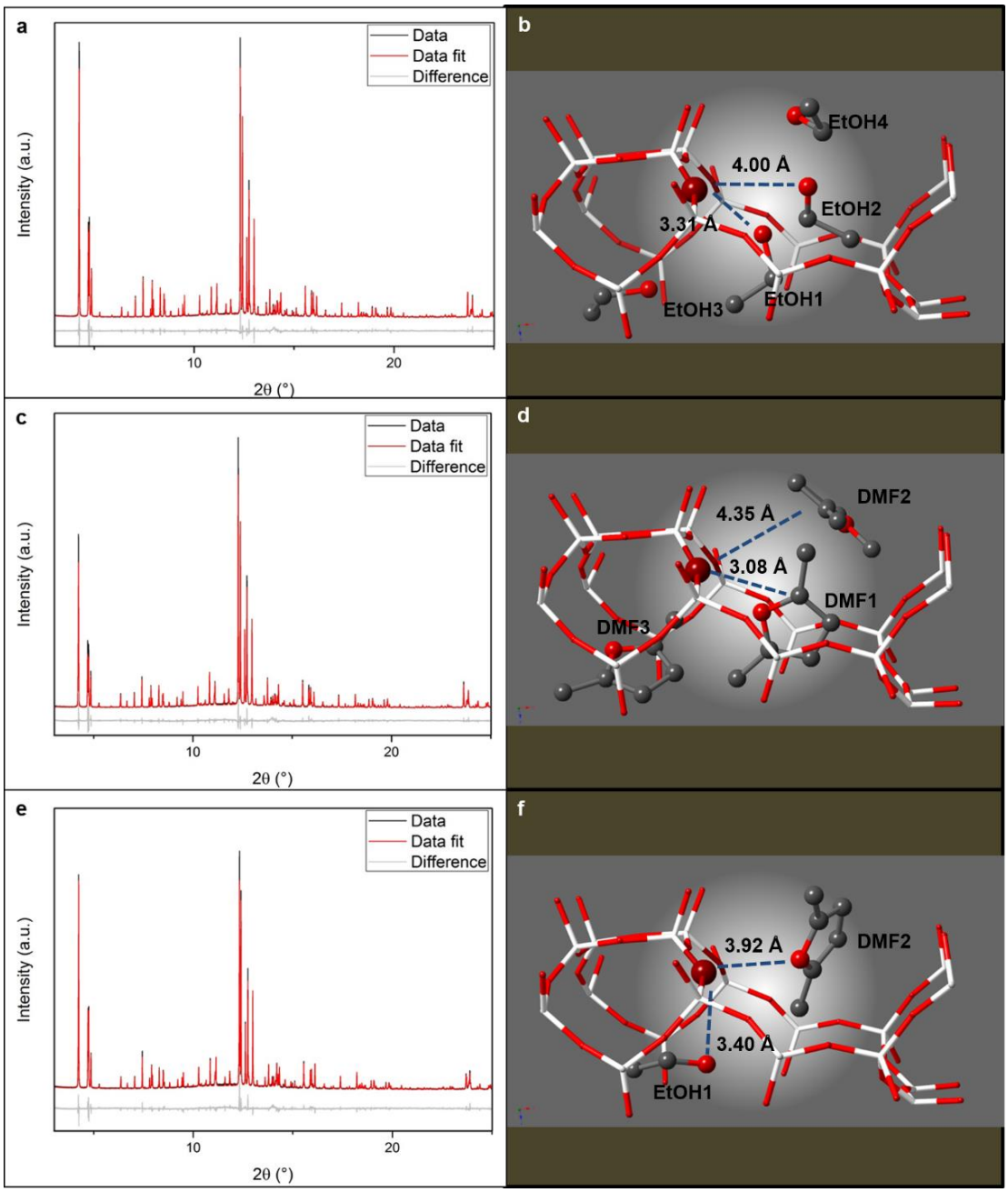


Figure 4.13 Rietveld refinement profiles of HZSM-5 pre-adsorbed with **a)** ethanol, **c)** DMF, and **e)** ethanol/DMF at 25 °C, and the corresponding crystal structures viewing from the [010] direction are displayed; **b)** ethanol, **d)** DMF, **f)** ethanol/DMF. Their crystallographic/atomic parameters from Rietveld refinement are summarised in **Table 4.6** and **Tables A1-A3** in Appendix. Atoms are represented in ball/sticks: white = Si/Al, red = O, black = C. For clarity hydrogen atoms are not plotted.

In the case of HZSM-5 pre-adsorbed only with ethanol or DMF, the two primary adsorbates (labelled as EtOH 1 and DMF 1) locate in the sinusoidal-straight cross-channel region of the framework. From the shortest interatomic/intermolecular distances the BAS selectively protonates the adsorbate molecules to form primary protonated adduct cations, which links other adsorbate molecules *via* weak H-bonding interactions. Comparing the interatomic/intermolecular distances, it clearly shows the first protonated ethanol or DMF molecule locates in the cross-channel region. The interatomic distances between these primary acid-base adducts are 3.2±0.1 Å. At > 4.0 Å from the framework O atoms a second weakly adsorbed molecule is detected.

However, when an equimolar mixture of ethanol and DMF is applied, ethanol is preferentially protonated by the BAS in the cross-channel region, then interacts with DMF *via* a weak intermolecular H-bonding. Thus, the DMF in the straight channel will be forced to interact with the $EtOH_2^+$ through a weak intermolecular H-bonding interaction, as described in **Figure 4.13**.

Excitingly, it was experimentally verified by SXRD the preferential protonation of ethanol in the case of ethanol/DMF. It agrees with our prediction based on the theoretical proton affinities (PA) values of the adsorbate species (see **Table 4.3**; ethanol > DMF > water > ethylene). This is also consistent with the ideal proton flux for this reaction, as demonstrated by our DFT calculations.

In short, as ethanol is readily adsorbed on the BAS in zeolites, the subsequent rapid dehydration will produce high concentration of ethylene and H_3O^+. There are two rate promoting effects in the catalytic conversion of DMF when ethanol is used instead of

ethylene (i) the H_3O^+ facilities the DA reaction by lowering the HOMO-LUMO gap, and (ii) the ethylene produced *in situ* has a higher local concentration than that of ethylene/DMF.

Table 4.6 Crystallographic parameters of the H-ZSM-5 samples measured at 25 °C, dehydrated, pre-adsorbed with ethanol, DMF, and an equimolar mixture of DMF and ethanol

Samples	**H-ZSM-5 (dehydrated)**	**H-ZSM-5 (ethanol)**	**H-ZSM-5 (DMF)**	**H-ZSM-5 (DMF & ethanol)**
Chemical formula	$H_{4.48}Al_{4.48}Si_{91.52}O_{192}$	$H_{4.48}Al_{4.48}Si_{91.52}O_{192}$ -*n*C_2H_5OH	$H_{4.48}Al_{4.48}Si_{91.52}O_{192}$ -*n*C_6H_8O	$H_{4.48}Al_{4.48}Si_{91.52}O_{192}$ -*m*C_6H_8O.*n*C_2H_5OH
X-ray source	Synchrotron	Synchrotron	Synchrotron	Synchrotron
Wavelength (Å)	0.825634(2)	0.825850(2)	0.825850(2)	0.825850(2)
2θ -zero point (°)	-0.002500(10)	0.010275(10)	0.010275(10)	0.010275(10)
Space group	*Pnma*	*Pnma*	*Pnma*	*Pnma*
Crystal system	Orthorhombic	Orthorhombic	Orthorhombic	Orthorhombic
a (Å)	20.13675(3)	20.12191(3)	20.16651(4)	20.09515(4)
b (Å)	19.95928(3)	19.93057(3)	19.97710(4)	19.96020(4)
c (Å)	13.43725(2)	13.42604(2)	13.45305(3)	13.43518(3)
V (Å^3)	5400.631(22)	5384.394(15)	5419.812(19)	5388.893(22)
2θ range for refinement (°)	3-55	3-55	3-55	3-55
Detector	MAC	MAC	MAC	MAC
Number of parameters	36	170	161	153
Number of *hkl*s	4190	4190	4190	4190
Refinement methods	Le Bail	Rietveld	Rietveld	Rietveld
$R_{wp}/R_p/R_{exp}$ (%)	6.621/5.077/4.958	7.649/5.808/3.364	8.457/6.461/3.339	8.955/7.030/3.883
X^2	1.335	2.274	2.533	2.306

4.4.3 Experiments with Deuterated Ethanol

The kinetic isotope effect (KIE) for the reaction with ethanol was investigated, in order to confirm some of the insights about the reaction mechanism obtained from the theoretical calculation and SXRD experiments. The reactions with deuterated ethanol were carried out under the same conditions, only replacing regular ethanol by ethanol-d or ethanol-d6 (**Figure 4.14**).

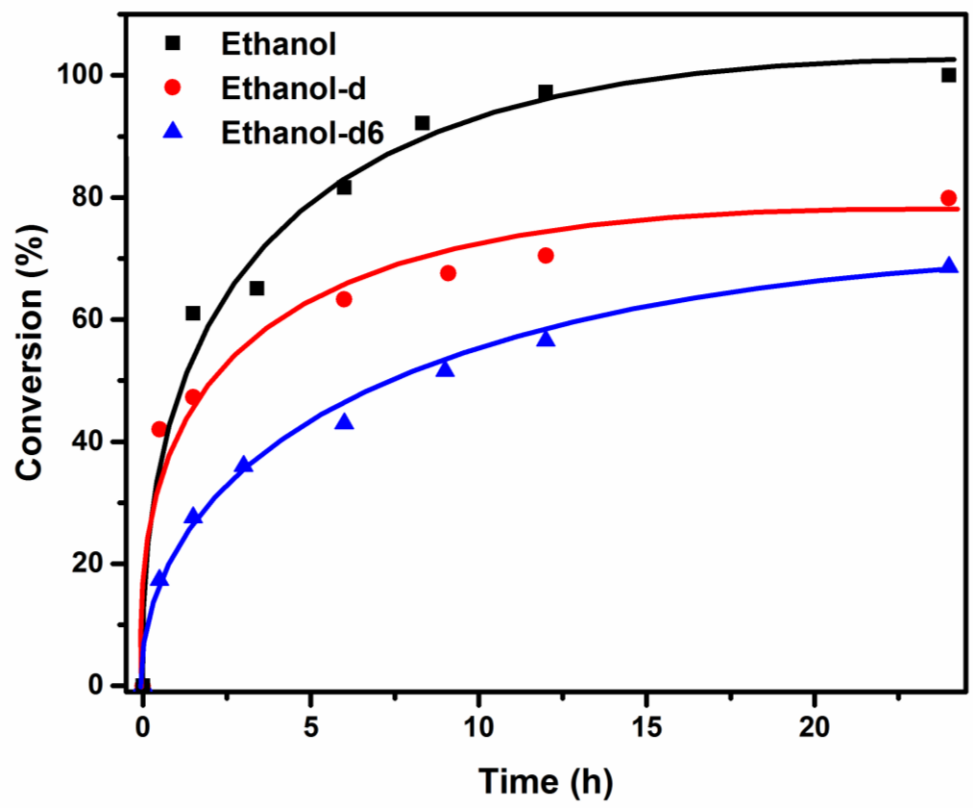


Figure 4.14. Kinetic data obtained for the ethanol and its isotopes (ethanol-d and ethanol-d6) reacted with (0.14 mole) of DMF to obtain aromatics, the reaction was catalysed by 0.4 g zeolite H-USY (Si/Al=6) in 100 mL at 300°C.

Figure 4.14 shows that the DMF conversion is clearly affected by the exchange of ethanol by its isotopes. The reaction performed with ethanol-d (C_2H_5OD) presents slower kinetics when compared with ethanol, while the reaction performed with ethanol-

d6 (C_2D_5OD) is even slower. The influence of the KIE can be measured through the initial rate ratios (r_H/r_D) between the reaction with ethanol and its deuterated counterpart (**Table 4.7**), where the initial rates were estimated by the rate for the first hour of reaction.

Table 4.7 Measured kinetic isotope effect (KIE) for the DMF transformation into aromatics replacing ethanol by deuterated ethanol (ethanol-d and ethanol-d6). Reaction conditions: 0.4 g of H-USY (Si/Al=6), temperature 300 °C, 0.14 mole of DMF and 0.14 mole of deuterated ethanol

KIE	Ethanol-d	Ethanol-d6
r_H/r_D	1.3	2.2

The initial rates for the reaction performed with ethanol-d and ethanol-d6 in an ideal system would be expected to show a significant decrease ($r_H/r_D>2$) for the ethanol-d only if the cleavage of the O-H bond is involved in the reaction rate determining step (RDS), or with ethanol-d6 only if the cleavage of a C-H bond is involved in the RDS.[24-27] Our theoretical calculations using DFT and ONIOM methods showed that the DA step is rate-limiting for the reaction. As there is no bond cleavage involved in this step and it is well stablished in the literature that the DA reaction is not significantly affected by the presence of isotopes,[28-30] the initial would not be expected to show any significant sensitivity to deuterated ethanol. However, due to the complexity of the system the KIE reveals a different trend to that expected. As shown in **Table 4.7**, the cleavage of the O-H bond does not seem to be involved in the reaction rate-limiting step, since the r_H/r_D is close to one, confirming our theoretical calculations results. On the other hand, the reaction performed with ethanol-d6 showed more significant modification in its rate ($r_H/r_D=2.2$). While this could mean that cleavage of a C-H bond is involved in the RDS, the most likely explanation for the observed r_H/r_D values is a proton exchange between

the deuterated ethanol and the BAS. As the BAS and the water molecule formed by the ethanol dehydration are directly involved in the RDS, as demonstrated by our calculations and the SXRD experiments, it is quite plausible that the reaction rate is affected by the formation of deuterated BAS and water molecules. Since the ethanol-d6 has more deuterium atoms it is expected that it will exchange more protons with the BAS[31] and consequently produce a larger number of deuterated water molecules, which will increase the effect on the rate. In conclusion, the experiments with deuterated ethanol did not completely confirm our proposed mechanism, however, they did confirm the importance of water and the BAS in the reaction rate-limiting step.

4.5 Conclusions

In summary, combining high quality SXRD data and Rietveld refinement analysis with detailed kinetic measurements and high-level first principles calculations, it was demonstrated that ethanol can act as a dienophile source for furan cycloaddition exhibiting substantially higher rates and lower reaction barriers than that of ethylene. It is believed that the realization of higher production rates of aromatics in zeolites using bio-ethanol can underpin the rational design of zeolite catalysts and the employment of other co-substrates for this new improved process. The [4+2]-cycloaddition with different furans and dienophiles derived from biomass, including alkynes and alkenes in spatially defined zeolites may also lead to tailored activity and stereochemistry.

4.6 References

1. Teixeira, I.F., B.T.W. Lo, P. Kostetskyy, M. Stamatakis, et al., *From Biomass-Derived Furans to Aromatics with Ethanol over Zeolite.* **Angewandte Chemie International Edition**, 2016. 55: p. 13061-13066.

2. Brandt, A., J. Graesvik, J.P. Hallett, and T. Welton, *Deconstruction of lignocellulosic biomass with ionic liquids.* **Green Chem.**, 2013. 15: p. 550-583.

3. Ragauskas, A.J., C.K. Williams, B.H. Davison, G. Britovsek, et al., *The path forward for biofuels and biomaterials.* **Science**, 2006. 311: p. 484-489.

4. Roman-Leshkov, Y., J.N. Chheda, and J.A. Dumesic, *Phase modifiers promote efficient production of hydroxymethylfurfural from fructose.* **Science**, 2006. 312: p. 1933-7.

5. Wright, M.M., Y. Roman-Leshkov, and W.H. Green, *Investigating the techno-economic trade-offs of hydrogen source using a response surface model of drop-in biofuel production via bio-oil upgrading.* **Biofuels, Bioprod. Biorefin.**, 2012. 6: p. 503-520.

6. Alonso, D.M., S.G. Wettstein, and J.A. Dumesic, *Bimetallic catalysts for upgrading of biomass to fuels and chemicals.* **Chem. Soc. Rev.**, 2012. 41: p. 8075-8098.

7. Climent, M.J., A. Corma, and S. Iborra, *Conversion of biomass platform molecules into fuel additives and liquid hydrocarbon fuels.* **Green Chemistry**, 2014. 16: p. 516-547.

8. Luterbacher, J.S., D. Martin Alonso, and J.A. Dumesic, *Targeted chemical upgrading of lignocellulosic biomass to platform molecules.* **Green Chemistry**, 2014. 16: p. 4816-4838.

9. Zheng, A., Z. Zhao, S. Chang, Z. Huang, et al., *Maximum synergistic effect in the coupling conversion of bio-derived furans and methanol over ZSM-5 for enhancing aromatic production.* **Green Chemistry**, 2014. 16: p. 2580-2580.

10. Williams, C.L., C.-C. Chang, P. Do, N. Nikbin, et al., *Cycloaddition of Biomass-Derived Furans for Catalytic Production of Renewable p-Xylene.* **ACS Catalysis**, 2012. 2: p. 935-939.

11. Williams, C.L., K.P. Vinter, C.-C. Chang, R. Xiong, et al., *Kinetic regimes in the tandem reactions of H-BEA catalyzed formation of p-xylene from dimethylfuran.* **Catalysis Science & Technology**, 2016. 6: p. 178-187.

12. Cheng, Y.-T. and G.W. Huber, *Production of targeted aromatics by using Diels–Alder classes of reactions with furans and olefins over ZSM-5.* **Green Chemistry**, 2012. 14: p. 3114-3114.

13. Kagyrmanova, A.P., V.A. Chumachenko, V.N. Korotkikh, V.N. Kashkin, et al., *Catalytic dehydration of bioethanol to ethylene: Pilot-scale studies and process simulation.* **XIX 4 International Conference on Chemical Reactors (CHEMREACTOR-19)**, 2011. 176–177: p. 188-194.

14. Zhang, M. and Y. Yu, *Dehydration of Ethanol to Ethylene.* **Industrial & Engineering Chemistry Research**, 2013. 52: p. 9505-9514.

15. Williams, C.L., *Production of Sustainable Aromatics from Biorenewable Furans*, in *Department of Chemical Engineering*. 2014, University of Massachusetts: Amherst.

16. Nikbin, N., P.T. Do, S. Caratzoulas, R.F. Lobo, et al., *A DFT study of the acid-catalyzed conversion of 2, 5-dimethylfuran and ethylene to p-xylene.* **Journal of catalysis**, 2013. 297: p. 35-43.

17. Zhao, Y. and D.G. Truhlar, *The M06 suite of density functionals for main group thermochemistry, thermochemical kinetics, noncovalent interactions, excited states, and transition elements: two new functionals and systematic testing of four M06-class functionals and 12 other functionals.* **Theoretical Chemistry Accounts**, 2008. 120: p. 215-241.

18. Zhao, Y. and D.G. Truhlar, *The M06 suite of density functionals for main group thermochemistry, thermochemical kinetics, noncovalent interactions, excited states, and transition elements: two new functionals and systematic testing of four M06-class functionals and 12 other functionals.* 2007. 120: p. 215-241.

19. Kozuch, S. and S. Shaik, *How to Conceptualize Catalytic Cycles? The Energetic Span Model.* **Accounts of Chemical Research**, 2011. 44: p. 101-110.

20. Morokuma, K., R. Froese, S. Dapprich, I. Komaromi, et al. *The ONIOM (our own integrated N-layered molecular orbital and molecular mechanics) method, and its applications to calculations of large molecular systems*. in *Abstracts of Papers of the American Chemical Society*. 1998: Amer Chemical Soc 1155 16th St, NW, Washington, Dc 20036 USA.

21. Stewart, J.J., *Optimization of parameters for semiempirical methods V: modification of NDDO approximations and application to 70 elements.* **Journal of Molecular modeling**, 2007. 13: p. 1173-1213.

22. Rappé, A.K., C.J. Casewit, K. Colwell, W. Goddard Iii, et al., *UFF, a full periodic table force field for molecular mechanics and molecular dynamics simulations.* **Journal of the American chemical society**, 1992. 114: p. 10024-10035.

23. Zhao, Y. and D.G. Truhlar, *The M06 suite of density functionals for main group thermochemistry, thermochemical kinetics, noncovalent interactions, excited states, and transition elements: two new functionals and systematic testing of four M06-class functionals and 12 other functionals.* **Theoretical Chemistry**

Accounts: Theory, Computation, and Modeling (Theoretica Chimica Acta), 2008. 120: p. 215-241.

24. DeWilde, J.F., H. Chiang, D.A. Hickman, C.R. Ho, et al., *Kinetics and Mechanism of Ethanol Dehydration on γ-Al2O3: The Critical Role of Dimer Inhibition.* **ACS Catalysis**, 2013. 3: p. 798-807.

25. DeWilde, J.F., C.J. Czopinski, and A. Bhan, *Ethanol dehydration and dehydrogenation on γ-Al2O3: mechanism of acetaldehyde formation.* **ACS Catalysis**, 2014. 4: p. 4425-4433.

26. Knözinger, H. and A. Scheglila, *The dehydration of alcohols on alumina.* **Journal of Catalysis**, 1970. 17: p. 252-263.

27. Bedard, J., H. Chiang, and A. Bhan, *Kinetics and mechanism of acetic acid esterification with ethanol on zeolites.* **Journal of Catalysis**, 2012. 290: p. 210-219.

28. Singleton, D.A., S.R. Merrigan, B.R. Beno, and K.N. Houk, *Isotope effects for Lewis acid catalyzed Diels-Alder reactions. The experimental transition state.* **Tetrahedron Letters**, 1999. 40: p. 5817-5821.

29. Beno, B.R., K.N. Houk, and D.A. Singleton, *Synchronous or Asynchronous? An "Experimental" Transition State from a Direct Comparison of Experimental and Theoretical Kinetic Isotope Effects for a Diels−Alder Reaction.* **Journal of the American Chemical Society**, 1996. 118: p. 9984-9985.

30. Singleton, D.A., B.E. Schulmeier, C. Hang, A.A. Thomas, et al., *Isotope effects and the distinction between synchronous, asynchronous, and stepwise Diels–Alder reactions.* **Tetrahedron**, 2001. 57: p. 5149-5160.

31. Cant, N.W. and W.K. Hall, *Studies of the hydrogen held by solids.* **Journal of Catalysis**, 1972. 25: p. 161-172.

Chapter 5

Influence of Site Blockages in the Conversion of DMF into Aromatics

Chapter 5: Influence of Site Blockages in the Conversion of DMF into Aromatics

Overview **129**

5.1 Introduction **130**

5.2 ^{27}Al and ^{31}P MAS NMR **133**

5.3 SXRD Experiments **135**

5.4 Catalytic Performance **142**

5.5 Conclusions **148**

5.6 References **150**

Overview

This chapter uses a site blockage strategy through K^+ exchange to understand the influence on the product distribution for the DMF transformation reaction into aromatics. The beginning of this chapter is focused on the characterization of USY zeolites, in particular with the correlation of Brønsted acidity with 3-D structure and global atomic arrangements. Using SXRD in combination with the basic probe molecule pyridine, and ^{27}Al NMR, it was possible to identify two types of Brønsted acid sites (BAS) for the H-USY zeolite (Si/Al=7.5), one relative weak and one strong, while the H-USY (Si/Al=250) shows only weak BAS. After locating the BAS, it was possible to link the acid strength of the sites with their location in the zeolite framework. The final part of the chapter is focused on the selective blockage of the strong BAS of the H-USY (Si/Al=7.5) and how it influences the product selectivity of the ethanol/DMF reaction introduced in the last chapter. The Synchrotron diffraction experiments and their interpretation were performed in collaboration with Dr. Lin Ye (University of Oxford). I was responsible for all the catalytic tests presented in this chapter. I also helped to plan and prepare the samples used in SXRD experiments and assisted in interpretation of the data. The data refinement was done exclusively by Dr. Lin Ye, as well as the ^{27}Al ssNMR experiments. The ^{31}P MAS ssNMR measurement were performed in collaboration by Will Yung-Kang Peng, I helped to prepare the samples and load them with TMPO.

The work in this chapter was accepted in Chemical Communications as: ‘Spatial Differentiation of Brønsted Acid Sites by Probe Molecule in Zeolite USY using Synchrotron X-ray Powder Diffraction’.

5.1 Introduction

The new/renewable facilitated process to convert DMF and ethanol into xylene presented in **Chapter 4** shows good yields when catalysed by some specific zeolites. Although zeolites catalyse the DA reaction as well as the dehydration, zeolites can also catalyse side reactions, such as DMF hydrolysis into 2,5-hexanedione. Thus, understanding the properties of these acid sites is an important step in designing high performance catalysts, however, a detailed understanding of its active sites is still lacking.

Acid-base reactions form the primary basis of zeolite catalysis.[1] A wide range of porous zeolitic structures with and without modifications have been used as microporous catalysts in industry for fuels processing and chemicals manufacture.[2, 3] The acidity and basicity of one of the more structurally robust zeolites, zeolite Y, have been extensively characterized.[2, 4] The crystal structure of zeolite Y is generated by connecting sodalite units (sodalite cage with a 2.6 Å window) *via* hexagonal prisms, which form empty cavities (a supercage with a 7.6 Å window). In general, the catalytically active sites of zeolite Y are the Brønsted acid sites (BAS), which are created through the substitution of silicon (tetravalent) with aluminium (trivalent) in the zeolite Y framework with an acidic proton associated with the bridging oxygen atom of Al-O-Si for charge compensation.[5] A mild steaming treatment is used to improve the hydrothermal stability of HY as the USY zeolite.[6-8] During the steaming treatment, part of framework Al^{3+} was found to leach into the extra-framework positions.[9] Corma *et al.* attributed the extra-framework Al^{3+} species to the rise of some stronger BAS.[10] Mirodatos *et al.* have suggested the superacid sites in dealuminated zeolites result from the interactions between protonic sites and extra-framework oxoaluminium deposited in the zeolite pores.[11] On the other hand, using

combined *in situ* X-ray techniques, Bokhoven et al. concluded some extra-framework Al^{3+} species took residence inside the sodalite cage that could affect the BAS.[12] By combining detailed solid state NMR studies and theoretical calculations, Deng *et al.* considered a range of possible oxoaluminium ions and neutral extra-framework species influencing the BAS: some prefer to stay in the supercage, but some occupy the sodalite cage.[13] However, the direct correlation of a particular extra-framework Al^{3+} species with respect to the enhanced BAS cannot be unambiguously assigned, due to the limitations in the spatial resolution of those techniques. In contrast, there are also some reports claiming that the extra-framework Al^{3+} species act only as spectators, which would not alter the strength of BAS.[14, 15] The contradictory views mainly arise due to the lack of advance characterization tools to link BAS acidity measurement with structure in 3-D local and global atomic arrangements. Practically, acidity measurement is commonly done with temperature programmed desorption (TPD) of basic probe molecules such as ammonia, propylamine, pyridine or TMP. However, the deconvolution of generally complex desorption peaks to differentiate strength and quantity of BAS sites is frequently challenging. More importantly, although some spectroscopic techniques can be used to identify the nature of acidic sites, they do not provide direct spatial relationships without controversy.[10, 11, 13] This poses huge difficulties for the correlation of BAS with specific catalytic reactions taking place in zeolites and thus limits the development of exciting concepts such as site engineering. For example, biomass derived furans can be catalysed by BAS into valuable aromatic products by a Diels-Alder cycloaddition with ethylene over zeolite.[16-27] However, some BAS in the zeolite can also accelerate the side

reactions of 2,5-dimethylfuran (DMF) hydrolysis into ketones (**Figure 5.1**). No rational differentiation of these BAS sites in zeolites has yet been achieved.

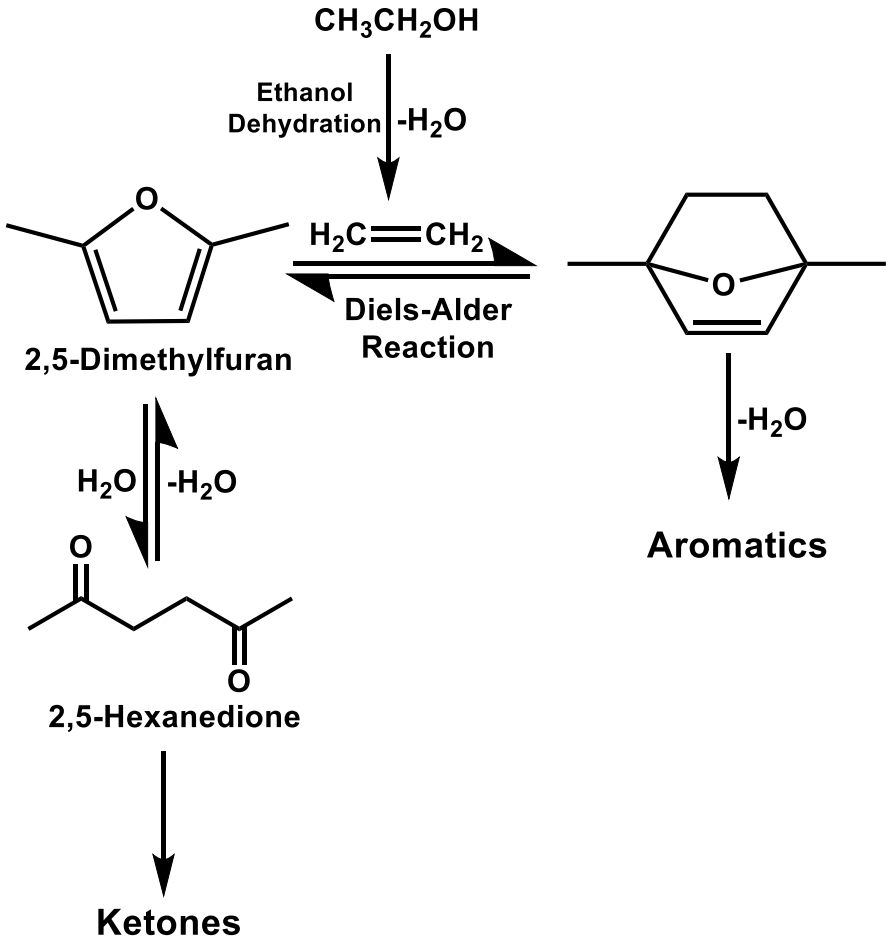


Figure 5.1 Schematic representation of the conversion of 2,5-dimethylfuran (DMF) into aromatics by Diels-Alder cycloaddition with ethylene, *in situ* generated by dehydration of ethanol, and the DMF hydrolysis equilibria forming 2,5-hexanedione.

Recently, we and other researchers have shown that high resolution synchrotron X-ray powder diffraction (SXRD) allows the elucidation of organic/inorganic adsorbate structures in zeolite and MOFs.[28-30] Combined with Rietveld refinement, atomic spatial information and local bonding interaction of organic adsorbates with respect to zeolite acid sites can be visualized in ways not possible with most spectroscopies (IR, Raman,

NMR) or thermal methods (TPD, TGA). In this work, the spatial distribution and the acidic strength of BAS in dealuminated H-USY (Si/Al=325) and H-USY (Si/Al=7.3) (ultra-stable zeolite Y), of different Si/Al ratios are investigated by using SXRD in combination with the basic pyridine probe molecule. After locating the BAS in both samples, by adopting a strategy of partially/totally blockage of the BAS of different acid strengths with K^+, the DMF/Ethanol reaction was investigated correlating the products distribution with the strength of the BAS.

5.2 ^{27}Al and ^{31}P MAS NMR

^{27}Al MAS NMR can provide local information about the Al distribution and coordination in zeolites.[12, 31, 32] **Figures 5.2a** and **5.2b** show the ^{27}Al MAS NMR spectra of H-USY (Si/Al=325) and H-USY (Si/Al=7.3). There is only one peak appearing at 62.8 ppm in the spectrum of H-USY (Si/Al=325) (**Figure 5.2a**), which belongs to the 4-CN framework Al^{3+} species (framework BAS). Due to the low Al^{3+} concentration of H-USY (Si/Al=325), the S/N ratio of the ^{27}Al NMR spectrum is poor (**Figure 5.2a**). On the other hand, two well-defined peaks at 62.3 ppm and 1.2 ppm corresponding to 4-CN framework Al^{3+} species (framework BAS) and 6-CN extra-framework Al^{3+} can be seen in the case of H-USY (Si/Al=7.3) (**Figure 5.2b**). An additional peak at 32.3 ppm can also be seen as the distorted 4 or 5-CN Al^{3+} species.[31] Peak deconvolution in **Figure 5.2b** shows that around 39% of Al^{3+} are 4-CN framework species, 13% are distorted 4,5-CN species and 48% are the 6-CN extra-framework Al^{3+} species in the H-USY (Si/Al=7.3). According to ICP-AES analysis, there are 23 Al atoms in each USY unit cell, corresponding to 9 4-CN framework Al^{3+}, 3 distorted 4,5-CN Al^{3+} and 11 6-CN extra-framework Al^{3+} per unit cell. In contrast, there is only 0.6 4-CN framework Al^{3+} per unit cell in H-USY (Si/Al=325).

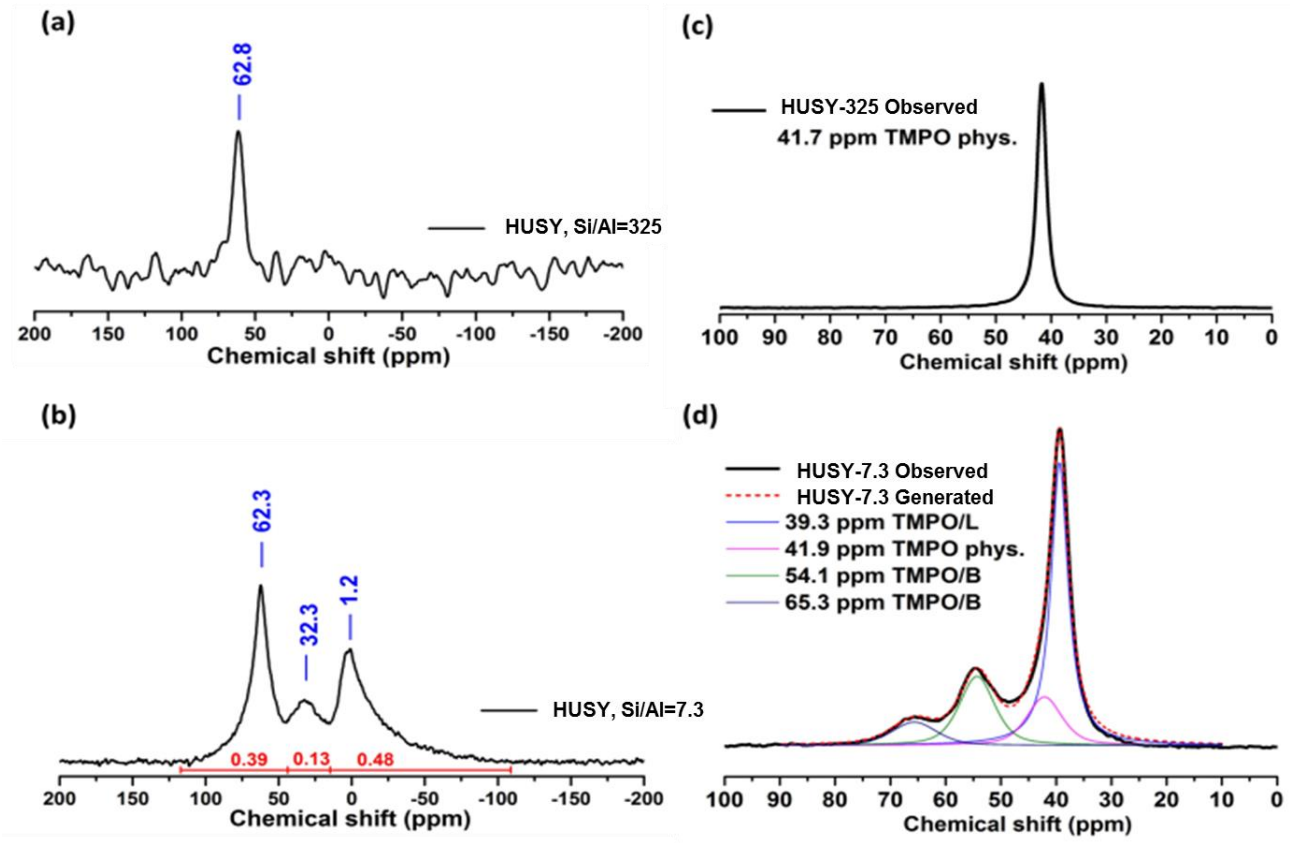


Figure 5.2 ^{27}Al MAS NMR spectra of a) H-USY (Si/Al=325) and b) H-USY (Si/Al=7.3), ^{31}P MAS NMR spectra and the deconvolution curves of (trimethylphosphine oxide) TMPO adsorbed on c) H-USY (Si/Al=325) and d) H-USY (Si/Al=7.3).

It is thus evident that at least two types of extra-framework Al^{3+} species are present in H-USY (Si/Al=7.3) alongside the observed framework BAS, whereas only the framework BAS is detected in H-USY (Si/Al=325) by NMR analysis. ^{31}P NMR with trimethylphosphine oxide (TMPO) was also applied to characterize the acidic nature of H-USY (Si/Al=325) and H-USY (Si/Al=7.3).[33] Because of the low Al^{3+} concentration, the NMR spectrum of TMPO-treated H-USY (Si/Al=325) (**Figure 5.2c**) mainly shows a single peak due to the TMPO physisorption (41.7 ppm). However, deconvolution of the spectrum of TMPO adsorbed on H-USY (Si/Al=7.3), see **Figure 5.2d**, clearly indicates resolved peaks due to a TMPO-Lewis acid 6-CN extra-framework adduct (39.3 ppm),

TMPO physisorption (41.9 ppm) and two TMPO-BAS adducts at 54.1 ppm and 65.3 ppm, respectively. In other words, H-USY (Si/Al=7.3) again shows two types of BAS, the relative weak framework BAS (54.1 ppm, relates to the 4-CN framework Al^{3+}) and strong BAS (65.3 ppm, relates to the 4-CN extra-framework Al^{3+}) with the ratio 2.4: 1 (versus ca. 3.0: 1 derived from ^{27}Al NMR) alongside the characteristic Lewis acid sites (39 ppm) of 6-CN extra-framework Al^{3+} species.

This observation matches with the previous characterization by ^{1}H NMR[13, 34] where two BAS with the signals at 5.0 and 4.3 ppm were noted from steam treated HY zeolite. HY is a highly symmetric structure with one spatial statistical tetrahedral site. When Al substitutes Si, the BAS should generate only one type of acidic strength. However, H-USY (Si/Al=7.3) (HY, Si/Al=7.3 after steam treatment) with a high Al/Si ratio shows two types of BAS acid strength. This suggests the dealuminated Al^{3+} somehow enhances the acid strength of BAS, confirming the findings of Bokhoven, Deng, and other research workers.[10, 12, 13, 35] However, as discussed, no direct correlation of encapsulated Al^{3+} in sodalite unit with exposed BAS site and adsorbate in the supercage can be undisputedly drawn due to the spatial limitations of the spectroscopic technique. As a result, synchrotron X-ray powder diffraction (SXRD) was also employed in this work.

5.3 SXRD Experiments

The SXRD patterns of H-USY (Si/Al=325) (**Figure 5.3a**) and H-USY (Si/Al=7.3) (**Figure 5.3b**) were refined by the Rietveld method using TOPAS software (Bruker AXS, version 5), see details in the **Chapter 3**. Both refinements started from the zeolite Y (purely siliceous) crystal structure.[36] The acceptable R-factors, R_{wp} 8.916% and 9.561% clearly show the high quality and accuracy of the refinement (**Table 5.1**). In **Figure 5.3c**,

no extra-framework Al^{3+} species exists in H-USY (Si/Al=325), consistent with the ^{27}Al NMR result. On the contrary, extra-framework Al^{3+} can be clearly refined in sodalite cages of H-USY (Si/Al=7.3) with 2.17(11) Al^{3+} per unit cell, see **Figure 5.3d**.

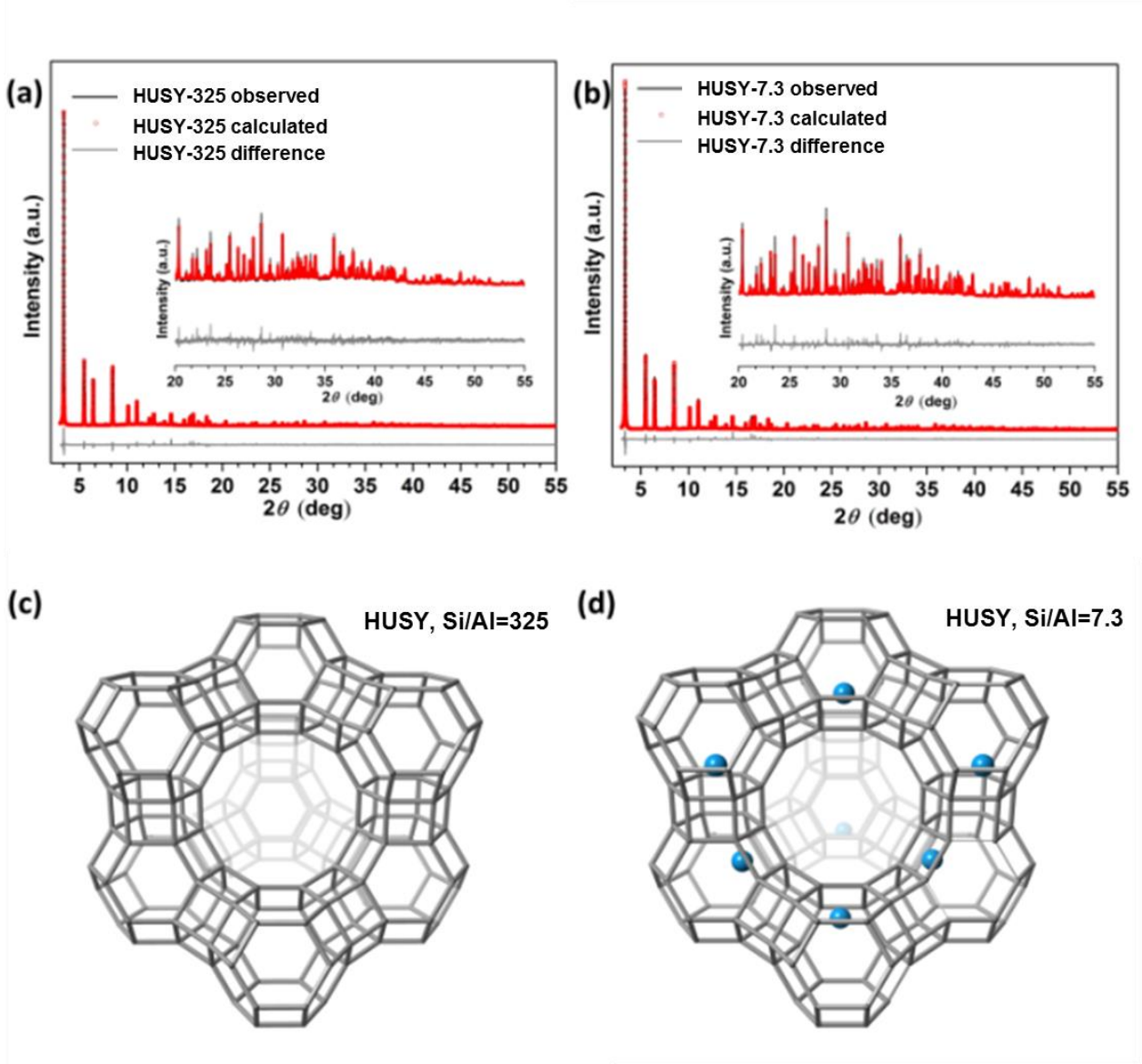


Figure 5.3 SXRD patterns and Rietveld refinement data of **a)** H-USY (Si/Al=325) and **b)** H-USY (Si/Al=7.3). The insets highlight the 20 – 55° 2θ range to illustrate the quality of the refinement. The structure of **c)** H-USY (Si/Al=325) and **d)** H-USY (Si/Al=7.3) with stick models without symmetrically appearing 4-CN extra-framework Al^{3+}. Grey represents the USY; Blue represents Al (4-CN extra-framework Al^{3+} species).

Rietveld refinement has also been applied to locate adsorbed pyridine molecules, in order to reveal the positions of the BAS. Furthermore, the adsorbate-zeolite inter-atomic distances may reflect the nature and strength of the acid site adducts.[28] The

refined SXRD patterns of pyridine-adsorbed H-USY (Si/Al=325) (**Figure 5.4a**) and H-USY (Si/Al=7.3) (**Figure 5.4b**) are shown, along with enlargements of the region of 20 – 55º 2θ to illustrate the high quality of the refinements and acceptable errors (**Table 5.1**).

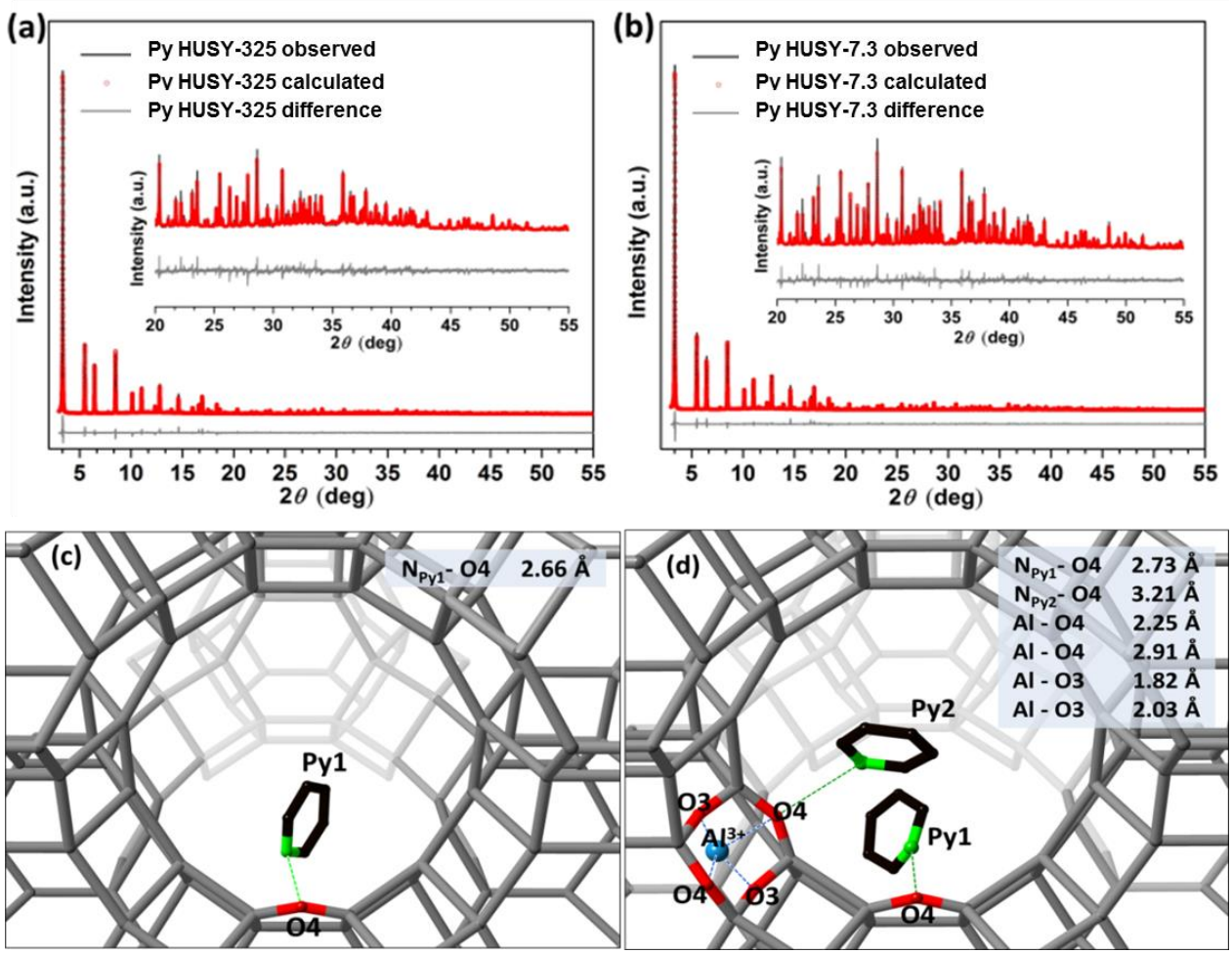


Figure 5.4 SXRD diffraction patterns and Rietveld refinement data of **a)** H-USY (Si/Al=325) and **b)** H-USY (Si/Al=7.3) after pyridine adsorption. The zooms highlight the 20 – 55º 2θ region to illustrate the quality of the refinement. The structures of **c)** H-USY (Si/Al=325) and **d)** H-USY (Si/Al=7.3) with stick models without symmetrically appearing 4-CN extra-framework Al^{3+} species and pyridine. Grey represents the USY; Blue ball represents Al (4-CN extra-framework Al^{3+} species); Green represents N of pyridine, black represents C of pyridine.

The refined structure of H-USY (Si/Al=325) shows only one pyridine site (Py1) located in the supercage, interacting with the framework O4 (BAS) with the shortest N_{Py}-$O_{framework}$ distance of 2.66(1) Å (**Figure 5.4c**). It is noted that this O4 atom is a part of the vertex of the sodalite unit exposed to the supercage and that no encapsulated pyridine is found inside the sodalite presumably, due to its large dynamic size (4.9 Å). Due to the low electron density of H atoms, it is not possible to locate them directly with XRD. However, the lone pair electrons of nitrogen in pyridine in the supercage can act as a Brønsted base to accept the proton from the BAS (Al-O(H)-Si) of the sodalite unit to form PyH^+ species. This interaction with Al-O^--Si can be partially electrostatic and partially covalent, depending on the strength of the BAS. Additionally, there are 0.59(1) pyridine per unit cell in H-USY (Si/Al=325), accounting for the site occupancy and symmetry multiplicity of Py1 obtained in the refinement, indicating that the number of BAS in H-USY (Si/Al=325) is 0.59(1). This is in excellent agreement with the 0.6 framework Al^{3+} per unit cell suggested by the ^{27}Al MAS NMR.

Table 5.1 Crystallographic data and details of the USY samples before and after pyridine-adsorbed

Samples	**H-USY-7.3**	**H-USY-325**	**Py·USY325**	**Py·USY7.3**
Crystal system	Cubic	Cubic	Cubic	Cubic
Space group	Fd-3m	Fd-3m	Fd-3m	Fd-3m
Py per unit cell	0	0	0.59	3.81
2θ range refinement (°)	3 – 55	3 – 55	3 - 55	3 – 55
Detector	Multi-analyser crystals			
Number of parameters	34	39	40	53
Number of *hkls*	563	563	563	563
Refinement methods	Rietveld	Rietveld	Rietveld	Rietveld
a (Å)	24.26653(4)	24.27051(3)	24.26613(4)	24.27194(3)
V (Å3)	14289.705(74)	14296.742(52	14288.991(72)	14299.250(4
Rwp / Rp. / Rexp. (%)	8.916/6.879/3.47	9.561/7.205/2.	9.718/7.469/2.9	8.790/6.938/
Gof χ2	2.567	3.654	3.303	3.387
Wavelength (Å)	0.82593(2)	0.82593(2)	0.826209(3)	0.826209(3)
2θ Zero point (°)	-0.00506(2)	-0.00506(2)	-0.000489(2)	-0.000489(2)

Interestingly, the refined structure of pyridine-adsorbed H-USY (Si/Al=7.3) shows an additional distorted 4-CN extra-framework Al^{3+} site in a sodalite cage that is normally unoccupied. In addition, there are also two distinctive pyridine sites in the supercage (**Figure 5.4d**). In fact, Al^{3+} and $Al(OH)^{2+}$ were both tested in the refinement, as both species could theoretically pass through the window of the sodalite cage, but the extra-framework Al^{3+} species as Al^{3+} is much better fitted than that of $Al(OH)^{2+}$ with a lower R_{wp}

value in our H-USY (Si/Al=7.3), which is also found to bind with the two O3 and O4 in the first coordination sphere, as shown **Figure 5.4d**. Moreover, both of the pyridine sites are closest to the framework O4 atoms in the 12-membered ring. The measured distances of N_{Py1}-O4 and N_{Py2}-O4 are 2.73(1) Å and 3.21(2) Å, respectively. The Py1 site position and N_{Py1}-O4 distance (2.73(1) Å) in USY-7.3 correspond to those of the Py1 site in H-USY (Si/Al=325), which means this Brønsted acid site is the typical BAS for the Al-substituted framework Si site.

Note that the new Py2 site with a longer N_{Py1}-O4 distance (3.21(2) Å) is clearly structurally linked to the extra-framework Al^{3+} through the first coordinated BAS O4 at the interface between the Al^{3+}-sodalite and supercage. It is not possible to totally rule out the possibility that there are some disordered oxoaluminium ions or neutral species deposited in close proximity to O4, influencing this BAS position. It is conceivable from the corresponding observed atomic arrangement that the additional strong Lewis acidity of the extra-framework Al^{3+} inside the sodalite cage is expected to polarize its BAS O4 at the vertex, leading to the higher propensity for proton release to pyridine from this strong BAS. Accordingly, the decrease in covalency between O4(H) with the increase in electrostatic interaction render the $O4^{-}\cdots Py2H^{+}$ longer than N_{Py1}-O4. Additionally, the comparable amount of Py2 (2.13(4) per unit cell) and the extra-framework Al^{3+} in sodalite cage (2.17(11) per unit cell) evaluated by the refinement reveals the direct link to the enhanced BAS acidity to the presence of the extra-framework Al^{3+}.

The use of Lewis acid species to enhance Brønsted acidic species is well demonstrated in a number of homogeneous super-acid systems such as $AlCl_3$-HCl and SbF_5-HF,[37, 38] but is still debatable over solid zeolite systems. It is believed this direct

observation of the acid-base adduct between pyridine probe and BAS O4 modified by encapsulated Lewis acid Al^{3+} in sodalite unit can give evidence to support such a proposition in the literature that has not been obtained by other techniques.

As it is evident that H-USY (Si/Al=7.3) possesses an additional stronger BAS than H-USY (Si/Al=325), strategic site blockage in a selective manner may allow the rational tailoring of specific BAS for zeolitic catalysis.

5.4 Catalytic Performance

To see if the different BAS exhibited by H-USY 7.3 and 325 lead to different reactivity, they were tested for the DMF/ethanol conversion reaction. Typical BAS dependent reactions, such as the catalytic conversion of 2,5-dimethylfuran (DMF) into aromatics by Diels-Alder cycloaddition with ethylene, *in situ* generated by dehydration of ethanol was therefore studied.[16] This desirable reaction involves the DMF cycloaddition, followed by the oxa-norbornene dehydration into xylene over BAS sites in the H-USY. However, some BAS can also catalyse hydrolysis of DMF into 2,5-hexanedione (**Figure 5.1**), which can be further converted to a range of ketones as side products.[39] Herein it was tested two zeolites with quite different kinetics for the DMF conversion (**Figure 5.5**): the H-USY (Si/Al=7.3) shows a reaction rate of 0.073 $mol.g^{-1}_{cat}.h^{-1}$, while the H-USY (Si/Al=325) shows a much slower rate (0.012 $mol.g^{-1}_{cat}.h^{-1}$). This difference is anticipated, since the zeolite H-USY-7.3 (2.13 strong BAS and 5.11 weak BAS per unit cell, giving a total BAS concentration of 0.63 mmol g^{-1}) has a higher concentration of BAS than the H-USY-325 (0.6 weak BAS per unit cell giving a BAS concentration of 0.052 mmol g^{-1}, see **Table 5.2**), which agrees with the previous observation of the BAS concentration dependent rate for this reaction.[40]

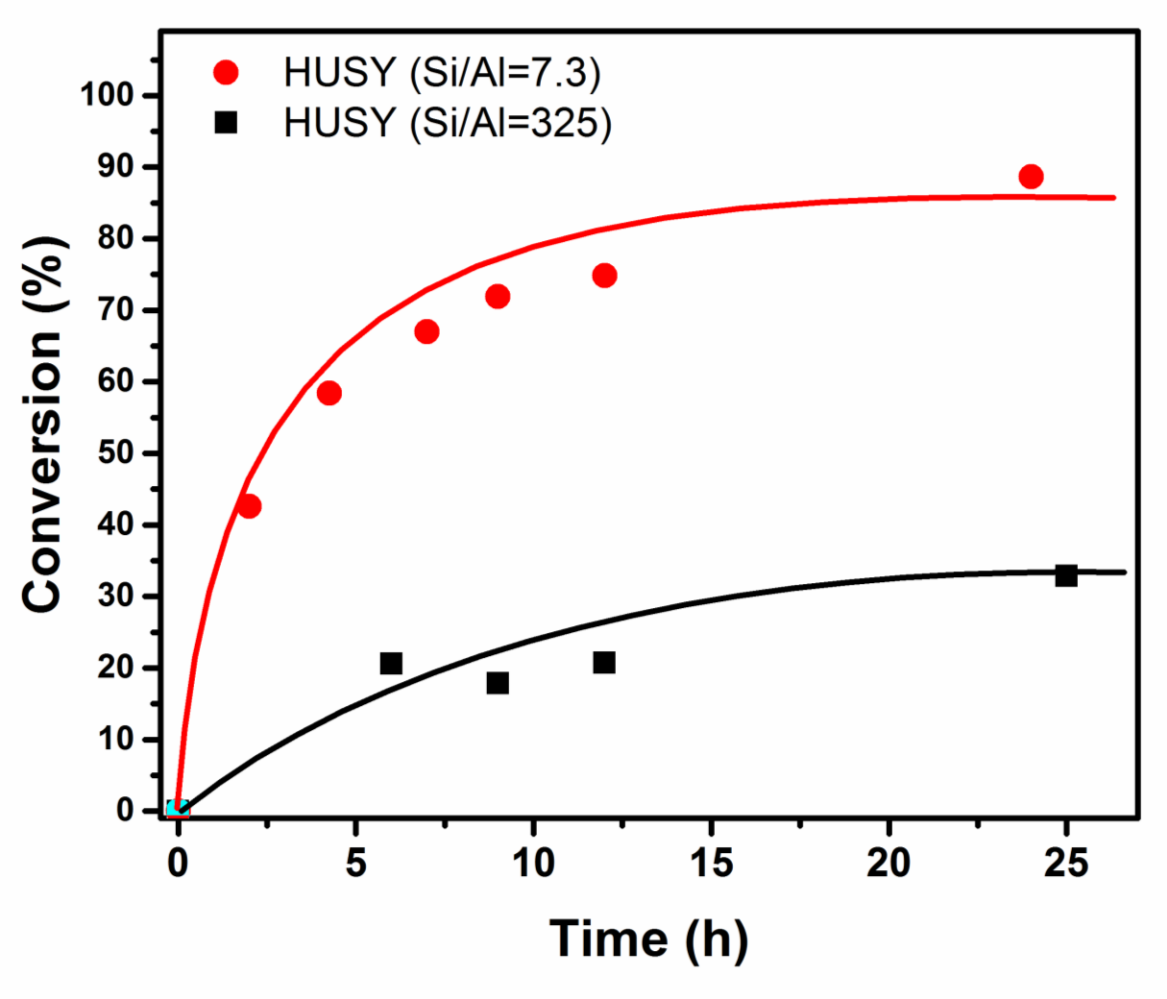


Figure 5.5 Kinetic data derived for 0.14 mole DMF transformation over 0.4 g catalyst with ethylene generated *in situ* from ethanol (0.14 mole) in 100 mL at 250 °C.

However, the product distributions are also drastically different: zeolite H-USY (Si/Al=7.3) shows a clear trend to promote aromatic products, while the H-USY (Si/Al=325) favors ketone formation (see later, **Figure 5.8**), mainly the 2,5-hexanedione (41.2%). The presence of a strong BAS in H-USY (Si/Al=7.3) associated with the encapsulated extra-framework Al^{3+} in sodalite units may thus facilitate protonation for the higher energetic C-O bond cleavages in the bicyclo activation to dehydrate the oxa-norbornene into xylene, accounting for higher aromatic selectivity. In order to ascertain

the major role(s) of the strong and weak BAS in the reaction catalysed by H-USY-7.3, a site blockage strategy was implemented. Two H-USY (Si/Al=7.3) samples were prepared by partial (blocking the strong BAS of the extra-framework Al^{3+} only - 0.3 Blocked/Total BAS) and total replacement (blocking all BAS protons – 1.0 Blocked/Total BAS) of the Brønsted acidic protons with K^{+}, referred herein as P-K-USY7.3 and T-K-USY7.3, respectively.

Table 5.2 Strong and weak Brønsted acid sites per unit cell, obtained by SXRD diffraction patterns and Rietveld refinement data after pyridine adsorption

Zeolite	Strong BAS	Weak BAS
H-USY-7.3	2.13	5.11
H-USY-325	-	0.60
P-K-USY7.3	-	5.11
T-K-USY7.3	-	Trace

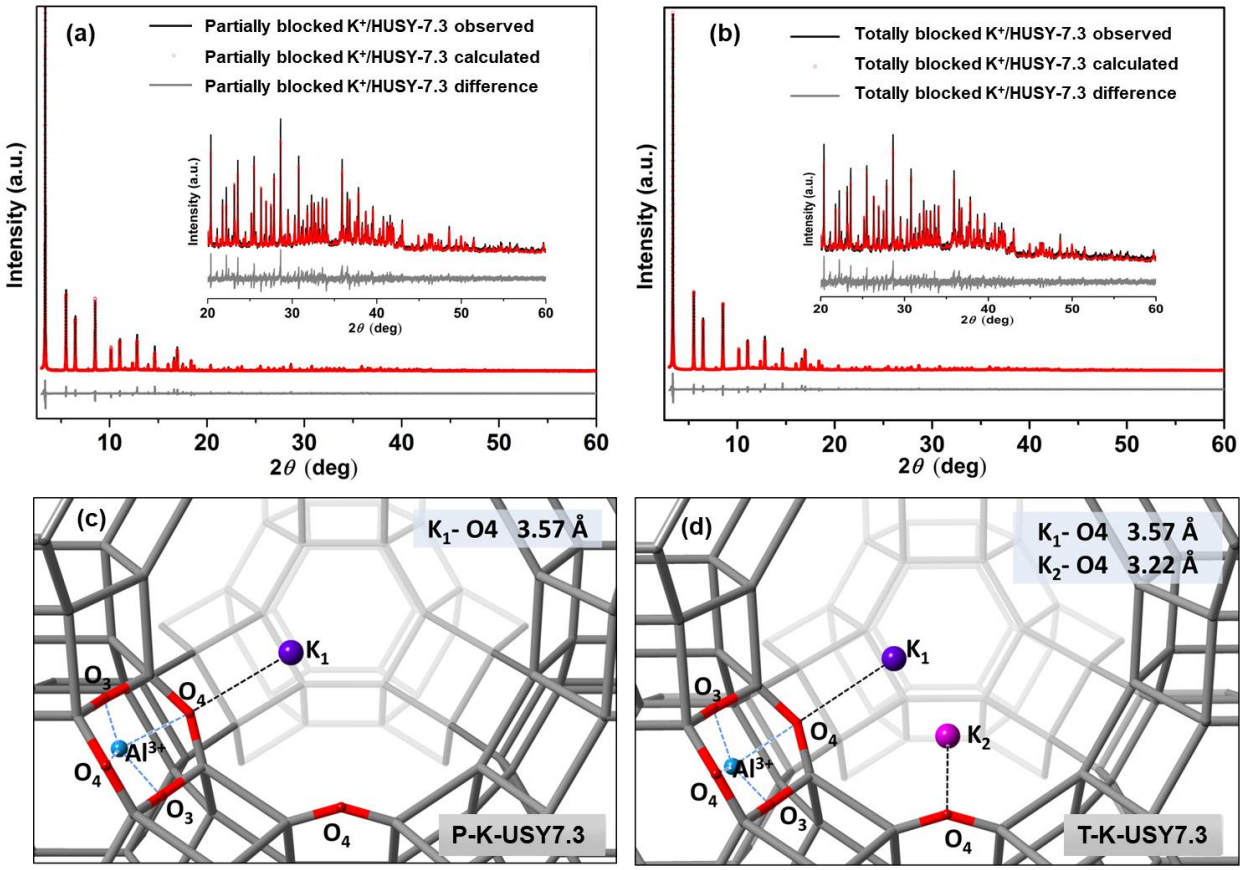


Figure 5.6 SXRD diffraction patterns and Rietveld refinement data of **a)** partially blocked H-USY-7.3 (P-K-USY7.3) and **b)** totally blocked H-USY-7.3 (T-K-USY7.3) after K^+ exchange. The zooms highlight the 20 – 60° 2θ region to illustrate the quality of the refinement. The structures of **c)** P-K-USY7.3 and **d)** T-K-USY7.3 with stick models without symmetrically appearing 4-CN extra-framework Al^{3+} and K^+ species. Grey represents the USY; Blue ball represents Al (4-CN extra-framework Al^{3+} species); Dark blue and purple represents K^+.

The crystallographic evidence (**Figure 5.6** and **Table 5.3**) confirms the ultra-specificity for strong BAS blockage by K^+ in the partial BAS replaced sample. The partially exchanged H-USY-7.3 shows a higher conversion (47.3%) and higher reaction rate (0.06 $mol.g^{-1}_{cat}.h^{-1}$) than that of H-USY-325 as it still contains a higher quantity of weak BAS (**Figure 5.7** and **Table 5.2**).

Table 5.3 Crystallographic data and details of the USY samples potassium loading

Samples	**P-K-USY7.3**	**T-K-USY7.3**
Crystal system	Cubic	Cubic
Space group	Fd-3m	Fd-3m
K+ per unit cell	0	0
2θ range refinement (o)	3 – 60	3 – 60
Detector	Multi-analyser crystals	
Number of parameters	43	47
Number of *hkls*	702	702
Refinement methods	Rietveld	Rietveld
a (Å)	24.27348(4)	24.26952(4)
V (Å3)	14301.978(68)	14294.984(74)
Rwp / Rp. / Rexp. (%)	9.631/7.098/3.201	8.053/5.056/3.056
Gof χ2	3.001	2.635
Wavelength (Å)	0.82601(2)	0.82602(1)
2θ Zero point (°)	0.01136(1)	0.01099(2)

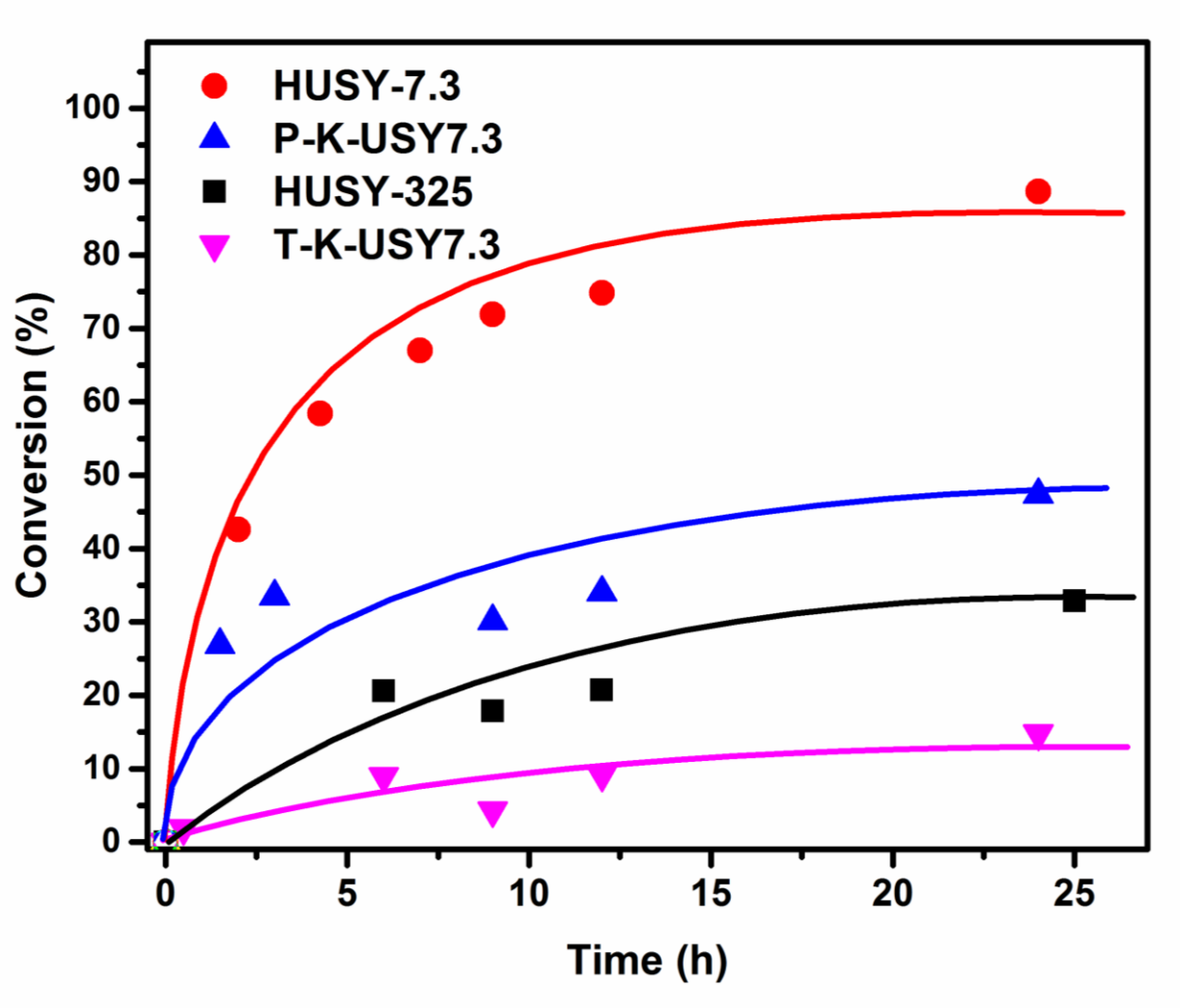


Figure 5.7 Kinetic data derived for 0.14 mole DMF transformation over 0.4 g catalyst with ethylene generated *in situ* from ethanol (0.14 mole) in 100 mL at 250 °C.

Interestingly, the product distribution for the reaction catalysed by P-K-USY7.3 is shifted to ketones (77.2%) since the breakage of two strong C-O bonds in the bridge oxa-norbornene intermediate cannot be overcome by the weak BAS which only favors hydrolysis reactions with lower activation energy (**Figure 5.8**). As expected, the sample with the total exchange of protons by K^+ shows a low activity, favouring formation of ketones.

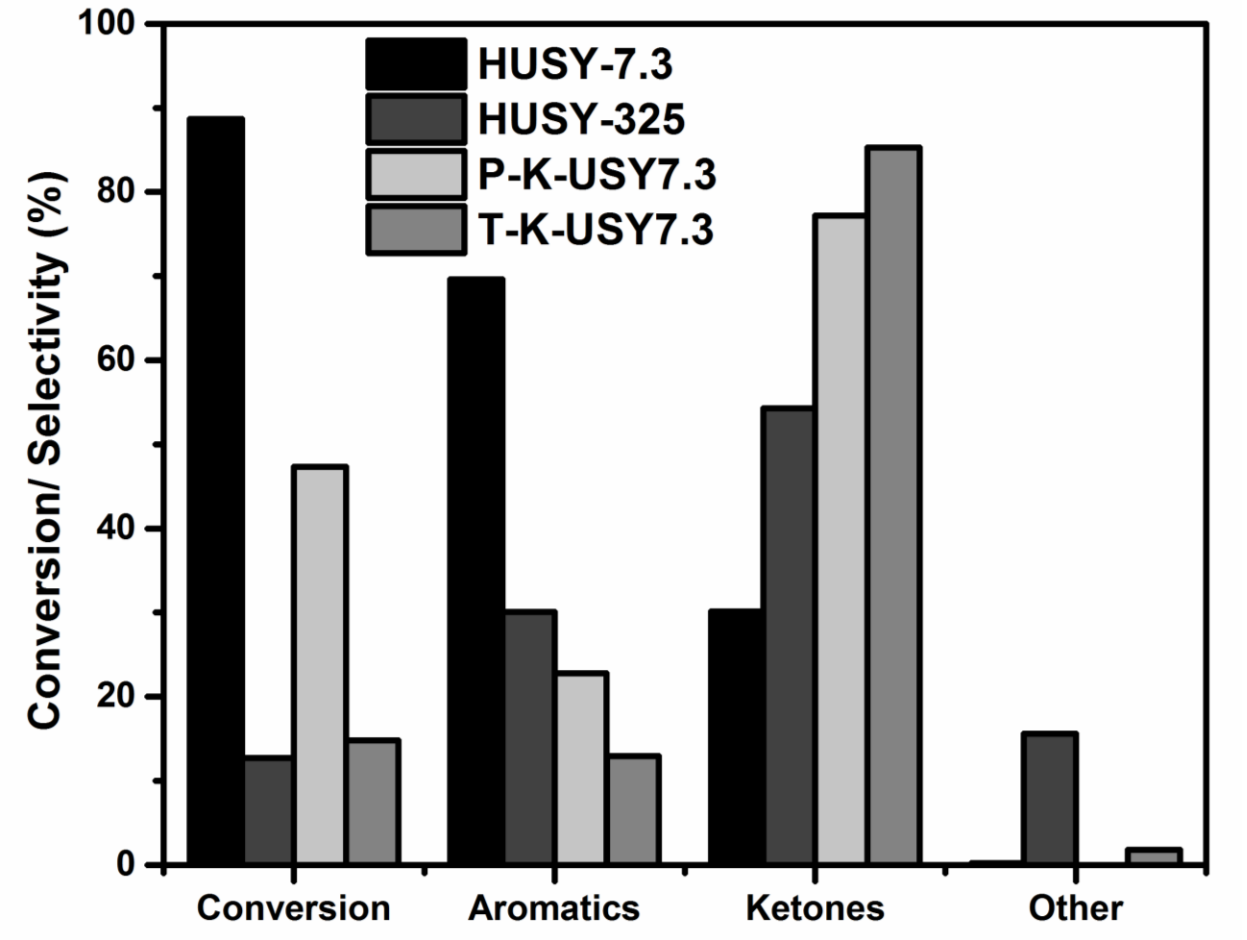


Figure 5.8 Conversion and selectivity for DMF transformation into aromatics catalysed by H-USY-7.3, H-USY-325, partially blocked H-USY-7.3 (P-K-USY7.3) and totally blocked H-USY-7.3 (T-K-USY7.3). Reaction conditions: 250 °C, molar ratio ethanol/DMF 1:1 and reaction time 24 h.

Using the strategy of partially/totally blockage of the BAS of different acid strengths with K^+, it was possible to correlate the product distribution for the ethanol/DMF reaction with the type/strength of the BAS which present on the zeolite catalyst.

5.5 Conclusions

In summary, the synchrotron X-ray diffraction techniques enabled us to study the crystal structure of zeolite at atomic resolution, even monitoring electron density changes from small molecule adsorption/desorption. By combining with the NMR and Rietveld

refinement, the structure of H-USY (Si/Al=325) and H-USY (Si/Al=7.3) has been illustrated without and with extra-framework Al^{3+} species in the sodalite cage, respectively. This extra-framework Al^{3+} species has been confirmed as an Al^{3+} ion with four coordinated framework Oxygen in H-USY-7.3. SXRD with pyridine adsorbed as a basic probe located the position of Brønsted acid sites at O4 in H-USY-325, while in H-USY-7.3 two acidic strengths of Brønsted acid sites at O4, which agreed well with the NMR observations. With the proximate extra-framework Al^{3+} (in the sodalite cage) present in H-USY-7.3, the Brønsted acid sites at O4 show an enhanced acidic strength in the form of a longer N_{Py2} - O4 distance of 3.21 Å compared to a N_{Py1} – O4 distance of 2.73 Å. The detailed information obtained by SXRD was utilised in a strategy of partially/totally blocking the BAS of different acid strengths with K^+. The corresponding product distributions clearly reflect the fact that the Diels-Alder cycloaddition is catalysed by strong acid sites, while hydrolysis of furan takes place over weak acid sites. Understanding how the BAS strength affects the product distribution for biomass valorisation reactions catalysed by zeolites can lead to catalysts with superior performance, an essential step towards making this technology economically viable.

5.6 References

1. Cheetham, A.K., G. Ferey, and T. Loiseau, *Open-framework inorganic materials.* **Angew. Chem. Int. Ed.**, 1999. 38: p. 3268-3292.

2. Hosseinpour, N., Y. Mortazavi, A. Bazyari, and A.A. Khodadadi, *Synergetic effects of Y-zeolite and amorphous silica-alumina as main FCC catalyst components on triisopropylbenzene cracking and coke formation.* **Fuel Process. Technol.**, 2009. 90: p. 171-179.

3. Corma, A., *Inorganic solid acids and their use in acid-catalyzed hydrocarbon reactions.* **Chemical Reviews**, 1995. 95: p. 559-614.

4. Costa, C., J.M. Lopes, F. Lemos, and F.R. Ribeiro, *Activity-acidity relationship in zeolite Y Part 1. Transformation of light olefins.* **J. Mol. Catal. A-Chem.**, 1999. 144: p. 207-220.

5. Ward, J.W., *The nature of active sites on zeolites: I. The decationated Y zeolite.* **Journal of Catalysis**, 1967. 9: p. 225-236.

6. Beyerlein, R., G. McVicker, L. Yacullo, and J. Ziemiak, *The influence of framework and nonframework aluminum on the acidity of high-silica, proton-exchanged FAU-framework zeolites.* **The Journal of Physical Chemistry**, 1988. 92: p. 1967-1970.

7. DeCanio, S.J., J.R. Sohn, P.O. Fritz, and J.H. Lunsford, *Acid catalysis by dealuminated zeolite-Y: I. Methanol dehydration and cumene dealkylation.* **Journal of Catalysis**, 1986. 101: p. 132-141.

8. Sohn, J.R., S.J. DeCanio, P.O. Fritz, and J.H. Lunsford, *Acid catalysis by dealuminated zeolite Y. 2. The roles of aluminum.* **The Journal of Physical Chemistry**, 1986. 90: p. 4847-4851.

9. Sanz, J., V. Fornés, and A. Corma, *Extraframework aluminium in steam-and SiCl 4-dealuminated Y zeolite. A 27 Al and 29 Si nuclear magnetic resonance study.* **Journal of the Chemical Society, Faraday Transactions 1: Physical Chemistry in Condensed Phases**, 1988. 84: p. 3113-3119.

10. Corma, A., V. Fornes, and F. Rey, *Extraction of extra-framework aluminium in ultrastable Y zeolites by (NH4) 2SiF6 treatments: I. physicochemical characterization.* **Applied catalysis**, 1990. 59: p. 267-274.

11. Mirodatos, C. and D. Barthomeuf, *Superacid Sites In Zeolites.* **J. Chem. Soc.-Chem. Commun.**, 1981: p. 39-40.

12. Agostini, G., C. Lamberti, L. Palin, M. Milanesio, et al., *In Situ XAS and XRPD Parametric Rietveld Refinement To Understand Dealumination of Y Zeolite Catalyst.* **J. Am. Chem. Soc.**, 2010. 132: p. 667-678.

13. Li, S.H., A.M. Zheng, Y.C. Su, H.L. Zhang, et al., *Bronsted/Lewis acid synergy in dealuminated HY zeolite: A combined solid-state NMR and theoretical calculation study.* **J. Am. Chem. Soc.**, 2007. 129: p. 11161-11171.

14. Kuehne, M.A., H.H. Kung, and J.T. Miller, *Effect of steam dealumination on H-Y acidity and 2-methylpentane cracking activity.* **J. Catal.**, 1997. 171: p. 293-304.

15. Remy, M.J., D. Stanica, G. Poncelet, E.J.P. Feijen, et al., *Dealuminated H-Y zeolites: Relation between physicochemical properties and catalytic activity in heptane and decane isomerization.* **J. Phys. Chem.**, 1996. 100: p. 12440-12447.

16. Teixeira, I.F., B.T.W. Lo, P. Kostetskyy, M. Stamatakis, et al., *From Biomass-Derived Furans to Aromatics with Ethanol over Zeolite.* **Angew. Chem. Int. Ed.**, 2016. 55: p. 13061-13066.

17. Williams, C.L., C.-C. Chang, P. Do, N. Nikbin, et al., *Cycloaddition of Biomass-Derived Furans for Catalytic Production of Renewable p-Xylene.* **ACS Catalysis**, 2012. 2: p. 935-939.

18. Jae, J., G.A. Tompsett, A.J. Foster, K.D. Hammond, et al., *Investigation into the shape selectivity of zeolite catalysts for biomass conversion.* **J. Catal.**, 2011. 279: p. 257-268.

19. Williams, C.L., *Production of Sustainable Aromatics from Biorenewable Furans*, in *Department of Chemical Engineering*. 2014, University of Massachusetts: Amherst.

20. Williams, C.L., K.P. Vinter, C.-C. Chang, R. Xiong, et al., *Kinetic regimes in the tandem reactions of H-BEA catalyzed formation of p-xylene from dimethylfuran.* **Catalysis Science & Technology**, 2016. 6: p. 178-187.

21. Cheng, Y.-T. and G.W. Huber, *Production of targeted aromatics by using Diels–Alder classes of reactions with furans and olefins over ZSM-5.* **Green Chemistry**, 2012. 14: p. 3114-3114.

22. Chang, C.-C., H. Je Cho, J. Yu, R.J. Gorte, et al., *Lewis acid zeolites for tandem Diels-Alder cycloaddition and dehydration of biomass-derived dimethylfuran and ethylene to renewable p-xylene.* **Green Chemistry**, 2016. 18: p. 1368-1376.

23. Wang, D., C.M. Osmundsen, E. Taarning, and J.A. Dumesic, *Selective production of aromatics from alkylfurans over solid acid catalysts.* **ChemCatChem**, 2013. 5: p. 2044-2050.

24. Chang, C.-C., S.K. Green, C.L. Williams, P.J. Dauenhauer, et al., *Ultra-selective cycloaddition of dimethylfuran for renewable p-xylene with H-BEA.* **Green Chemistry**, 2014. 16: p. 585-588.

25. Nikbin, N., S. Feng, S. Caratzoulas, and D.G. Vlachos, *p-Xylene formation by dehydrative aromatization of a Diels–Alder product in Lewis and Brønsted acidic zeolites.* **The Journal of Physical Chemistry C**, 2014. 118: p. 24415-24424.

26. Patet, R.E., N. Nikbin, C.L. Williams, S.K. Green, et al., *Kinetic regime change in the tandem dehydrative aromatization of furan Diels–Alder products.* **ACS Catalysis**, 2015. 5: p. 2367-2375.

27. Green, S.K., R.E. Patet, N. Nikbin, C.L. Williams, et al., *Diels–Alder cycloaddition of 2-methylfuran and ethylene for renewable toluene.* **Applied Catalysis B: Environmental**, 2016. 180: p. 487-496.

28. Lo, B.T.W., L. Ye, J. Qu, J. Sun, et al., *Elucidation of adsorbate structures and interactions on Brønsted acid sites in H-ZSM-5 by synchrotron X-ray powder diffraction.* **Angew. Chem. Int. Ed.**, 2016. 55: p. 1-5.

29. Yang, S.H., J. Sun, A.J. Ramirez-Cuesta, S.K. Callear, et al., *Selectivity and direct visualization of carbon dioxide and sulfur dioxide in a decorated porous host.* **Nature Chem.**, 2012. 4: p. 887-894.

30. Ye, L., B.T.W. Lo, J. Qu, I. Wilkinson, et al., *Probing atomic positions of adsorbed ammonia molecules in zeolite.* **Chem. Commun.**, 2016. 52: p. 3422-3425.

31. Li, S.H., A.M. Zheng, Y.C. Su, H.J. Fang, et al., *Extra-framework aluminium species in hydrated faujasite zeolite as investigated by two-dimensional solid-state NMR spectroscopy and theoretical calculations.* **Phys. Chem. Chem. Phys.**, 2010. 12: p. 3895-3903.

32. Klinowski, J., *Solid-state NMR studies of molecular sieve catalysts.* **Chemical reviews**, 1991. 91: p. 1459-1479.

33. Rakiewicz, E.F., A.W. Peters, F. Wormsbecher, K.J. Sutovich, et al., *Characterization of acid sites in zeolitic and other inorganic systems using solid-state P-31 NMR of the probe molecule trimethylphosphine oxide.* **J. Phys. Chem. B**, 1998. 102: p. 2890-2896.

34. Freude, D., M. Hunger, H. Pfeifer, and W. Schwieger, *1H MAS NMR studies on the acidity of zeolites.* **Chemical physics letters**, 1986. 128: p. 62-66.

35. Bhering, D.L., A. Ramirez-Solis, and C.J.A. Mota, *A density functional theory based approach to extraframework aluminum species in zeolites.* **Journal of Physical Chemistry B**, 2003. 107: p. 4342-4347.

36. Colligan, M., P.M. Forster, A.K. Cheetham, Y. Lee, et al., *Synchrotron X-ray powder diffraction and computational investigation of purely siliceous zeolite Y under pressure.* **J. Am. Chem. Soc.**, 2004. 126: p. 12015-12022.

37. Raugei, S. and M.L. Klein, *Hydrocarbon reactivity in the superacid SbF5/HF: an ab initio molecular dynamics study.* **J. Phys. Chem. B**, 2002. 106: p. 11596-11605.

38. Berenblyum, A.S., E.A. Katsman, and Y.Z. Karasev, *The nature of catalytic activity and deactivation of chloroaluminate ionic liquid.* **Appl. Catal. A- Gen.**, 2006. 315: p. 128-134.

39. Berenblyum, A.S., E.A. Katsman, and Y.Z. Karasev, *The nature of catalytic activity and deactivation of chloroaluminate ionic liquid.* **Applied Catalysis A: General**, 2006. 315: p. 128-134.

40. Patet, R.E., N. Nikbin, C.L. Williams, S.K. Green, et al., *Kinetic Regime Change in the Tandem Dehydrative Aromatization of Furan Diels–Alder Products.* **ACS Catal.**, 2015. 5: p. 2367-2375.

Chapter 6

A New Strategy to Convert Biomass-Derived Furan into Aromatics

Chapter 6: A New Strategy to Convert Biomass-Derived Furan into Aromatics

Overview **156**

6.1 Introduction **157**

6.2 Catalytic Performance **159**

6.3 Kinetic Studies **166**

6.4 SXRD Experiments **169**

6.5 FTIR Experiments **172**

6.6 Mechanism **174**

6.7 Conclusions **175**

6.8 References **176**

Overview

This chapter reports a new strategy to convert biomass-derived furan into aromatics with high selectivity to aromatics, while reducing the formation of the side product benzofuran, over zeolite catalysts. It is acknowledged that the conversion of furan into aromatics under mild conditions is quite challenging, due to the coupling reaction between the two furan molecules, forming benzofurans. Herein ethanol was used as a source of dienophile for the Diels-Alder (DA) cycloaddition in a comparable way to the results presented in the previous chapters. The use of the reaction presented in **Chapter 4** to furan is shown to be quite promising: the selectivity to aromatics is increased significantly and the selectivity to the side product benzofuran is considerably reduced. Further investigations by detailed kinetic experiments, SXRD and FTIR experiments showed that the key step to prevent the benzofuran formation and favour the aromatic products is the alkylation of the furan molecule by an ethyl formed from the ethanol dehydration. This step occurs before the DA reaction and has a double effect to promote the aromatic products: 1) the alkylated furans (dienophile) undergo DA cycloaddition more readily, due its higher energy HOMO orbital; 2) the substituent alkyl groups on the furan ring create greater steric hindrance, thus circumventing the direct coupling reaction between two furan molecules to form benzofuran.

In this chapter I was responsible for all the catalytic tests presented in this chapter, including kinetic evaluations and experiments related to mechanistic understanding. I also helped to plan and prepare the samples used in SXRD experiments and assisted in interpretation of the data. The data refinement was done exclusively by Dr. Benedict T. W. Lo

6.1 Introduction

The conversion of lignocellulosic biomass to renewable fuels and chemicals has attracted significant attention as a key technology to enable the replacement of petroleum.[1, 2] Lignocellulosic biomass is the most promising renewable carbon energy source, as it is widely available around the world at a relatively low cost.[3] Although it is the most abundant plant material resource, its conversion into chemical faces a range of technological and economic challenges.[4] In order to overcome these challenges, several different processes to obtain chemicals and biofuels from biomass are currently under development.[5, 6] The most promising is the multistep strategy using platform molecules as intermediates.[7] The most important platform molecules that can be obtained from biomass in good yields are biomass-derived furans, such as furfural, 5-hydroxymethylfurfural (HMF), 2-methylfuran (MF), furan and 2,5-dimethylfuran (DMF).[8]

Furan and 2-methyfuran can be derived from the further conversion of furfural. Furan is obtained by furfural decarbonylation (97% yield),[9, 10] while 2-methylfuran by the direct hydrogenolysis of the furfural (50% yield)[10] or by its hydrogenation followed by dehydration of furfuryl alcohol (99% overall yield).[3] Many recent studies have reported the Diels-Alder [4+2]-cycloaddition reaction between these biomass-derived furans (DMF, MF and furan) and ethylene followed by dehydration producing aromatics, such as xylene, toluene and benzene.[11-16] Although relatively high yields of xylene (90%) and toluene (50%) can be achieved from the conversions of DMF and MF respectively, the conversion of furan into benzene is quite challenging. This is primarily due to the coupling reaction between the two furan molecules, forming benzofurans (see **Figure 6.1**). Chang *et al.* reported only 5% of selectivity to benzene at 250 °C over Zr-BEA zeolite catalyst [14] and

35% over BEA zeolite under extremely high pressure of ethylene (62 bar).[17] Cheng *et al.* also showed that under 600 °C, the major products of the furan conversion are benzofuran and coke (60% carbon selectivity); the benzofuran intermediates can be further converted into aromatics at higher temperatures (>500 °C).[18] However, it is clear that the benzofuran is an inevitable product in the furan conversion into aromatics.

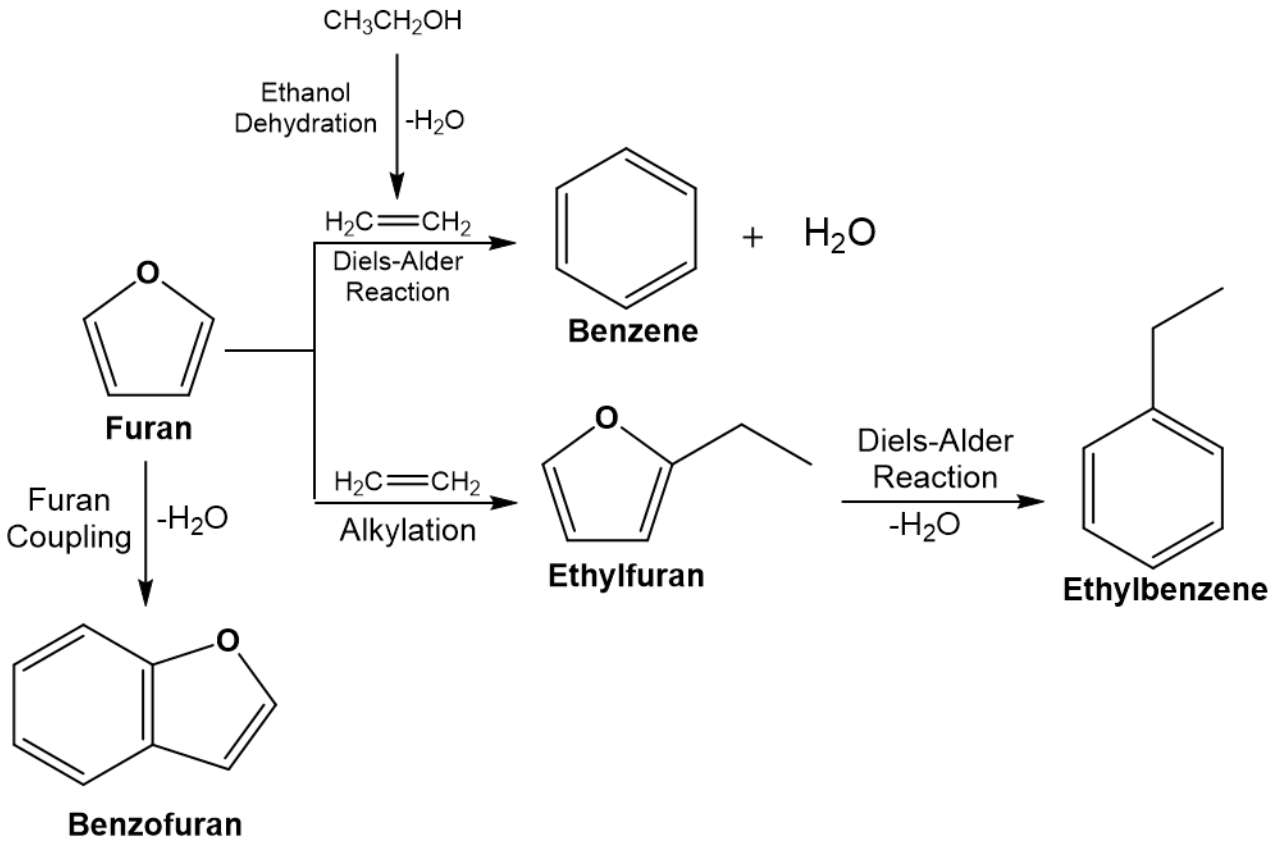


Figure 6.1 Furan conversion into aromatics and the side product benzofuran.

Herein it was reported the conversion of biomass-derived furan into aromatics with high selectivity to aromatics, while attenuating the formation of the side product benzofuran, over zeolite catalysts. The conversion is based on the DA [4+2]-cycloaddition with *in situ* produced ethylene from ethanol dehydration (ED) in a one-pot solvent-free reaction.

6.2 Catalytic Performance

Firstly, the catalytic performance of furan with ethanol or ethylene over H-USY zeolite (Si/Al=325) was compared. Under our optimized reaction conditions, the conversion of furan with ethylene produces benzofuran as the major product, with 63% of selectivity (see **Figure 6.2**), followed by benzene 35% and only 2% of alkylated aromatics. When the same reaction is performed by using ethanol at a high molar ratio (instead of ethylene), the product selectivity is completely changed. The selectivity for benzofuran and alkylated benzofurans is reduced to only 24% and the overall selectivity to aromatics is improved to 67%, with 45% ethylbenzene, 22% other alkylated aromatics mainly diethylbenzene (8%). The majority of the remaining products are essentially ethylfuran (12%) (**Figure 6.3**).

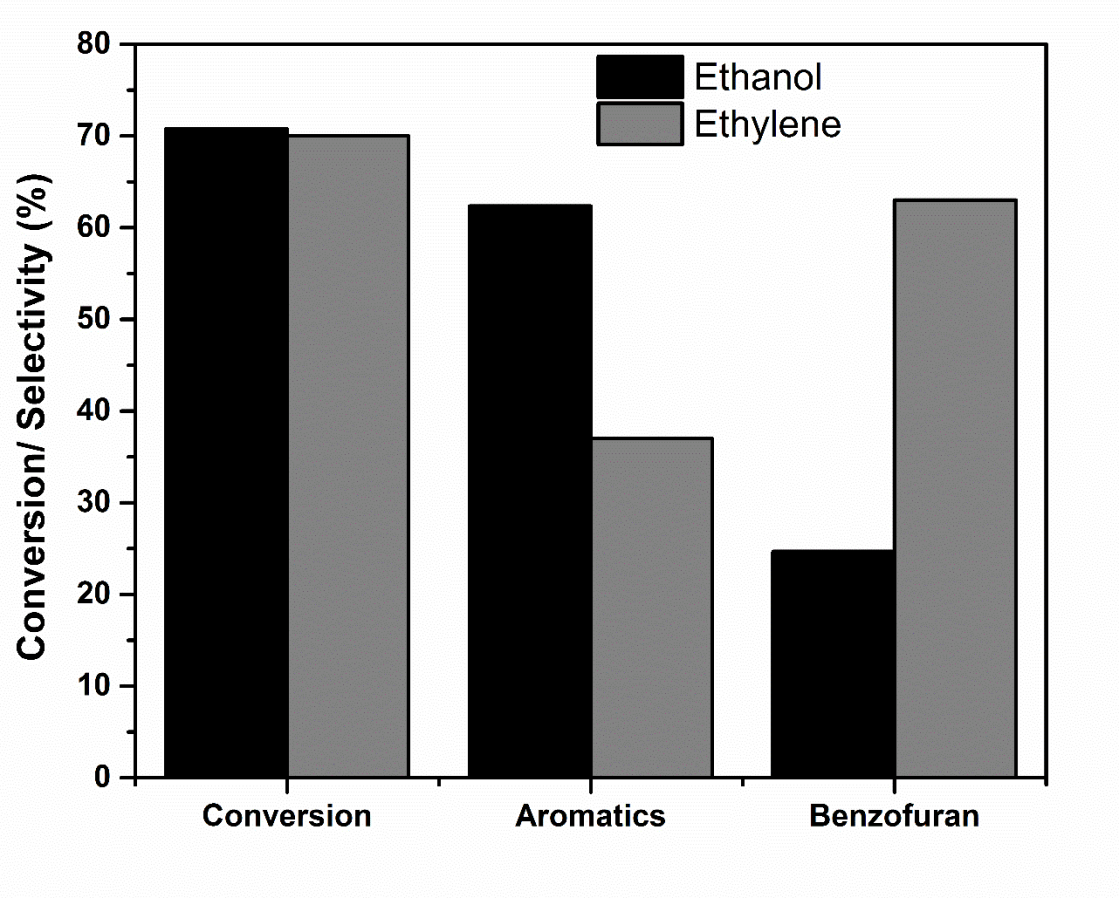


Figure 6.2 Conversion and selectivity for furan conversion into aromatics catalysed by zeolite H-USY (Si/Al=325) with ethylene or ethanol, under optimized reaction conditions. Temperature 300 °C, reaction time 8 h, and (black) molar ratio of ethanol to furan of 10:1, (grey) 40 bar of ethylene.

The initial rate of reaction also increases from 0.12 to 0.23 mol g_{cat}^{-1} h^{-1} by switching ethylene to ethanol, but the conversion after prolonged periods (e.g. 8 h) is not very different (ca. 70% for both ethylene and ethanol). Despite the broad distribution of aromatic products, the main product ethylbenzene is valuable for the petrochemical industry. Ethylbenzene is generally used to produce styrene, whereas the other alkylated aromatics can be further transalkylated in order to improve the quality of the aromatic products.[19, 20]

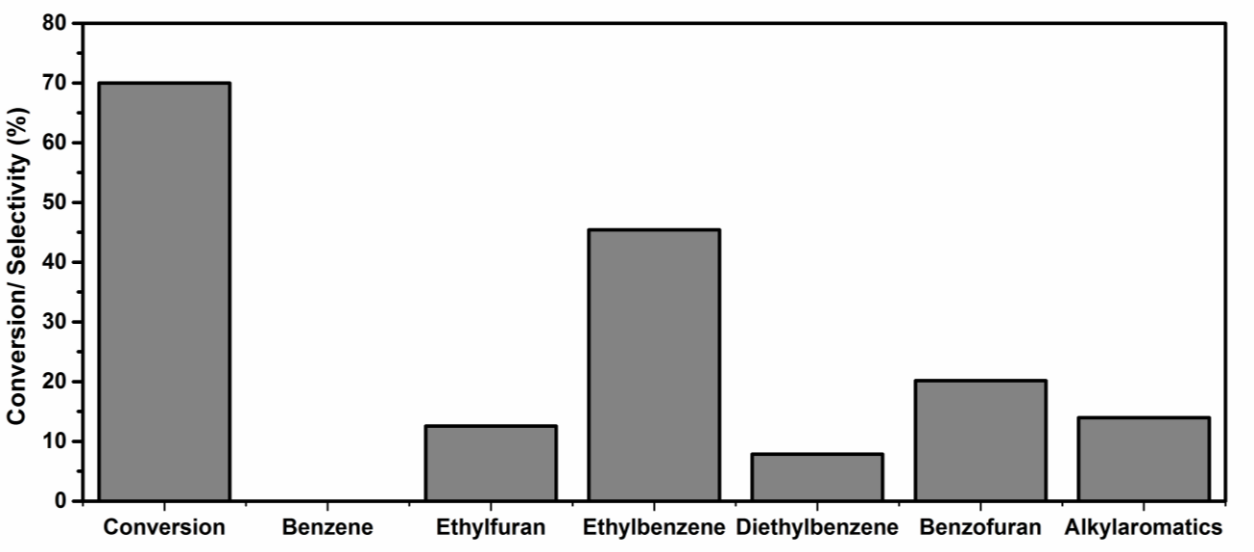


Figure 6.3 Conversion and selectivity for furan transformation into aromatics catalysed by 0.4g of zeolite H-USY (Si/Al=325). Reaction conditions: temperature 300 °C, 10:1 Ethanol/Furan molar ratio and reaction time 8 h in 100 mL reactor.

Clearly, the reaction performed with ethanol favors alkylation, which has already been discussed in previous chapters.[21] This may be critical to avoid the formation of benzofuran, as alkylated furans (dienophile) undergo DA cycloaddition more readily, due to its higher energy HOMO orbital. Furthermore, the substituent alkyl groups on the furan ring create greater steric hindrance, thus circumventing the direct coupling reaction between two furan molecules to form benzofuran.

The catalytic performance appears to be dependent on the framework type and the acidity of the zeolite catalysts (see **Figure 6.4**). The zeolites with larger pores, i.e. USY and BEA, have more superior aromatic selectivity. Although all the zeolites show lower selectivity to benzofuran than that reported in the literature for the reaction performed with ethylene,[15, 17] HZSM-5 zeolite still produces benzofuran as the major product. It is well-reported in literature that the HZSM-5 zeolite has poor activity to convert

biomass-derived furans into aromatics,[11] this might be related with its smaller pore structure. As the DA cycloaddition reaction requires an extremely rigid HOMO-LUMO overlap, HZSM-5 with smaller pore size may not be able to accommodate a suitable transition geometry for orbitals overlap between the diene and the dienophile.

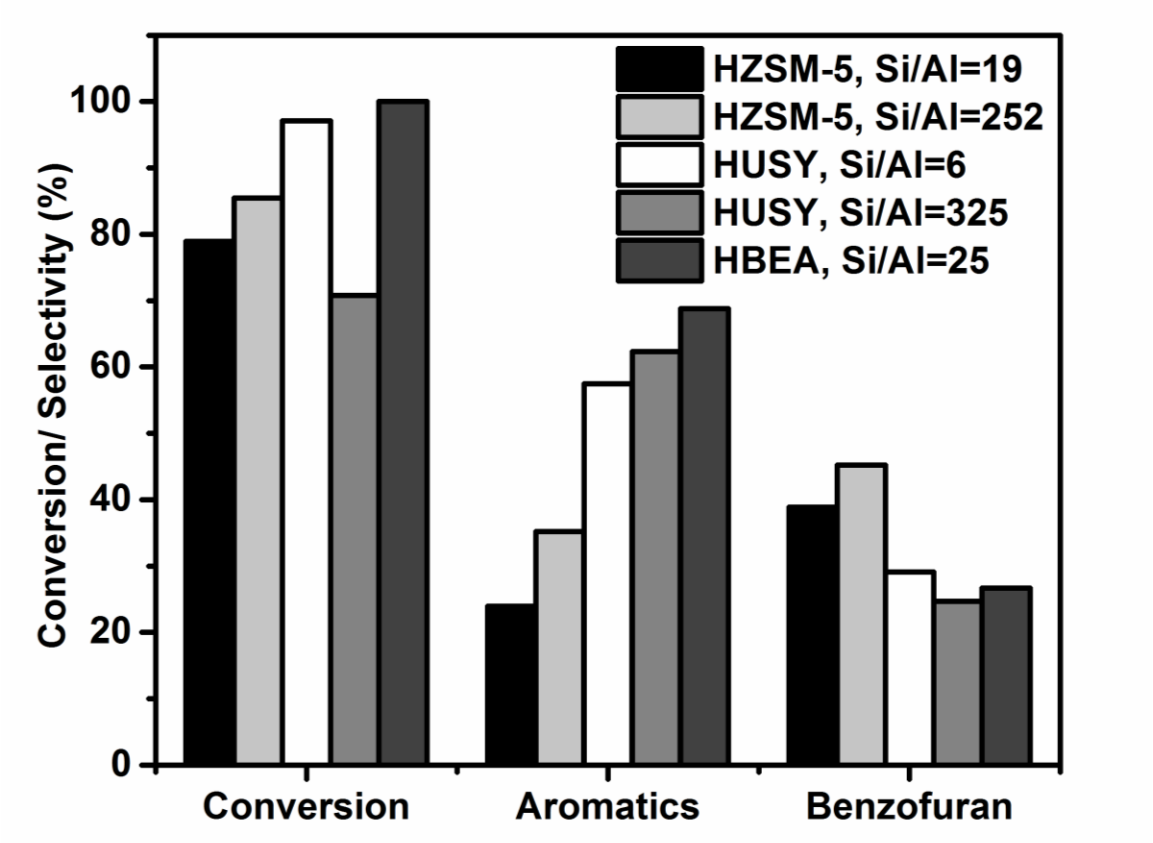


Figure 6.4 Conversion and selectivity for furan transformation into aromatics catalysed by different zeolites. Reaction conditions: temperature 300 °C, 0.4 g of catalyst, molar ratio Ethanol/Furan of 10:1 and reaction time 8 h.

It was also investigated the effect of the acid site concentration in the zeolite catalysts. The acid site concentration only marginally hinders the product distribution. However, more acidic zeolites favors higher furan conversion, with 100% conversion catalysed over HBEA (Si/Al=25) and 97% conversion catalysed over H-USY (Si/Al=6).

This matches with our initial expectation, as the series of reactions can all be catalysed by the Brønsted acid sites in zeolites.

Table 6.1 Acid site concentrations and surface area of the zeolite samples

Catalyst	Si/Al ratio[a]	Brønsted acid sites[b] (mmol g^{-1})	Total acid sites[b] (mmol g^{-1})	Surface Area[c] (m^2 g^{-1})	H-TOF[d] (10^2 h^{-1})
HZSM-5	19	0.760	0.789	349	1.32
HZSM-5	252	-	0.002	329	-
H-USY	6	0.55	-	650	11.5
H-USY	325	0.052	-	620	45.7
HBEA	25	0.26	-	575	16.28

[a] from ICP-AES
[b] Obtained using ammonia-TPD.
[c] from BET over $0.05 < P/P_0 < 0.3$.
[d] rate of mol. DMF to mol. products per Brønsted acid site per hour.

The conversion of furan into aromatics over H-USY (Si/Al=325) was optimized in terms of the Ethanol/Furan ratio (see **Figure 6.5**). Briefly, the higher the Ethanol/Furan ratio, the higher the conversion and the selectivity to aromatics. However, the aromatic product distribution is significantly changed, producing a larger amount of di/tri-ethylbenzene (**Figure 6.6**).

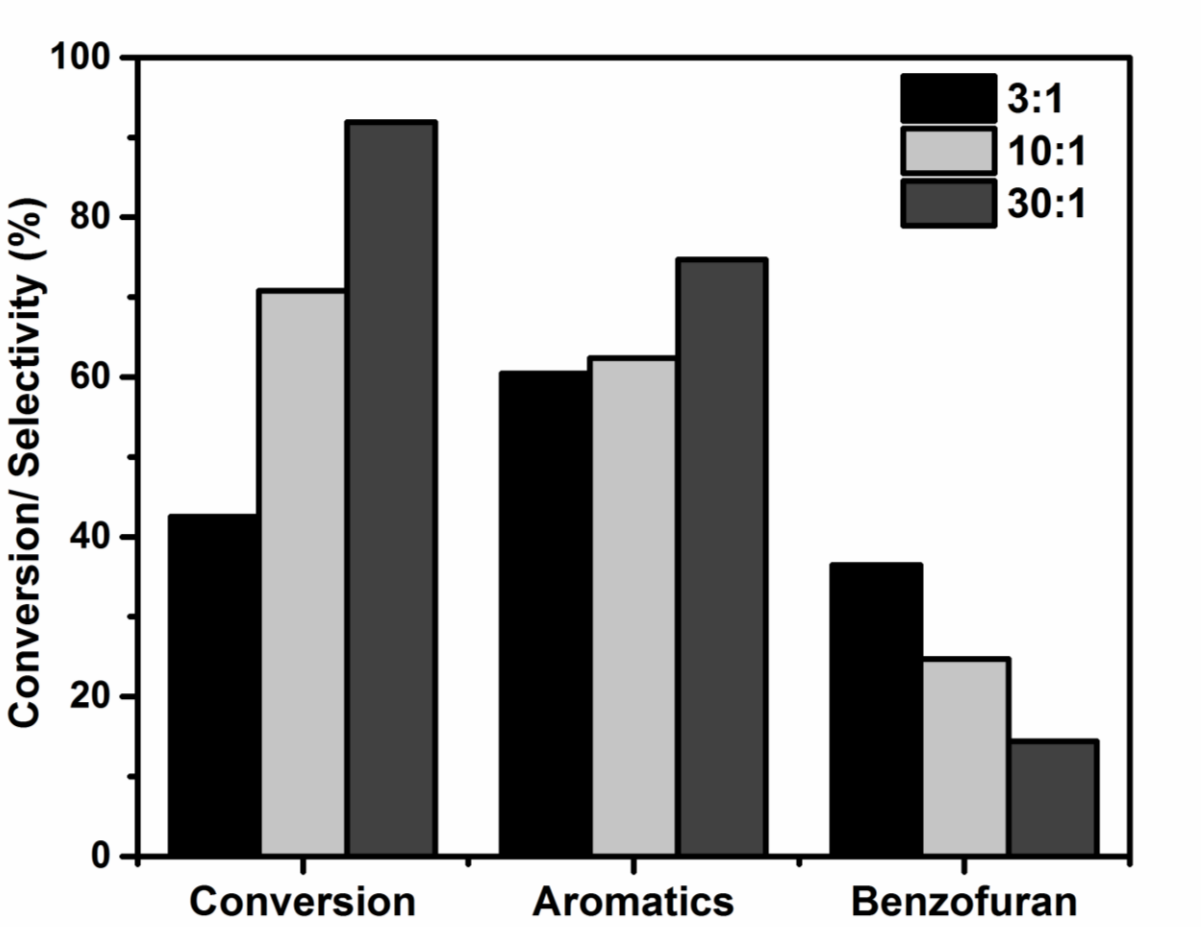


Figure 6.5 Conversion and selectivity for furan transformation into aromatics catalysed by 0.4 g of H-USY zeolite (Si/Al=325) with different molar ratios of ethanol to furan. Reaction conditions: temperature 300 °C and reaction time 8 h in a 100 mL reactor.

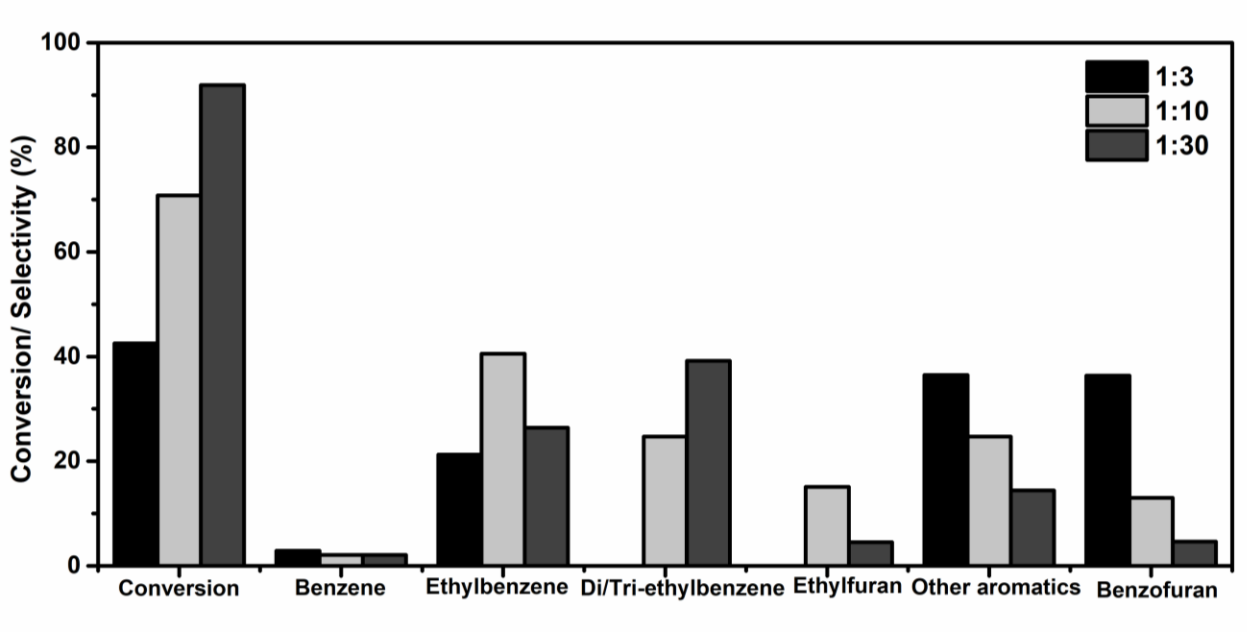


Figure 6.6 Conversion and selectivity for furan transformation into aromatics catalysed by 0.4 g of zeolite H-USY (Si/Al=325) with different molar ratios Ethanol/Furan. Reaction conditions: temperature 300 °C and reaction time 8 h in 100 mL reactor.

Interestingly, higher molar ratios of Ethanol/Furan disfavor the benzofuran formation (undesirable product), reducing it from 36% to only 14% for the Ethanol/Furan ratio of 3:1 to 30:1; additionally, it increases the corresponding furan conversion from 42% to 92%. In short, a higher Ethanol/Furan ratio increases significantly the conversion of furan and the selectivity towards the desired aromatic products. Therefore, it was further investigated the initial production rate for ethylfuran and the aromatic products (see **Figure 6.7**) to gain a better understanding on this increment on the aromatics selectivity when more ethanol is used.

6.3 Kinetic Studies

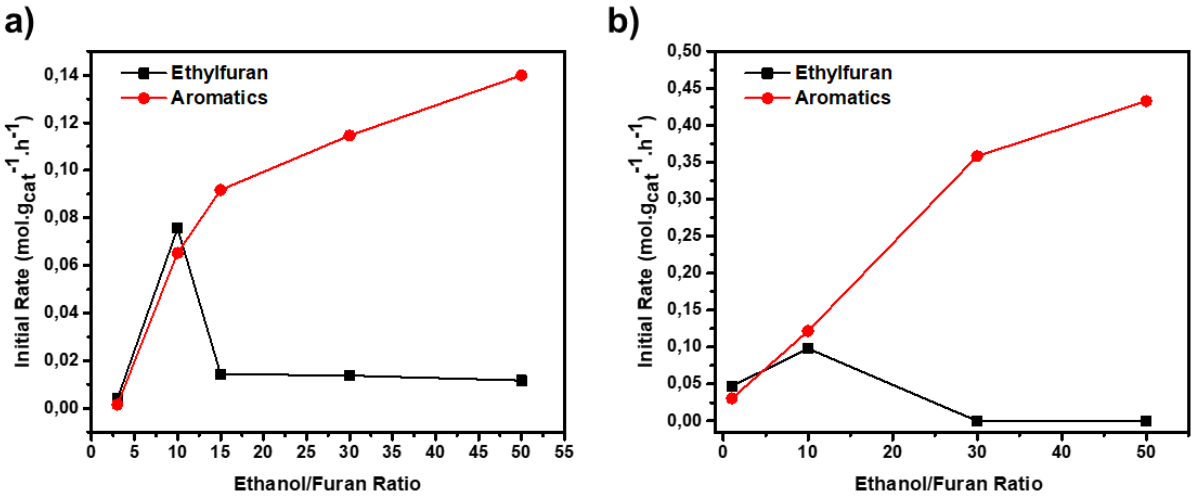


Figure 6.7 a) Initial production rate of ethylfuran and aromatics catalysed by 0.4 g of zeolite H-USY (Si/Al=325) with different molar ratios Ethanol/Furan at 300 °C in a 100 mL reactor; **b)** Reaction initial rate for the products ethylfuran and aromatics catalysed by 0.4 g of zeolite H-USY (Si/Al=6) with different molar ratios Ethanol/Furan at 300 °C in 100 mL reactor.

The initial production rate of aromatics increases remarkably with the concentration of ethanol. On the other hand, the initial production rate of ethylfuran presents a similar behaviour for lower Ethanol/Furan molar ratios (3:1 and 10:1) and a decrease at a molar ratio of 30:1. It seems the initial production rate of aromatics products in lower molar ratios of Ethanol/Furan is limited by a low local concentration of ethanol inside the zeolite pores.

The [4+2] DA cycloaddition between furan and ethylene is particularly challenging because of a large energy gap between the HOMO of the furan (diene) and the LUMO of the ethylene (dienophile). However, the alkylation of furan (to ethylfuran) notably increases the energy of the HOMO by 77.2 kJ mol^{-1},[22] which greatly narrows the HOMO-LUMO energy gap. This means that the reaction rate for the DA cycloaddition with

ethylfuran and ethylene can be much faster than the direct DA reaction between furan and ethylene. After the DA step, the reaction proceeds *via* the oxabicyclic intermediate, which is further dehydrated into ethylbenzene (see **Figure 6.1**). As a result, it was observed higher selectivity towards ethylbenzene than benzene in a typical experiment. Both the initial production rate of aromatics and the increase in HOMO energy level suggest that the reaction first occurs through the furan alkylation by ethyl carbocations (from the acid catalysed dehydration of ethanol). Then the ethylfuran reacts with *in situ* formed ethylene *via* the Diels-Alder cycloaddition.

As the local concentration of ethanol limits the reaction for molar ratios of Ethanol/Furan lower than 10:1 its rate increases with the increment on Ethanol/Furan molar ratio, under very high concentrations of ethanol (molar ratio of 30:1). It no longer limits the formation of aromatic products, consequently the aromatics initial rate increases significantly surpassing the ethylfuran rate (**Figure 6.7a**). In other words, the high concentration of ethanol molecules inside the zeolites pores promotes the rapid DA cycloaddition of the ethylfuran. A similar trend was also observed for the H-USY zeolite (Si/Al=6), the initial rates, however, were an order of magnitude higher. This is likely due to the significant difference in the concentration of Brønsted acid sites (see **Figure 6.7b**), cf. 0.55 mmol g^{-1} for the H-USY (Si/Al=6) and 0.10 mmol g^{-1} for the H-USY (Si/Al=325).

Therefore H-USY (Si/Al=6) was chosen for the kinetic studies using the Arrhenius plot (see **Figure 6.8**), as it showed the highest initial rate (0.64 mol g_{cat}^{-1} h^{-1}) for the conversion of furan.

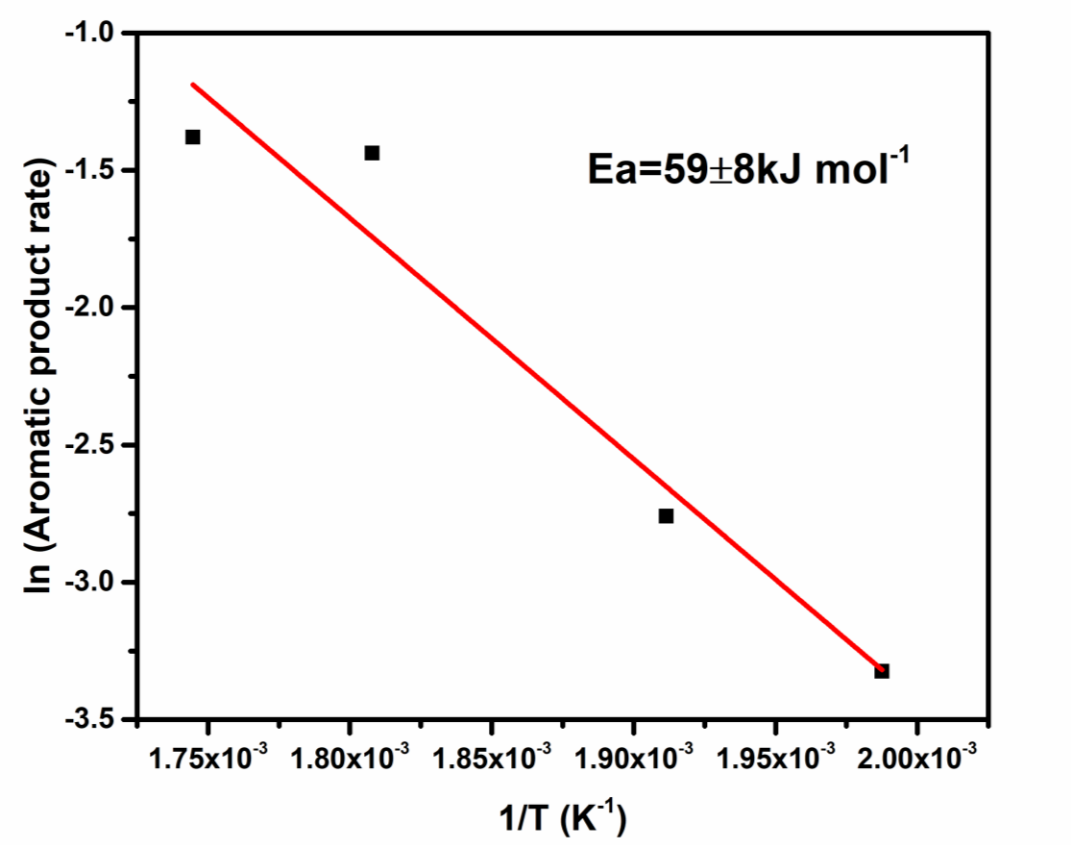


Figure 6.8 Arrhenius plot for the conversion of furan into aromatics over 0.4 g of H-USY (Si/Al=6) and the estimated activation energy.

The apparent activation energy was estimated to be 59±8 kJ mol^{-1} from the Arrhenius plot, this value was remarkably lower than the value reported by Dinadayalane *et al.* (232.6 kJ mol^{-1}, using ethylene as the reaction substrate).[23] This can be primarily due to several reasons: (i) First, the DA reaction is significantly affected by the nature of the diene, as alkylated dienes have lower energies and in general require lower activation energies. (ii) Secondly, as reported in **Chapter 4** for the DMF (dimethylfuran) reaction with ethanol (instead of ethylene), the reaction can take place *via* an alternative route which has lowers activation energies.[24] It is believed the locations and interactions of the reactants with respect to the Brønsted acid sites are fundamentally affecting the furan

conversion reaction. The reaction fitted the first order kinetics with a reaction constant rate of 0.053 h^{-1} (**Figure 6.9**).

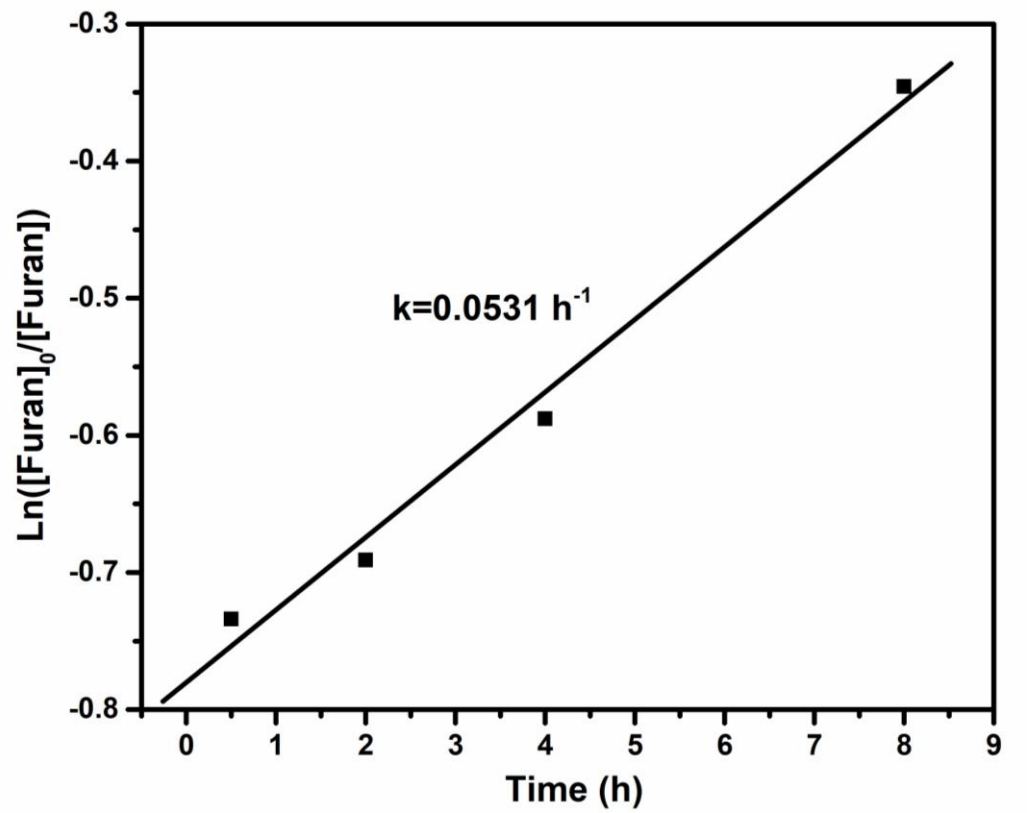


Figure 6.9 First order fitting and constant rate values for furan transformation into aromatics catalysed by zeolite H-USY (Si/Al=325) with ethylene generated *in situ* from ethanol. Reaction conditions: temperature 300 °C, 10:1 Ethanol/Furan molar ratio in 100 mL reactor.

6.4 SXRD Experiments

Herein, the recently reported technique of using synchrotron X-ray powder diffraction (SXRD) combined with Rietveld refinement was again used to elucidate adsorbate structures in zeolites. The alteration in scattering parameters of modified framework atoms by the molecule(s) enables the probing of adsorption geometries and interactions with the Brønsted acid site in terms of atomic distances and angles, within

experimental error.[24] In our previous work, it was experimentally verified by SXRD the preferential protonation of ethanol over DMF in HZSM-5. The preferential protonation allows an *in situ* formation of 'ethylene' from the dehydration of ethanol. This effectively increases the local concentration of the intermediate 'ethylene' for the subsequent DA reaction, forming an oxabicyclic intermediate. It is followed by dehydration and ultimately forms *p*-xylene.

Herein, we again applied SXRD and Rietveld refinement to study the adsorbate chemistry over the zeolite pores surface in an atomic scale. The H-USY (Si/Al=6) sample was independently loaded with a mixture of (i) furan applied with 5 bar of ethylene, and (ii) equimolar of ethanol and furan; see **Figure 6.10** (**a** and **b**) for their corresponding SXRD and Rietveld refinement profiles. The quantity of furan was particularly measured to match the quantity of the Brønsted acid sites in H-USY. As seen in **Figure 6.10c**, upon the adsorption of ethylene and furan, only furan can be detected. By measuring the closest interatomic distances between furan and the framework oxygen atoms, two furan molecules are co-adsorbed onto a Brønsted acid site (framework O1 site) through its α-carbon; O1-C_{furan1} = 3.20(3) Å and O1-C_{furan2} = 3.65 (3) Å. The total amount of furan detected by SXRD is 19.15(2), which matches with the total number of Brønsted acid sites based on its empirical formula. A slight experimental discrepancy is noted due to incomplete adsorption. Ethylene is not detected by SXRD which is to be expected, as the adsorption of ethylene onto Brønsted acid sites is generally unfavourable (comparing to propene and butene); the 'ethyl' carbocationic structure is intrinsically less stable.

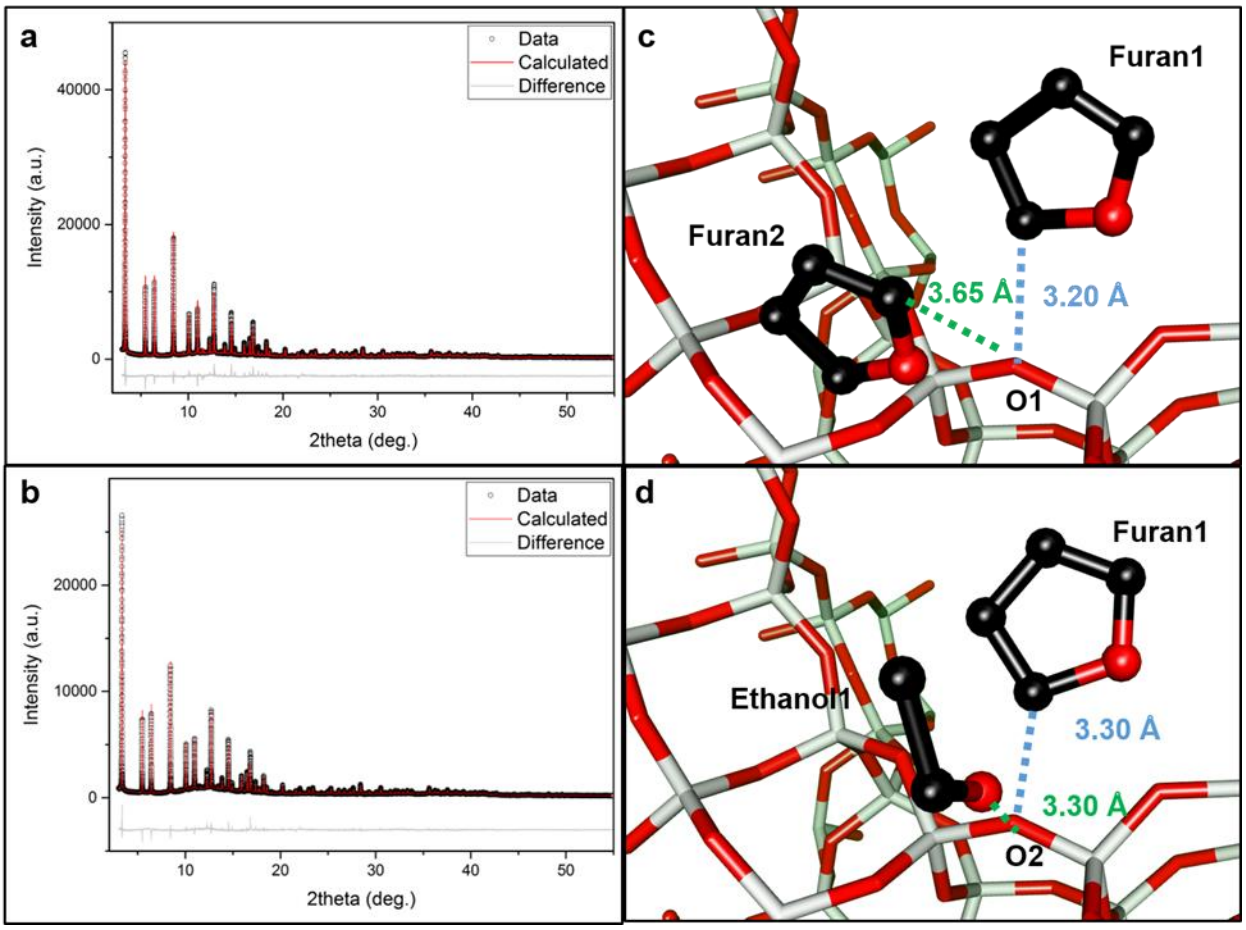


Figure 6.10 SXRD and Rietveld refinement profiles of **a)** furan and 5 bar of ethylene, **b)** equimolar of ethanol to furan, **c)** and **d)** their corresponding crystal structures showing a fraction of a unit cell for illustration. All the symmetry related molecules are disregarded for clarity. The crystallographic and atomic parameters from Rietveld refinement are summarized in **Tables A8-A11** in Appendix. Atoms are represented in ball/sticks: white = Si/Al, red = O, black = C. No hydrogen atoms are plotted for clarity.

Excitingly, upon the adsorption of an equimolar of ethanol and furan, a co-adsorption structure is also detected. The closest interatomic distances between the adsorbates and the H-USY framework are: O1-$O_{ethanol}$ (= 3.30(4) Å) and O1-C_{furan} (= 3.30(3) Å), see **Figure 6.10d**. Both ethanol and furan seem to interact with the Brønsted acid sites in similar manner and strength. Therefore, it is logical to assume that when the ethanol to furan ratio is increased, the local concentration of ethanol around a Brønsted

acid site will be higher. Hence, the statistical probability of ethanol being protonated will be also increased.

6.5 FTIR Experiments

Experiments were conducted to further investigate the local concentration of ethanol and/or furan, and their corresponding interactions with the Brønsted acid sites for H-USY (Si/Al=6) loaded with Ethanol/Furan molar ratios of 3:1 and 10:1 using FTIR spectroscopy. The IR spectrum for the sample loaded with 3:1 Ethanol/Furan (**Figure 6.11**) shows characteristic bands for adsorbed ethanol and furan; for ethanol: 2978 cm^{-1} (C-H stretching), 1448 cm^{-1} (-CH_3 degenerate bending) and 1395 cm^{-1} (-CH_3 symmetric bending);[25] for furan: 1478 and 1468 cm^{-1} (ring stretching (adsorbed)) and 1490 and 1460 cm^{-1} (ring stretching (free)).[26]

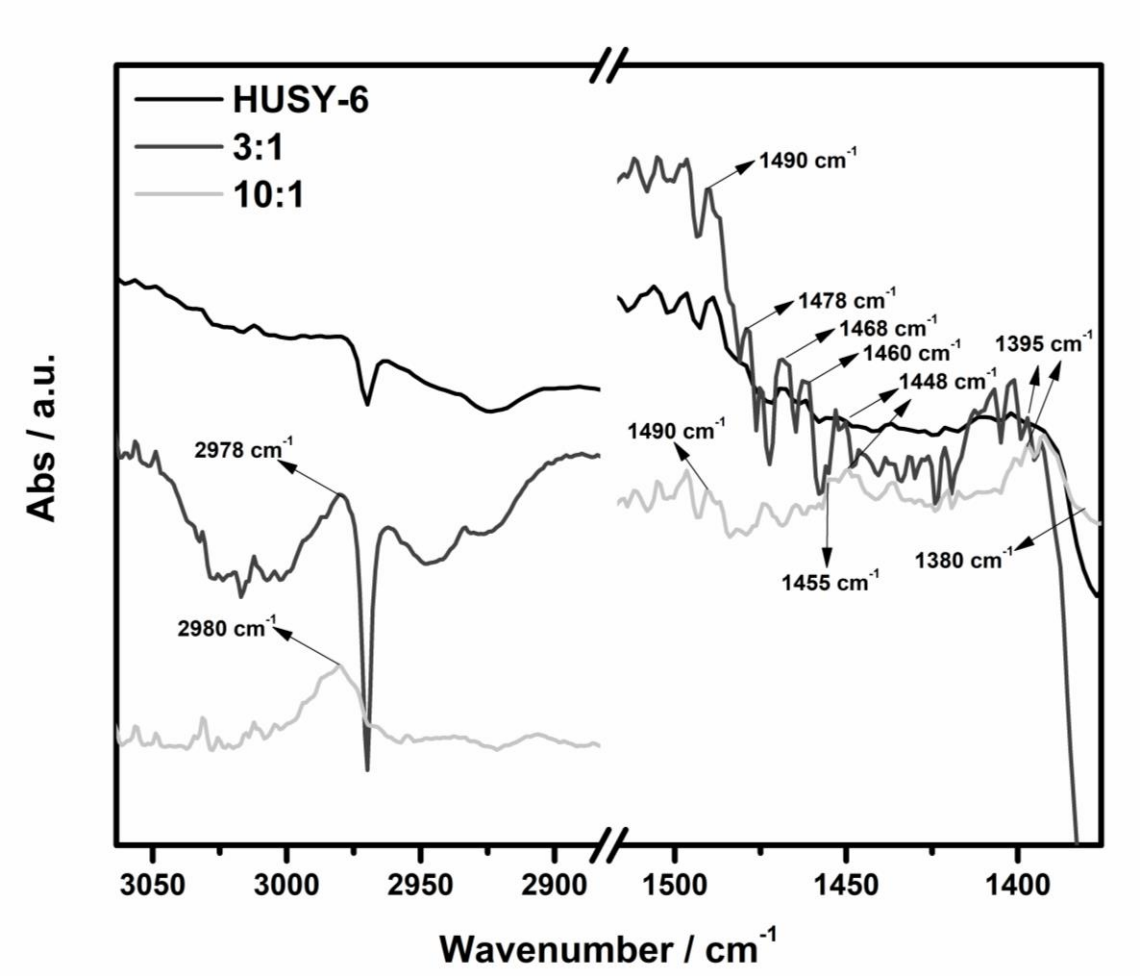


Figure 6.11 IR spectra for H-USY (Si/Al=6) with different molar ratios of Ethanol/Furan measured at room temperature.

Apparently, the IR data corroborates with the SXRD observations, which also shows a co-adsorption of ethanol and furan. In contrast, for the 10:1 Ethanol/Furan sample, aside from the same characteristic bands for adsorbed ethanol, new bands related with free ethanol molecules are also observed at 2980 cm^{-1} (C-H stretching), 1455 cm^{-1} (-CH_3 degenerate bending) and 1380 cm^{-1} (-CH_3 symmetric bending).[27] Most of the furan bands at this molar ratio are too small to be identified, apart from the band 1490 cm^{-1} related with free furan molecule. In short, the FTIR experiments evidently show that under higher molar ratios of Ethanol/Furan, ethanol is preferentially protonated. Whereas

under large excess of ethanol, free ethanol is also present inside the zeolite pores, thus increases the ethanol local concentration.

6.6 Mechanism

It is acknowledged that both ethylene and the ethyl carbocation can be formed from the dehydration of a protonated ethanol, which is dependent on the extent of protonation. When a higher local concentration of ethanol is present, more ethanol can be dehydrated to form the ethyl carbocation, reacting with the co-adsorbed furan to form ethylfuran, *via* alkylation. As previously discussed, ethylfuran has a higher HOMO energy level than that of furan. Thus, the ethylfuran reacts in preference to the furan *via* the DA reaction with the *in situ* generated ethylene, forming the oxabicyclic, which is dehydrated into ethylbenzene – the final product (**Figure 6.12**).

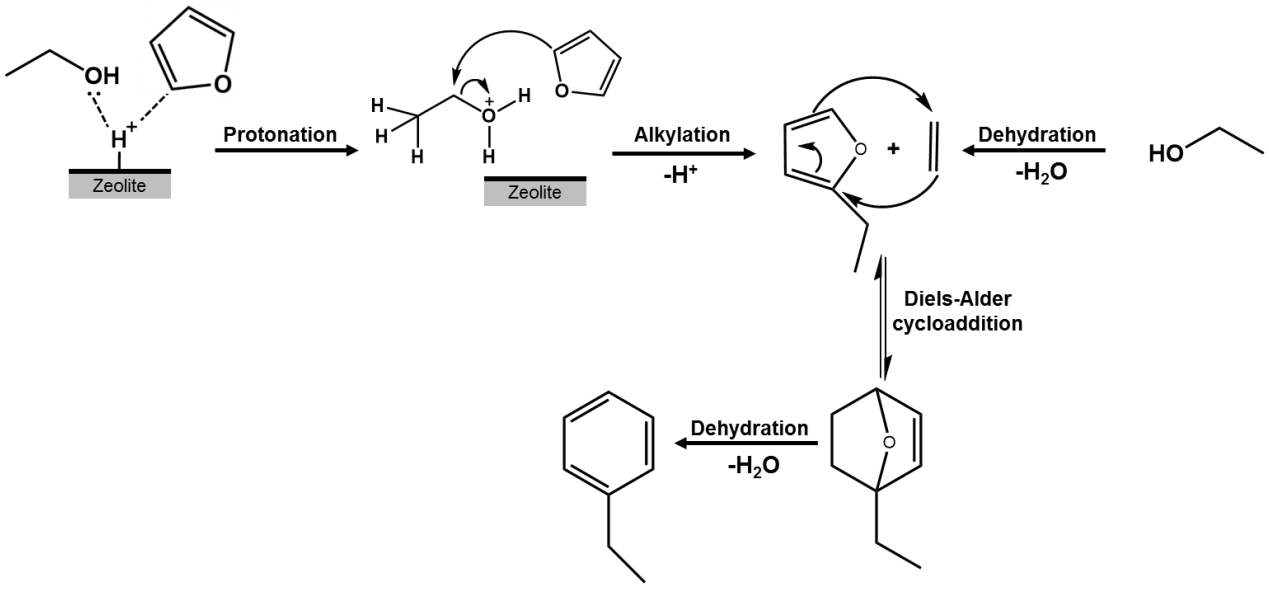


Figure 6.12 Furan alkylation, followed by DA cycloaddition and dehydration, catalyzed by the Brønsted acid sites in zeolite catalysts.

These structural findings confirm our experimental results that the alkylation of furan is the key step to obtain higher selectivity to aromatics. Therefore, not only does the higher local concentration of ethanol over the Brønsted acid sites in zeolites play a key role (versus free flowing marginally adsorbed ethylene in the case of ethylene and furan), but the intrinsic geometric alignment of the two adsorbed substrates also promotes the alkylation reaction.

6.7 Conclusions

In short, this work has demonstrated a valuable biomass conversion route into useful products. The zeolite catalysts provide unique and geometrically defined active sites for a cascade one-pot reaction to form useful aromatics *via* the DA cycloaddition. The use of ethanol instead of traditionally used ethylene reduces the formation of the undesired side product – benzofuran, making possible for the first time the conversion of the important platform molecule furan into aromatics at high yields and mild conditions. This strategy of carefully tuning the local concentration of ethanol may provide inspiration to the chemical industry on how to harness biomass molecules to produce useful products. By combining our experimental catalysis results with the structural findings, it is believed that this method of rational engineering and optimization of catalysts can be readily transferred into the conversions of other biomass-derived products.

6.8 References

1. Roman-Leshkov, Y., J.N. Chheda, and J.A. Dumesic, *Phase modifiers promote efficient production of hydroxymethylfurfural from fructose.* **Science**, 2006. 312: p. 1933-7.

2. Wright, M.M., Y. Roman-Leshkov, and W.H. Green, *Investigating the techno-economic trade-offs of hydrogen source using a response surface model of drop-in biofuel production via bio-oil upgrading.* **Biofuels, Bioprod. Biorefin.**, 2012. 6: p. 503-520.

3. Alonso, D.M., S.G. Wettstein, and J.A. Dumesic, *Bimetallic catalysts for upgrading of biomass to fuels and chemicals.* **Chem. Soc. Rev.**, 2012. 41: p. 8075-8098.

4. Singh, N.R., W.N. Delgass, F.H. Ribeiro, and R. Agrawal, *Estimation of Liquid Fuel Yields from Biomass.* **Environmental Science & Technology**, 2010. 44: p. 5298-5305.

5. Huber, G.W., S. Iborra, and A. Corma, *Synthesis of transportation fuels from biomass: chemistry, catalysts, and engineering.* **Chemical reviews**, 2006. 106.

6. Lin, Y.-C. and G.W. Huber, *The critical role of heterogeneous catalysis in lignocellulosic biomass conversion.* **Energy & Environmental Science**, 2009. 2: p. 68-80.

7. Luterbacher, J.S., D. Martin Alonso, and J.A. Dumesic, *Targeted chemical upgrading of lignocellulosic biomass to platform molecules.* **Green Chemistry**, 2014. 16: p. 4816-4838.

8. Zheng, A., Z. Zhao, S. Chang, Z. Huang, et al., *Maximum synergistic effect in the coupling conversion of bio-derived furans and methanol over ZSM-5 for enhancing aromatic production.* **Green Chemistry**, 2014. 16: p. 2580-2580.

9. Pushkarev, V.V., N. Musselwhite, K. An, S. Alayoglu, et al., *High Structure Sensitivity of Vapor-Phase Furfural Decarbonylation/Hydrogenation Reaction Network as a Function of Size and Shape of Pt Nanoparticles.* **Nano Letters**, 2012. 12: p. 5196-5201.

10. Lange, J.P., E. van der Heide, J. van Buijtenen, and R. Price, *Furfural—a promising platform for lignocellulosic biofuels.* **ChemSusChem**, 2012. 5: p. 150-166.

11. Williams, C.L., C.-C. Chang, P. Do, N. Nikbin, et al., *Cycloaddition of Biomass-Derived Furans for Catalytic Production of Renewable p-Xylene.* **ACS Catalysis**, 2012. 2: p. 935-939.

12. Williams, C.L., K.P. Vinter, C.-C. Chang, R. Xiong, et al., *Kinetic regimes in the tandem reactions of H-BEA catalyzed formation of p-xylene from dimethylfuran.* **Catalysis Science & Technology**, 2016. 6: p. 178-187.

13. Cheng, Y.-T. and G.W. Huber, *Production of targeted aromatics by using Diels–Alder classes of reactions with furans and olefins over ZSM-5.* **Green Chemistry**, 2012. 14: p. 3114-3114.

14. Chang, C.-C., H. Je Cho, J. Yu, R.J. Gorte, et al., *Lewis acid zeolites for tandem Diels-Alder cycloaddition and dehydration of biomass-derived dimethylfuran and ethylene to renewable p-xylene.* **Green Chemistry**, 2016. 18: p. 1368-1376.

15. Wang, D., C.M. Osmundsen, E. Taarning, and J.A. Dumesic, *Selective production of aromatics from alkylfurans over solid acid catalysts.* **ChemCatChem**, 2013. 5: p. 2044-2050.

16. Williams, C.L., *Production of Sustainable Aromatics from Biorenewable Furans*, in *Department of Chemical Engineering*. 2014, University of Massachusetts: Amherst.

17. Chang, C.-C., S.K. Green, C.L. Williams, P.J. Dauenhauer, et al., *Ultra-selective cycloaddition of dimethylfuran for renewable p-xylene with H-BEA.* **Green Chemistry**, 2014. 16: p. 585-588.

18. Cheng, Y.-T. and G.W. Huber, *Chemistry of Furan Conversion into Aromatics and Olefins over HZSM-5: A Model Biomass Conversion Reaction.* **ACS Catalysis**, 2011. 1: p. 611-628.

19. Gallego, E.M., M.T. Portilla, C. Paris, A. León-Escamilla, et al., *"Ab initio" synthesis of zeolites for preestablished catalytic reactions.* **Science**, 2017. 355: p. 1051-1054.

20. Serra, J.M., E. Guillon, and A. Corma, *A rational design of alkyl-aromatics dealkylation–transalkylation catalysts using C8 and C9 alkyl-aromatics as reactants.* **Journal of Catalysis**, 2004. 227: p. 459-469.

21. Teixeira, I.F., B.T.W. Lo, P. Kostetskyy, M. Stamatakis, et al., *From Biomass-Derived Furans to Aromatics with Ethanol over Zeolite.* **Angewandte Chemie International Edition**, 2016. 55: p. 13061-13066.

22. John, I.G. and L. Radom, *Conformations, stabilities, and charge distributions in 2- and 3-monosubstituted furans. An ab initio molecular orbital study.* **Journal of the American Chemical Society**, 1978. 100: p. 3981-3991.

23. Dinadayalane, T.C., R. Vijaya, A. Smitha, and G.N. Sastry, *Diels−Alder Reactivity of Butadiene and Cyclic Five-Membered Dienes ((CH)4X, X = CH2, SiH2, O, NH, PH, and S) with Ethylene: A Benchmark Study.* **The Journal of Physical Chemistry A**, 2002. 106: p. 1627-1633.

24. Teixeira, I.F., B.T.W. Lo, P. Kostetskyy, M. Stamatakis, et al., *From Biomass-Derived Furans to Aromatics with Ethanol over Zeolite.* 2016: p. 13061.

25. Kondo, J.N., K. Ito, E. Yoda, F. Wakabayashi, et al., *An ethoxy intermediate in ethanol dehydration on Brønsted acid sites in zeolite.* **The Journal of Physical Chemistry B**, 2005. 109: p. 10969-10972.

26. Spoto, G., F. Geobaldo, S. Bordiga, C. Lamberti, et al., *Heterocycles oligomerization in acidic zeolites: a UV-visible and IR study.* **Topics in Catalysis**, 1999. 8: p. 279-292.

27. Duan, H.Q., R. Yan, L.C.C. Koe, and X.L. Wang, *Combined effect of adsorption and biodegradation of biological activated carbon on H2S biotrickling filtration.* **Chemosphere**, 2007. 66: p. 1684-1691.

Chapter 7

Conclusions and Future Perspective

Chapter 7: Conclusions and Future Perspective

7.1 Conclusions 181

7.2 Future Perspective 183

7.2.1 Alcohol Chain Length and Group Position 183

7.2.2 Stereoselectivity 185

7.3 References 187

7.1 Conclusions

In this thesis, a novel catalytic conversion of the biomass-derived furans and ethanol into aromatics over zeolite catalysts is reported. The use of liquid ethanol instead of the commonly used gaseous ethylene, as a source of dienophile in this one pot synthesis, permits aromatics production in a much simpler and renewable manner, and circumvents the use of ethylene at high pressure.

In **Chapter 4**, the concept was demonstrated using DMF as a model compound. It was shown that ethanol can act as a dienophile source for furan cycloaddition and in fact it exhibits substantially higher rates and lower reaction barriers than that of ethylene. Combining high quality SXRD data and Rietveld refinement analysis with detailed kinetic measurements and high-level first principles calculations it was confirmed that the reaction takes place *via* a facilitated process, with the preferential protonation of the ethanol molecule and the presence of a water molecule, formed by the ethanol dehydration inside the restricted pore of the zeolite catalyst, leading to lower activation barriers over the solid acid sites with higher rates and higher selectivity to aromatics.[1]

In the **Chapter 5**, it was demonstrated how the Ethanol/DMF reaction is influenced by the strength of the acid sites in the zeolites. Using SXRD in combination with the basic pyridine probe molecule and ^{27}Al NMR it was possible to link the Brønsted acidity with its 3-D structure and global atomic arrangements. After locating and determining the nature of the BAS, the selective site blockage strategy by K^+ exchange was employed, in order to control the product distribution for the DMF transformation reaction into aromatics. Comparing the product distribution obtained for the pure catalyst with the partially and totally blocked it was possible to affirm that the Diels-Alder

cycloaddition is catalysed by strong acid sites while hydrolysis of furan takes place over weak acid sites. Although the BAS selective site blockage strategy did not lead to higher selectivity or conversion to desirable products, this study revealed for the first time the nature of the BAS with product distribution for the complex reaction of DMF conversion into aromatics *via* Diels-Alder cycloaddition. Such an understanding is extremely important to develop superior catalytic processes for a wider range of Biomass-derived furans.

Finally, in **Chapter 6**, the use of the novel catalytic reaction presented in **Chapter 4** was investigated as a new strategy to convert biomass-derived furan into aromatics with high selectivity to aromatics, while reducing the formation of the main side product, benzofuran. The use of ethanol as a source of dienophile in the reaction with furan showed promising results: the selectivity to aromatics increased significantly, especially for the highly desired aromatic product ethylbenzene, and the selectivity to the side product, benzofuran, was considerably reduced. Further investigations by detailed kinetic experiments, SXRD and FTIR experiments showed that the key step to avoid the benzofuran formation and favour the aromatic products is the alkylation of the furan molecule by an ethyl species formed from ethanol dehydration. This step occurs before the DA reaction and has a double effect to promote the aromatic products: 1) the alkylated furans (dienophile) undergo DA cycloaddition more readily, due its higher energy HOMO orbital; 2) the substituent alkyl groups on the furan ring create greater steric hindrance, thus circumventing the direct coupling reaction between two furan molecules to form benzofuran.

7.2 Future Perspective

Aromatics, especially BTX, are one of the most important feedstocks for the petrochemical industry. The Diels–Alder cycloadditions have recently emerged as a prominent route to address this large demand in a renewable way, by coupling biomass-derived chemical intermediates with dienes such as ethylene.[2-5] This reaction is particularly promising to convert biomass-derived furans into BTX, however, it is not entirely renewable since the ethylene commonly used as a dienophile comes from fossil sources.[2-5] Thus, the novel catalytic reaction presented in this thesis is a breakthrough for the biomass derivatives conversion into aromatics, at once making the reaction simpler and entirely renewable. Moreover, this novel approach can allow better yields for challenging biomass-derived furans, such as furan itself. Furthermore, the highly efficient Diels–Alder conversion routes and the associated mechanistic understandings on fundamental steps now make it possible to transition from model compound studies to complex lignocellulosic biomasses, avoiding competition with food resources and providing lower feedstock costs in the future.[2]

Exploitation of these new findings beyond of the biomass field may open many topics to investigation, the most important ones will be briefly presented here.

7.2.1 Alcohol Chain Length and Group Position

Diels-Alder reactions that use alcohols, as source of dienophiles, instead of alkenes open many new possibilities for further investigation. For example, how the reactions are affected by the nature of alcohols with different chain lengths and their positions of the OH group (**Figure 7.1a-d**).

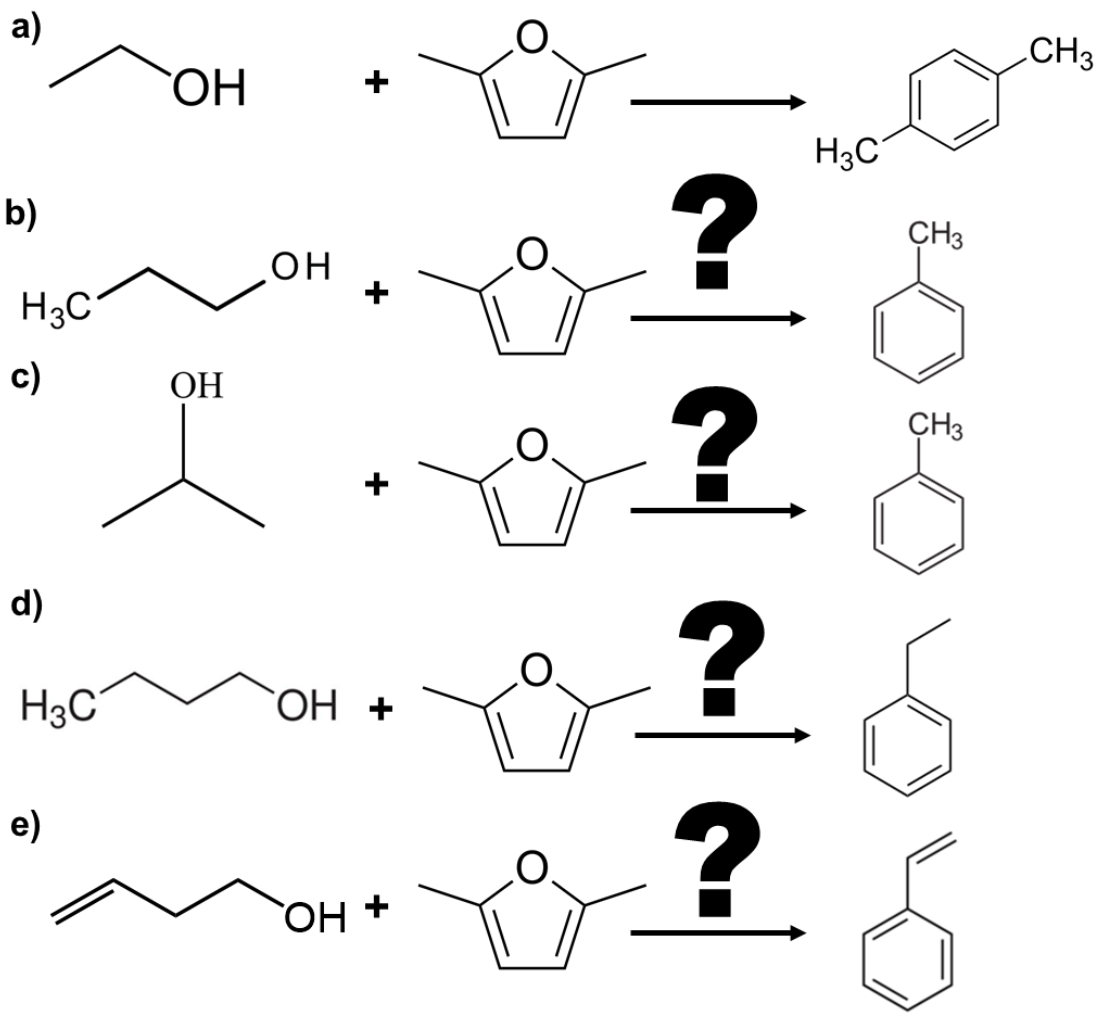


Figure 7.1 Schematic representation of the DA reactions using different alcohols as a source of dienophile; **a)** Ethanol; **b)** Propanol; **c)** Isopropanol; **d)** Butanol; **e)** 3-Buten-1-ol.

As a typical DA reaction apparently takes place after the alcohol dehydration, it may be affected by the OH group position in the specific hydrocarbon chain (**Figure 7.1b-c**). Our previous results have demonstrated that the adsorption geometry of the reactants inside the zeolite pore is crucial for the reaction, thus the position of the OH group in the reactant may affect the catalytic activity and the product distribution for this reaction. Another interesting topic which worth of investigation is that how would the reaction behaviour when the dienophile has two functional groups (e.g 3-Buten-1-ol), see **Figure**

7.1e. It could be interesting to answer the following: 1) Which group would react preferentially?; 2) can the highly desired product styrene be obtained?

7.2.2 Stereoselectivity

Another possibility is to exploit the stereochemistry of the reaction, as ethanol is achiral (do not have stereoisomers) it is not yet possible to investigate this aspect of reaction. However, choosing some specific dienophiles (**Figure 7.2**), such as (R) or (S)-4-hydroxycyclopentane-1,3-dione it could be possible to investigate how the stereoselectivity of the DA reaction is affected when alcohols are used as a source of dienophiles.

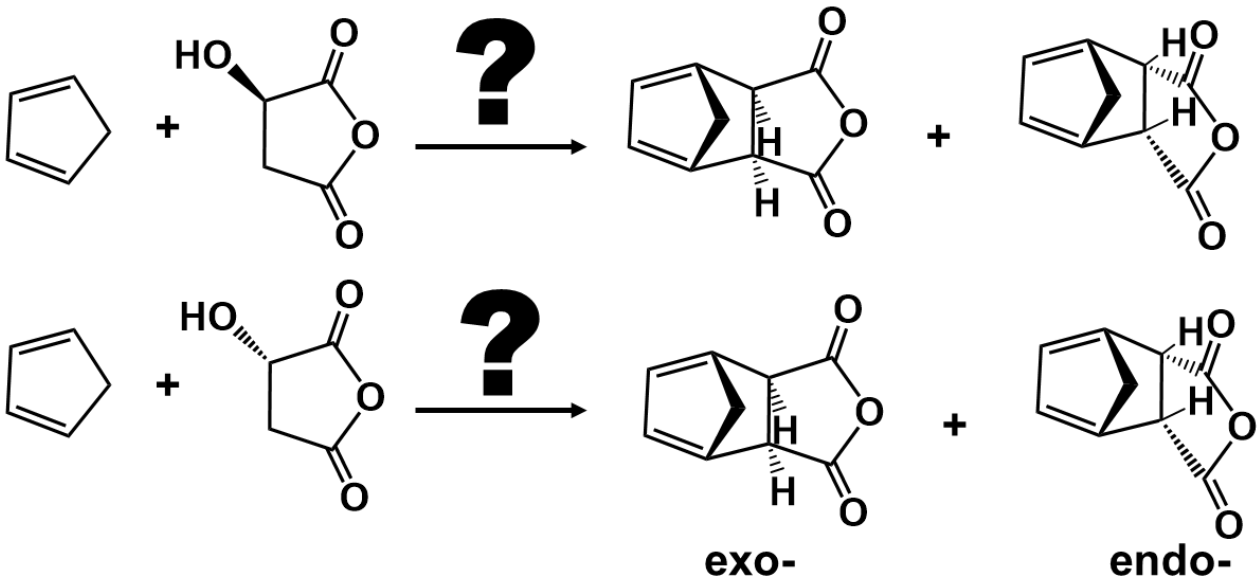


Figure 7.2 Schematic representation of the DA reaction using stereoisomers as a source of dienophile.

Further exploitation of these new findings in the Diels–Alder field may enable the rational design of zeolite catalysts and the employment of other co-substrates for this new improved process. Furthermore, the use of [4+2]-cycloaddition reactions with different

dienophiles, including alkynes and alkenes, in spatially defined zeolites may permit tailoring of activity and stereochemistry, with applications in fine and speciality chemicals synthesis from biomass conversion.

7.3 References

1. Teixeira, I.F., B.T.W. Lo, P. Kostetskyy, M. Stamatakis, et al., *From Biomass-Derived Furans to Aromatics with Ethanol over Zeolite.* **Angewandte Chemie International Edition**, 2016. 55: p. 13061-13066.

2. Settle, A.E., L. Berstis, N.A. Rorrer, Y. Roman-Leshkov, et al., *Heterogeneous Diels-Alder catalysis for biomass-derived aromatic compounds.* **Green Chemistry**, 2017.

3. Williams, C.L., C.-C. Chang, P. Do, N. Nikbin, et al., *Cycloaddition of Biomass-Derived Furans for Catalytic Production of Renewable p-Xylene.* **ACS Catalysis**, 2012. 2: p. 935-939.

4. Williams, C.L., K.P. Vinter, C.-C. Chang, R. Xiong, et al., *Kinetic regimes in the tandem reactions of H-BEA catalyzed formation of p-xylene from dimethylfuran.* **Catalysis Science & Technology**, 2016. 6: p. 178-187.

5. Cheng, Y.-T. and G.W. Huber, *Production of targeted aromatics by using Diels–Alder classes of reactions with furans and olefins over ZSM-5.* **Green Chemistry**, 2012. 14: p. 3114-3114.

Appendix

8.1 X-Ray Diffraction (XRD) 189

8.2 Thermogravimetric Analysis (TGA) 192

8.3 Scanning Electron Microscopy (SEM) 195

8.4 Transmission Electron Microscopy (TEM) 199

8.5 BET surface area analysis 200

8.6 Diffusional controlled (mass limitations) reaction 201

8.7 Crystallographic and atomic parameters 204

8.8 References 224

8.1 X-Ray Diffraction (XRD)

The zeolites samples structures were confirmed by powder X-ray diffractions performed as described in **Chapter 3**. The obtained diffraction patterns were compared with the patterns in the International Zeolite Association (IZA) database.[1]

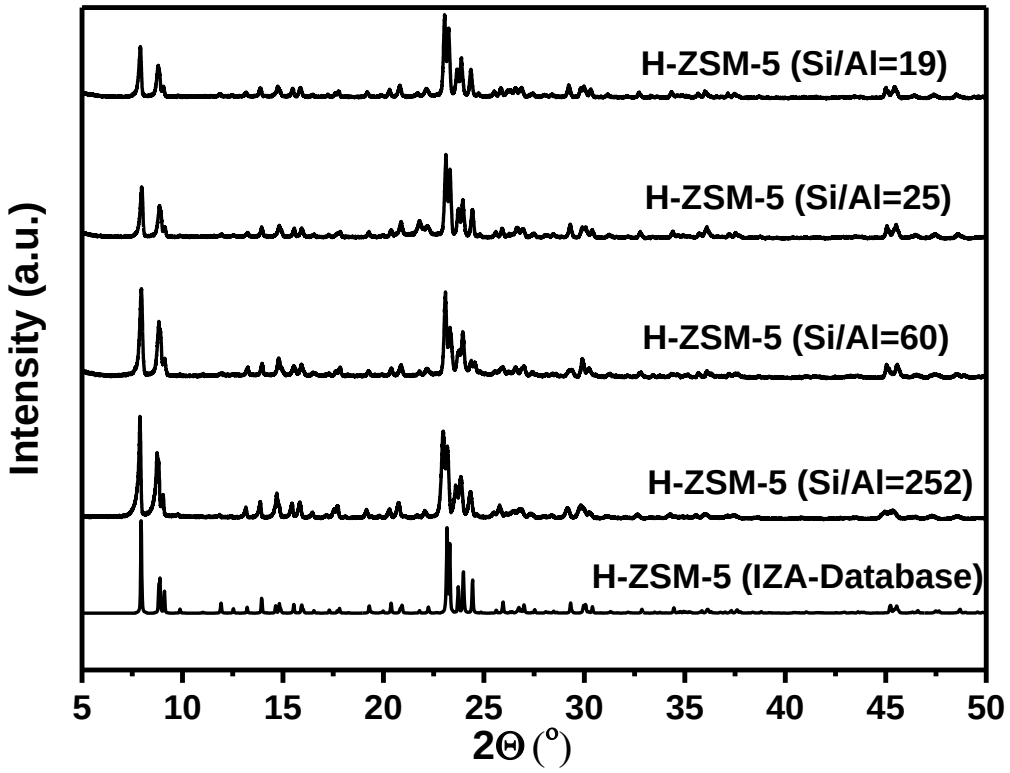


Figure A1. XRD patterns for the zeolites H-ZSM-5 with different Si/Al ratios compared with its reference obtained from IZA database.

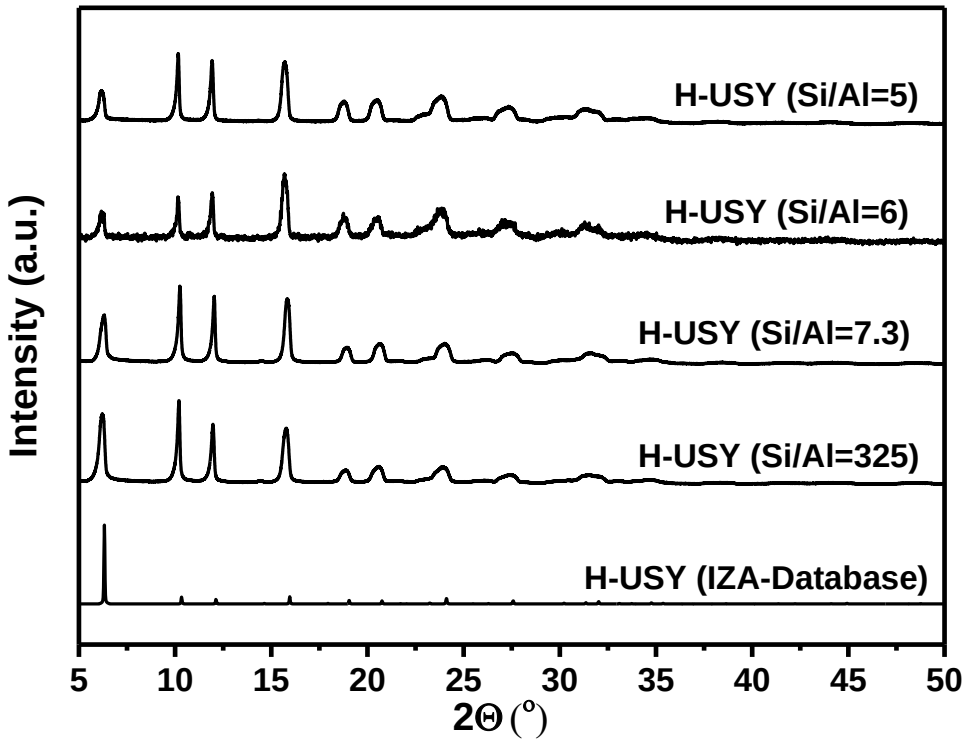


Figure A2. XRD patterns for the zeolites H-USY with different Si/Al ratios compared with its reference obtained from IZA database.

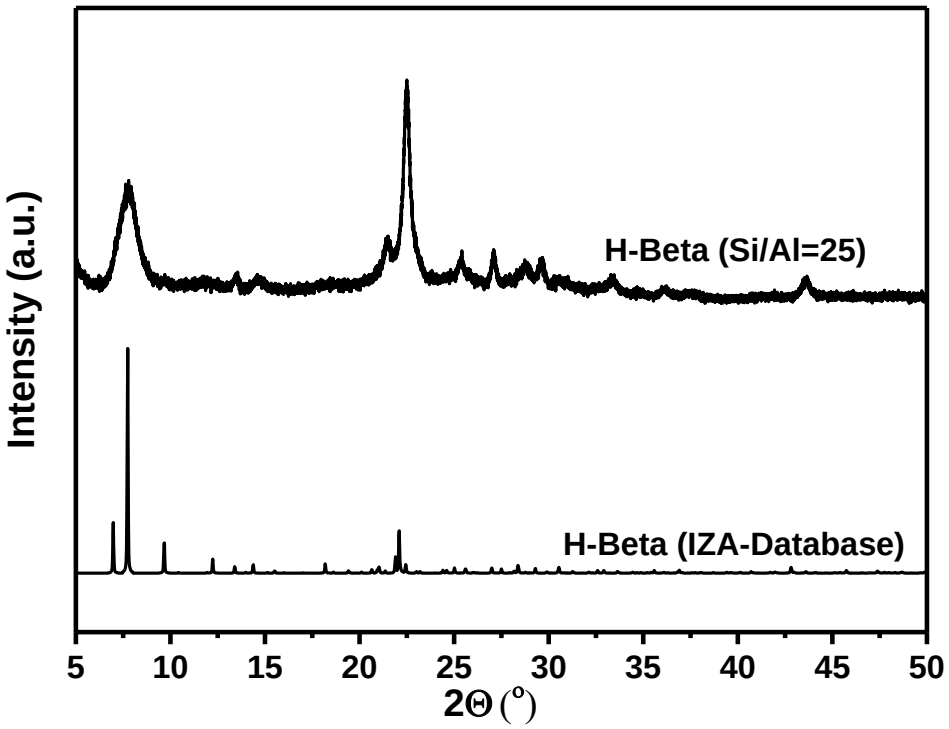


Figure A3. XRD patterns for the zeolite H-Beta with different Si/Al=25 compared with its reference obtained from IZA database.

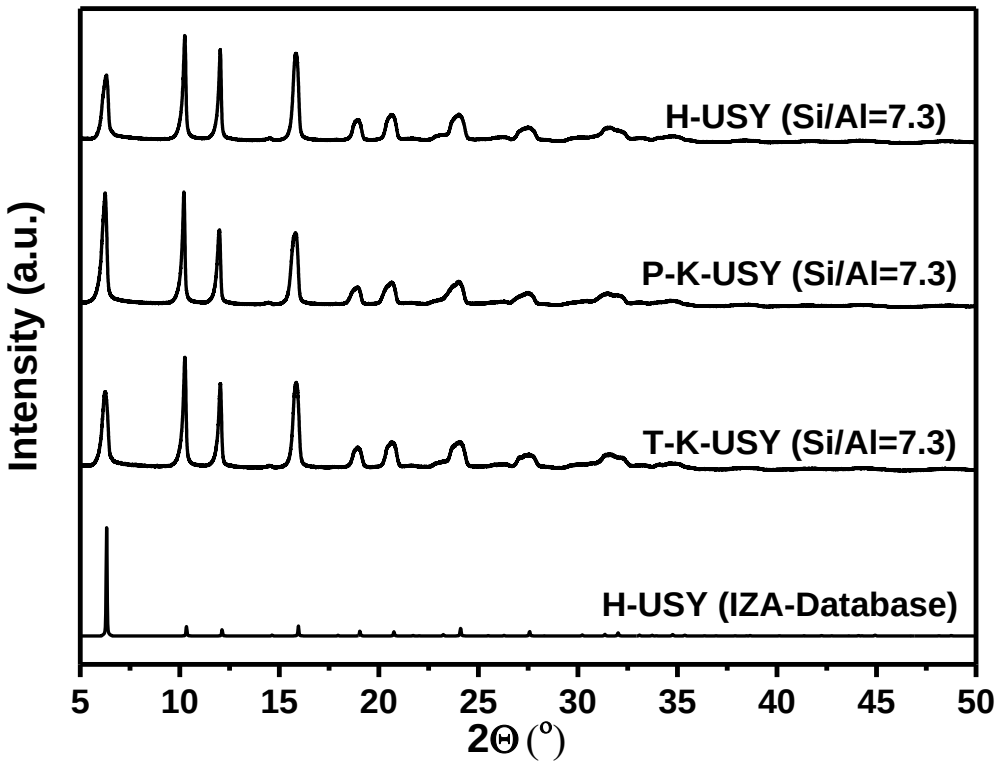


Figure A4. XRD patterns for the zeolites H-USY (Si/Al=7.3) before and after exchanging with K^+ compared with its reference obtained from IZA database. No potassium oxide peaks are observed confirming that all the potassium present in the zeolite is K^+ attached to the zeolite framework replacing protons, as also confirmed by the SXRD experiments.

8.2 Thermogravimetric Analysis (TGA)

Thermogravimetric analysis (TGA) was performed for all the samples, in order to quantify surface moisture and evaluate thermostability (**Figure A5**). TGA was used also to quantify the extent of carbon deposition after catalytic reactions through the weight loss related with the carbon oxidation into CO_2, some examples are presented in **Figure A6** and **A7**, however, all the results for carbon deposition are shown in **Figure 4.4** in **Chapter**

4 as carbon yield for coke. The TGA measurements were performed as described in **Chapter 3**.

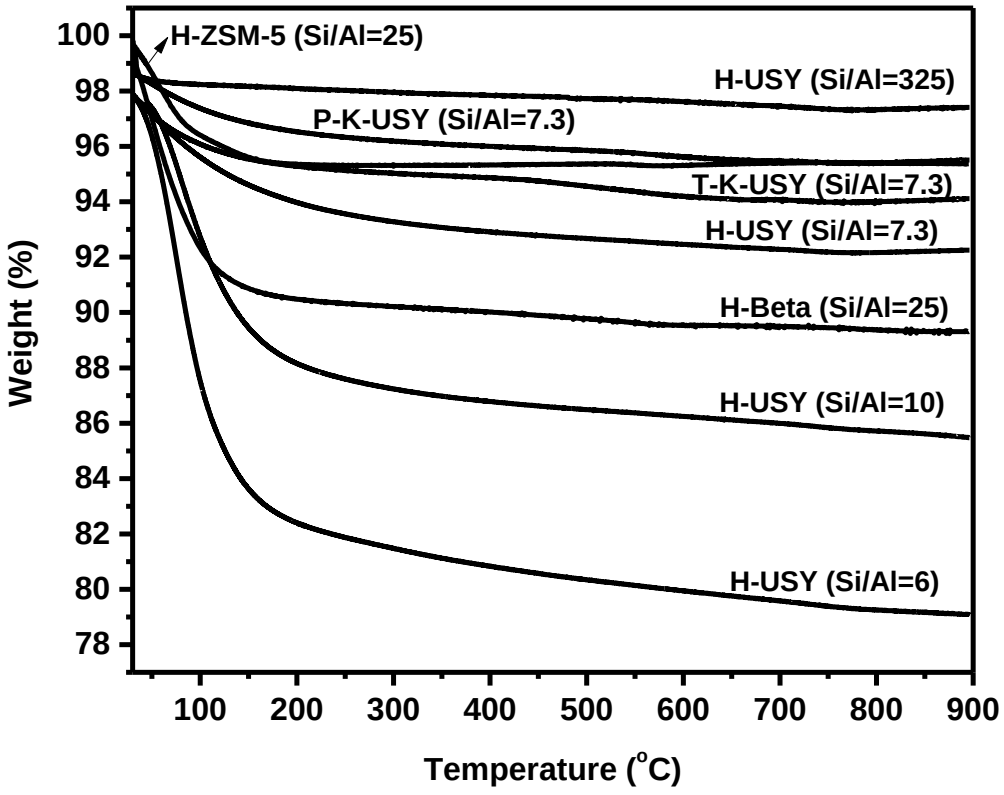


Figure A5. TGA curves for zeolites with different shapes and Si/Al ratios under flow of air (60 mL.min^{-1}). All the samples present a weight loss between 50 and 200 °C, which is related to water molecules adsorbed on the zeolites surface.

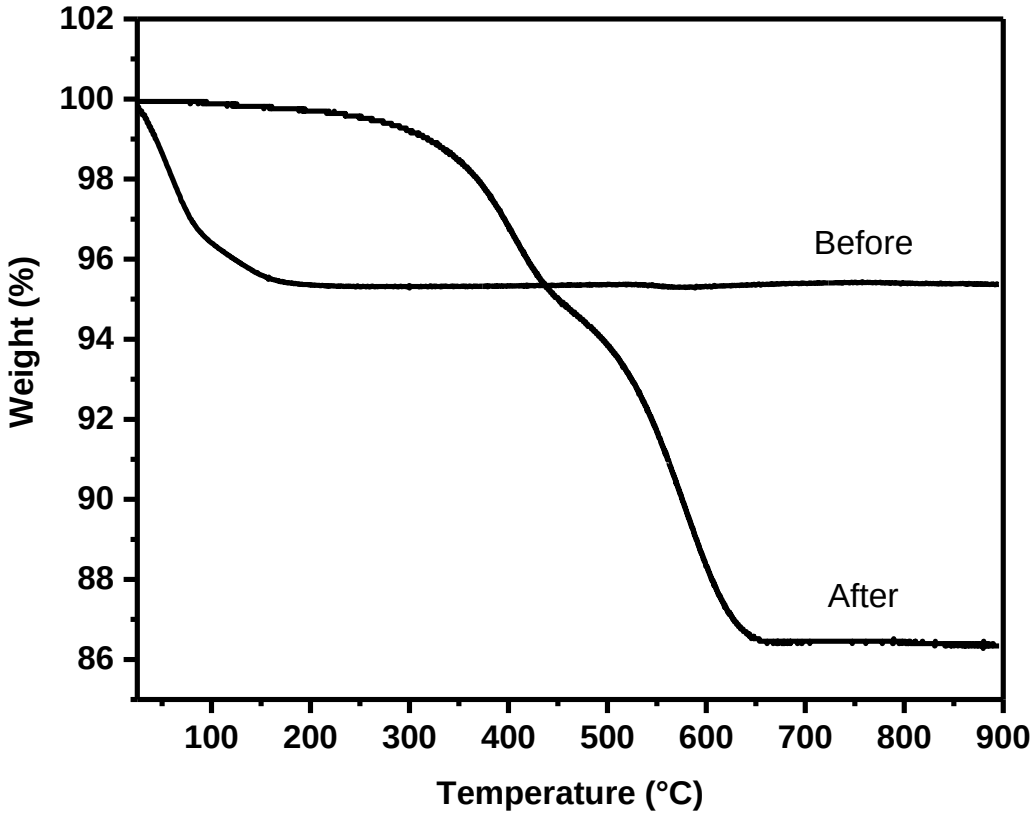


Figure A6. TGA curves for zeolite H-ZSM-5 (Si/Al=25) under flow of air (60 mL.min^{-1}) before and after catalyses the DMF/Ethanol reaction. The weight loss between 400 and 650 °C is related to oligomers and carbon produced from side reactions, mainly from ketones polymerization.

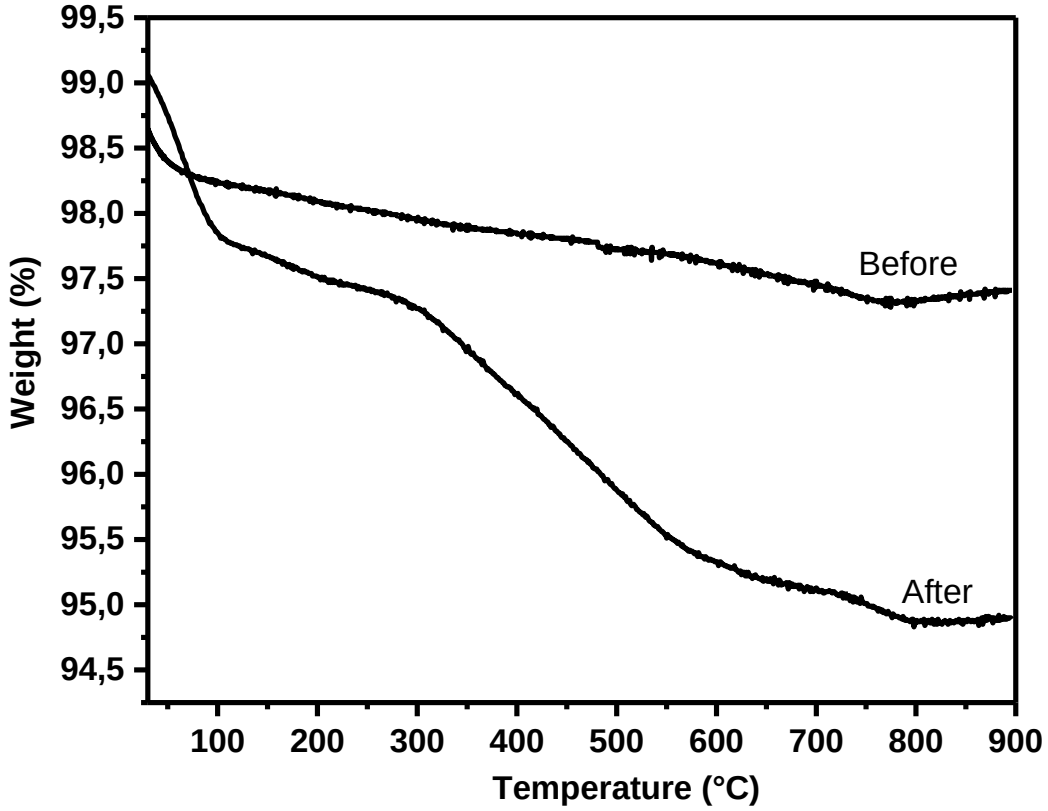


Figure A7. TGA curves for zeolite H-USY (Si/Al=325) under flow of air (60 mL.min^{-1}) before and after catalyses the DMF/Ethanol reaction. The weight loss between 400 and 650 °C is related to oligomers and carbon produced from side reactions, mainly from ketones polymerization.

8.3 Scanning Electron Microscopy (SEM)

The morphologies of the samples were investigated on SEM, see **Figure A8, A9, A10, A11** and **A12**.

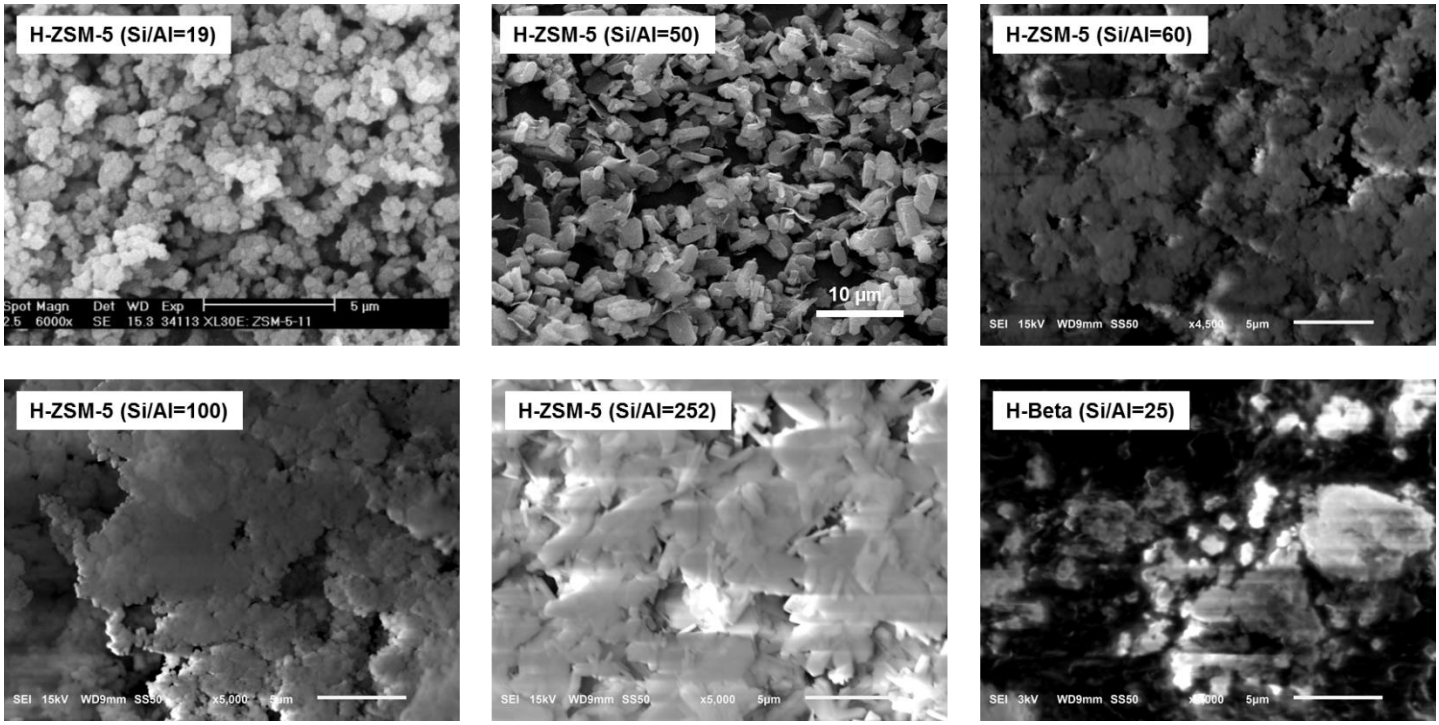


Figure A8. SEM micrographs for zeolites H-ZSM-5 with different Si/Al ratios.

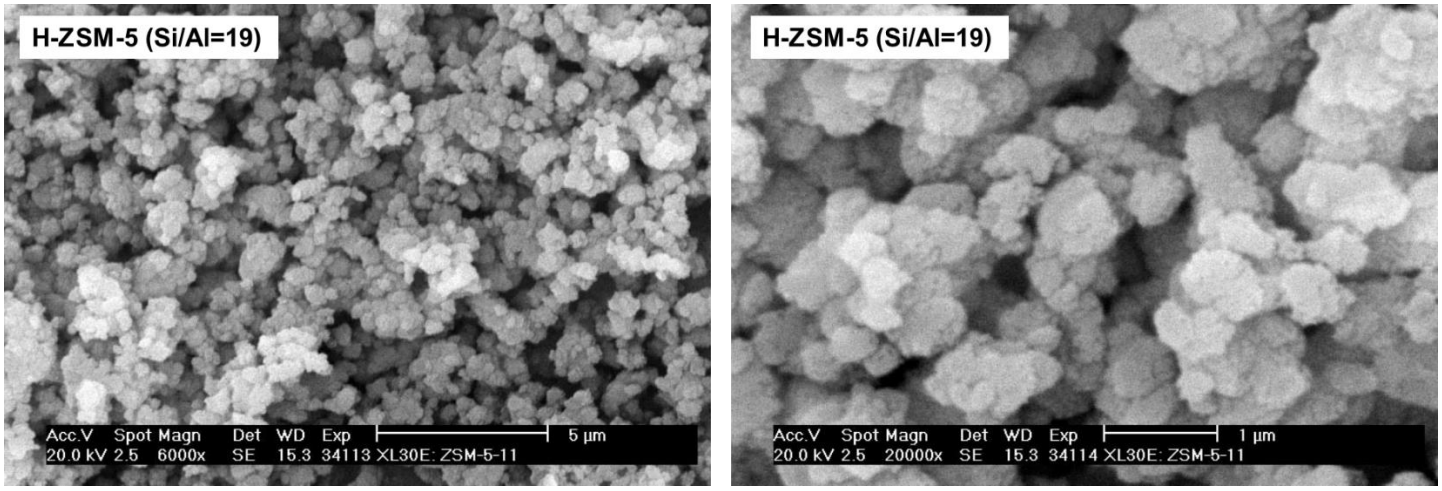


Figure A9. SEM micrographs for the zeolite H-ZSM-5 (Si/Al=19) in two different magnifications. In general, the sample is composed by particles with less than 1µm.

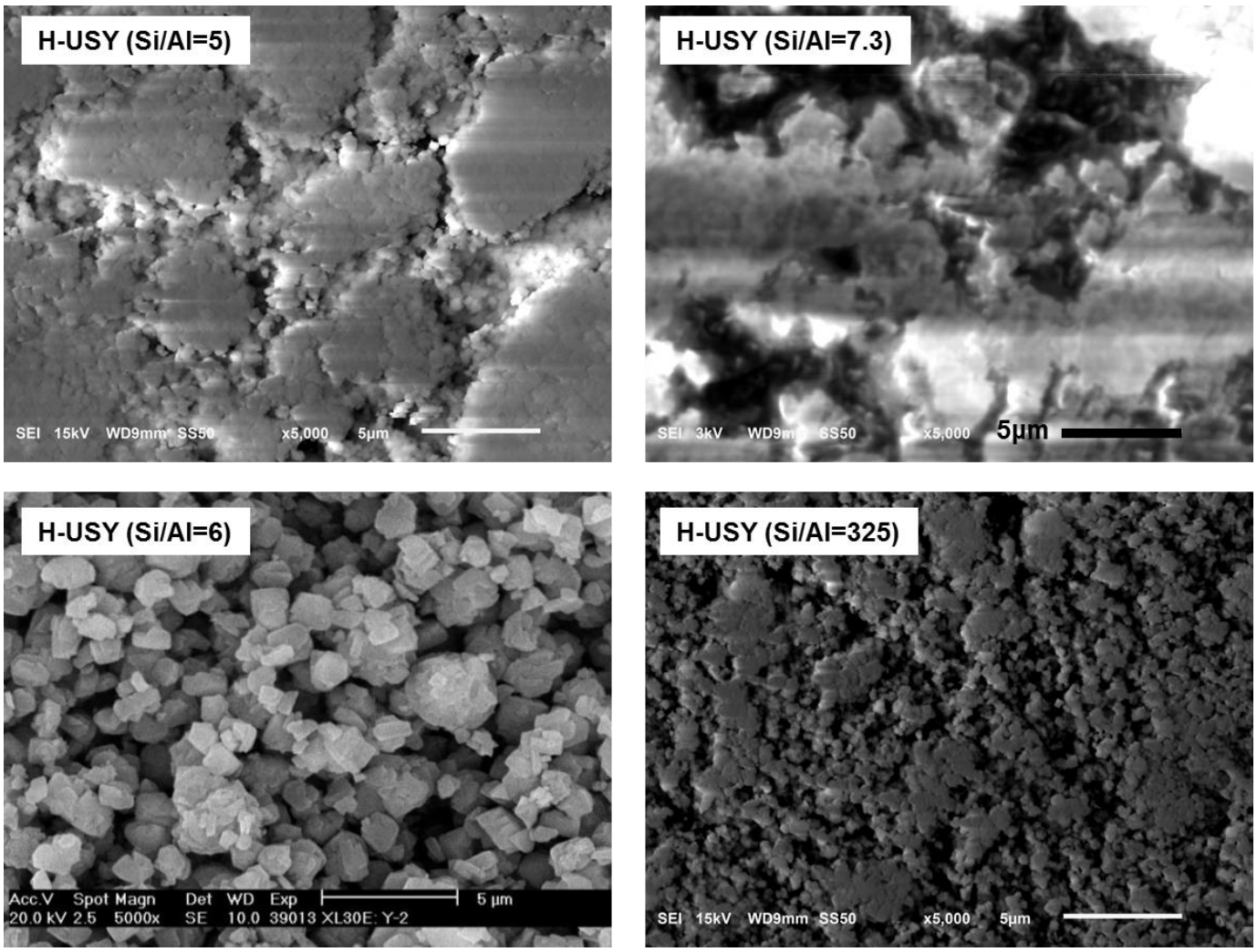


Figure A10. SEM images for zeolites H-USY with different Si/Al ratios.

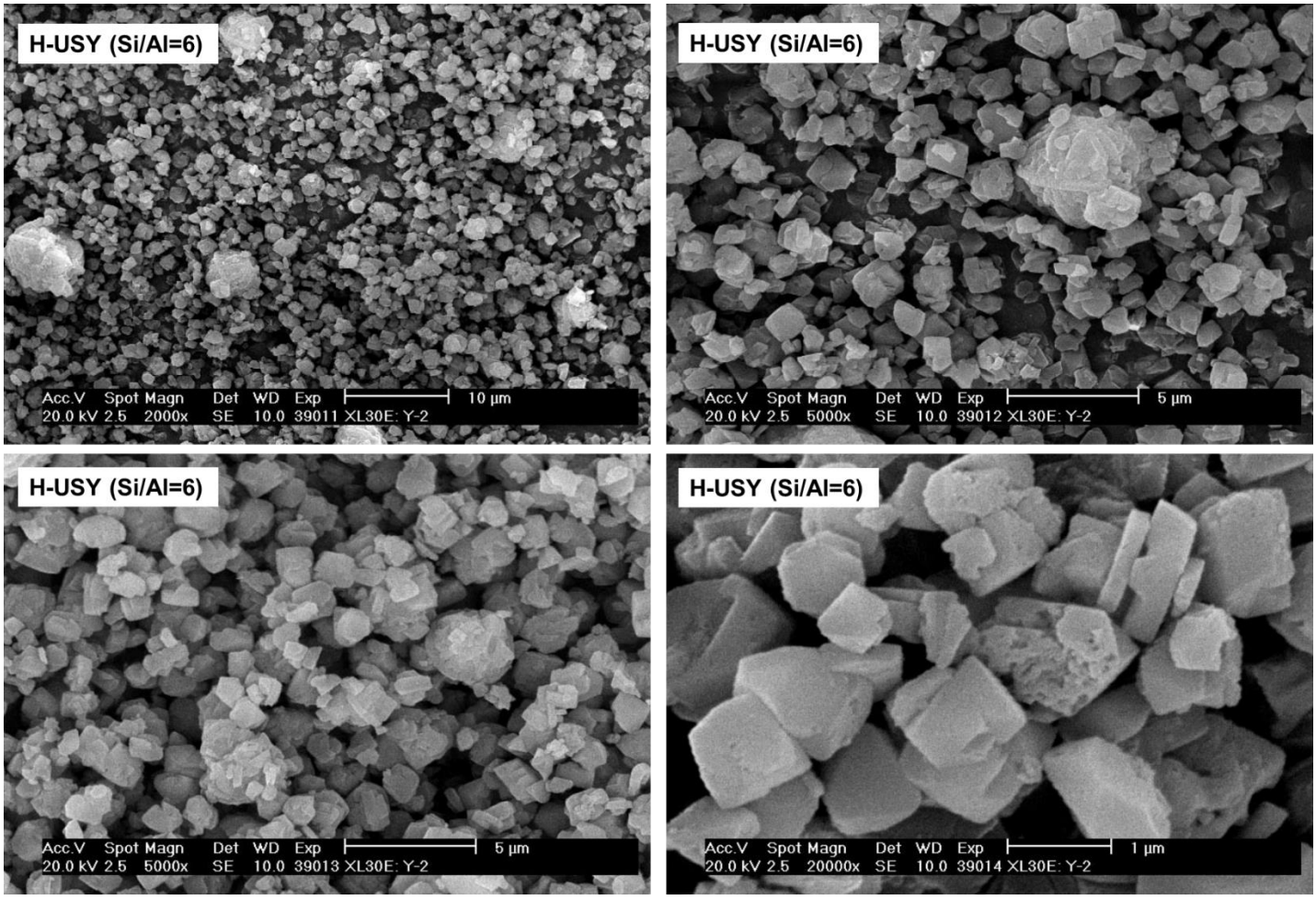


Figure A11. SEM micrographs for the zeolite H-USY (Si/Al=6) in four different magnifications. In general, the sample is composed by particles with size around 1µm.

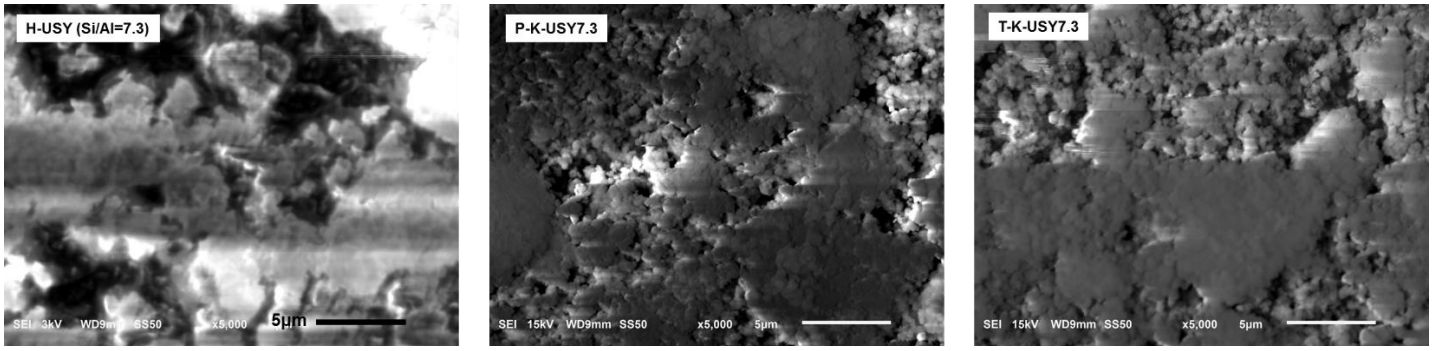


Figure A12. SEM images for the zeolite H-USY (Si/Al=7.3) before and after the partial or total proton exchange with K^+. No significant morphological modifications can be noted.

8.4 Transmission Electron Microscopy (TEM)

The morphologies of the samples and porous structure were investigated on TEM (**Figure A13**).

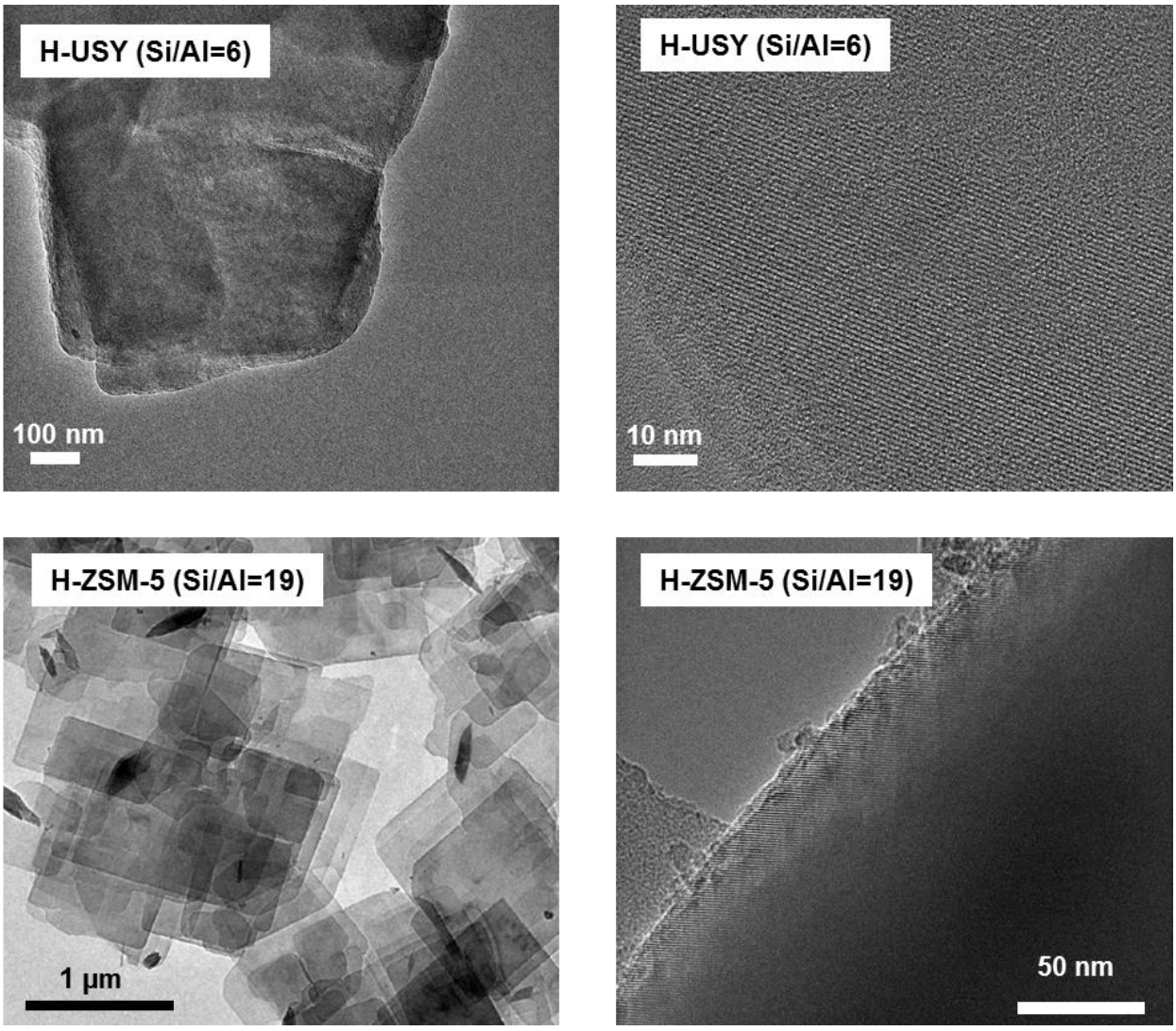


Figure A13. TEM images for the zeolites H-ZSM-5 (Si/Al=19) and H-USY (Si/Al=6).

8.5 BET surface area analysis

Nitrogen sorption was carried out as described in **Chapter 3**. The BET surface area values are presented in **Table 4.1** and **Table 6.1**, those values are derived from the isotherms presented in **Figure A14**. In **Figure A15** the pore distribution, also obtained from the N_2 sorption analysis, is presented.

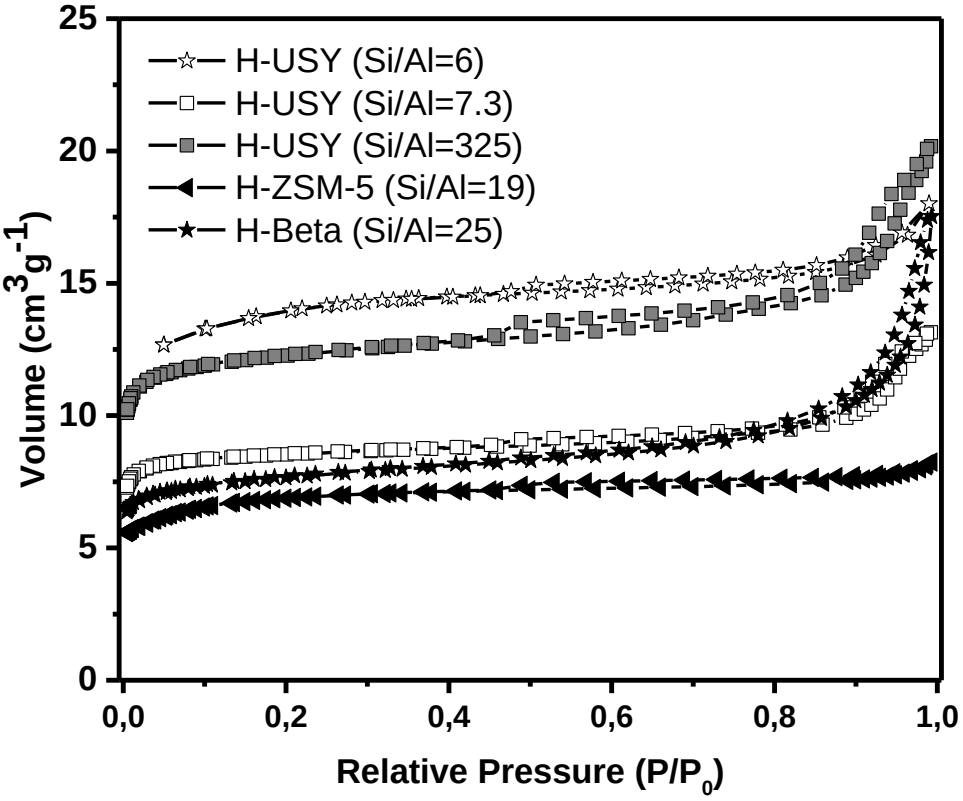


Figure A14. Nitrogen adsorption-desorption isotherms of various zeolite samples.

The BET surface area for zeolites H-USY were significantly higher than zeolites H-ZSM-5, which is in agreement with literature,[2] since zeolites USY are submitted to a dealumination process that tends to increases the surface area.

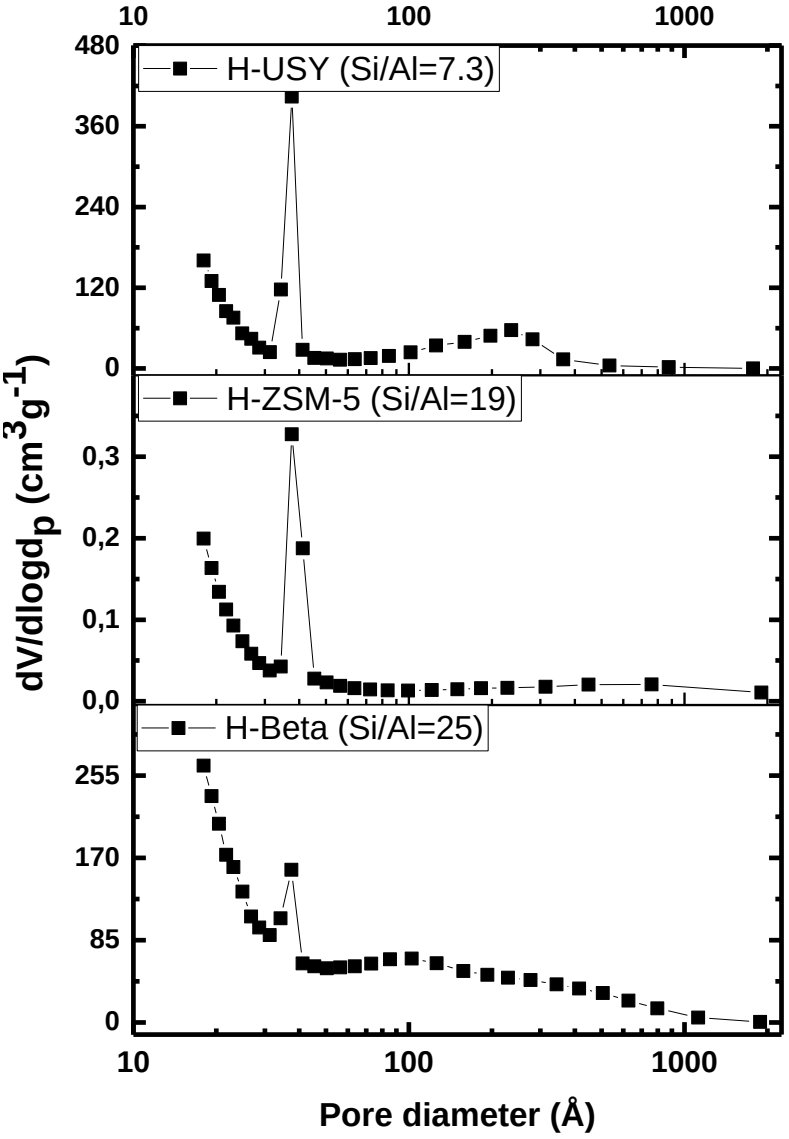


Figure A14. Pore distribution for zeolite samples with different shapes.

8.6 Diffusional controlled (mass limitations) reaction

The reaction conditions for ethylene gas or ethanol liquid placed with DMF liquid (generated pressurized vapors at 300 ^{o}C) were employed following the conditions established in reference,[3] which carefully eliminated the potential for interphase mass

transfer limitations. Weisz-Prater criterion was also considered based on our experimental parameters below. In any case, assuming ideal gases, the value of the Weisz-Prater coefficient is on the order of 10^{-14} to 10^{-15}, which indicates no mass transfer limitations.[4, 5] In the liquid phase, the diffusion coefficients are typically up to 4 orders of magnitude smaller, and in that case the Weisz-Prater coefficient would be around 10^{-10}, indicating again no mass transfer limitations measuring the intrinsic kinetics. Thus, according to the calculations, there was no evidence on mass transfer limitation (the Weisz-Prater number is << 1 for all temperatures reported). For the calculation of the worst case scenario, i.e. the highest temperature and thus highest reaction rate was used.

The reaction between ethylene or ethanol with DMF (generated from pressurized vapors at 300 ºC) was studied, following the experimental protocol established in reference,[3] carefully eliminating the possibility of mass transfer limitations. Assuming that under the reaction conditions all species behave as ideal gases, molecular diffusivities were calculated from the following equation (1):

$$D_{AB} = \frac{2}{3} \cdot \sqrt{\frac{k_B{}^3}{\pi^2}} \cdot \sqrt{\frac{1}{2 \cdot m_A} + \frac{1}{2 \cdot m_B}} \cdot \frac{4 \cdot T^{\frac{3}{2}}}{P \cdot \left(d_A + d_B\right)^2} \qquad (1)$$

where D_{AB} denotes the binary diffusion coefficient between ideal gases A and B, k_B Boltzmann's constant, m_A and m_B the mass of molecules A and B, respectively, T the temperature, P the pressure, and d_A and d_B the diameter of molecules A and B, respectively (estimated to 4.4 Å, 4.0 Å and 8.0 Å, respectively for ethanol, ethylene and DMF). Under experimental conditions that result in the lowest diffusivities (573 K, 140 bar) we obtain the following values for self- and binary diffusion:

D_{AB} (cm²/s) B→ A↓	EtOH	Ethylene	DMF
EtOH	$1.992 \cdot 10^{-3}$	$2.513 \cdot 10^{-3}$	$8.629 \cdot 10^{-4}$
Ethylene		$3.089 \cdot 10^{-3}$	$1.103 \cdot 10^{-3}$
DMF			$4.172 \cdot 10^{-4}$

Moreover, Knudsen diffusivities were estimated from equation (2):

$$D_{Knudsen} = \frac{d_{pore}}{3} \cdot \sqrt{\frac{8 \cdot k_B \cdot T}{\pi \cdot m_A}} \tag{2}$$

where $D_{Knudsen}$ denotes the Knudsen diffusion coefficient and d_{pore} the diameter of the pore of the zeolite. Under experimental conditions that result in the lowest diffusivities, and for the smallest pore diameter of 20 Å, we obtain the following values for the Knudsen diffusion coefficients:

$D_{Knudsen}$ (cm²/s)	EtOH
EtOH	$3.421 \cdot 10^{-3}$
Ethylene	$4.384 \cdot 10^{-3}$
DMF	$2.369 \cdot 10^{-3}$

The effective diffusion coefficient was calculated for the slowest diffusing species DMF as follows:

$$D_{eff,DMF} = \left(\frac{1}{D_{DMF,DMF}} + \frac{1}{D_{Knudsen,DMF}} \right)^{-1} = 3.547 \cdot 10^{-4} \frac{cm^2}{s} \tag{3}$$

To assess the presence of mass transfer limitations the Weisz-Prater criterion was considered. The Weisz-Prater parameter was calculated as:

$$C_{WP} = \frac{R_{obs} \cdot \rho_c}{D_{eff} \cdot C_{reac}} \cdot \left(\frac{d_{particle}}{2} \right)^2 \quad (4)$$

where R_{obs} denotes the observed reaction rate, ρ_c the density of the catalytic particle, C_{reac} the concentration of the reactant, and $d_{particle}$ the particle diameter. Values of $C_{WP} << 1$ indicate that there are no mass transfer limitations. Under the conditions of the experiment (assuming ideal gas phases) we get a value of C_{WP} on the order of 10^{-14}. If there is condensation under the reaction conditions, the liquid phase diffusion coefficients would typically be expected to be up to 4 orders of magnitude lower and the densities up to 3 orders of magnitude higher. In this case, the Weisz-Prater coefficient would be around 10^{-13}, indicating again that there are no mass transfer limitations and that the intrinsic kinetics are indeed measured.[4, 5]

8.7 Crystallographic and atomic parameters

From Rietveld refinements of the SXRD data, the crystallographic details of the zeolite H-ZSM-5 measured at 25 °C were obtained and summarised in **Table 4.6**. The fractional atom positions (*x, y, z*), site occupation factor (SOF) and isotropic temperature factor or thermal parameters (B_{eq}) of the H-ZSM-5 sample pre-adsorbed with ethanol are given in **Table A1**. For the H-ZSM-5 sample pre-adsorbed with DMF, the atomic parameters measured at 25 °C are presented in **Table A2**. For the H-ZSM-5 sample pre-adsorbed with limited ethanol and DMF, the atomic parameters are presented in **Table A3**.

Table A1(a). Atomic parameters from the Rietveld refinement of H-ZSM-5 pre-adsorbed with ethanol measured at 25 °C (R_{wp} = 7.649%, R_{exp} = 3.365%, X^2= 2.274)

Species	Atom	*X*	*y*	*Z*	SOF	B_{eq} (Å^2)	Wyckoff
Framework	O1	0.37346(45)	0.05149(62)	0.75410(57)	1	2.099(23)	8d
	O2	0.30627(54)	0.05716(52)	0.92008(54)	1	2.099(23)	8d
	O3	0.19923(44)	0.05827(45)	0.02005(40)	1	2.099(23)	8d
	O4	0.09506(38)	0.06229(55)	0.91329(62)	1	2.099(23)	8d
	O5	0.11620(45)	0.04839(55)	0.72565(57)	1	2.099(23)	8d
	O6	0.24673(40)	0.06016(59)	0.75345(55)	1	2.099(23)	8d
	O7	0.37308(47)	0.84215(49)	0.76509(66)	1	2.099(23)	8d
	O8	0.30857(52)	0.84282(39)	0.93245(57)	1	2.099(23)	8d
	O9	0.19539(50)	0.84636(32)	0.03209(49)	1	2.099(23)	8d
	O10	0.08777(43)	0.83897(46)	0.92199(71)	1	2.099(23)	8d
	O11	0.11477(44)	0.83726(45)	0.74053(63)	1	2.099(23)	8d
	O12	0.23986(44)	0.84962(49)	0.75554(69)	1	2.099(23)	8d
	O13	0.31079(46)	0.94840(46)	0.81731(46)	1	2.099(23)	8d
	O14	0.07952(35)	0.95448(51)	0.82108(57)	1	2.099(23)	8d
	O15	0.42233(46)	0.12706(51)	0.60269(64)	1	2.099(23)	8d
	O16	0.40969(50)	1.00129(50)	0.58709(68)	1	2.099(23)	8d
	O17	0.40488(47)	0.86747(49)	0.57131(73)	1	2.099(23)	8d
	O18	0.19211(58)	0.12849(43)	0.61891(54)	1	2.099(23)	8d
	O19	0.20463(54)	0.00367(44)	0.59379(61)	1	2.099(23)	8d
	O20	0.20156(57)	0.87023(46)	0.58355(58)	1	2.099(23)	8d
	O21	0.99693(46)	0.04676(56)	0.79233(58)	1	2.099(23)	8d
	O22	0.99505(48)	0.85142(49)	0.79070(59)	1	2.099(23)	8d
	O23	0.41960(66)	0.75	0.64682(83)	1	2.099(23)	4c
	O24	0.19149(82)	0.75	0.64986(75)	1	2.099(23)	4c
	O25	0.28440(61)	0.75	0.05534(83)	1	2.099(23)	4c
	O26	0.10992(66)	0.75	0.0624(10)	1	2.099(23)	4c
	Si1	0.42491(22)	0.05671(31)	0.66327(31)	1	1.049(11)	8d

	Si2	0.27891(19)	0.06068(24)	1.03346(32)	1	1.049(11)	8d
	Si3	0.30834(30)	0.03098(19)	-0.18939(31)	1	1.049(11)	8d
	Si4	0.11967(22)	0.06401(25)	0.02769(34)	1	1.049(11)	8d
	Si5	0.07071(23)	0.02983(22)	0.81467(35)	1	1.049(11)	8d
	Si6	0.18862(25)	0.05696(25)	0.67589(30)	1	1.049(11)	8d
	Si7	0.42292(24)	0.82909(23)	0.67228(37)	1	1.049(11)	8d
	Si8	0.30910(28)	0.87051(22)	0.81671(30)	1	1.049(11)	8d
	Si9	0.27422(21)	0.82685(21)	0.03309(35)	1	1.049(11)	8d
	Si10	0.12073(24)	0.82612(22)	0.03050(36)	1	1.049(11)	8d
	Si11	0.07261(23)	0.87075(27)	0.82161(35)	1	1.049(11)	8d
	Si12	0.18757(27)	0.82643(19)	0.68213(33)	1	1.049(11)	8d
Ethanol1	O1	-2.10743	0.75557	1.25099	0.3825(68)	20.0(17)	4c
	H2	-2.08704	0.79846	1.28459	0.3825(68)	24.0(20)	4c
	C3	-2.09765	0.76177	1.14514	0.3825(68)	26.0(22)	4c
	H4	-2.07417	0.80486	1.13039	0.3825(68)	30.0(26)	4c
	H5	-2.07024	0.7233	1.12067	0.3825(68)	30.0(26)	4c
	C6	-2.16377	0.76131	1.09357	0.3825(68)	28.0(24)	4c
	H7	-2.16968	0.80418	1.0559	0.3825(68)	34.0(29)	4c
	H8	-2.16578	0.72262	1.04625	0.3825(68)	34.0(29)	4c
	H9	-2.2	0.75683	1.14412	0.3825(68)	34.0(29)	4c
Ethanol2	O1	0.02961	0.32422	1.47871	0.5969(53)	15.12(73)	4c
	H2	-0.00282	0.2861	1.45523	0.5969(53)	18.15(88)	4c
	C3	-0.01034	0.37741	1.51974	0.5969(53)	19.66(95)	4c
	H4	-0.05837	0.36484	1.51561	0.5969(53)	22.7(11)	4c
	H5	0.00216	0.38479	1.59099	0.5969(53)	22.7(11)	4c
	C6	0.00129	0.4407	1.46185	0.5969(53)	21.2(10)	4c
	H7	-0.04156	0.45625	1.432	0.5969(53)	25.7(12)	4c
	H8	0.019	0.47618	1.50733	0.5969(53)	25.7(12)	4c
	H9	0.03419	0.43192	1.40756	0.5969(53)	25.7(12)	4c
Ethanol3	O1	-0.97621	0.17557	0.64367	0.2723(79)	6.5(12)	4c

	H2	-0.94124	0.13727	0.65542	0.2723(79)	7.9(14)	4c
	C3	-0.96682	0.22492	0.72073	0.2723(79)	8.5(16)	4c
	H4	-0.92979	0.2105	0.76555	0.2723(79)	9.8(18)	4c
	H5	-0.95549	0.26912	0.68985	0.2723(79)	9.8(18)	4c
	C6	-1.02957	0.23174	0.78019	0.2723(79)	9.2(17)	4c
	H7	-1.02043	0.22035	0.85143	0.2723(79)	11.1(20)	4c
	H8	-1.04615	0.27894	0.77568	0.2723(79)	11.1(20)	4c
	H9	-1.064	0.20048	0.75318	0.2723(79)	11.1(20)	4c
Ethanol4	O1	-1.08952	0.17105	0.59341	0.4383(63)	20.0(14)	4c
	H2	-1.05627	0.15065	0.64553	0.4383(63)	24.0(17)	4c
	C3	-1.12174	0.22747	0.63985	0.4383(63)	26.0(18)	4c
	H4	-1.10456	0.23299	0.70926	0.4383(63)	30.0(21)	4c
	H5	-1.11226	0.26906	0.60068	0.4383(63)	30.0(21)	4c
	C6	-1.19533	0.21567	0.64292	0.4383(63)	28.0(20)	4c
	H7	-1.21086	0.21594	0.71367	0.4383(63)	34.0(24)	4c
	H8	-1.21855	0.25196	0.60507	0.4383(63)	34.0(24)	4c
	H9	-1.20571	0.17121	0.61208	0.4383(63)	34.0(24)	4c

Table A1(b). Translational and rotational axes for the matrices describing the adsorbate ethanol molecules, together with their corresponding systematic errors

	X	***Y***	***z***
Translational			
Ethanol1	-2.1074(18)	0.7556(86)	1.2510(23)
Ethanol2	0.02961(88)	0.32422(63)	1.4787(15)
Ethanol3	-0.9762(16)	0.1756(18)	0.6437(25)
Ethanol4	-1.0895(13)	0.1711(18)	0.5934(29)
Rotational			
Ethanol1	190.7(75)	244.1(82)	52.4(27)
Ethanol2	108.3(26)	17.8(23)	-34.8(11)

Ethanol3	-75.5(25)	53.2(29)	-125.6(36)
Ethanol4	-26.9(47)	41.6(39)	-68.7(29)

Table A2(a). Atomic parameters from the Rietveld refinement of H-ZSM-5 pre-adsorbed with DMF measured at 25 °C (R_{wp} = 8.457%, R_{exp} = 3.339%, X^2 = 2.533)

Species	Atom	*X*	*y*	*Z*	SOF	B_{eq} (Å^2)	Wychoff
Framework	O1	0.37684(48)	0.05499(68)	0.75255(65)	1	1.832(25)	8d
	O2	0.30932(50)	0.05871(54)	0.92543(59)	1	1.832(25)	8d
	O3	0.19809(46)	0.06165(43)	0.02543(45)	1	1.832(25)	8d
	O4	0.09579(38)	0.05807(57)	0.91475(65)	1	1.832(25)	8d
	O5	0.11354(48)	0.04504(55)	0.72940(62)	1	1.832(25)	8d
	O6	0.24622(43)	0.05293(70)	0.75865(61)	1	1.832(25)	8d
	O7	0.37427(51)	0.84195(50)	0.75952(71)	1	1.832(25)	8d
	O8	0.30251(56)	0.84755(42)	0.93166(61)	1	1.832(25)	8d
	O9	0.19652(51)	0.84845(33)	0.03241(52)	1	1.832(25)	8d
	O10	0.08424(47)	0.84053(46)	0.92706(73)	1	1.832(25)	8d
	O11	0.11719(47)	0.83640(46)	0.74246(67)	1	1.832(25)	8d
	O12	0.24036(48)	0.84717(52)	0.76361(74)	1	1.832(25)	8d
	O13	0.31361(43)	0.95152(49)	0.81623(49)	1	1.832(25)	8d
	O14	0.07984(36)	0.95337(55)	0.82822(55)	1	1.832(25)	8d
	O15	0.41967(48)	0.12367(51)	0.60807(72)	1	1.832(25)	8d
	O16	0.40289(52)	1.00242(54)	0.58739(76)	1	1.832(25)	8d
	O17	0.40537(49)	0.87167(51)	0.57239(75)	1	1.832(25)	8d
	O18	0.19076(60)	0.12924(45)	0.61922(60)	1	1.832(25)	8d
	O19	0.20281(60)	0.00204(48)	0.59549(66)	1	1.832(25)	8d
	O20	0.19965(60)	0.87055(49)	0.58780(60)	1	1.832(25)	8d
	O21	0.99733(51)	0.04932(64)	0.79526(60)	1	1.832(25)	8d
	O22	0.99596(52)	0.85111(52)	0.79386(67)	1	1.832(25)	8d
	O23	0.41913(73)	0.75	0.64018(89)	1	1.832(25)	4c

	O24	0.19650(83)	0.75	0.65447(80)	1	1.832(25)	4c
	O25	0.28593(62)	0.75	0.04753(82)	1	1.832(25)	4c
	O26	0.11467(68)	0.75	0.06522(96)	1	1.832(25)	4c
	Si1	0.42464(26)	0.05924(33)	0.66587(36)	1	0.916(13)	8d
	Si2	0.27852(20)	0.06072(27)	1.03645(34)	1	0.916(13)	8d
	Si3	0.31074(31)	0.02973(21)	-0.18602(36)	1	0.916(13)	8d
	Si4	0.12108(23)	0.06360(28)	0.02698(36)	1	0.916(13)	8d
	Si5	0.06991(25)	0.03036(24)	0.81778(36)	1	0.916(13)	8d
	Si6	0.18663(26)	0.05780(27)	0.67567(33)	1	0.916(13)	8d
	Si7	0.42310(27)	0.82944(23)	0.66747(38)	1	0.916(13)	8d
	Si8	0.30950(30)	0.86991(24)	0.81522(33)	1	0.916(13)	8d
	Si9	0.27425(23)	0.82715(22)	0.03047(38)	1	0.916(13)	8d
	Si10	0.12082(26)	0.82569(23)	0.03173(39)	1	0.916(13)	8d
	Si11	0.07270(25)	0.87069(28)	0.82009(37)	1	0.916(13)	8d
	Si12	0.18727(30)	0.82621(20)	0.68486(35)	1	0.916(13)	8d
DMF 1	O1	-2.10446	0.77858	1.26435	0.4296(35)	14.40(82)	4c
	C2	-2.09845	0.75538	1.16989	0.4296(35)	17.28(98)	4c
	C3	-2.03265	0.74961	1.14424	0.4296(35)	20.2(11)	4c
	C4	-1.996	0.77064	1.2284	0.4296(35)	20.2(11)	4c
	C5	-2.042	0.78776	1.29952	0.4296(35)	17.28(98)	4c
	C6	-2.0255	0.81297	1.40135	0.4296(35)	20.2(11)	4c
	C7	-2.15541	0.73846	1.10309	0.4296(35)	20.2(11)	4c
	H8	-2.0077	0.70499	1.11431	0.4296(35)	24.5(14)	4c
	H9	-1.95627	0.74283	1.26628	0.4296(35)	24.5(14)	4c
	H10	-1.97068	0.81559	1.41013	0.4296(35)	24.5(14)	4c
	H11	-2.04643	0.77829	1.45799	0.4296(35)	24.5(14)	4c
	H12	-2.04713	0.86376	1.41162	0.4296(35)	24.5(14)	4c
	H13	-2.13617	0.72067	1.03018	0.4296(35)	24.5(14)	4c
	H14	-2.18654	0.7838	1.09154	0.4296(35)	24.5(14)	4c

	H15	-2.18585	0.69834	1.13791	0.4296(35)	24.5(14)	4c
DMF 2	O1	-1.96795	0.86786	1.45559	0.4868(31)	14.58(59)	4c
	C2	-1.99818	0.92089	1.49958	0.4868(31)	17.50(70)	4c
	C3	-2.04431	0.89929	1.56778	0.4868(31)	20.42(82)	4c
	C4	-2.0422	0.82845	1.56539	0.4868(31)	20.42(82)	4c
	C5	-1.99493	0.81181	1.49592	0.4868(31)	17.50(70)	4c
	C6	-1.97592	0.74174	1.46863	0.4868(31)	20.42(82)	4c
	C7	-1.9834	0.99274	1.47705	0.4868(31)	20.42(82)	4c
	H8	-2.04797	0.91419	1.6463	0.4868(31)	24.8(10)	4c
	H9	-2.03544	0.79459	1.62906	0.4868(31)	24.8(10)	4c
	H10	-2.00582	0.70573	1.51307	0.4868(31)	24.8(10)	4c
	H11	-1.9223	0.73394	1.48444	0.4868(31)	24.8(10)	4c
	H12	-1.98548	0.73347	1.38808	0.4868(31)	24.8(10)	4c
	H13	-2.01535	1.02549	1.5238	0.4868(31)	24.8(10)	4c
	H14	-1.99351	1.00284	1.39711	0.4868(31)	24.8(10)	4c
	H15	-1.93033	1.00331	1.49347	0.4868(31)	24.8(10)	4c
DMF 3	O1	-1.85598	0.77216	1.31054	0.3328(35)	19.1(12)	4c
	C2	-1.86218	0.71832	1.37145	0.3328(35)	23.0(14)	4c
	C3	-1.8017	0.70143	1.41159	0.3328(35)	26.8(17)	4c
	C4	-1.75547	0.74793	1.37275	0.3328(35)	26.8(17)	4c
	C5	-1.79099	0.78993	1.31164	0.3328(35)	23.0(14)	4c
	C6	-1.76204	0.84717	1.25442	0.3328(35)	26.8(17)	4c
	C7	-1.92586	0.68239	1.39203	0.3328(35)	26.8(17)	4c
	H8	-1.78994	0.69483	1.49083	0.3328(35)	32.6(20)	4c
	H9	-1.72077	0.77931	1.41528	0.3328(35)	32.6(20)	4c
	H10	-1.70781	0.85022	1.26911	0.3328(35)	32.6(20)	4c
	H11	-1.78624	0.89464	1.27807	0.3328(35)	32.6(20)	4c
	H12	-1.77056	0.83919	1.17354	0.3328(35)	32.6(20)	4c
	H13	-1.91651	0.64031	1.44442	0.3328(35)	32.6(20)	4c
	H14	-1.94637	0.66235	1.32122	0.3328(35)	32.6(20)	4c

	H15	-1.96205	0.7178	1.42574	0.3328(35)	32.6(20)	4c

Table A2(b). Translational and rotational axes for the matrices describing the adsorbate DMF molecules, together with their corresponding systematic errors

	X	***y***	***z***
Translational			
DMF1	-2.10446(84)	0.7786(13)	1.2643(15)
DMF2	-1.96795(73)	0.86786(65)	1.4556(11)
DMF3	-1.8560(13)	0.7722(18)	1.3105(19)
Rotational			
DMF1	-200.1(12)	-4.65(78)	2.17(31)
DMF2	58.57(84)	-33.31(66)	-131.53(89)
DMF3	52.04(81)	-11.1(13)	1.92(13)

Table A3(a). Atomic parameters from the Rietveld refinement of H-ZSM-5 pre-adsorbed with limited DMF and ethanol at 25 °C (R_{wp} = 9.005%, R_{exp} = 5.259%, X^2 = 1.712)

Species	**Atom**	***x***	***y***	***z***	**SOF**	**B_{eq} (Å^2)**	**Wychoff**
Framework	O1	0.36816(50)	0.06015(63)	0.74449(73)	1	1.718(30)	8d
	O2	0.29519(55)	0.06478(49)	0.91155(70)	1	1.718(30)	8d
	O3	0.20000(50)	0.05169(57)	0.02262(55)	1	1.718(30)	8d
	O4	0.09514(48)	0.05082(62)	0.92036(78)	1	1.718(30)	8d
	O5	0.11615(53)	0.04771(65)	0.71605(74)	1	1.718(30)	8d
	O6	0.23764(47)	0.05105(67)	0.74567(68)	1	1.718(30)	8d
	O7	0.36641(50)	0.84642(51)	0.75978(73)	1	1.718(30)	8d
	O8	0.30329(57)	0.84794(43)	0.92707(66)	1	1.718(30)	8d
	O9	0.20262(55)	0.84233(44)	0.03986(60)	1	1.718(30)	8d
	O10	0.09086(50)	0.83272(51)	0.91736(83)	1	1.718(30)	8d

	O11	0.12136(51)	0.84033(50)	0.72749(78)	1	1.718(30)	8d
	O12	0.23326(48)	0.85372(56)	0.74264(79)	1	1.718(30)	8d
	O13	0.30281(53)	0.95322(54)	0.81407(55)	1	1.718(30)	8d
	O14	0.07423(43)	0.95268(59)	0.82301(67)	1	1.718(30)	8d
	O15	0.41283(52)	0.12406(52)	0.59261(83)	1	1.718(30)	8d
	O16	0.41001(57)	1.00514(57)	0.57015(94)	1	1.718(30)	8d
	O17	0.40626(55)	0.87189(57)	0.57146(90)	1	1.718(30)	8d
	O18	0.18609(56)	0.12848(51)	0.61341(67)	1	1.718(30)	8d
	O19	0.19906(64)	-0.00304(50)	0.59427(70)	1	1.718(30)	8d
	O20	0.20508(62)	0.86455(52)	0.57121(77)	1	1.718(30)	8d
	O21	0.99504(53)	0.04374(66)	0.78773(79)	1	1.718(30)	8d
	O22	0.99488(58)	0.85313(59)	0.78702(77)	1	1.718(30)	8d
	O23	0.42169(75)	0.75	0.6357(11)	1	1.718(30)	4c
	O24	0.19631(92)	0.75	0.65161(94)	1	1.718(30)	4c
	O25	0.29415(80)	0.75	0.0652(10)	1	1.718(30)	4c
	O26	0.11518(73)	0.75	0.0661(11)	1	1.718(30)	4c
	Si1	0.42418(26)	0.05246(32)	0.65964(39)	1	0.859(15)	8d
	Si2	0.27955(24)	0.06519(26)	1.02249(39)	1	0.859(15)	8d
	Si3	0.30701(32)	0.02964(23)	-0.19411(40)	1	0.859(15)	8d
	Si4	0.12224(24)	0.05826(32)	0.02829(39)	1	0.859(15)	8d
	Si5	0.06841(27)	0.02989(26)	0.80727(42)	1	0.859(15)	8d
	Si6	0.18370(26)	0.06265(26)	0.66179(36)	1	0.859(15)	8d
	Si7	0.42446(29)	0.82906(26)	0.66408(41)	1	0.859(15)	8d
	Si8	0.30297(33)	0.86993(27)	0.80714(36)	1	0.859(15)	8d
	Si9	0.27728(26)	0.82723(23)	0.03058(38)	1	0.859(15)	8d
	Si10	0.12154(28)	0.82232(25)	0.02161(41)	1	0.859(15)	8d
	Si11	0.07141(28)	0.86702(30)	0.81750(39)	1	0.859(15)	8d
	Si12	0.18798(31)	0.82429(23)	0.67949(37)	1	0.859(15)	8d
Ethanol1	O1	-2.10464	0.75904	1.22838	0.7520(59)	29.32(94)	4c
	H2	-2.07265	0.80007	1.2183	0.7520(59)	35.2(11)	4c

	C3	-2.13891	0.748	1.13569	0.7520(59)	38.1(12)	4c
	H4	-2.12381	0.78179	1.08559	0.7520(59)	44.0(14)	4c
	H5	-2.1288	0.70191	1.11071	0.7520(59)	44.0(14)	4c
	C6	-2.21247	0.75493	1.15161	0.7520(59)	41.1(13)	4c
	H7	-2.23006	0.79178	1.1086	0.7520(59)	49.8(16)	4c
	H8	-2.23504	0.71192	1.1338	0.7520(59)	49.8(16)	4c
	H9	-2.22141	0.76571	1.22306	0.7520(59)	49.8(16)	4c
DMF1	O1	-3.02226	1.85689	0.49902	0.5396(30)	12.91(65)	4c
	C2	-3.0041	1.79275	0.47906	0.5396(30)	15.49(78)	4c
	C3	-2.95026	1.79157	0.41582	0.5396(30)	18.07(91)	4c
	C4	-2.93442	1.85937	0.39574	0.5396(30)	18.07(91)	4c
	C5	-2.97971	1.89716	0.44815	0.5396(30)	15.49(78)	4c
	C6	-2.98177	1.97213	0.44896	0.5396(30)	18.07(91)	4c
	C7	-3.03791	1.73189	0.5201	0.5396(30)	18.07(91)	4c
	H8	-2.92467	1.74696	0.38672	0.5396(30)	21.9(11)	4c
	H9	-2.89405	1.87804	0.3479	0.5396(30)	21.9(11)	4c
	H10	-2.94125	1.99211	0.40091	0.5396(30)	21.9(11)	4c
	H11	-2.97486	1.99051	0.52649	0.5396(30)	21.9(11)	4c
	H12	-3.03074	1.98949	0.4201	0.5396(30)	21.9(11)	4c
	H13	-3.01277	1.68608	0.49154	0.5396(30)	21.9(11)	4c
	H14	-3.09098	1.73168	0.49643	0.5396(30)	21.9(11)	4c
	H15	-3.03511	1.7327	0.60282	0.5396(30)	21.9(11)	4c

Table A3(b). Translational and rotational axes for the matrices describing the adsorbate molecules, together with their corresponding systematic errors

	X	***y***	***z***
Translational			
Ethanol1	-2.05677(87)	0.76004(41)	1.1929(17)
DMF1	-1.97832(66)	0.69500(30)	1.45665(90)

Rotational			
Ethanol1	106.3(25)	-4.07(51)	47.9(25)
DMF1	60.80(40)	33.04(50)	-45.36(63)

Synchrotron X-ray powder diffraction (SXRD) was employed also in **Chapter 5**. The SXRD patterns of H-USY (Si/Al=325) (**Figure 5.2c**) and H-USY (Si/Al=7.3) (**Figure 5.2d**) were refined by the Rietveld method using TOPAS software (Bruker AXS, version 5). Both refinements started from the zeolite Y (purely siliceous) crystal structure.[6] The negligible electron scattering density inside the cage after the high temperature and vacuum pre-treatment enabled an accurate optimization of the atoms of the framework. The acceptable R-factors, R_{wp} 8.916% and 9.561% clearly show the high quality of the refinement. In **Figure 5.2c**, no extra-framework Al^{3+} species exists in H-USY (Si/Al=325) (**Table A4**), consistent with the ^{27}Al NMR result. On the contrary, extra-framework Al^{3+} can be clearly refined in sodalite cages of H-USY (Si/Al=7.3) with 2.17(11) Al^{3+} per unit cell (**Table A5**). To balance the charge of the H-USY (Si/Al=7.3) when those Al^{3+} exist, some proton obtained from the 4-CN framework Al^{3+} will be lost. So, the detectable number of the BAS will less than the number of the 4-CN framework Al^{3+}. Rietveld refinement has also been applied to locate the adsorbed pyridine molecules with respect to the positions of the BAS. Their inter-atomic distances may reflect the nature and strength of the acid site adducts (**Table A6** and **A7**).[7]

Table A4. Crystallographic information files from the Rietveld refinement of H-USY (Si/Al=325)

Species	Atom	*X*	*y*	*z*	SOF	B_{eq} (Å^2)	Symmetry multiplicity/ Wyckoff
Zeolite framework	Si1	-0.05445	0.12551	0.03467	1	0.909(14)	192i
	O1	0	0.89629	0.10371	1	0.967(27)	96h
	O2	-0.00766	-0.00766	0.14149	1	0.967(27)	96g
	O3	0.07811	0.07811	-0.03595	1	0.967(27)	96g
	O4	0.07193	0.07193	0.31444	1	0.967(27)	96g

All the T-sites (T=Al, Si) of USY500 refined using the same B_{eq} parameter.
All the O-sites of USY500 share the same B_{eq} parameter.

Table A5. Crystallographic information files from the Rietveld refinement of H-USY (Si/Al=7.3)

Species	Atom	*X*	*y*	*Z*	SOF	B_{eq} (Å^2)	Symmetry multiplicity/ Wyckoff
Zeolite framework	Si1	-0.05409	0.12560	0.03495	1	0.765(11)	192i
	O1	0	0.89589	0.10411	1	0.737(18)	96h
	O2	-0.00739	-0.00739	0.13986	1	0.737(18)	96g
	O3	0.07919	0.07919	-0.03568	1	0.737(18)	96g
	O4	0.07140	0.07140	0.31774	1	0.737(18)	96g
Extra-framework Al	Al	1.365(3)	-0.142(2)	0.255(4)	0.0113(6)	5.0(17)	192i

All the T-sites (T=Al, Si) of USY500 refined using the same B_{eq} parameter.
All the O-sites of USY500 share the same B_{eq} parameter.

Table A6. Crystallographic information files from the Rietveld refinement of Py-H-USY (Si/Al=325)

Species	Atom	*X*	*y*	*Z*	SOF	B_{eq} (Å^2)	Symmetry multiplicity/ Wyckoff
Zeolite framework	Si1	-0.05445	0.12551	0.03467	1	0.685(15)	192i
	O1	0	0.89629	0.10371	1	1.152(25)	96h
	O2	-0.00766	-0.00766	0.14149	1	1.152(25)	96g
	O3	0.07811	0.07811	-0.03595	1	1.152(25)	96g
	O4	0.07193	0.07193	0.31444	1	1.152(25)	96g
Py1	translate	0.248(1)	0.251(2)	0.403(3)			

	N	0.248	0.251	0.403	0.0371(4)	5	16
	C1	0.301	0.233	0.401	0.0371(4)	7.5	16
	C2	0.333	0.224	0.447	0.0371(4)	7.5	16
	C3	0.311	0.236	0.499	0.0371(4)	7.5	16
	C4	0.228	0.262	0.453	0.0371(4)	7.5	16
	C5	0.319	0.224	0.360	0.0371(4)	7.5	16

All the T-sites (T=Al, Si) of USY500 refined using the same B_{eq} parameter.
All the O-sites of USY500 share the same B_{eq} parameter.
All the C-sites and N-sites of pyridine refined using the fixed B_{eq} 5 and 7.5, respectively.

Table A7. Crystallographic information files from the Rietveld refinement of Py-H-USY (Si/Al=7.3)

Species	**Atom**	***X***	***y***	***Z***	**SOF**	**B_{eq} (Å^2)**	**Symmetry multiplicity/ Wyckoff**
Zeolite framework	Si1	-0.05409	0.12560	0.03495	1	0.766(10)	192i
	O1	0	0.89589	0.10411	1	0.737(18)	96h
	O2	-0.00739	-0.00739	0.13986	1	0.737(18)	96g
	O3	0.07919	0.07919	-0.03568	1	0.737(18)	96g
	O4	0.07140	0.07140	0.31774	1	0.737(18)	96g
Extra-framework Al	Al	1.365(3)	-0.142(2)	0.255(4)	0.0113(6)	20(4)	192i
Py1	translate	0.249(1)	0.252(2)	0.403(3)			
	N	0.249	0.252	0.403	0.1056(46)	5	16
	C1	0.288	0.244	0.442	0.1056(46)	7.5	16
	C2	0.279	0.251	0.498	0.1056(46)	7.5	16
	C3	0.2227	0.266	0.515	0.1056(46)	7.5	16
	C4	0.185	0.274	0.476	0.1056(46)	7.5	16
	C5	0.198	0.266	0.421	0.1056(46)	7.5	16
Py2	translate	0.119(3)	1.902(4)	-0.371(4)			
	N	0.119	1.902	-0.371	0.1327(26)	5	16
	C1	0.122	1.878	-0.422	0.1327(26)	7.5	16
	C2	0.122	1.906	-0.471	0.1327(26)	7.5	16
	C3	0.118	1.964	-0.469	0.1327(26)	7.5	16

C4	0.115	1.990	-0.418	0.1327(26)	7.5	16
C5	0.116	1.958	-0.371	0.1327(26)	7.5	16

All the T-sites (T=Al, Si) of USY500 refined using the same B_{eq} parameter.
All the O-sites of USY500 share the same B_{eq} parameter.
All the C-sites and N-sites of pyridine refined using the fixed B_{eq} 5 and 7.5, respectively.

Synchrotron X-ray powder diffraction (SXRD) was employed also in **Chapter 6**. The crystallographic and atomic parameters from Rietveld refinement are summarized in **Tables A8-A11.**

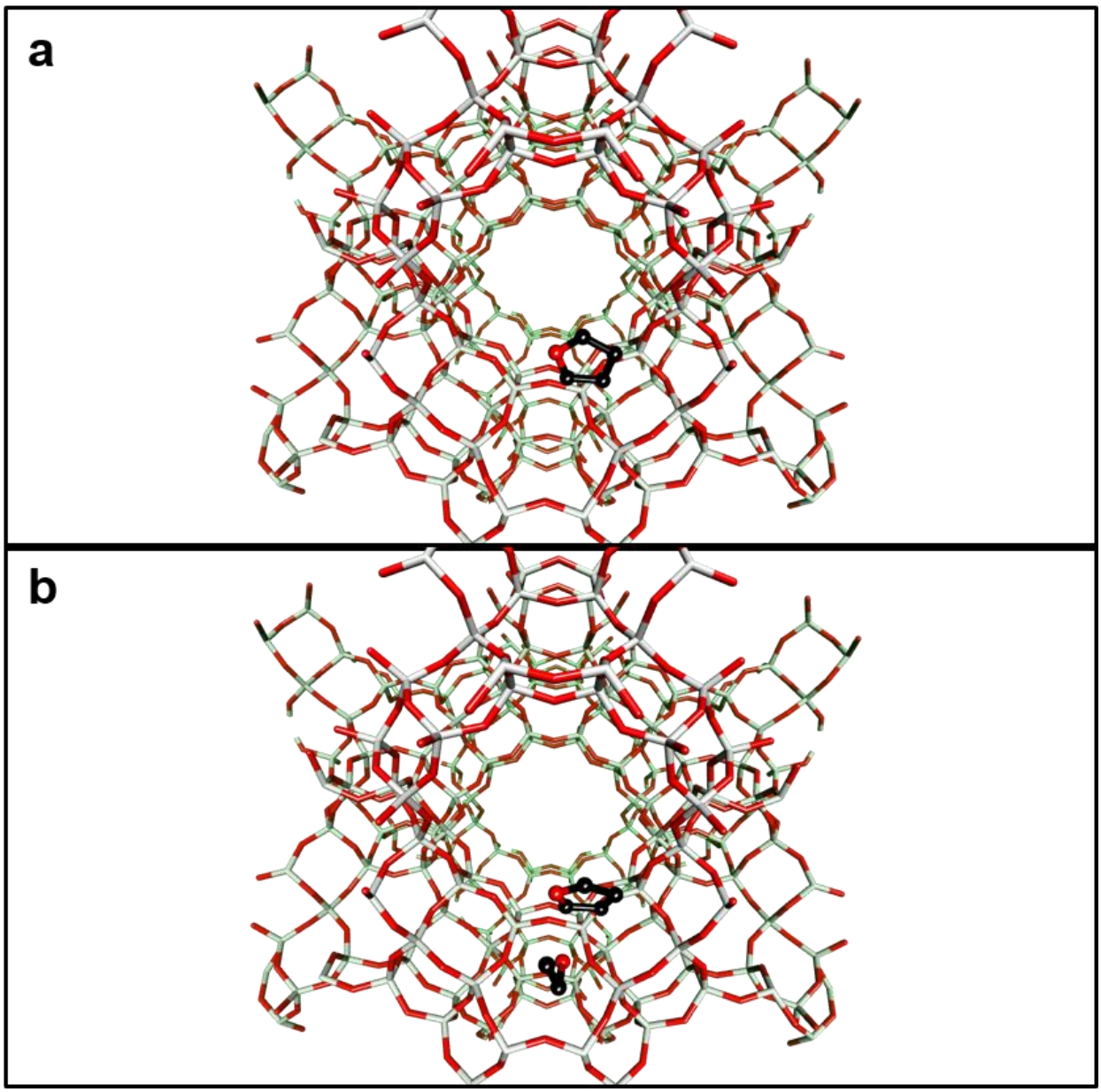


Figure A15. Rietveld refinement derived crystal structures of a unit cell of H-USY (Si/Al=6) pre-adsorbed with (**a**) ethylene and furan, and (**b**) ethanol and furan. Their corresponding atomic parameters are summarized in **Tables A8-A9**. Symmetry for the adsorbed molecules is disregarded for clarity. Atoms are displayed in the ball-and-stick model, with red = oxygen, white = silicon/aluminium, and black = carbon.

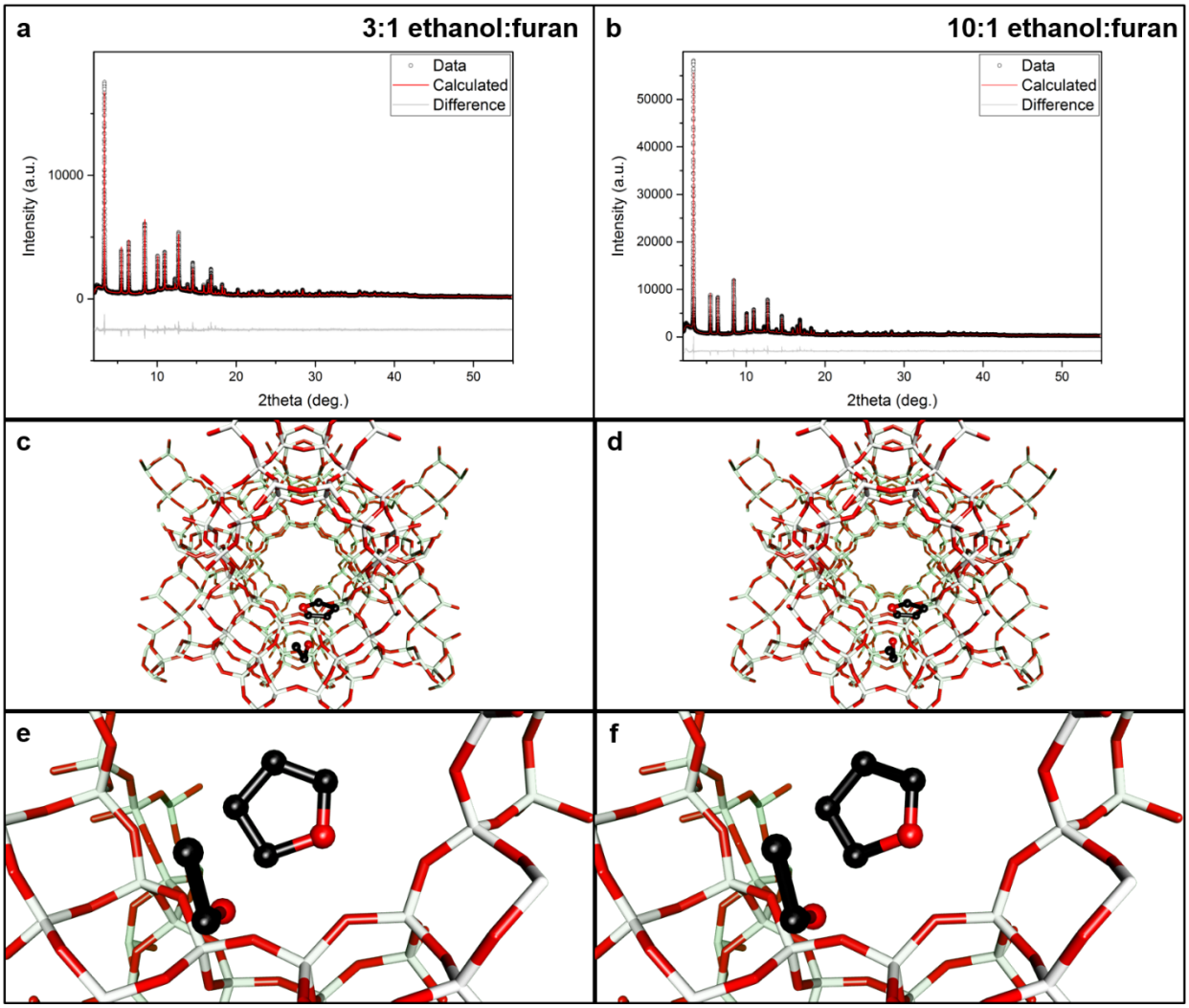


Figure A16. (**a,b**) Rietveld refinement profiles, and the derived crystal structures of a unit cell (**c,d**), a zoom-in (**e,f**), of H-USY (Si/Al=6) pre-adsorbed with ethanol and furan at ratios of 3:1 and 10:1. Their corresponding atomic parameters are summarized in **Tables A10-A11**. Symmetry for the adsorbed molecules is disregarded for clarity. Atoms are displayed in the ball-and-stick model, with red = oxygen, white = silicon/aluminium, and black = carbon.

Table A8. Atomic parameters derived from the SXRD measurements of H-USY (Si/Al=6) pre-adsorbed with ethylene and furan, measured at 25 °C. R_{wp} = 9.165%, space group = *Fd-3m*, a = 24.40977(7) Å

Species	Atom	*x*	*y*	*Z*	SOF	B_{eq} (Å^2)	Wychoff
Zeolite framework	Si	0.12595(5)	-0.05326(5)	0.03561(5)	1	0.740(19)	192i
	O1	-0.00314(10)	-0.00314(10)	0.14509(11)	1	0.487(31)	192i
	O2	0.17493(9)	0.17493(8)	-0.03131(11)	1	0.487(31)	192i
	O3	0.17973(10)	0.17972(9)	0.31495(13)	1	0.487(31)	192i
	O4	0.10593(9)	-0.10592(8)	0	1	0.487(31)	96h
Furan	Cg1	0.09006	0.29866	0.67781	0.19951(52)	8	192i
	Og2	0.12946	0.27345	0.65907	0.19951(52)	8	192i
	Cg3	0.12891	0.22699	0.67857	0.19951(52)	8	192i
	Cg4	0.06060	0.26775	0.71225	0.19951(52)	8	192i
	Cg5	0.08604	0.21963	0.71325	0.19951(52)	8	192i
	Hg6	0.08446	0.34132	0.66441	0.19951(52)	9.6	192i
	Hg7	0.16173	0.19880	0.66593	0.19951(52)	9.6	192i
	Hg8	0.02343	0.27934	0.73493	0.19951(52)	9.6	192i
	Hg9	0.07526	0.18254	0.73645	0.19951(52)	9.6	192i

Site occupancy factor (SOF). Isotropic displacement factor (B_{eq}). The sites of the adsorbed molecules are generated by rigid-body Z-matrices, their corresponding e.s.d. are reflected by the rotational and translational axes.

Table A9. Atomic parameters derived from the SXRD measurements of H-USY (Si/Al=6) pre-adsorbed with ethanol and furan at a ratio of 1:1, measured at 25 °C. Rwp = 7.936%, space group = Fd-3m, a = 24.42246(7) Å

Species	Atom	*x*	*y*	*Z*	SOF	B_{eq} (Å^2)	Wychoff
Zeolite framework	Si	0.12589(6)	-0.05300(5)	0.03647(5)	1	1.106(21)	192i
	O1	-0.00123(11)	-0.00123(11)	0.14277(12)	1	1.038(35)	192i

	O2	0.17110(10)	0.17110(10)	-0.02782(14)	1	1.038(35)	192i
	O3	0.17888(12)	0.17888(12)	0.31986(15)	1	1.038(35)	192i
	O4	0.10810(10)	-0.10810(10)	0	1	1.038(35)	96h
Furan	Cg1	0.08556	0.29714	0.67033	0.15429(41)	8	192i
	Og2	0.12340	0.26976	0.68917	0.15429(41)	8	192i
	Cg3	0.10985	0.25394	0.73502	0.15429(41)	8	192i
	Cg4	0.04342	0.30039	0.70526	0.15429(41)	8	192i
	Cg5	0.05898	0.27170	0.74879	0.15429(41)	8	192i
	Hg6	0.09106	0.31455	0.62916	0.15429(41)	9.6	192i
	Hg7	0.13936	0.22866	0.75779	0.15429(41)	9.6	192i
	Hg8	0.00432	0.32199	0.69951	0.15429(41)	9.6	192i
	Hg9	0.03639	0.26396	0.78698	0.15429(41)	9.6	192i
Ethanol	Oe1	-2.23285	0.78013	1.29382	0.15429(41)	8	192i
	He2	-2.24459	0.78227	1.25252	0.15429(41)	9.6	192i
	Ce3	-2.24773	0.83124	1.31917	0.15429(41)	8	192i
	He4	-2.26531	0.85566	1.29139	0.15429(41)	9.6	192i
	He5	-2.27405	0.82419	1.34973	0.15429(41)	9.6	192i
	Ce6	-2.19740	0.85852	1.34143	0.15429(41)	8	192i
	He7	-2.19261	0.89504	1.32355	0.15429(41)	9.6	192i
	He8	-2.20133	0.86354	1.38187	0.15429(41)	9.6	192i
	He9	-2.16466	0.83517	1.33371	0.15429(41)	9.6	192i

Site occupancy factor (SOF). Isotropic displacement factor (B_{eq}). The sites of the adsorbed molecules are generated by rigid-body Z-matrices, their corresponding e.s.d. are reflected by the rotational and translational axes.

Table A10. Atomic parameters derived from the SXRD measurements of H-USY (Si/Al=6) pre-adsorbed with ethanol and furan at a ratio of 3:1, measured at 25 °C. R_{wp} = 7.631%, space group = *Fd-3m*, a = 24.40260(8) Å

Species	Atom	*x*	*y*	*Z*	SOF	B_{eq} (Å^2)	Wychoff
Zeolite framework	Si	0.12441(8)	-0.05256(6)	0.03682(6)	1	0.743(23)	192i
	O1	0.00191(10)	0.00191(10)	0.13833(17)	1	0.654(41)	192i
	O2	0.17106(11)	0.17106(11)	-0.02552(15)	1	0.654(41)	192i
	O3	0.17911(15)	0.17911(15)	0.32073(15)	1	0.654(41)	192i
	O4	0.10960(12)	-0.10960(12)	0	1	0.654(41)	96h
Furan	Cg1	0.08592	0.28031	0.73964	0.05754(72)	8	192i
	Og2	0.08664	0.24876	0.77894	0.05754(72)	8	192i
	Cg3	0.03962	0.24492	0.79669	0.05754(72)	8	192i
	Cg4	0.03543	0.29934	0.72970	0.05754(72)	8	192i
	Cg5	0.00391	0.27607	0.76751	0.05754(72)	8	192i
	Hg6	0.12507	0.28836	0.71879	0.05754(72)	9.6	192i
	Hg7	0.03299	0.21799	0.83223	0.05754(72)	9.6	192i
	Hg8	0.02251	0.32799	0.69739	0.05754(72)	9.6	192i
	Hg9	-0.0404	0.28068	0.77395	0.05754(72)	9.6	192i
Ethanol	Oe1	-2.15297	0.79217	1.32821	0.1173(11)	8	192i
	He2	-2.15085	0.75091	1.34023	0.1173(11)	9.6	192i
	Ce3	-2.19440	0.79637	1.28639	0.1173(11)	8	192i
	He4	-2.21056	0.75937	1.27938	0.1173(11)	9.6	192i
	He5	-2.22386	0.82198	1.29884	0.1173(11)	9.6	192i
	Ce6	-2.16918	0.81782	1.23460	0.1173(11)	8	192i
	He7	-2.17412	0.79036	1.20458	0.1173(11)	9.6	192i
	He8	-2.18739	0.85298	1.22406	0.1173(11)	9.6	192i
	He9	-2.12918	0.82443	1.24058	0.1173(11)	9.6	192i

Site occupancy factor (SOF). Isotropic displacement factor (B_{eq}). The sites of the adsorbed molecules are generated by rigid-body Z-matrices, their corresponding e.s.d. are reflected by the rotational and translational axes.

Table A11. Atomic parameters derived from the SXRD measurements of H-USY (Si/Al=6) pre-adsorbed with ethanol and furan at a ratio of 10:1, measured at 25 °C. R_{wp} = 7.281%, space group = *Fd-3m*, a = 24.42587(10) Å

Species	Atom	*x*	*y*	*Z*	SOF	B_{eq} (Å^2)	Wychoff
Zeolite framework	Si	0.12523(8)	-0.05271(6)	0.03672(6)	1	0.992(25)	192i
	O1	0.00078(13)	0.00078(13)	0.14356(15)	1	1.097(45)	192i
	O2	0.17219(11)	0.17219(11)	-0.02599(15)	1	1.097(45)	192i
	O3	0.18063(14)	0.18063(14)	0.31936(16)	1	1.097(45)	192i
	O4	0.10971(12)	-0.10971(12)	0	1	1.097(45)	96h
Furan	Cg1	0.05052	0.28828	0.73082	0.0885(11)	8	192i
	Og2	0.02195	0.26585	0.76569	0.0885(11)	8	192i
	Cg3	0.04983	0.23048	0.78823	0.0885(11)	8	192i
	Cg4	0.10107	0.26714	0.72922	0.0885(11)	8	192i
	Cg5	0.10133	0.22839	0.76740	0.0885(11)	8	192i
	Hg6	0.03164	0.32125	0.70664	0.0885(11)	9.6	192i
	Hg7	0.03026	0.20631	0.82081	0.0885(11)	9.6	192i
	Hg8	0.13518	0.27902	0.70232	0.0885(11)	9.6	192i
	Hg9	0.13496	0.20100	0.77950	0.0885(11)	9.6	192i
Ethanol	Oe1	-2.22026	0.82594	1.28083	0.2173(17)	8	192i
	He2	-2.23245	0.78485	1.27749	0.2173(17)	9.6	192i
	Ce3	-2.18259	0.83690	1.23683	0.2173(17)	8	192i
	He4	-2.17755	0.80302	1.21440	0.2173(17)	9.6	192i
	He5	-2.19752	0.86680	1.21319	0.2173(17)	9.6	192i
	Ce6	-2.12846	0.85429	1.26004	0.2173(17)	8	192i
	He7	-2.09937	0.82815	1.24793	0.2173(17)	9.6	192i

He8	-2.11935	0.89192	1.24675	0.2173(17)	9.6	192i
He9	-2.13052	0.85439	1.30093	0.2173(17)	9.6	192i

Site occupancy factor (SOF). Isotropic displacement factor (B_{eq}). The sites of the adsorbed molecules are generated by rigid-body Z-matrices, their corresponding e.s.d. are reflected by the rotational and translational axes.

8.8 References

1. Association, I.Z. *Database of Zeolite Structures*. 2017 [Accessed May 31 2017].

2. Tao, Y., H. Kanoh, L. Abrams, and K. Kaneko, *Mesopore-Modified Zeolites: Preparation, Characterization, and Applications.* **Chemical Reviews**, 2006. 106: p. 896-910.

3. Williams, C.L., K.P. Vinter, C.-C. Chang, R. Xiong, et al., *Kinetic regimes in the tandem reactions of H-BEA catalyzed formation of p-xylene from dimethylfuran.* **Catalysis Science & Technology**, 2016. 6: p. 178-187.

4. Ruthven, D.M. and M.F. Post, *Diffusion in zeolite molecular sieves.* **Studies in surface science and catalysis**, 2001. 137: p. 525-577.

5. Jacobs, P.A. and R.A. van Santen, *Zeolites: facts, figures, future*. Vol. 49. 1989: Elsevier.

6. Colligan, M., P.M. Forster, A.K. Cheetham, Y. Lee, et al., *Synchrotron X-ray powder diffraction and computational investigation of purely siliceous zeolite Y under pressure.* **J. Am. Chem. Soc.**, 2004. 126: p. 12015-12022.

7. Lo, B.T.W., L. Ye, J. Qu, J. Sun, et al., *Elucidation of adsorbate structures and interactions on Brønsted acid sites in H-ZSM-5 by synchrotron X-ray powder diffraction.* **Angew. Chem. Int. Ed.**, 2016. 55: p. 1-5.